

Document Version

Final published version

Citation (APA)

Valencia, A. A. (2026). *The Impact of Syn-Depositional Compaction on Simulated River-Dominated Deltas*. [Dissertation (TU Delft), Delft University of Technology]. <https://doi.org/10.4233/uuid:6d091d54-cb0f-4abe-a387-977c13671e10>

Important note

To cite this publication, please use the final published version (if applicable). Please check the document version above.

Copyright

In case the licence states “Dutch Copyright Act (Article 25fa)”, this publication was made available Green Open Access via the TU Delft Institutional Repository pursuant to Dutch Copyright Act (Article 25fa, the Taverne amendment). This provision does not affect copyright ownership. Unless copyright is transferred by contract or statute, it remains with the copyright holder.

Sharing and reuse

Other than for strictly personal use, it is not permitted to download, forward or distribute the text or part of it, without the consent of the author(s) and/or copyright holder(s), unless the work is under an open content license such as Creative Commons.

Takedown policy

Please contact us and provide details if you believe this document breaches copyrights. We will remove access to the work immediately and investigate your claim.

The Impact of Syn-Depositional Compaction on Simulated River-Dominated Deltas



Ayunda Aulia Valencia

The Impact of Syn-Depositional Compaction on Simulated River-Dominated Deltas

Dissertation

For the purpose of obtaining the degree of doctor
at Delft University of Technology
by the authority of the Rector Magnificus Prof. dr. ir. H. Bijl,
Chair of the Board for Doctorates
To be defended publicly on
Wednesday 13, May 2026 at 15:00 o'clock

by

Ayunda Aulia VALENCIA

This dissertation has been approved by the promotor

Dr. J.E.A. Storms

Prof. dr. A.W. Martinus

Composition of Doctoral Committee:

Rector Magnificus

Chairperson

Dr. J.E.A. Storms

Delft University of Technology, promotor

Prof. dr. A.W. Martinus

Delft University of Technology, promotor

Independent members:

Prof. dr. P.J. Vardon

Delft University of Technology

Prof. dr. E. Stouthamer

Utrecht University

Prof. dr. E. Anthony

Aix-Marseille University, France

dr. P.S.J. Minderhoud

Wageningen University and Research

Prof. dr. ir. J.D. Jansen

Delft University of Technology, reserve member

Other Members:

Dr. H. van der Vegt

Deltares, The Netherlands

Dr. H.R.A. Jagers of Deltares has contributed to the preparation of this dissertation

This research was financially supported by LPDP

Cover Design: ProefschriftMaken

and Printed by: ProefschriftMaken

ISBN/EAN: 978-94-6518-307-7

An electronic version of this dissertation is available at: <https://tinyurl.com/ycxk8hpz>

Contents	
Summary.....	9
Samenvatting.....	11
Chapter 1: Introduction	13
1.1. Motivation	13
1.2. Approach for Investigating Syn-Depositional Compaction Impact on Delta Development.....	15
1.3. Background Knowledge of Sediment Compaction	18
1.4. Background Knowledge of Compaction Modelling Methods.....	19
1.5. Background Knowledge of Delta Morphodynamics, Sediment Distribution, and Levee Breaching	21
1.5.1. Delta Morphodynamics.....	21
1.5.2. Sediment Distribution.....	23
1.5.3. Levee Breaching	23
1.6. Research Questions	24
1.6.1. How does syn-depositional compaction impact simulated delta morphodynamics?	25
1.6.2. How does syn-depositional compaction affect sediment distribution in the simulated delta?	25
1.6.3. How does syn-depositional compaction influence simulated levee breaching?	26
1.7. Thesis Outline	26
Chapter 2: The impact of clastic syn-depositional compaction on fluvial-dominated delta morphodynamics.....	27
2.1. Introduction.....	28
2.2. Methodology	29
2.2.1. Primary Compaction	30
2.2.2. Secondary Compaction	31
2.2.3. Implementation of Compaction Formula into Delft3D	32
2.3. Building 4D Synthetic Deltas	34
2.3.1. Model Setup.....	34
2.3.2. Scenario Setup	36
2.4. Post-processing Delft3D Output Data	39

2.4.1. Delta Top Geometry	39
2.4.2. Distribution of Deposited Mass	41
2.4.3. Accommodation	42
2.5. Impact of Compaction on Delta Evolution	42
2.5.1. Delta Top Geometry	43
2.5.2. Distribution of Deposited Mass	46
2.5.3. Accommodation Generated by Compaction.....	49
2.6. Interpretation of The Impact of Compaction on Delta Morphodynamics	50
2.7. Discussion	53
2.8. Conclusion	54
Chapter 3: The influence of syn-depositional compaction on clastic sediment distribution in river-dominated deltas: a modelling study.....	57
3.1. Introduction.....	58
3.2. Methodology for Compacting Simulated Delta Deposits	60
3.2.1. Primary Compaction	61
3.2.2. Secondary Compaction	61
3.2.3. Subsidence	62
3.3. Modelling Parameters and Scenarios.....	63
3.3.1. Modelling Parameters.....	63
3.3.2. Modelling Scenarios	66
3.4. Description of Metrics Used to Analyse the Impact of Syn-depositional Compaction on Sediment Distribution in Simulated Deltas.....	69
3.4.1. Depositional Elements	69
3.4.2. Distribution of Sedimentation in Depositional Elements.....	69
3.4.3. Accommodation	70
3.4.4. Depositional Segments	70
3.5. Delta Simulation Results Analysis.....	72
3.5.1. Distribution of Sedimentation in Depositional Elements.....	72
3.5.2. Accommodation	75
3.5.3. Depositional Segment.....	76
3.6. Interpretation of Sediment Distribution in Delta Simulation under the Influence of Syn-Depositional Compaction	78
3.7. Discussion.....	79

3.8. Conclusion	81
3.9. Data Availability.....	82
Chapter 4: The Effect of Compaction-Influenced Sediment Erodibility on Simulated Levee Breaching	83
4.1. Compaction and Erodibility of Sediment in Delft3D.....	84
4.2. Compaction and Erodibility of Sediment in Delft3D.....	85
4.2.1. Compaction	85
4.2.2. Critical Bed Shear Stress for Erosion	86
4.3. Model Setup and Scenario	87
4.4. Metrics for Analysing Simulation Results	88
4.5. Analysis of Simulation Results	92
4.5.1. Description of Levee Breaching.....	92
4.5.2. Interpretation of Levee Breaching	94
4.5.3. Critical Bed Shear Stress for Erosion in Modelled Stratigraphy	94
4.5.4. Conceptual Model of Levee Breaching	97
4.6. Discussion.....	99
4.7. Conclusion	100
4.8. Data Availability.....	101
Chapter 5: Synthesis	103
5.1. Answer to Research Questions.....	103
5.1.1. How does syn-depositional compaction impact simulated delta morphodynamics?	103
5.1.2. How does syn-depositional compaction affect sediment distribution in the simulated delta?	105
5.1.3. How does syn-depositional compaction influence simulated levee breaching?	106
5.2. Future Work	108
5.2.1. Improving Compaction Formulations in Delft3D 4 – FLOW Code.....	108
5.2.2. Comparing Models to Natural Systems	110
5.2.3. Assessing The Impact of Syn-Depositional Compaction on Delta Plain and Mouth Bar Processes	112
Supplementary Materials	115
Supplementary Materials A.....	115
A1. Validation of Compaction formulas	115

A2. Compaction Implementation in Delft3D.....	116
A3. Temporal Bathymetry Development of Simulated Deltas.....	120
A4. Identification of Simulated Deltas' Sub-environments.....	145
A5. Morphology Plots in Time Series	148
Supplementary Materials B.....	149
B1. Derivation of Improved Secondary Compaction Formula	149
B2. Implementation of Compaction Formulations into Delft3D.....	151
B3. Implementation of New Erosion Formula into Delft3D	154
B4. Ratio of Sedimentation and Erosion in Simulated Deltas	155
B5. Compaction Realization Vs Compaction Potential in Simulated Deltas.....	156
B6. Bathymetry Development of the Simulated Deltas	157
B7. Identification of Depositional Elements.....	167
B8. Fringe Areas	178
B9. Validation of Depositional Elements.....	181
B10. Sediment Distribution Plots.....	183
B11. Backwater Effect	187
Supplementary Materials C.....	188
C1. Deposition and Erosion in Simulated Deltas.....	188
C2. Validation of Critical Bed Shear Stress Formula.....	190
C3. Levee Identification.....	191
C4. Superelevation & Gradient Advantage	191
C5. Channel Aggradation.....	192
C6. Water Depth at Breach Sites.....	193
C7. Strike and Dip Sections	195
REFERENCES.....	201
ACKNOWLEDGEMENT.....	215
CURRICULUM VITAE	217

Summary

Deltas are dynamic landforms that develop through the interaction of sediment supply, hydrodynamic, and accommodation. They support large human populations and important ecosystems, yet many deltas are increasingly threatened by subsidence and sea-level rise. One of key processes contributing to subsidence is sediment compaction. Compaction is an inherent process in delta systems. However, the impact of syn-depositional compaction during active delta formation over millennial timescales remains poorly constrained. This dissertation investigates how syn-depositional compaction influences delta morphodynamics, sediment distribution, and levee breaching, using a process-based numerical modelling approach. These questions are addressed in Chapter 2, 3, and 4 of this dissertation.

To address the above-mentioned questions, we apply and progressively refine compaction formulations within the Delft3D 4 - FLOW code. This approach focuses on mechanical compaction because it contributes to the largest sediment volume reduction compared to biological and chemical compaction. Additionally, it mainly operates within the active part of the delta top. This compaction type occurs in two phases, primary and secondary compaction, driven by overburden weight and simulated time. Both phases lead to pore fluid expulsion, resulting in sediment volume reduction and lowering of bed surface (subsidence). By switching compaction on and off in model simulations, the effects of syn-depositional compaction on delta development are assessed. Quantitative metrics are developed to enable comparison between simulations, including changes in delta geometry, sediment mass distribution, accommodation generation, and sediment erodibility.

Modelling results show that syn-depositional compaction generates additional accommodation during delta development, which alters delta morphology. Morphological changes are more prominent in the mud-rich deltas than sand-rich deltas, which experience larger compaction-induced volume reduction for the same compaction rate scenario. In higher compaction rate scenarios, accommodation increases at the delta top, leading to more sedimentation and evenly distributed sediment at the delta top. This leads to a less significant area increase and a wider delta top with a smoother coastline. These morphological responses emerge from feedback between compaction-induced additional accommodation, sedimentation, and channel dynamics.

Additional accommodation generated by syn-depositional compaction also affects the distribution of sediment mass across delta depositional areas. Modelling results show that increased accommodation on the delta plain promotes sedimentation in this area,

thereby reducing sediment delivery to the mouth bar and beyond. Further increases in accommodation lead to enhanced lateral sediment redistribution associated with channel relocation, with sedimentation mainly occurs in the mouth bar. Changes in sedimentation within a depositional area are accompanied by compensating changes elsewhere, indicating interdependencies within the delta-wide sediment budget influenced by syn-depositional compaction. These results demonstrate that compaction-induced accommodation redistributes sediment beyond the immediate subsidence area, affecting sedimentation across the entire delta system.

In addition to generating additional accommodation, syn-depositional compaction increases sediment resistance to resuspension. Levees act as key sediment conduits in delta systems, and the location and timing of levee breaching are commonly assessed using proxies that describe the influence of topography on hydraulic forcing acting on levee deposits. However, the role of sediment properties, particularly levee resistance to resuspension, remains poorly constrained. The modelling results show that commonly used proxies, such as superelevation and gradient advantage, are relevant in predicting when and where levee breaching is initiated, but they are insufficient to describe breach progression, which depends on the balance between flow-induced shear stress and sediment resistance to resuspension. Syn-depositional compaction modifies both bed elevation and sediment erodibility, thereby influencing whether breaches are sustained or abandoned.

Overall, this dissertation demonstrates that syn-depositional compaction is a fundamental process influencing simulated delta evolution over millennial timescale. While numerical models cannot capture all processes operating in natural deltas, they provide a controlled framework to explore process interactions that are difficult to observe directly in the field. The results show that syn-depositional compaction affects delta morphology, sediment distribution, and levee breaching, and therefore represents a critical mechanism that should be included in process-based delta modelling studies.

Samenvatting

Delta's zijn dynamische landvormen die ontstaan door de interactie tussen sedimentaanvoer, hydrodynamica en accommodatie. Zij herbergen grote menselijke populaties en belangrijke ecosystemen, maar worden in toenemende mate bedreigd door bodemdaling en zeespiegelstijging. Een van de belangrijkste processen die bijdraagt aan bodemdaling is sedimentcompactie. Compactie is een inherent proces in deltasystemen, maar de invloed van syn-depositionele compactie tijdens actieve deltavorming op millennialle tijdschalen is nog onvoldoende gekwantificeerd. Dit proefschrift onderzoekt hoe syn-depositionele compactie de delta-morfodynamica, sedimentverdeling en doorbraak van oeverwallen (levees) beïnvloedt, met behulp van een procesgebaseerde numerieke modelbenadering. Deze onderzoeksvragen worden behandeld in hoofdstukken 2, 3 en 4 van dit proefschrift.

Om deze vragen te beantwoorden, worden compactieformuleringen toegepast en stapsgewijs verfijnd binnen de Delft3D 4-FLOW-code. De aanpak richt zich op mechanische compactie, omdat deze in vergelijking met biologische en chemische compactie de grootste reductie in sedimentvolume veroorzaakt. Daarnaast vindt mechanische compactie voornamelijk plaats binnen het actieve deel van de deltavlakte. Dit type compactie treedt op in twee fasen, primaire en secundaire compactie, gedreven door overbelasting en gesimuleerde tijd. Beide fasen leiden tot het uitpersen van poriënvloeistof, wat resulteert in een afname van het sedimentvolume en verlaging van het bodemoppervlak (bodemdaling). Door compactie in modelsimulaties aan en uit te schakelen, worden de effecten van syn-depositionele compactie op de deltavorming geëvalueerd. Kwantitatieve maatstaven worden ontwikkeld om simulaties met elkaar te vergelijken, waaronder veranderingen in deltageometrie, sedimentmassaverdeling, accommodatiegeneratie en sedimentgevoeligheid voor erosie.

De modelresultaten tonen aan dat syn-depositionele compactie tijdens de deltavorming extra accommodatie creëert, wat leidt tot veranderingen in de deltavorm. Morfologische veranderingen zijn duidelijker zichtbaar in modderrijkere delta's dan in zandrike delta's, omdat deze bij hetzelfde compactiescenario een grotere compactiegeïnduceerde volumevermindering ondervinden. Bij hogere compactiesnelheden neemt de accommodatie op de deltavlakte toe, wat leidt tot meer sedimentatie en een gelijkmatigere sedimentverdeling op de deltavlakte. Dit resulteert in een minder sterke toename van het delta-oppervlak, een bredere deltavlakte en een gladdere kustlijn. Deze morfologische responsen ontstaan uit terugkoppelingen tussen compactiegeïnduceerde accommodatie, sedimentatie en kanaaldynamiek.

De extra accommodatie die door syn-depositionele compactie wordt gegenereerd, beïnvloedt ook de verdeling van sedimentmassa over de verschillende afzettingsomgevingen binnen de delta. Modelresultaten laten zien dat een toename van accommodatie op de deltavlake sedimentatie in dit gebied bevordert, waardoor de sedimentaanvoer naar de mondingsbanken en verder offshore afneemt. Verdere toename van accommodatie leidt tot versterkte laterale sedimentherverdeling als gevolg van kanaalverplaatsing, waarbij sedimentatie voornamelijk in de mondingsbanken plaatsvindt. Veranderingen in sedimentatie binnen één afzettingsgebied gaan gepaard met compenserende veranderingen elders, wat wijst op onderlinge afhankelijkheden binnen het delta-brede sedimentbudget dat door syn-depositionele compactie wordt beïnvloed. Deze resultaten tonen aan dat door compactie geïnduceerde accommodatie sediment herverdeelt buiten het directe gebied van bodemdaling en de sedimentatie in het gehele deltasysteem beïnvloedt.

Naast het creëren van extra accommodatie vergroot syn-depositionele compactie ook de weerstand van sediment tegen resuspensie. Oeverwallen fungeren als belangrijke sedimenttransportstructuren in deltasystemen, en de locatie en timing van oeverwaldoorbraken worden doorgaans beoordeeld met behulp van indicatoren die de invloed van topografie op de hydraulische belasting van oeverwalafzettingen beschrijven. De rol van sedimenteigenschappen, in het bijzonder de weerstand van oeverwallen tegen resuspensie, is echter nog onvoldoende bekend. De modelresultaten tonen aan dat veelgebruikte indicatoren, zoals superelevatie en gradiëntvoordeel, relevant zijn voor het voorspellen van wanneer en waar oeverwaldoorbraken worden geïnitieerd, maar onvoldoende zijn om de verdere ontwikkeling van een doorbraak te beschrijven. De voortgang van een doorbraak wordt bepaald door de balans tussen door stroming veroorzaakte schuifspanning en de weerstand van het sediment tegen resuspensie. Syn-depositionele compactie beïnvloedt zowel de bodemhoogte als de sedimentgevoeligheid voor erosie, en bepaalt daarmee of doorbraken aanhouden of worden verlaten.

Samenvattend laat dit proefschrift zien dat syn-depositionele compactie een fundamenteel proces is dat de gesimuleerde delta-evolutie op millenniaire tijdschalen beïnvloedt. Hoewel numerieke modellen niet alle processen in natuurlijke delta's kunnen weergeven, bieden zij een gecontroleerd kader om procesinteracties te onderzoeken die in het veld moeilijk direct waar te nemen zijn. De resultaten tonen aan dat syn-depositionele compactie invloed heeft op deltavorm, sedimentverdeling en oeverwaldoorbraken, en daarom een essentieel mechanisme vormt dat moet worden opgenomen in procesgebaseerde deltamodelstudies.

Chapter 1: Introduction

1.1. Motivation

Deltas form where a sediment-laden river flow enters a standing body of water, such as a sea or a lake, causing a reduction in flow velocity and subsequent sediment deposition. Delta regions sustain high biodiversity and provide fertile soils for agriculture, abundant natural resources (including freshwater, oil, and gas), and productive fisheries (Day & Giosan, 2008). Consequently, many deltas have become major centers of economic activity, hosting large cities and ports that support millions of inhabitants (Anthony et al., 2024; Day & Giosan, 2008; Edmonds et al., 2020; Nienhuis et al., 2023).

Delta development is affected by many factors. Previous field, flume, and modelling studies linked delta plan-view geometry (planform) to the distribution of sediment across delta regions, which is governed by sediment delivery through distributary channels and sediment redistribution by waves and tides (Galloway, 1975). Additional controls influencing delta development include grain size and composition (Burpee et al., 2015; Caldwell & Edmonds, 2014; Orton & Reading, 1993; van der Veegt et al., 2020), sediment cohesiveness (Edmonds & Slingerland, 2010; Hoyal & Sheets, 2009; Martin et al., 2009), sediment transport (van der Veegt et al., 2016), vegetation (Albernaz et al., 2020; Nienhuis et al., 2018), relative sea-level variations (Jerolmack, 2009; Liang et al., 2016; Nienhuis et al., 2023), and sediment volume delivered to the delta (Nienhuis et al., 2020; Syvitski & Saito, 2007)

When deposition rates exceed the capacity waves and tides to distribute the sediment, significant sediment accumulation occurs in both subaerial and subaqueous regions, causing the delta to build up and out (Anthony, 2015; Anthony et al., 2024). For the delta surface to build up, accommodation must be available for new sediment to accumulate. Otherwise, the sediment is transported further seaward or diverted to other regions (Blum & Törnqvist, 2000). In modern delta, accommodation is increasingly influenced by relative sea-level rise, driven by bed-surface lowering (subsidence) and global sea-level rise, posing flooding hazards to populated coastal regions (Anthony et al., 2024; Edmonds et al., 2020; Syvitski et al., 2009).

The subsidence can be intensified by human activities. In rapidly urbanizing delta such as Jakarta, for instance, excessive groundwater extraction to meet human water demands has caused rapid subsidence that, combined with global sea-level rise, leads to accelerated relative sea-level rise and amplified flood hazards (Abidin et al., 2011; Edmonds et al., 2020; Minderhoud et al., 2017, 2020; Nienhuis et al., 2023). Mitigating these risks requires better understanding of the mechanisms causing subsidence, including sediment

compaction. The first step towards this goal is to investigate natural compaction, a critical yet underexplored control on delta development. This dissertation focuses on delta formation over millennial timescales, consistent with timescales over which many Holocene deltas have formed and continue to evolve.

Syn-depositional compaction occurs during delta formation, driven by sediment self-weight and/or overlying weight. This mechanism expels pore fluid and rearranges grains, leading to a reduction of bulk sediment volume through porosity reduction and resulting in subsidence, while grain mass is conserved (Alberts, 2005; Mesri, 2003; von Terzaghi, 1923). Grain tightening increases bulk density and decreases fluid content, which in turn enhances sediment resistance to resuspension (Bale et al., 2006, 2007; Grabowski et al., 2011; van Rijn et al., 2020; Winterwerp & van Kesteren, 2004). Although syn-depositional compaction always occurs in all deltas, its role in delta formation remains poorly understood, as most studies address only the effects of volume reduction (Nienhuis et al., 2018; Winterwerp et al., 2018; Xotta et al., 2022; Zoccarato et al., 2018), excluding the increase in sediment resistance to resuspension.

The volume reduction caused by syn-depositional compaction has geomorphic implications. It creates additional accommodation, promoting sedimentation and forming a feedback loop among compaction, accommodation, and sedimentation (Nienhuis et al., 2018). This dynamic, in turn, may affect sediment distribution across delta regions and shape delta planform morphology. Syn-depositional compaction also modulates distributary channel flow. Distributary channels are flanked by levees, elevated ridges constructed through repeated overbank deposition that slope towards the adjacent delta plain (Brierley et al., 1997). Levee breaching redirects flow and sediment pathways, altering sediment distribution across the delta. Previous field, flume, and conceptual studies showed that breach initiation is sensitive to relative elevation and slope among distributary channels, levees, and delta plains (Ganti et al., 2016; Gearon et al., 2024; Gearon & Edmonds, 2025; Hoyal & Sheets, 2009; Slingerland & Smith, 1998; Törnqvist & Bridge, 2002).

By altering sediment volume, syn-depositional compaction perturbs local elevations and slopes among distributary channels, levees, and delta plains, thereby influencing flow-induced shear stress along levees. Moreover, compaction affects the resistance of levee deposits to resuspension. The interplay between flow-induced shear stress and levee resistance likely governs the initiation and progression of levee breaches, which remain poorly understood. Overall, investigating the influence of syn-depositional compaction on delta planform morphology, sediment distribution, and levee breaching constitutes the main motivation of this dissertation.

1.2. Approach for Investigating Syn-Depositional Compaction Impact on Delta Development

Understanding the impact of syn-depositional compaction on delta development requires an approach that captures its spatiotemporal effects on the sediment bed, particularly changes in volume and resistance to resuspension, as well as its interactions with hydrodynamics and morphodynamics. Laboratory studies in flumes or settling columns isolate compaction effects on sediment volume and resistance to resuspension under controlled conditions (Bale et al., 2006; Merckelbach & Kranenburg, 2004; Taheri et al., 2020; Tan et al., 2007; Torfs et al., 1996), but they cannot replicate the spatiotemporal variability of sediment transport, deposition, and erosion in natural deltas. Field measurements of compaction are limited by instrumentation, preventing long-term ($>10^3$ years) observations over large areas ($>10^3$ m²). Similarly, preserved outcrops record compaction during delta development but lack the detailed depositional and erosional histories needed to reconstruct relationships between compaction and landscape development. These limitations highlight the value of process-based modelling, which simulates 3D deltaic stratigraphy and landscape development with complete sediment transport, deposition, and erosion histories, enabling switching compaction on and off, and comparing result without and with varying compaction rate scenarios.

Process-based modelling provides an alternative to laboratory, field, and outcrop data by translating physical laws governing processes of sediment transport, deposition, and erosion into numerical simulations under prescribed boundary conditions. Such models have advanced understanding of delta formation by quantifying the relative controls of riverine & marine processes and sediment properties (Broaddus et al., 2022; Burpee et al., 2015; Caldwell & Edmonds, 2014; Edmonds & Slingerland, 2007, 2008, 2010; Geleynse et al., 2010, 2011; Hillen et al., 2014; Storms et al., 2012; van der Vegt et al., 2016, 2020; Zăinescu et al., 2024). Accordingly, a process-based modelling approach is adopted in this dissertation. All results presented herein are therefore from model-land simulations, and interpretations of real-world delta behavior are based solely on model-land insights.

Among process-based modelling tools, the open-source Delft3D couples hydrodynamics and morphodynamics and has become a standard platform for simulating delta development (Edmonds et al., 2022). It has also been widely applied to sedimentary processes in fluvial, lacustrine, and shallow-marine environments (Lesser et al., 2004; Storms et al., 2020; van der Vegt et al., 2020; Zăinescu et al., 2024) and is used in this dissertation. However, compaction has not been incorporated in previous versions of Delft3D to evaluate its role in delta development. Delft3D is available in two packages: structured-grid (Delft3D 4 - FLOW) and unstructured-grid (Delft3D - FLOW Flexible Mesh or

FM). The main distinction is in the grid design: Delft3D 4 - FLOW uses fixed rectangular grid, whereas Delft3D - FLOW FM supports flexible meshes up to six-sided shapes (Deltares, 2025a, 2025b).

This dissertation employs Delft3D 4 - FLOW for the following reasons: (1) Delft3D - FLOW FM has mainly been applied to hydrodynamic studies (Borba et al., 2025; Okon et al., 2025; Symonds et al., 2017), and lacks established application to long-term morphodynamic simulations; (2) Delft3D 4 - FLOW has demonstrated numerical stability in such simulations (Broaddus et al., 2022; Burpee et al., 2015; Caldwell & Edmonds, 2014; Edmonds & Slingerland, 2007, 2008, 2010; Geleynse et al., 2010, 2011; Hillen et al., 2014; Storms et al., 2012; van der Vegt et al., 2016, 2020; Zăinescu et al., 2024); (3) Both packages perform comparably in reproducing hydrodynamic in domain with complex shape, such as estuaries (Symonds et al., 2017); (4) Delft3D 4 - FLOW benefits from extensive use in morphodynamic studies, offering substantial expertise and validation, making it suitable for investigating compaction-driven delta development.

In this study, compaction formulations were implemented into Delft3D 4 – FLOW code. To do so, we first characterize the hydro-morphodynamic processes simulated by Delft3D 4 – FLOW (Figure 1.1). Simulations begin with an initial bathymetry and prescribed boundary conditions at river inlets and basin margins, including sediment types and concentrations, flow, and transport parameters. The model computes flow fields that drive sediment transport, leading to deposition and/or erosion, which update the bed level and, consequently, the bathymetry. In the modified framework, bed-level changes also alter overburden stress, triggering compaction that further adjusts the bed level and porosity (Figure 1.1). The compaction-adjusted bed level is used to update the bathymetry. This approach has been applied to assess the impact of syn-depositional compaction on delta morphodynamics and sediment distribution (Chapters 2 and 3). Additionally, compaction influences sediment resistance to resuspension by modifying the critical bed shear stress for erosion, which is applied in subsequent sediment transport calculations (Figure 1.1). The updated approach has been applied to assess the impact of syn-depositional compaction on levee breaching (Chapter 4).

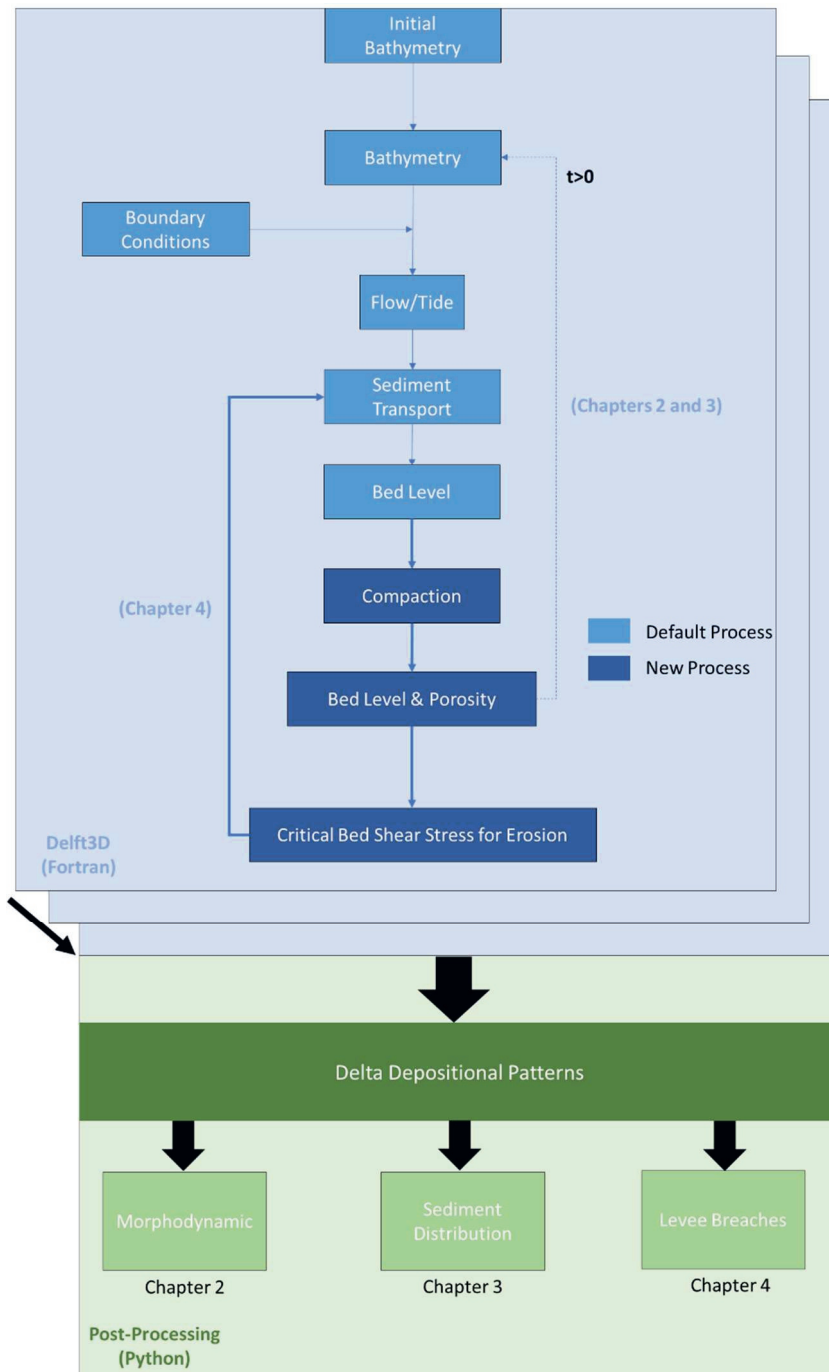


Figure 1.1. Simplified hydro-morphodynamic processes in Delft3D 4 - FLOW. Compaction impacts bed level and sediment resistance to resuspension, influencing self-organization of sediment and resultant depositional patterns in simulated deltas.

1.3. Background Knowledge of Sediment Compaction

Sediment compaction occurs through mechanical, biological, and chemical processes (Wangen, 2001). Mechanical compaction is driven by self-weight and overburden weight as sediments accumulate, which expels pore fluids and tightens grain contacts. This compaction type occurs in two phases. Primary compaction causes significant bulk volume reduction as excess pore pressure dissipates due to increased loading (Mesri & Ajlouni, 2007; von Terzaghi, 1923). Secondary compaction leads to further volume reduction due to continued pore-pressure dissipation under sustained loading (Mesri & Ajlouni, 2007; Taylor & Merchant, 1940; van Asselen et al., 2009; Waples & Couples, 1998). Fine-grained deposits (clay & silt) and peat experience both compaction phases due to their high compressibility, whereas coarse-grained sediments (sand and gravel) primarily undergo primary compaction (Bjerrum, 1967; Mesri & Ajlouni, 2007; Zain, 2019).

Biological compaction results mainly from microbial decomposition of organic matter. This process is accelerated under aerobic conditions, when oxidation convert organic matter into gases, acids, and biomass, causing mass loss and porosity generation (Al-Khafaji & Andersland, 1981; Zain, 2019). The porosity generated within the sediment framework is subsequently compressed by overburden, causing volume reduction and densification. This process is particularly significant in peat and has caused substantial subsidence in deltas like the Sacramento–San Joaquin Delta in California, USA (Drexler et al., 2009). Other biological activities, including root growth and bioturbation, also create additional porosity (Meysman et al., 2006; Tracy et al., 2011), leading to temporally increase in sediment volume or swelling. Subsequent root decay or burrow collapse ultimately result in volume reduction. Microbial secretion of extracellular polymeric substances (EPS) and microbial-induced mineral precipitation binds grains, reduce pore space, and increase resistance to resuspension (Malarkey et al., 2015; Moqsud & Gochi, 2024).

Chemical compaction is more dominant at greater depths, where high pressure and temperature enhance mineral dissolution at grain contacts. The dissolved minerals are transported via diffusion and reprecipitated in nearby pore spaces and fractures (Bjørlykke & Høeg, 1997; Rutter & Elliott, 1997). This pressure-solution process, common in lithified rocks, such as sandstones, limestones, and shales, decreases sediment volume through grain-contact dissolution, reduces porosity, and can produce stylolites (Bjørlykke & Høeg, 1997). The onset depth of chemical compaction varies from a few hundred meters to several kilometers (Bjørlykke & Høeg, 1997; Bloch et al., 1986; Dunnington, 1967).

Beyond reducing volume, compaction alters sediment resistance to resuspension. Resuspension occurs when flow-induced shear stress exceeds resisting forces from

sediment weight and cohesion (Dade et al., 1992). In uncompacted mixtures, increasing mud content enhances resistance to resuspension through cohesion (van Rijn et al., 2020). Compaction further modifies this resistance (Grabowski et al., 2011), particularly in cohesive sediments (Roberts et al., 1998; Thomsen & Gust, 2000). Compaction increases bulk density, which correlates with higher resistance to resuspension (Bale et al., 2006, 2007; van Rijn et al., 2020). In addition, pore-fluid expulsion shifts sediments from a liquid-like to a plastic state, further enhancing resistance to resuspension (van Ledden et al., 2004; Winterwerp & van Kesteren, 2004).

This dissertation focuses on mechanical compaction for two reasons. First, it contributes the most to volume reduction (Wangen, 2001), thus has the strongest influence on the generation of additional accommodation. Second, it mainly operates within the active part of the delta top (Bloch et al., 1986; Giles et al., 1998). In contrast, biological compaction is confined to near-surface, oxygenated zones where organic decomposition accelerates (Zain, 2019), while chemical compaction is restricted to deeply buried, lithified sediments (few hundred meters to several kilometers) (Bjørlykke & Høeg, 1997; Bloch et al., 1986).

1.4. Background Knowledge of Compaction Modelling Methods

Compaction was initially investigated in engineering contexts, where understanding soil compressibility and strength is crucial to prevent construction design failures. In the context of this dissertation, we describe two methods to model compaction numerically. The first, proposed by von Terzaghi (1923), describes primary compaction phase due to increased loading. This model is 1D, assuming fluid expulsion occurs only vertically, and was later generalized to 3D by Biot (1941) to incorporate differential fluid expulsion within a 3D stress field. Terzaghi's model assumes constant soil compressibility, implying a linear stress-strain relationship, where increases effective stress produces proportional reductions in porosity and consequent subsidence. The second, developed by Gibson et al. (1967), incorporates non-linear compressibility, enabling an explicit description of 1D compaction by relating porosity reduction with effective stress. Unlike Terzaghi, Gibson's model allows for substantial changes of porosity and bed-surface over time. However, both models do focus only on the primary compaction phase.

Building on these foundations, Gambolati (1973a, 1973b) extended Gibson's method by fully coupling groundwater flow, governed by effective stress, with porosity reduction. All three methods have been applied to simulate compaction under varying sedimentation rate (e.g., Pizzuto & Schwendt, 1997; Zoccarato et al., 2020), but they do not

couple compaction with hydrodynamic or morphodynamic processes, which are essential for simulating delta development. Recent advances have attempted to couple compaction with hydrodynamics and morphodynamics, notably in Delft3D 4 - FLOW and NATSUB2D/3D tools. Zhou et al. (2016) implemented Gibson's method for cohesive sediments into Delft3D 4 - FLOW, covering from hindered settling to compaction. Porosity-effective stress relationships evolve over time to track porosity reduction and associated subsidence. This module is constrained by several limitations: (1) it is designed to mud-dominated environment with small spatial and temporal scales ($<10^3$ m² and $<10^3$ years), (2) it is computationally intensive with difficult-to-measure parameters.

Winterwerp et al. (2018) later derived an analytical solution to the Gibson equation, omitting the hindered-settling phase by assuming that initial compaction has already occurred. Here, compaction rates are assumed to exceed sedimentation rates. While this solution works in larger spatial and temporal scale than Zhou's model, it only applies to low energy, mud-dominated systems. Notably, neither Zhou's nor Winterwerp's models consider how compaction influences sediment resistance to resuspension. A more recent development by Zoccarato et al. (2018, 2020) employed the NATSUB2D model, coupling 2D groundwater flow with 1D compaction based on Gambolati's method. This framework has been applied to simulate compaction in the Mississippi and Mekong deltas. Xotta et al. (2022) further extended the model to NATSUB3D, enabling simulation of 3D groundwater flow using adaptive meshes that capture evolving bed surface. While the NATSUB2D/3D models couple compaction with morphodynamic development, they lack coupling with hydrodynamics (e.g., Baldan et al., 2025; Xotta et al., 2022), which is essential for simulating distributary channel and levee development. Additionally, they do not account for sediment resistance to resuspension.

In summary, existing compaction models represent substantial progress but remain constrained by dimensionality, computational cost, parameters that are difficult to obtain, and the lack of coupling among compaction, hydrodynamics, and morphodynamics. There is therefore a clear need for a generalized compaction model that: (1) uses easily obtainable parameters, (2) dynamically couples compaction with hydrodynamic and morphodynamic processes, (3) links compaction to sediment resistance to resuspension, and (4) distinguishes between primary and secondary phases, as secondary compaction can occur even without changes in overburden weight. This is evident from remote sensing studies, which demonstrate that subsidence continues in areas where no active sedimentation takes place (e.g., Aly et al., 2012; Becker & Sultan, 2009; Gebremichael et al., 2018; Higgins et al., 2014; Saleh & Becker, 2018; Steckler et al., 2022). In this dissertation,

new compaction formulations are developed and used to advance our understanding of delta development.

1.5. Background Knowledge of Delta Morphodynamics, Sediment Distribution, and Levee Breaching

1.5.1. Delta Morphodynamics

Galloway (1975) suggested that delta planform morphology is controlled by sediment distribution across delta regions, governed by relative influence of fluvial, wave, and tidal energies. When fluvial energy dominates, delta tends to prograde seaward, forming elongated delta planform with lobate shoreline, such as the Volga Delta (Broaddus et al., 2022). Waves and tides redistribute sediment delivered to the river mouth. Frontal and oblique approaching waves increase bottom friction and promote resuspension, which suppresses mouth bar growth and channel network developments, decreasing the number of distributary channels (Geleynse et al., 2011; Jerolmack & Swenson, 2007; Nardin et al., 2013; Nardin & Fagherazzi, 2012). Additionally, oblique waves can deflect river jet direction, promoting alongshore transport that leads to asymmetry of deposition along the shoreline. This favors sediment accumulation on the downdrift side, leading to wider delta planform with smooth shorelines (Broaddus et al., 2022; Zăinescu et al., 2024).

Tides also influence delta planform morphology. Under weak to moderate tidal conditions, the river jet is enhanced during ebb tides, promoting seaward lengthening of distributary channel & levee, and weakens during flood tides (Geleynse et al., 2011; Hoitink et al., 2017). Tidal oscillations generate residual currents that transport sediment laterally, producing wider and deeper mouth bars than those formed without tidal influence (Leonardi et al., 2013). As the mouth bar builds both vertically and laterally, it confines the flow, leading to bifurcation. Under strong tidal influence, sediment transport occurs in both landward and seaward directions. Ebb tides tend to concentrate flow through the central part of the river mouth, scouring the mouth bar and forming a central channel, whereas flood tides dominate along the bifurcated channels, driving mouth-bar formation on either side of the central channel (Hoitink et al., 2017; Leonardi et al., 2013). Consequently, delta morphology exhibits a dendritic planform with rougher shorelines compared to those primarily shaped by fluvial or wave energies (Broaddus et al., 2022; Fagherazzi, 2008; Geleynse et al., 2011).

Sediment characteristics, particularly grain size and composition, affect sediment resistance to resuspension through the critical bed shear stress for erosion. This effect is especially pronounced in cohesive sediments (Grabowski et al., 2011; Winterwerp & van

Kesteren, 2004). Model insights suggest that deltas dominated by cohesive sediments tend to develop fewer but more stable distributary channels than those primarily composed of non-cohesive sediments (Burpee et al., 2015; Caldwell & Edmonds, 2014; van der Vegt et al., 2020). This distinction affects delta planform morphology. Cohesive deltas typically exhibit more elongated planform with rugose shoreline compared to non-cohesive deltas (Burpee et al., 2015; Caldwell & Edmonds, 2014; Edmonds & Slingerland, 2010; Geleynse et al., 2011; Hoyal & Sheets, 2009; Martin et al., 2009). Similarly, a reduced proportion of bedload transport can produce cohesive-like morphologies characterized by fewer, deeper distributary channels (van der Vegt et al., 2016).

Vegetation influences delta planform morphology by increasing surface roughness and reducing overbank flow velocity across levees and delta plains (Baustian et al., 2018; Lauzon & Murray, 2018). Model insights suggest that sparse to intermediate vegetation densities promote optimal sedimentation on these areas, whereas dense vegetation confines flow within distributary channels (Albernaz et al., 2020; Lauzon & Murray, 2018, 2022; Nardin & Edmonds, 2014; Nienhuis et al., 2018). However, once a levee breaches, dense vegetation retains more sediment on the delta plain than sparse vegetation (Esposito et al., 2017; Nienhuis et al., 2018). Apart from vegetation effects on flow, it also affects sediment resistance to resuspension, where denser root density increases sediment resistance to resuspension (Nienhuis et al., 2018; Tengbeh, 1993). Dense vegetation on the levee stabilizes levee deposits, reducing channel migration while channel-bed erosion continues, resulting in deeper and stable channels (Lauzon & Murray, 2018; Nardin & Edmonds, 2014). Therefore, the presence of vegetation on levees and delta plains, depending on its density, can alter channel width-to-depth ratios and the spatial distribution of flow and sediment across the delta plain. As a result, simulated densely vegetated deltas tend to exhibit greater shoreline rugosity than sparsely vegetated or unvegetated deltas (Lauzon & Murray, 2018). Overall, the morphological effects of vegetation are comparable to those induced by increased cohesive sediment content within the delta.

Relative sea-level rise, driven sea-level rise and/or subsidence, also influences delta planform morphology by enhancing channel mobility through avulsion, which redistributes sediment to fill newly created accommodation (Jerolmack, 2009; Nienhuis et al., 2023). However, model insights suggest that when relative sea-level rise is excessive, it can instead promote channel stability, as the channel flow transport sediments to areas where accommodation is generated rapidly (Liang et al., 2016). This leads to more elongated delta planform with rugose shorelines (Liang et al., 2016). Although substantial progress has been made in understanding how hydrodynamics, grain size & composition,

sediment transport, sediment cohesiveness, and vegetation, affect delta morphology, the mechanisms governing the spatiotemporal development of sediment bed and their implications on delta morphology remain poorly constrained in model simulations. The sediment bed undergoes local changes in volume and resistance to resuspension due to syn-depositional compaction, a process largely overlooked in delta modelling studies and central to this dissertation.

1.5.2. Sediment Distribution

Accommodation refers to the space available for sediment accumulation and is primarily governed by relative sea-level changes (Jervey, 1988; Muto & Steel, 1997, 2000). It is typically evaluated at the basin scale. Delta development reflects the dynamic balance between sediment supply and accommodation (Colombera & Mountney, 2020; Nienhuis et al., 2023; Olariu et al., 2021; Paumard et al., 2020; Zhang et al., 2019). When accommodation on the delta top—including distributary channels, levees, and delta plains—increases more rapidly than sediment supply, less sediment is transported seaward through distributary channels. This enhances sedimentation at the delta top and promotes shoreline retreat. Conversely, when sediment supply exceeds the rate of accommodation creation, more sediment is transported seaward, driving shoreline progradation.

Syn-depositional compaction creates additional accommodation that changes locally in the delta as a result of locally varying bulk volume reduction, driven by spatiotemporal differences in overburden weight associated with local sediment supply and in substrate properties such as grain size and composition, as shown in model simulations (Nienhuis et al., 2018; Xotta et al., 2022). However, how this local accommodation interacts with delta morphodynamics and influences sediment distribution across delta regions remains poorly understood. A morphodynamic understanding of how syn-depositional compaction modulates local accommodation in clastic delta models is therefore essential, which will be addressed in this dissertation.

1.5.3. Levee Breaching

Natural levees are elevated ridges that confine flow within distributary channels (Brierley et al., 1997; Han et al., 2025). Levee breaching creates new distributary pathways that reshape channel networks, promoting sediment delivery to the delta plain (Esposito et al., 2017; Hajek & Edmonds, 2014; Nienhuis et al., 2018), and also poses significant flood hazards to nearby settlements and infrastructures (Syvitski et al., 2012). Based on field and remote sensing data, Gearon et al. (2024) showed that levee breaching mechanism changes

seaward. In alluvial fans, channels are relatively shallow and levees are relatively steep, allowing channel bed aggradation to more readily raise the channel bed above the surrounding floodplain. This enhances flow velocity toward the levee (Han et al., 2025). In deltas, channel-bed aggradation minimally affects flow depth because distributary channels are relatively deep and experience rising water-surface level. However, the aggradation steepens the water-surface slope toward the delta plain, increasing hydraulic gradient and flow velocity. The increased flow velocity promotes resuspension of levee deposits and breaching.

Controls on levee breaching are characterized using metrics, such as superelevation, defined as the ratio of levee height to channel bankfull depth and gradient advantage, the ratio of levee slope to channel slope. These metrics describe how channel–levee–delta plain geometry influences flow diversion and breach potential (Ganti et al., 2016; Gearon et al., 2024; Hoyal & Sheets, 2009; Slingerland & Smith, 1998; Törnqvist & Bridge, 2002). These metrics have been integrated into a breach likelihood metric (Λ) to predict levee breaching along distributary channels (Gearon et al., 2024; Gearon & Edmonds, 2025). However, empirical and experimental values of the breach likelihood metric exhibit wide variability (~ 0.2 – 14) (Ganti et al., 2016; Gearon et al., 2024; Gearon & Edmonds, 2025; Slingerland & Smith, 1998), suggesting that additional factors also affect levee breaching, such as syn-depositional compaction.

Syn-depositional compaction may influence levee breaching through two processes: (1) compaction-induced subsidence alters local elevations and slopes among distributary channels, levees, and delta plains, thereby modifying flow velocity along the levee; and (2) compaction increases bulk density and reduces fluid content within levee deposits, rendering them more resistance to resuspension. Although superelevation and gradient advantage describe flow conditions acting on the levee, they do not capture how levee deposits responds to flow-induced shear stress. The balance between flow-induced shear stress and the resistance of levee deposits to resuspension likely governs breach initiation and progression in model simulations, a relationship that remains poorly constrained and will be a focus in this dissertation.

1.6. Research Questions

The research questions are addressed exclusively in model-land simulations. All inferences about real-world delta behavior are based on model-land insights.

1.6.1. How does syn-depositional compaction impact simulated delta morphodynamics?

Syn-depositional compaction reduces volume of deposited sediment during delta development, generating additional accommodation that promotes further sedimentation. This process can modify how sediment is distributed across delta regions and, in turn, influences the emergent delta planform morphology. The impact of syn-depositional compaction on simulated delta morphology is evaluated using metrics, such as delta top area increase, shoreline rugosity, and aspect ratio, enabling comparison between models with and without compaction in muddy and sandy delta systems.

The analysis of simulated morphological changes driven by syn-depositional compaction forms the basis of Chapter 2. This chapter introduces compaction formulations and metrics to quantify the impact of syn-depositional compaction on simulated delta morphology. It also provides a foundational understanding based on simulation data of how syn-depositional compaction influences modelled deltaic processes and forms, laying the groundwork for investigations in subsequent chapters.

1.6.2. How does syn-depositional compaction affect sediment distribution in the simulated delta?

Accommodation is typically defined at the basin scale, yet syn-depositional compaction also generates localized accommodation through spatiotemporally variable bulk volume reduction. How this localized accommodation affects sediment distribution across delta regions remains poorly understood. Here, we investigate this process using a modeling approach that allows compaction to be switched on and off. We test the hypothesis that localized accommodation introduces feedback that redistributes sediment beyond immediate high accommodation area, affecting the entire simulated delta system. Sediment redistribution is quantified by comparing deposited sediment mass across delta regions between scenarios without compaction and with increasing compaction rates. This analysis forms the basis for Chapter 3, which highlights the link between compaction-influenced accommodation and the interdependency of sediment budgets across the simulated delta regions.

1.6.3. How does syn-depositional compaction influence simulated levee breaching?

Sediment is distributed across delta regions via distributary channels confined by levees. Levee breaching can trigger crevasse splay or avulsion, providing key pathways for sediment transfer between regions. Because syn-depositional compaction modifies both topography and the resistance of deposits to resuspension, it may influence the likelihood and development of levee breaching. We reconsider the traditional hydrodynamic view of breaching, typically assessed using proxies such as superelevation and gradient advantage, by demonstrating that simulated breach initiation and progression are governed by the interplay between compaction-modified, flow-induced shear stress and sediment resistance to resuspension, expressed as the erodibility index. Evaluating the effects of erodibility index on simulated levee breaching forms the basis for Chapter 4. We argue that the erodibility index provides a more comprehensive understanding and predictive framework for levee breaching processes.

1.7. Thesis Outline

Chapter 1 introduces the motivation for investigating syn-depositional compaction in delta systems using modelling approach as well as outlines research questions. Chapters 2 and 3 examine how bed-level changes driven by syn-depositional compaction affect simulated delta morphodynamics and sediment distribution. Chapter 4 incorporates full compaction process, modifying bed level and resistance to resuspension, to investigate simulated levee breaching. Across Chapters 2–4, the compaction implementation in Delft3D 4 - FLOW code is progressively refined, and quantitative metrics are developed to enable a comparative evaluation of the impact of syn-depositional compaction on simulated deltas. Chapter 5 synthesizes the findings from Chapters 2 – 4, situating them within the broader literature. Additionally, potential research avenues are described to further improve our understanding of how syn-depositional compaction influences on delta development.

Chapter 2: The impact of clastic syn-depositional compaction on fluvial-dominated delta morphodynamics

This chapter has been published in The Depositional Record Journal in 2022

Abstract

In natural deltaic settings, mixed hydrodynamic forcings and sediment properties are known to influence the preserved delta deposits. One process that has not received much attention yet is syn-depositional compaction of clastic sediment on millennial-scale delta evolution. To study how compaction interacts with delta morphodynamics and preserved sediment, a modelling approach is proposed. 1D grain-size dependent compaction model was implemented into Delft3D 4 - FLOW, which provides an opportunity to understand the underexplored connection between grain sizes supplied to the deltas and sediment compaction. The compaction model allows deposited sediment to decrease in volume due to the accumulation of newly deposited sediments above or the elapsed time. Differences in morphological trends are presented for scenarios defined by the composition of sediment supply (mud-rich and sand-rich) and the maximum allowed compaction rate in the model ($0 - 10 \text{ mm y}^{-1}$). The resultant deposits are classified into sub-environments: delta top, delta front and pro delta. The delta top geometry (e.g., area increase, rugosity and aspect ratio), sediment distribution alongshore and across sub-environments, and delta top accommodation (e.g., volume reduction and average water depth) are compared. The modelling results show that compaction of the underlying delta front and pro delta deposits increases the average water depth at the delta top, driving morphological variability observed in the mud-rich and sand-rich deltas. The morphological changes are more prominent in the mud-rich deltas, which experience larger compaction-induced volume reduction for the same scenario. Moreover, higher compaction rates further increase the delta top accommodation, resulting in more deposition and evenly distributed sediment at the delta top. This leads to a less significant area increase and a wider delta top with a smoother coastline. The presented modelling results bridge the knowledge gap in the influence of syn-depositional compaction on long-term delta morphodynamics and preserved sediment.

KEYWORDS: accommodation, delta morphology, preserved sediment, process-based forward models, syn-depositional compaction

2.1. Introduction

Compaction occurs in all deltas during and after their evolution, causing volume reduction of the deposited sediments. The leading cause of compaction is the expulsion of over-pressured pore fluid induced by increasing overburden weight due to ongoing deposition (von Terzaghi, 1923). This dewatering process is syn-depositional, occurring during active deposition. Compaction also occurs post-depositionally under constant overburden stress, caused by time-dependent pore fluid expulsion in fine-grained sediments (van Asselen et al., 2009; Zoccarato et al., 2018).

Delta evolution is thought to be controlled by hydrodynamic forcings and sediment properties (Galloway, 1975; Orton & Reading, 1993). As these controls differ between deltas, many studies have been conducted to decipher their process interactions using the preserved delta deposits (Bhattacharya & Willis, 2001; Goodbred et al., 2003; Rice et al., 2020). However, delta deposits are not straightforward to interpret, which is further complicated by autogenic processes in the delta, such as syn-depositional compaction. Very little is known about the impact of syn-depositional compaction on millennial-scale delta evolution, mainly due to a lack of field measurements and limited possibilities to acquire such measurements considering the spatial ($> 10^3 \text{ km}^2$) and temporal ($> 10^3$ years) scale of delta evolution. Compaction datasets from contemporary deltas are available in the literature (Aly et al., 2012; Becker & Sultan, 2009; Gebremichael et al., 2018; Higgins et al., 2014; Minderhoud et al., 2018; Saleh & Becker, 2018; Stanley, 1990; Teatini et al., 2011). However, sedimentation is low in the measurement sites due to reduced sediment supply imposed by dams and artificial levee construction. Therefore, these compaction measurements are most likely post-depositional rather than syn-depositional. Compaction datasets are also available from laboratory experiments, which provide a first-order approximation of compaction behavior (Bjerrum, 1967; Merckelbach & Kranenburg, 2004; Mesri, 2003; Mesri et al., 1997; Taylor & Merchant, 1940; Toorman, 1996, 1999; Townsend & McVay, 1990; von Terzaghi, 1923; Winterwerp & van Kesteren, 2004). Despite some shortcomings, these are the most reliable published compaction datasets.

Syn-depositional compaction occurs in active depositional areas where the freshly deposited sediments dewater and compact by subsequent deposition. This creates additional accommodation to store more sediments (Colombera & Mountney, 2020; Paumard et al., 2020; van Asselen et al., 2011), leading to a feedback loop between sedimentation and accommodation. This shows the potential impact of compaction on delta morphodynamics and the sediment archive, which is still underexplored. Therefore, it is important to include compaction in the simulation of deltas to better understand its influence on natural delta evolution.

To this end, this chapter has two objectives: (1) formulate, implement and evaluate a new compaction algorithm into the existing open-source coupled hydrodynamic-morphodynamic model (Delft3D) (Lesser et al., 2004), and use the updated code to (2) demonstrate how compaction interacts with syn-depositional delta evolution by analysing delta top morphology (i.e., area increase, rugosity and aspect ratio), sediment distribution alongshore and across sub-environments (i.e., delta top, delta front and pro delta), and delta top accommodation.

This work builds on previous research using Delft3D that simulates delta development and characterises the impact of grain size on delta evolution (Burpee et al., 2015; Caldwell & Edmonds, 2014; Edmonds et al., 2010; Edmonds & Slingerland, 2007, 2008, 2010; Geleynse et al., 2010, 2011; Hillen et al., 2014; van der Vegt et al., 2016, 2020). Previous compaction studies using Delft3D, which focus on a shorter timescale model evolution, were used to guide the implementation of the compaction algorithm into Delft3D (Winterwerp et al., 2018; Zhou et al., 2016). The modified Delft3D was used to generate progradational and aggradational fluvial-dominated deltas. These datasets were then analysed to gain insight into the role of compaction on delta morphodynamics.

2.2. Methodology

Laboratory experiments show that compaction occurs in two phases: primary and secondary compaction (Bjerrum, 1967; Mesri, 2003; Mesri et al., 1997; Taylor & Merchant, 1940; von Terzaghi, 1923). The primary compaction is a syn-depositional process, imposing volume reduction due to the weight of depositing sediments. This phase is characterised by a large magnitude of volume reduction that occurs over a short timescale. Subsequently, the secondary compaction continues post-depositionally with a lower magnitude over a longer timescale.

Once increased pore pressure due to overburden exceeds hydrostatic conditions, the pore fluid is expelled from the pores, ultimately flowing to the surface as groundwater flow. This means that local porosity and permeability will interfere with the actual compaction rates of the sediments. If the fluid cannot escape the pores, an overpressure condition will occur. This study does not incorporate complex 3D groundwater flow and assumes that the expelled pore water can always escape vertically to the surface (Meckel et al., 2006, 2007). Furthermore, it was assumed that different pore fluid types (i.e., air and water) have a negligible impact on compaction over geological timescales ($> 10^3$ years). Therefore, there is no differentiation between compaction and consolidation, which is important in geotechnical applications.

For this purpose, new 1D primary and secondary compaction formulas were developed for clastic sediments (e.g., sand and mud) based on methods described by Terzaghi and Mesri (Mesri, 2003; Verruijt, 2010; von Terzaghi, 1923), which exclude the permeability variation of sediments. Subsequently, the compaction formulas were implemented into Delft3D to simulate compaction's impact on seaward building deltas that actively aggrade. This is not the first time compaction has been incorporated into a process-based numerical simulation. Previous studies have used a simpler model with uniform compaction that occurs regionally to study delta evolution (Liang et al., 2016a, 2016b).

It is important to note that the secondary compaction is included in the modelling because this compaction type operates over a long timescale (Bjerrum, 1967), comparable to the timescale over which the simulated deltas evolve ($>10^3$ years). However, the primary compaction is still the dominant mechanism when the simulated deltas are actively depositing, triggering compaction due to the increased weight of the deposited sediment. Below, the compaction formulas are described together with their implementation into Delft3D 4 - FLOW version 6.02.08.62644 (Deltares, 2021)

2.2.1. Primary Compaction

von Terzaghi (1923) shows that the vertical strain of a sediment bed (ε_v , dimensionless) due to primary compaction is proportional to the change in effective stress, defined as the difference between the overburden stress (σ in Pa) and the opposing pore fluid pressure (p in Pa), and the inverse of the oedometric modulus ($\frac{1}{E}$ in Pa), as shown by Equation 2.1. E represents bed stiffness under 1D compression in laterally confined conditions.

$$\varepsilon_v = \frac{1}{E} \cdot \Delta(\sigma - p) \quad (2.1)$$

It is assumed that the sediment grains and pore fluid are incompressible and insoluble. Therefore, the subsidence only occurs by porosity reduction due to pore fluid expulsion. Given a sediment bed thickness (H in m), the subsidence for each simulation time interval ($\frac{\Delta H_p}{\Delta t}$ in m y^{-1}) can be estimated using Equations 2.2 and 2.3:

$$\frac{\Delta H_p}{\Delta t} = \int_0^H \frac{1}{E} \cdot \Delta(\sigma - p) dz \quad (2.2)$$

$$\frac{\Delta H_p}{\Delta t} = \frac{1}{E} \cdot H \cdot \Delta\sigma - \frac{1}{E} \int_0^H \Delta p dz \quad (2.3)$$

For geological timescales simulation, detailed modelling of pore fluid expulsion rate, indicated by the second term on the right-hand side of Equation 2.3, is simplified by

using a proportional rate of subsidence (C_p in y^{-1}), excluding the effects of the sediment's permeability variation by assuming the porosity is uniformly connected. Consequently, pore fluid can always escape during compaction, which allows compaction to be modelled with less complexity than in previous studies (Winterwerp et al., 2018; Zhou et al., 2016). The simplified Equation 2.4 is shown below, which was implemented into Delft3D.

$$\frac{\Delta H_p}{\Delta t} = C_p \cdot \frac{1}{E} \cdot H_{t-1} \cdot (\sigma_t - \sigma_{t-1}) \quad (2.4)$$

here, H_{t-1} represents the bed thickness at the previous simulation time (in m), and $\sigma_t - \sigma_{t-1}$ indicates the net increase in overburden stress between two successive simulation time intervals (in Pa), which is positive during deposition. However, if the net increase in overburden stress is zero or negative due to hiatus or erosion, respectively, the primary compaction that occurs previously is deactivated, whereas the secondary compaction is activated because only one compaction type is active at each simulation time. The primary compaction is applied to coarse-grained and fine-grained sediments.

C_p (y^{-1}) in Equation 2.4 defines the proportion of potential subsidence due to primary compaction that is realized per simulation time. The resulting subsidence per simulation time interval ($\frac{\Delta H_p}{\Delta t}$) has a unit of $m y^{-1}$, i.e. the compaction rate. $\frac{\Delta H_p}{\Delta t}$ can also be expressed as ΔH_p within a timestep in the calculation. In this study, simulations are conducted under flooding conditions resulting relatively thick sediment layers. As a result, subsidence per simulation time interval is assumed small relative to the total thickness, yet often can exceed reasonable values and the maximum can be approximated in proportion to the rate (as it is permeability limited). A pragmatic approach taken here is that C_p values are used also as a limit to the primary compaction rates (with a change of unit to $m y^{-1}$), which are later used to compare modelling results.

2.2.2. Secondary Compaction

After the pore pressure set up by the overburden stress has dissipated due to pore fluid expulsion, the secondary compaction continues at a slower rate (Mesri et al., 1997). This compaction type occurs for an extended period (on the order of thousands of years) (Bjerrum, 1967). The secondary compaction was formulated as a function of time, assuming an independent relationship with overburden stress, as shown by Equation 2.5.

$$\frac{\Delta H_s}{\Delta t} = \frac{C_s \cdot H_{t-1}}{(1 + \eta_{t-1})} \cdot \log \left(\frac{t}{t_0} \right) \quad (2.5)$$

here, the subsidence due to secondary compaction per simulation time interval ($\frac{\Delta H_s}{\Delta t}$, in m y^{-1}) depends on the bed thickness at the previous simulation time (H_{t-1} in m), the bed porosity at the previous simulation time (η_{t-1}), the proportional rate of subsidence due to secondary compaction (C_s in y^{-1}), and the elapsed time relative to a reference time ($\frac{t}{t_0}$). The secondary compaction occurs in fine-grained sediments due to their low hydraulic permeability, resulting in delayed pore fluid dissipation (Minderhoud et al., 2018; Zoccarato et al., 2018). The secondary compaction only occurs after the onset of the primary compaction. Therefore, if the deposited sediment never experiences any overburden to turn the primary compaction on, the sediment will never experience the time-dependent dewatering (secondary compaction).

C_s (y^{-1}) in Equation 2.5 defines the proportion of potential subsidence due to secondary compaction that is realized per simulation time. The resulting subsidence per simulation time interval ($\frac{\Delta H_s}{\Delta t}$) has a unit of m y^{-1} , which represents compaction rate. $\frac{\Delta H_s}{\Delta t}$ can also be expressed as ΔH_s within a time interval in the calculation. Consistent with C_p , C_s values are also used as a limit to the secondary compaction rates (m y^{-1}). The compaction formulations (Equations 2.4 and 2.5) are based on laboratory studies measured over a short timescale (days), whereas delta evolution occurs over geological timescales (10^3 years). To bridge this gap, C_p and C_s are adjusted to the compaction rate of natural deltas (see Subchapter 2.3.2). In addition, the morphological changes are accelerated by upscaling the modelling time (t and t_0) using the morphological scaling factor (MORFAC) (see Subchapter 2.3.1). As a result, the resulting subsidence due to primary and secondary compaction (ΔH_p and ΔH_s) is over geologic time. Note that the actual compaction rates vary locally due to spatial and temporal variations of sedimentation and erosion. This leads to complex feedback between compaction and morphodynamics and preserved sediment. The compaction formulations (Equations 2.4 and 2.5) are validated with measurement data (Text A1).

2.2.3. Implementation of Compaction Formula into Delft3D

In Delft3D, sediments smaller than or equal to $64 \mu\text{m}$ are assumed cohesive and transported as suspended load. Sediments larger than $64 \mu\text{m}$ are partially transported in suspension, adding to the suspended load, and partially through saltation and creep, constituting bedload. In this study, the cohesive suspended load is transported using a cohesive transport formulation, calculated by solving a depth-averaged (2DH) advection-diffusion (mass-balance) equation for the suspended sediment (Galappatti, 1983). The non-cohesive suspended and bedload are transported using the Engelund-Hansen formulation

(Engelund & Hansen, 1967), allowing the partitioning of sand into suspended and bedload, for which the transport is calculated separately. For information about the governing equations behind processes in Delft3D and their implementations, refer to Delft3D documentation, which is available online (Deltares, 2025).

The deposited sediment is stored in a stratigraphic column, schematised according to the multi-layer concept (Ribberink, 1987), consisting of a transport layer, underlayers, and a base layer (Figure 2.1 and Text A2). The compaction formulas (Equations 2.4 and 2.5) were implemented in the underlayers of Delft3D. During compaction, the bed porosity in each underlayer decreases over time from its initial to minimum values. The upper and lower limit of bed porosity is determined from the depositional and compacted porosity of mud and sand based on their proportion in the supply (Text A2). Porosity is calculated by first updating the solid volume fraction of each layer due to compaction using Equation 2.6, and subsequently converting it to porosity using Equation 2.7.

$$\phi_t = \phi_{t-1} \cdot \frac{H_t}{H_{t-1}} \quad (2.6)$$

$$\eta_t = 1 - \phi_t \quad (2.7)$$

$$H_t = H_{t-1} - \Delta H_{p/s,t} \quad (2.8)$$

here, the solid volume fraction (ϕ_t) is updated for each simulation time by multiplying the solid volume fraction at the previous time (ϕ_{t-1}) with the ratio of bed thickness between two successive simulation time intervals (H_{t-1} and H_t). In case of no compaction (H_t equals H_{t-1}), no change in solid volume fraction will be recorded (ϕ_t equals ϕ_{t-1}). The bed porosity (η_t) is calculated as one minus solid volume fraction (ϕ_t). The bed thickness for each simulation time (H_t) is derived by subtracting bed thickness at the previous simulation time (H_{t-1}) with subsidence due to primary or secondary compaction at the given time ($\Delta H_{p/s,t}$), as shown by Equation 2.8. It is important to note the second-order impact of compaction, which influences the erodibility of the deposited sediment, was not included in the modelling. Therefore, the erodibility did not change regardless of how much the deposited sediment experiences compaction-induced subsidence.

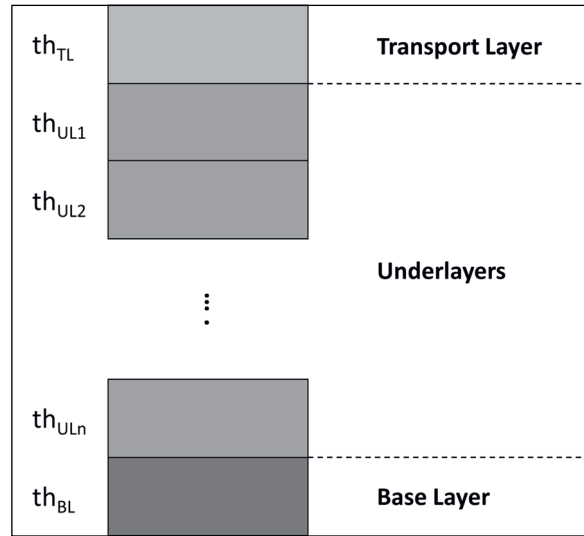


Figure 2.1. Multi-layer administration in Delft3D, consisting of a transport layer, n numbers of underlayers, and a base layer. The transport layer has a fixed thickness of 0.2 m (th_{TL}). Seventy-five underlayers were used in the simulation (th_{UL}), each with a maximum thickness of 0.3 m. The base layer has a flexible thickness (th_{BL}).

2.3. Building 4D Synthetic Deltas

This chapter discusses the model geometry and parameters used to create 4D synthetic deltas using Delft3D. Subsequently, the modelling scenarios are explained.

2.3.1. Model Setup

Following a similar approach as previous studies (Geleynse et al., 2010, 2011; van der Vegt et al., 2016, 2020), the modelling setup consists of a channel debouching into a sloped basin with a 0.1° gradient (Figure 2.2). The parameters used in the simulation are shown in Table 2.1. The stratigraphic column consists of a transport layer, 75 underlayers, and a base layer containing sediment whose grain size consists of the initial bed size (sand = $100 \mu\text{m}$) and the grain size of the supplied sediment (mud = 20 and $50 \mu\text{m}$ & sand = $100 \mu\text{m}$). Grain sizes are homogeneously mixed in the stratigraphic column. The oedometric modulus for mud and sand is set to $5 \times 10^6 \text{ Pa}$ and $25 \times 10^6 \text{ Pa}$, respectively (USACE, 1990). The bed porosity of deposited sediment has initial and minimum values, which are set to 0.75 & 0.08 and 0.52 & 0.18 for mud-rich and sand-rich deltas, respectively (see also Text A2).

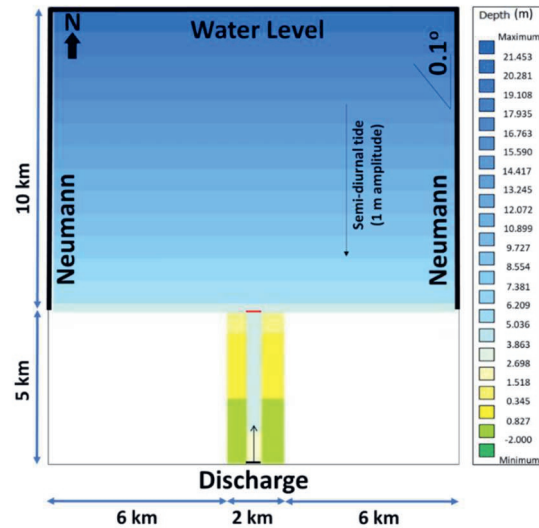


Figure 2.2. The model setup consists of a channel debouching into a sloped basin with a 0.1° gradient. The boundary condition at the channel inflow (horizontal thin black line) is water and sediment discharge, whereas the open boundaries in the basin (horizontal and vertical thick black lines) are the Neumann at the west and east combined with water level along the north boundary. The initial water depth ranges from 4 m at the delta apex (horizontal thin red line) to 21.5 m at the basin edge.

Table 2.1. User-defined parameters used in all Delft3D simulations.

No	User-Defined Model Parameter	Value	Unit
1	Grid Cell Dimension in x and y	50 x 50	m x m
2	Initial Bed Thickness	4	m
3	Water Discharge	1600	m ³ /s
4	Sediment Discharge	0.15	kg/s
5	Total Hydrodynamic Time	57	day
6	Morphological Scaling Factor	120	-
7	Spin-up Interval Before Morphological Updating Begins	720	min
8	Grain Sizes (Sand and Two Mud Fractions)	1E-04, 5E-05, and 2E-05	m
9	Dry Bed Density of Sand and Mud	500 and 1600	kg/m ³
10	Settling Velocity of Mud Fractions	0.0022 and 0.00056	m/s
11	Maximum Allowed Erosion Rate of Mud Fractions	0.0001	s/m
12	Critical Shear Stress for Erosion of Mud Fractions	0.12 and 0.15	N/m ²
13	Critical Shear Stress for Deposition of Mud Fractions	1000	N/m ²
14	Initial Bed Porosity in Mud-rich Deltas	0.75	-
15	Initial Bed Porosity in Sand-rich Deltas	0.52	-
16	Minimum Bed Porosity in Mud-rich Deltas	0.08	-
17	Minimum Bed Porosity in Sand-rich Deltas	0.18	-
18	Oedometric Modulus for Mud	5E+06	Pa
19	Oedometric Modulus for Sand	25E+06	Pa

The channel conveys a constant discharge of $1600 \text{ m}^3 \text{ s}^{-1}$, which should be considered a continuous bankfull discharge. The sediment concentration in the discharge is 0.15 kg s^{-1} , which agrees well with modern deltas' suspended load measurements (Milliman & Farnsworth, 2011). Although the simulated deltas are fluvially-dominated, it is necessary to stir up smaller-grained sediment deposited in the basin to simulate the sediment distribution similar to active coastal systems (van der Vegt et al., 2020). This was performed by including a semi-diurnal tide with a 1 m amplitude arriving perpendicular to the initial coastline (Figure 2.2). No waves were implemented in the model to limit the offshore reworking force and reduce the computation time.

The total simulation output time is 57 days of hydrodynamic time. The simulated deltas development is extended to the geological timescale by accelerating their morphology development using the morphological scaling factor (MORFAC) of 120 and bankfull discharge (Li et al., 2018). The geologic time can be computed by multiplying the hydrodynamic time with the acceleration factors, which yields 3363 years, assuming the bankfull discharge occurs for two days a year (Li et al., 2018). Therefore, each simulation output time interval indicates approximately 60 years of change. Other modelling parameters are shown in Table 2.1.

2.3.2. Scenario Setup

Twenty-two modelling scenarios were defined by varying the sediment supply compositions and primary and secondary compaction rates (parameters C_p and C_s in Equations 2.4 and 2.5) (Table 2.2). The supplied compositions consist of 15% sand and 85% mud for mud-rich deltas, contrasting with 70% sand and 30% mud for sand-rich deltas. The primary compaction rate (C_p) is based on the post-depositional compaction rate of recent Holocene deposits in muddy and sandy deltas, such as the Nile and Ganges-Brahmaputra, respectively (Aly et al., 2012; Becker & Sultan, 2009; Gebremichael et al., 2018; Higgins et al., 2014; Saleh & Becker, 2018; Stanley, 1990; Steckler et al., 2022).

The adjustment of the primary compaction rate using the post-depositional compaction rate is based on the following reasons: (1) No syn-depositional compaction rates measured over the delta scale ($>10^3 \text{ km}^2$ and $>10^3$ years) are available in literature. (2) The post-depositional rates measured in the Holocene deltas are still relatively high, reaching 18 mm y^{-1} , indicating that compaction might still be transitioning from a syn-depositional to a post-depositional rate. The measured rates show that sand-rich deltas compact slower than mud-rich deltas. This is supported by the fact that sand only experiences primary compaction with higher compacted porosity than mud (Text A2),

thereby potentially reaching compaction equilibrium before compaction measurements. Therefore, although the reported post-depositional rates of sand-rich deltas are lower than mud-rich deltas, sand compacts faster than mud. As a result, C_p for mud was set from 0 to 10 mm y^{-1} , whilst sand was set from 0 to 100 mm y^{-1} (Table 2.2). In contrast, mud is more compacted than sand over a longer timescale, which undergoes both primary and secondary compaction. In addition, different grain geometry between mud (sheet-like) and sand (rounded) contributes to more efficient mud compaction (Revil et al., 2002).

Table 2.2. The table shows the modelling scenarios for mud-rich (MS01 - MS11) and sand-rich deltas (CS01 - CS11), developed under different compaction scenarios (C_p and C_s).

Run ID	Supplied Sediment Concentration Per Year (kg/m ³)				Cp Sand (mm/year)	Cp Mud (mm/year)	Cs Mud (mm/year)
	Sand (0.1 mm)	Mud (0.05 mm)	Mud (0.02 mm)	Total			
MS01	0.0225	0.06375	0.06375	0.15	0	0	0
MS02	0.0225	0.06375	0.06375	0.15	0.1	0.01	0.000003
MS03	0.0225	0.06375	0.06375	0.15	0.5	0.05	0.000015
MS04	0.0225	0.06375	0.06375	0.15	0.75	0.075	0.0000225
MS05	0.0225	0.06375	0.06375	0.15	1	0.1	0.00003
MS06	0.0225	0.06375	0.06375	0.15	5	0.5	0.00015
MS07	0.0225	0.06375	0.06375	0.15	7.5	0.75	0.000225
MS08	0.0225	0.06375	0.06375	0.15	10	1	0.0003
MS09	0.0225	0.06375	0.06375	0.15	50	5	0.0015
MS10	0.0225	0.06375	0.06375	0.15	75	7.5	0.00225
MS11	0.0225	0.06375	0.06375	0.15	100	10	0.003
CS01	0.105	0.0225	0.0225	0.15	0	0	0
CS02	0.105	0.0225	0.0225	0.15	0.1	0.01	0.000003
CS03	0.105	0.0225	0.0225	0.15	0.5	0.05	0.000015
CS04	0.105	0.0225	0.0225	0.15	0.75	0.075	0.0000225
CS05	0.105	0.0225	0.0225	0.15	1	0.1	0.00003
CS06	0.105	0.0225	0.0225	0.15	5	0.5	0.00015
CS07	0.105	0.0225	0.0225	0.15	7.5	0.75	0.000225
CS08	0.105	0.0225	0.0225	0.15	10	1	0.0003
CS09	0.105	0.0225	0.0225	0.15	50	5	0.0015
CS10	0.105	0.0225	0.0225	0.15	75	7.5	0.00225
CS11	0.105	0.0225	0.0225	0.15	100	10	0.003

The secondary compaction rate (C_s) was determined by a sensitivity analysis using two criteria: (1) C_s is lower than C_p , and (2) the model is numerically stable. The C_s were set 3×10^{-4} times lower than the C_p of mud (Table 2.2). It is important to note that, as deposition and erosion vary across the model domain, the actual compaction rates may also vary locally. However, these local compaction rates never exceed C_p , which is considered the maximum allowed compaction rate in the model. Figure 2.3 shows an example of a modelling scenario for a non-compacted mud-rich delta. The bathymetry development

indicates that the delta experiences different stages of evolution, starting with a rapid basin infilling that occurs during the early simulation period (simulation output times 15 to 25), which causes seaward delta progradation. As the delta front progrades and the shoreline of active deposition reaches deeper water depth, the progradation slows down. Delta top dynamics influence the morphology evolution of the delta, shown by avulsion that occurs at simulation output times 30 and 50, promoting land building towards the avulsion directions. The influence of delta top dynamics decreases due to compaction, as shown by the bathymetry evolution of compacted mud-rich deltas (Text A3). In contrast, compaction has less impact on the morphology evolution of sand-rich deltas (Text A3).

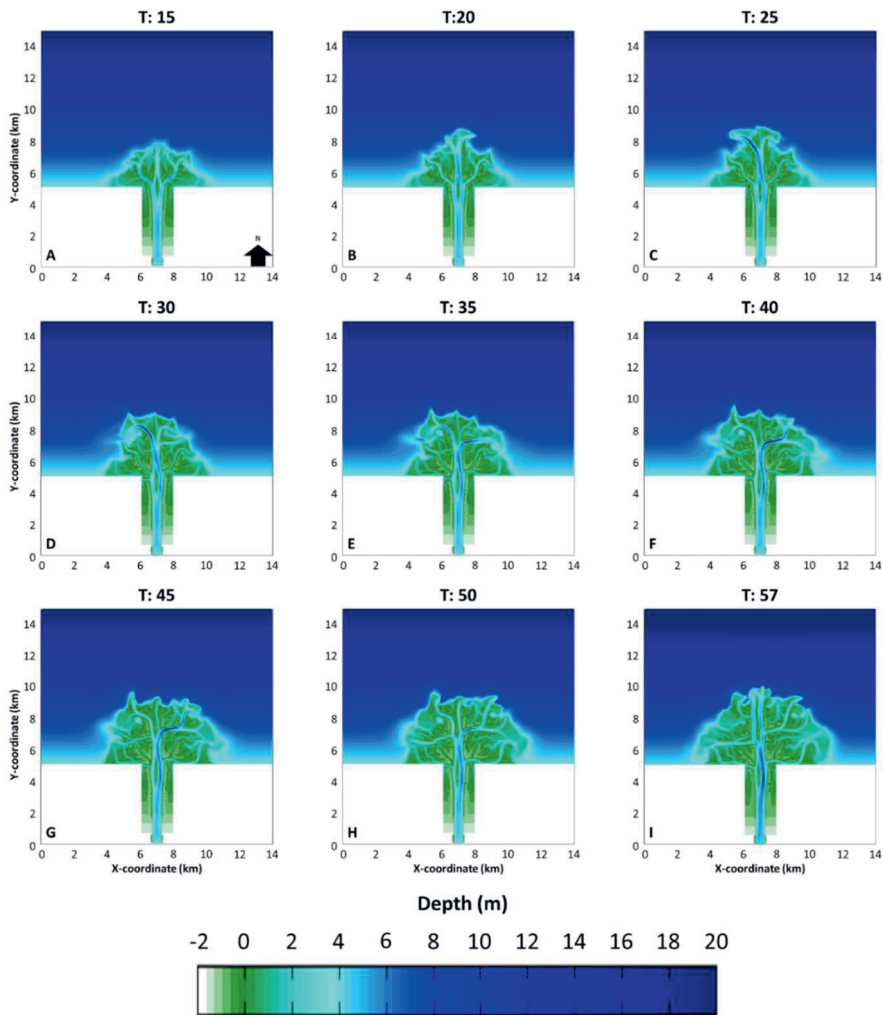


Figure 2.3. Plan view bathymetry of non-compacted mud-rich delta for selected simulation output times (A – I). Each simulation output time interval equals approximately 60 years of delta development.

2.4. Post-processing Delft3D Output Data

The impact of syn-depositional compaction on the simulated deltas was analysed using their spatial and temporal characteristics. For this purpose, the Delft3D outputs containing sediment mass, elevation, water depth and porosity were post-processed for each simulation output time, resulting in metrics that show delta top geometry (area increase, rugosity and aspect ratio), delta top accommodation, and delta-wide sediment distribution. An explanation of how to compute these metrics for mud-rich and sand-rich deltas is provided below.

2.4.1. Delta Top Geometry

The deposited sediments were characterised into sub-environments: delta top, delta front and pro delta (Figure 2.4A, B), based on their elevation. All grid cells with elevations higher than the brink point, which indicates the transition between upstream and downstream of the delta, were classified as the delta top (van der Vegt et al., 2016, 2020). Distributary channel and floodplain are included in the delta top. The delta front is below the brink point and contains at least 1% sand, whilst the pro delta is located below the wave base. A more detailed algorithm for classifying sub-environments is explained in Text A4. The delta top's geometrical characteristics were estimated per simulation output time, consisting of area increase, rugosity and aspect ratio (Figure 2.4C). These metrics quantify the net effects of delta top dynamics, indicating the interaction between distributary channels that avulse, bifurcate, migrate, and become abandoned with non-distributary channels (e.g., floodplain).

The delta top area increase per simulation output time interval (A_{dt} in m^2/dt) was derived by multiplying the difference of the number of delta top's grid cells between two successive simulated output time intervals ($ngrid_{dt} - ngrid_{dt-1}$) with grid cell dimension ($dx \cdot dy$ in m^2) (Figure 2.4C), as shown in Equation 2.9.

$$A_{dt} = (ngrid_{dt} - ngrid_{dt-1}) \cdot dx \cdot dy \quad (2.9)$$

The rugosity (R) was calculated by dividing the shoreline length ($L_{shore,dt}$ in m) represented by the outermost contour of the delta top with the square root of the delta top area ($\sqrt{A_{dt}}$ in m) (Wolinsky et al., 2010) (Figure 2.4C), as shown by Equation 2.10. A smaller value of this metric indicates a smoother shoreline.

$$R = \frac{L_{shore,dt}}{\sqrt{A_{dt}}} \quad (2.10)$$

The aspect ratio (S_{dt}) was quantified by dividing the delta width (W_{dt} in m) measured parallel to the initial shoreline with two times delta top length (L_{dt} in m) measured perpendicular to the initial shoreline (Caldwell & Edmonds, 2014) (Figure 2.4C), as shown in Equation 2.11. The aspect ratio of 1 indicates an ideal semi-circular or triangular delta top. In contrast, the aspect ratio less or higher than 1 ($S_{dt} < 1$ and $S_{dt} > 1$) shows an elongated or a wide delta top, respectively.

$$S_{dt} = \frac{W_{dt}}{2L_{dt}} \quad (2.11)$$

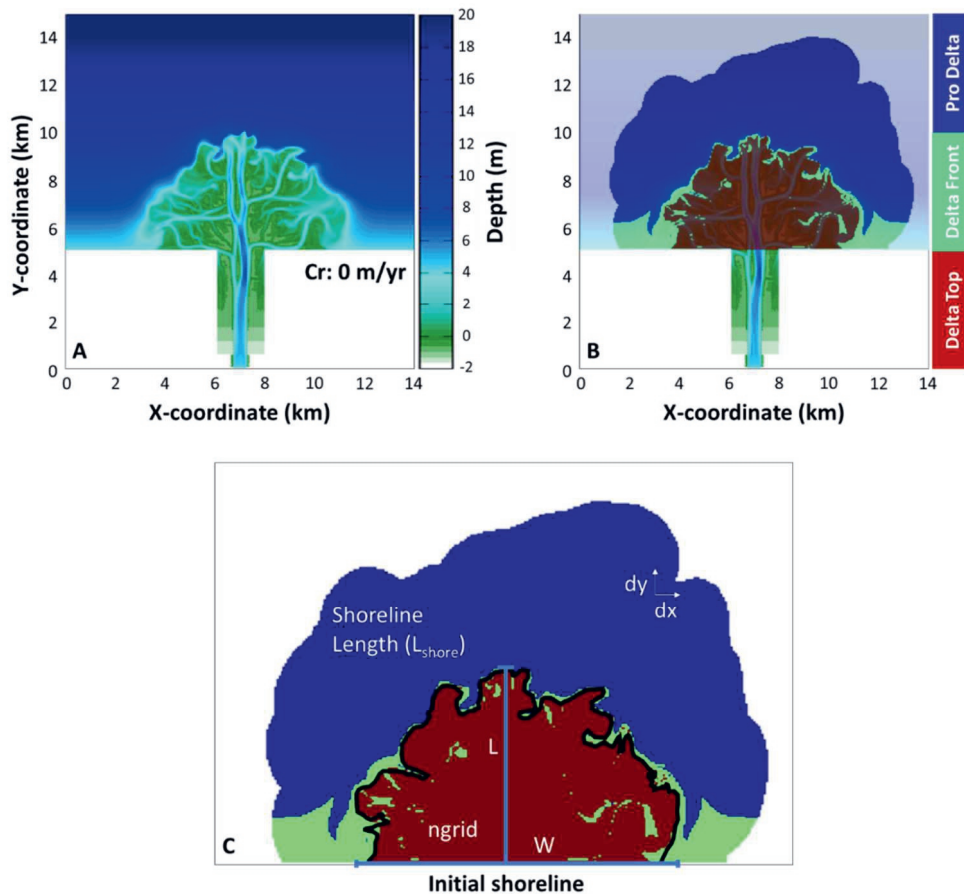


Figure 2.4. (A) Plan-view bathymetry of the non-compacted mud-rich delta at the last simulation output time. (B) The delta regions were classified into delta top, delta front, and pro delta. (C) The delta top characteristics, which are shoreline length (L_{shore}), width (W), length (L), and total grid cells ($ngrid$), were used to calculate the delta top geometry metrics (area increase, rugosity, and aspect ratio).

The results calculated by morphology metrics were plotted for all compaction scenarios. As a gradual process, the influence of compaction on delta morphology enhances over time. To account for this effect, a trendline was calculated for each compaction scenario accounting for temporal variation in the morphology trend (Text A5). It was used to estimate a linear equation. Then, the area increase, rugosity and aspect ratio were determined using this equation at the end of the simulation. The calculation was repeated for all compaction scenarios. Finally, the results were plotted over compaction scenarios.

2.4.2. Distribution of Deposited Mass

Two metrics were developed to analyse the deposition trends in simulated deltas. The first metric indicates sediment distribution alongshore, calculated by mapping the simulated deltas to a radial coordinate system consisting of three segments: western (-90° to -30°), central (-30° to 30°) and eastern (30° to 90°) (Figure 2.5). Next, the cumulative deposited mass was calculated in each segment, normalised by the cumulative deposited mass in the delta at the end of the simulation. However, it is still unclear how evenly the deposition occurs alongshore. Therefore, an additional calculation was performed by taking the ratio of cumulative deposited mass in the central segment (-30° to 30°) to an average cumulative deposited mass in western and eastern segments (-90° to -30° and 30° to 90°) at the end of the simulation. The second metric indicates the deposition trends across delta sub-environments. This metric was measured by calculating the ratio between the cumulative deposited mass at each sub-environment (i.e., delta top, delta front, and pro delta) and the delta's cumulative deposited mass.

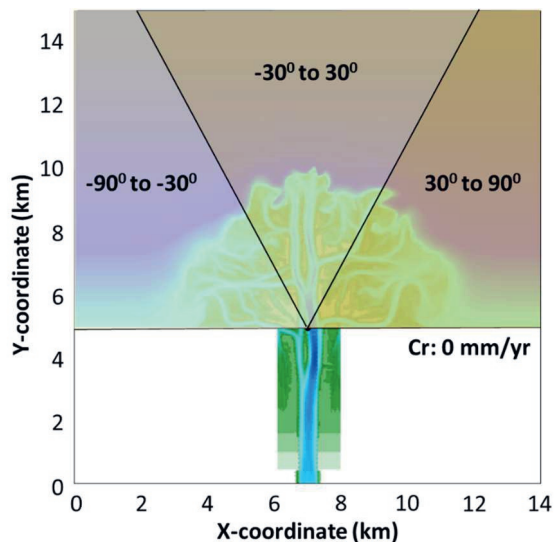


Figure 2.5. The non-compacted mud-rich delta at the final simulation output time was mapped into radial coordinates centering at the delta apex, which consists of three segments relative to the delta apex: -90° to -30° , -30° to 30° , and 30° to 90° .

2.4.3. Accommodation

Compaction-induced subsidence increases relative water depth, influencing the accommodation available for sediment deposition. Therefore, two metrics were developed to estimate the accommodation at the delta top: volume reduction and water depth.

To calculate volume reduction, the subsidence due to compaction in each grid cell was first estimated by subtracting the compacted from the uncompacted bed thickness. The uncompacted thickness was measured by multiplying the porosity ratio between two successive simulation output time intervals with the compacted thickness, assuming the subsidence only occurs due to porosity reduction (Subchapter 2.2.3). This subsidence calculation concomitantly neglects the erosion effect, as porosity does not change during erosion. Next, the volume reduction was calculated by multiplying the total subsidence with the grid cell dimension, normalised by the uncompacted volume for the area within the delta top.

The second metric is water depth, which indicates the average water depth of the delta top for each simulation output time. The calculation only includes all wet grid cells with water depths larger than 0.1 m that experience deposition of at least 15 mm. The deeper water depth reflects a more significant accommodation (Muto & Steel, 2000).

2.5. Impact of Compaction on Delta Evolution

The temporal characteristics of the simulated deltas were analysed by first showing the morphological metrics (area increase, rugosity and aspect ratio). Subsequently, the sediment distribution and accommodation metrics are presented. These metrics were analysed after simulation output time 20 when the simulated deltas reached dynamic equilibrium, indicated by relatively stable development. To simplify the description of the modelling results, the compaction scenarios refer to the values of the maximum allowed primary compaction rate of mud (C_p), which varies from 0 to 10 mm y^{-1} .

2.5.1. Delta Top Geometry

Mud-rich Deltas

The largest area increase occurs in the non-compacted scenario (0 mm y^{-1}), reaching $5.6 \times 10^5 \text{ m}^2/\text{dt}$ (Figure 2.6A, B). When the compaction of 0.01 mm y^{-1} is added, the delta top area expands with a significantly slower rate of up to $3.4 \times 10^5 \text{ m}^2/\text{dt}$. The increasing compaction scenario to 10 mm y^{-1} leads to a gradual decrease in the area expansion rate ($R^2 = 0.72$). As a result, the compaction scenarios $5 - 10 \text{ mm y}^{-1}$ have the lowest rate of area increase at the end of the simulation.

Mud-rich Deltas

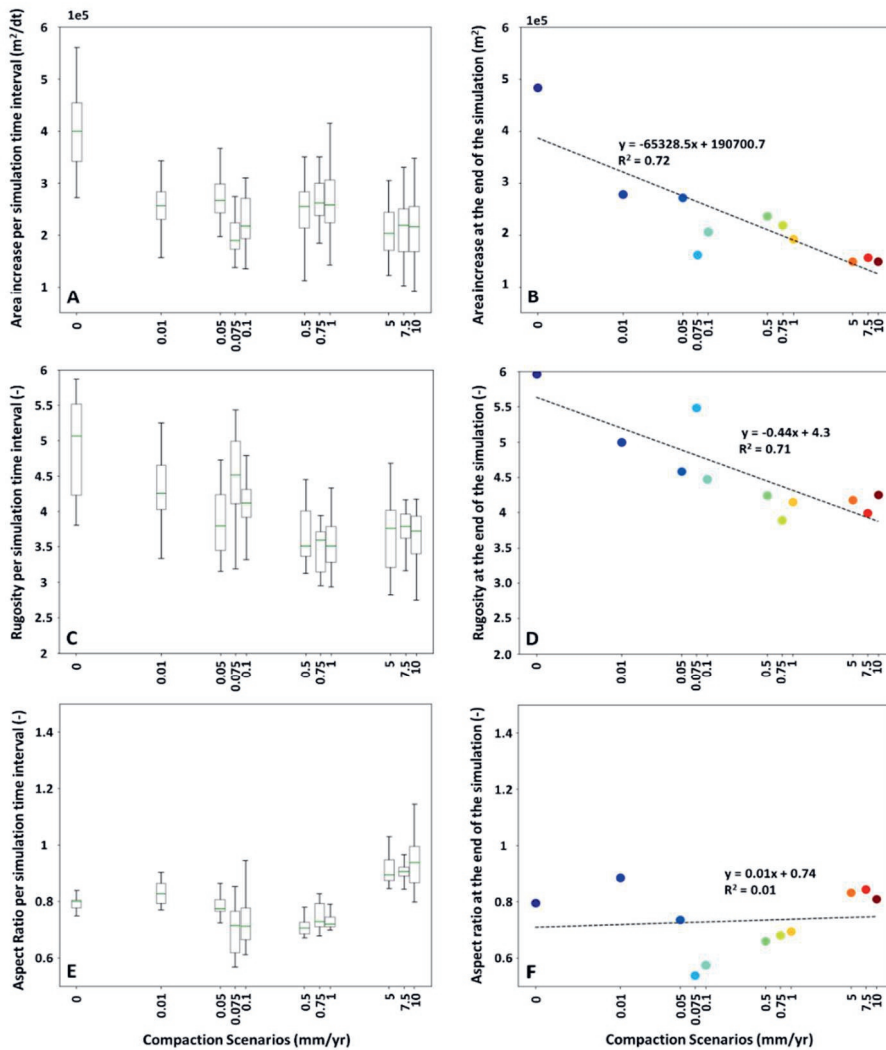


Figure 2.6. The first column shows box plots, which indicate a collapse time series of the area increase, rugosity, and aspect ratio for mud-rich deltas with compaction scenarios ranging from 0 to 10 mm y⁻¹ (A, C, and E). Each box plot shows a median value (second quartile, horizontal green lines) between the first and third quartiles (interquartile range, grey boxes). The vertical black lines indicate the maximum and minimum data range. The second column indicates the area increase, rugosity, and aspect ratio at the end of the simulation, accounting for temporal variation of morphology trends (B, D, and F). Trendlines with linear equations and coefficient correlations are also included for each morphology trend. Note that the x-axis is in the log scale.

The rugosity changes between compaction scenarios, with the non-compacted scenario having the most rugose shoreline (Figure 2.6C, D). The rugosity decreases linearly with increasing compaction scenarios ($R^2 = 0.71$). Consequently, the compaction scenarios 5 – 10 mm y⁻¹ have the smoothest coastline at the end of the simulation.

The aspect ratio decreases from compaction scenario 0 to 0.075 mm y⁻¹, reaching the most elongated delta shape for compaction scenario 0.075 mm y⁻¹. The trend reverses for compaction scenarios higher than 0.075 mm y⁻¹, leading to a more semi-circular delta top (Figure 2.6E, F). Two distinct aspect ratio trends lead to a low coefficient correlation ($R^2 = 0.01$). Compaction scenarios between 0.075 and 0.1 mm y⁻¹ show the largest spread in aspect ratio values.

Sand-rich Deltas

Although less apparent than in mud-rich deltas, a slower area increase over compaction scenarios was also observed in sand-rich deltas (Figure 2.7A, B). The non-compacted scenario (0 mm y⁻¹) has the highest rate of delta top expansion, reaching 5.2×10^5 m²/dt, which is smaller than its mud-rich delta counterpart (Figure 2.6A, B). The delta top expands at a slightly slower rate as the compaction scenario increases to 10 mm y⁻¹ ($R^2 = 0.14$).

The rugosity shows a gently decreasing trend as the compaction scenario increases to 10 mm y⁻¹ ($R^2 = 0.28$), indicating a slightly smoother coastline (Figure 2.7C, D). No clear aspect ratio trend can be observed as the compaction scenario increases to 10 mm y⁻¹ ($R^2 = 0.02$) (Figure 2.7E, F). This suggests that compaction does not influence the ultimate shape of sand-rich deltas.

It is important to note that the aspect ratio is more sensitive to the delta top dynamics than other morphological metrics. This metric assumes that net deposition occurs parallel and/or perpendicular to the initial shoreline (x- and y-axis) (Subchapter 2.4.1). Therefore, it is less responsive to a net land building that occurs diagonally to the axis, which

is the case for sand-rich deltas with compaction scenarios 0.01 and 0.1 mm y⁻¹ (Text A3). This leads to a less obvious aspect ratio trend than other morphological metrics in sand-rich deltas (Figure 2.7E, F).

Sand-rich Deltas

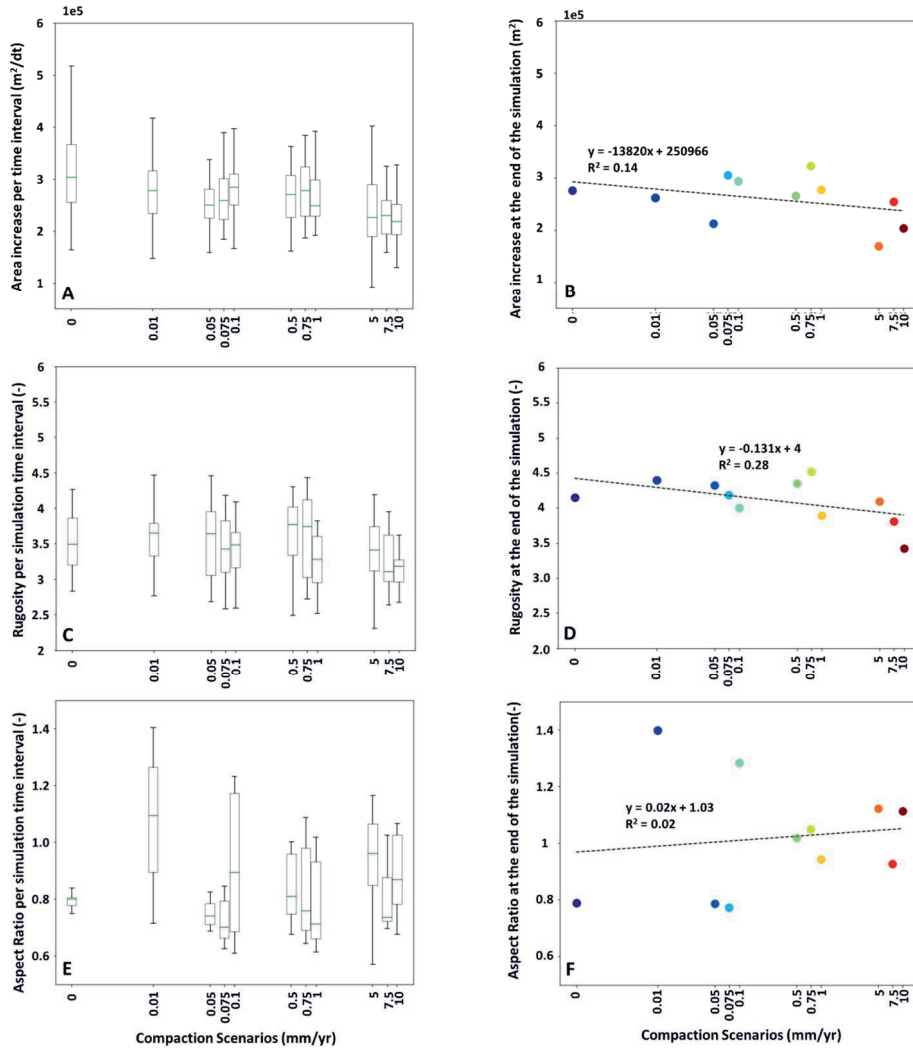


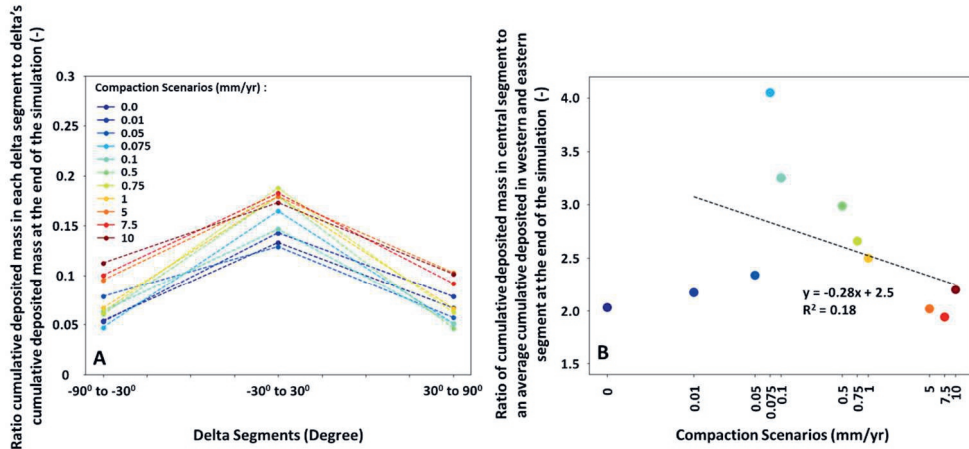
Figure 2.7. The first column shows box plots, which indicate a collapse time series of the area increase, rugosity, and aspect ratio for sand-rich deltas with compaction scenarios ranging from 0 to 10 mm y⁻¹ (A, C, and E). Each box plot shows a median value (second quartile, horizontal green lines) between the first and third quartiles (interquartile range, grey boxes). The vertical black lines indicate the maximum and minimum data range. The second column indicates the area increase, rugosity, and aspect ratio at the end of the simulation, accounting for temporal variation of morphology trends (B, D, and F). Trendlines with linear equations and coefficient correlations are also included for each morphology trend. Note that the x-axis is in the log scale.

2.5.2. Distribution of Deposited Mass

The observed morphological characteristics are influenced by the sedimentation patterns alongshore and downdip. First, the deposition patterns alongshore were analysed using the normalised cumulative deposited mass in three segments and the ratio of cumulative deposited mass in the central segment to an average of two side segments (Figure 2.8). The results show that the deposition mainly occurs in the delta centerline area for mud-rich and sand-rich deltas, which increases for higher compaction scenarios. The increasing compaction also leads to more evenly distributed sediment alongshore ($R^2 = 0.18$), which is particularly evident for mud-rich deltas with compacted scenarios higher than 0.1 mm y^{-1} (Figure 2.8B). However, delta top dynamics (e.g., avulsion), which tend to redirect sediment delivery to one side of the delta, can dampen the compaction impact, leading to asymmetric deposition alongshore, such as in non- to low compacted mud-rich deltas ($0 - 0.1 \text{ mm y}^{-1}$) and all sand-rich deltas (Figure 2.8).

The distribution of sediment downdip is shown by the cumulative deposited mass at each sub-environment relative to the delta (Figure 2.9). The non-compacted mud-rich and sand-rich deltas show a steady increase in sediment deposition being concentrated in the delta top through time, whereas deposition in the delta front decreases through delta growth. Deposition in the pro delta remains relatively constant. This shows that the deltas gradually transition to being more delta top-dominated throughout their growth. Compaction influences this trend by causing further sediment retention in the delta top, limiting sediment delivery to the delta front and pro delta. This promotes faster transitioning to the delta top-dominated.

Mud-rich Deltas



Sand-rich Deltas

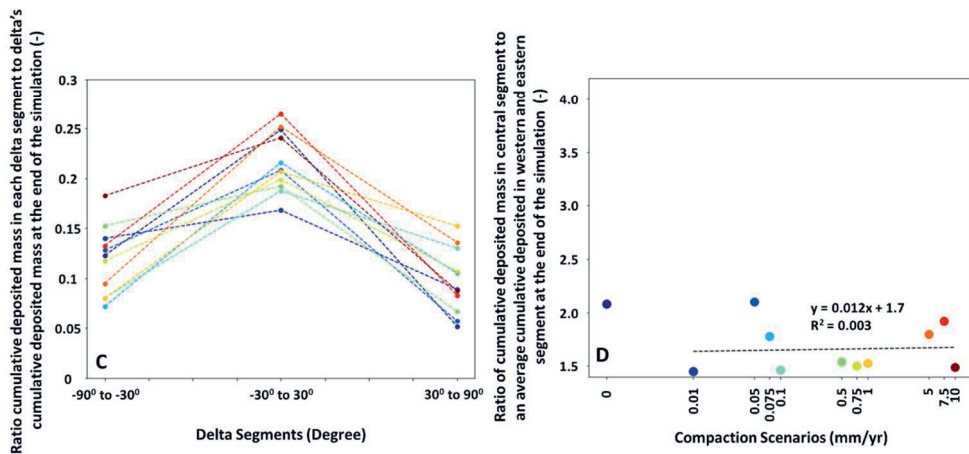


Figure 2.8. The left figures indicate the distribution of deposited sediment alongshore, shown by the ratio of cumulative deposited mass in each delta segment (-90° to -30° , -30° to 30° , and 30° to 90°) and the delta's cumulative deposited mass at the end of the simulation for mud- and sand-rich deltas (A and C). To show how evenly the deposition occurs alongshore, we also calculate the ratio of cumulative deposited mass in the delta centerline (-30° to 30°) to an average of two side segments (-90° to -30° and 30° to 90°) at the end of the simulation, shown in the right figures for mud- and sand-rich deltas (B and D). Trendlines with linear equations and coefficient correlations are also included. The calculation of delta segments is explained in Subchapter 2.4.2. Different colored lines and dots indicate compaction scenarios, from 0 to 10 mm y^{-1}

Mud-rich Deltas

Sand-rich Deltas

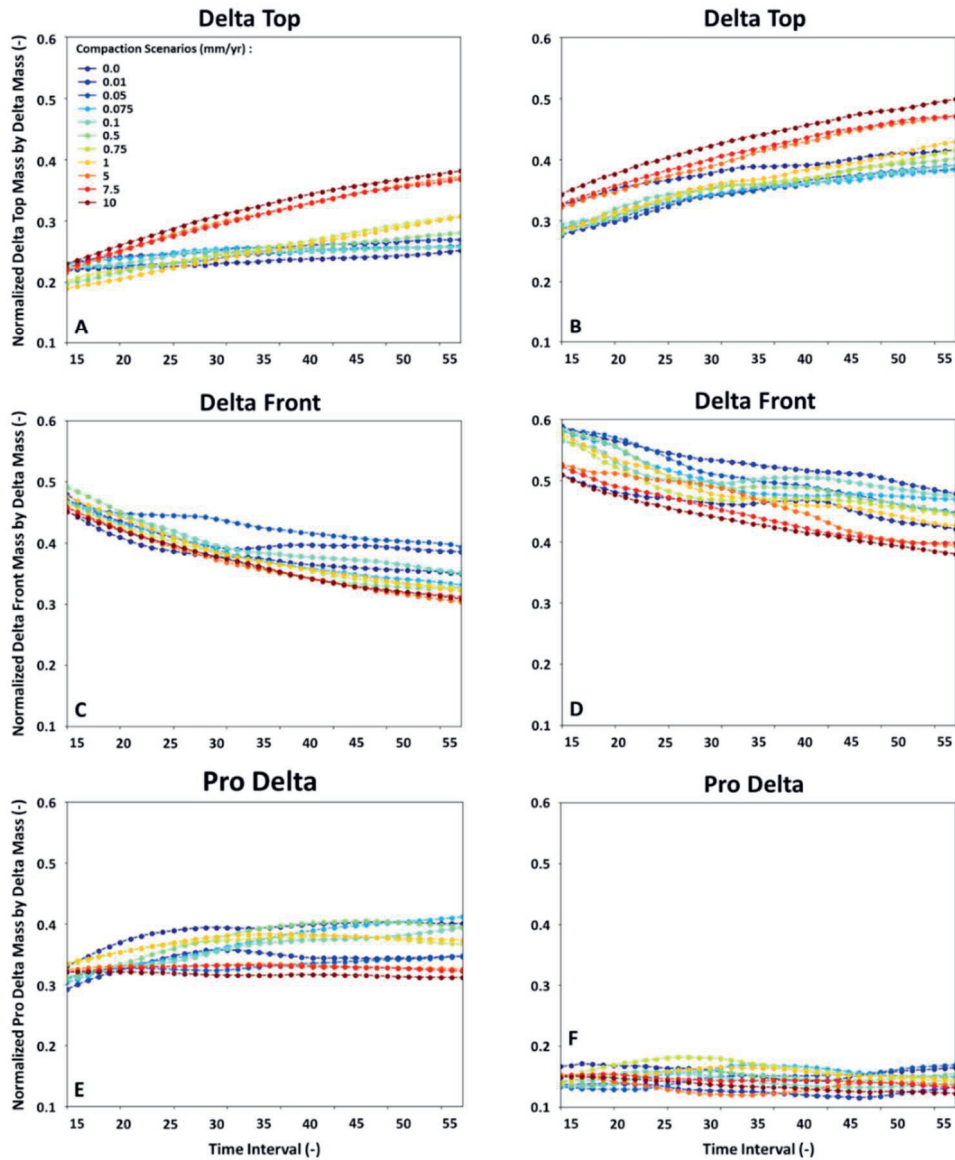


Figure 2.9. The deposited mass at each sub-environment (i.e., delta top, delta front, and pro delta) relative to the delta at each simulated output time interval for mud- (A, C, and E) and sand-rich deltas (B, D, and F). Different colored lines and dots indicate compaction scenarios, varied from 0 to 10 mm γ^{-1} . Each simulation output time interval equals approximately 60 years of delta development.

2.5.3. Accommodation Generated by Compaction

The degree of morphological alteration of the simulated deltas depends on how much compaction occurs in the model, which differs for mud-rich and sand-rich deltas. This relationship was analysed using plots showing the volume reduction and average water depth at the delta top (Figures 2.10 and 2.11). The result shows that both mud-rich and sand-rich deltas experience increased volume reduction due to compaction through time. The trend changes over compaction scenarios, showing up to three times more volume reduction experienced by mud-rich deltas than sand-rich deltas for the same compaction scenario (Figure 2.10).

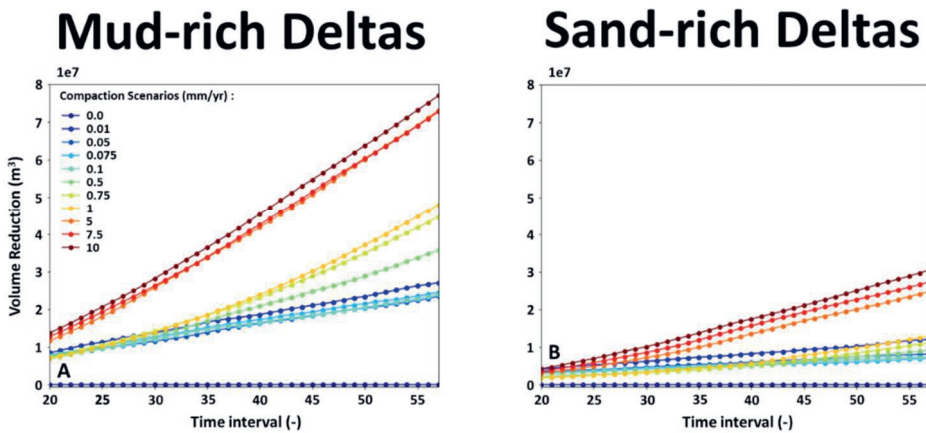


Figure 2.10. The cumulative volume reduction in the delta top at each simulation output time interval for mud- and sand-rich deltas (A and B). Each simulation output time interval equals approximately 60 years of delta development.

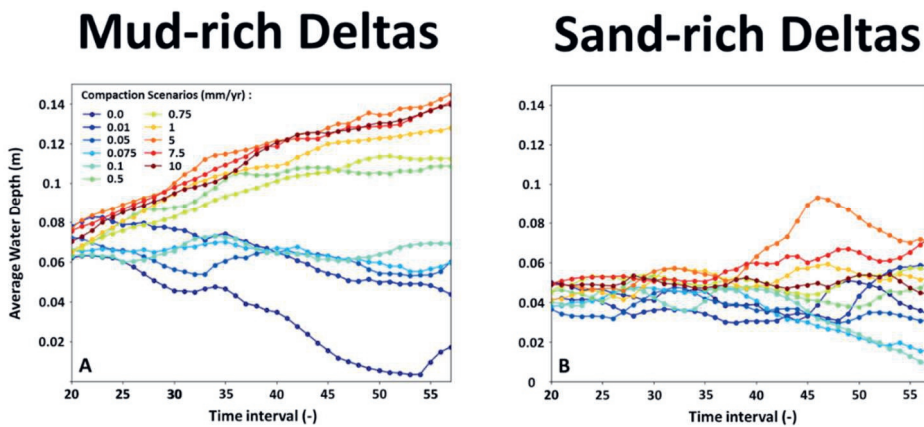


Figure 2.11. The average water depth in the delta top at each simulation output time interval for mud- and sand-rich deltas (A and B). Each simulation output time interval equals approximately 60 years of delta development.

The delta top in natural deltas is mainly dry (except for the channels), as deposition occasionally occurs due to flooding. In contrast, the delta top in the simulated deltas receives deposition continuously due to flooding through the entire simulation output time intervals (bankfull discharge parameter in Subchapter 2.3.1), which only occurs in wet grid cells activated once the threshold water depth (0.1 m) is reached.

The non-compacted mud-rich and sand-rich delta show decreasing water depth at the delta top through time. The increasing compaction scenario leads to more severe flooding at the delta top, resulting in increasing water depth through time, reaching 0.14 m and 0.07 m in mud-rich and sand-rich deltas, respectively (Figure 2.11). Mud-rich deltas have a greater water depth influenced by more significant volume reduction than sand-rich deltas.

2.6. Interpretation of The Impact of Compaction on Delta Morphodynamics

We have identified morphological trends for the simulated mud-rich and sand-rich deltas in response to syn-depositional compaction rates. This chapter combines the understanding gained from analysing the simulation results to explain the evolution of the simulated mud-rich and sand-rich deltas under compaction influence.

Compaction occurs more efficiently in the simulated mud-rich deltas as the porosity can be reduced by up to 90% compared to only 65% in the simulated sand-rich deltas for the same compaction scenario (Subchapter 2.3.1 and Text A2). This is also the case in natural systems due to the plate-like shapes of the mud grains' geometry, allowing a smaller intergranular space when compacted (Revil et al., 2002). As a result, the volume reduction occurs more considerably in the simulated mud-rich deltas (Figure 2.10), leading to greater average water depth than in the simulated sand-rich deltas, a proxy for accommodation (Figure 2.11). The additional accommodation in the delta top is created by compaction of the underlying delta front and pro delta deposits. More compaction results in larger accommodation available for deposition, driving the observed morphological variability (Figures 2.6 and 2.7).

Limited compaction leads to delta top-accommodation-limited deltas (e.g., the non-compacted mud-rich and sand-rich delta) (Figure 2.12). The supplied sediment fills the limited accommodation in the delta top. This leads to a rapidly aggrading delta top, indicated by decreasing water depth over time (Figure 2.11). For such conditions, a relatively small portion of sediment will be stored at the delta top, whereas most of the

supplied sediment will be transported downdip (Figure 2.9). The sediment bypassing the delta top builds the delta front and pro delta. As the down-dip deposition continues, the delta front and pro delta elevation increases, which will be classified as the delta top once their elevation reaches the brink point elevation (Text A4). This promotes rapid delta top area expansion (Figures 2.6A, 2.7A and 2.12). The deposition along-shore is mostly influenced by the delta top dynamics (e.g., avulsion), resulting in unevenly distributed sediment on the western and eastern segments of the delta (Figure 2.8). This leads to an elongated delta top (Figures 2.6F and 2.7F) with a rugose coastline (Figures 2.6D and 2.7D).

More compaction results in delta top-accommodation-supply balance deltas (e.g., mud-rich deltas with compaction scenarios $0.01 - 1 \text{ mm y}^{-1}$ and sand-rich deltas with compaction scenarios $0.1 - 10 \text{ mm y}^{-1}$) (Figure 2.12). The deltas respond to the increasing accommodation by promoting more deposition than the delta top-accommodation-limited deltas (Figures 2.9 and 2.11) (Colombera & Mountney, 2020). This reduces sediment bypassing to the delta front and pro delta, leading to a slower delta top area expansion (Figures 2.6A, 2.7A and 2.12). The influence of delta top dynamics on the deposition alongshore is dampened as the accommodation increases. This concentrates the deposition in the delta top centerline, while the western and eastern segments of the delta receive comparable sediment, leading to a more elongated delta top (Figures 2.6F and 2.7F) with a smoother coastline (Figures 2.6D and 2.7D) than the delta top-accommodation-limited deltas.

Large compaction leads to delta top-accommodation-dominated deltas (e.g., the compaction scenarios $5 - 10 \text{ mm y}^{-1}$ of mud-rich deltas) (Figure 2.12), characterised by insufficient deposition to fill the additional accommodation, shown by the ever-increasing average water depth over time (Figure 2.11A). This is remarkably similar to previous compaction studies using numerical simulation, which shows an up-dip increase in sediment trapping efficiency in response to the increasing compaction scenario (Liang et al., 2016a, 2016b). As a result, limited sediment bypassing the delta top to delta front and pro delta (Figure 2.9), leading to the slowest rate of the delta top area increase at the end of the simulation (Figures 2.6A, 2.7A and 2.12). Furthermore, as the accommodation is created everywhere in the delta top, the deltas distribute the sediments more evenly across the delta top, resulting in the most semi-circular delta top (Figures 2.6F and 2.7F) with the smoothest coastline at the end of the simulation (Figures 2.6D and 2.7D).

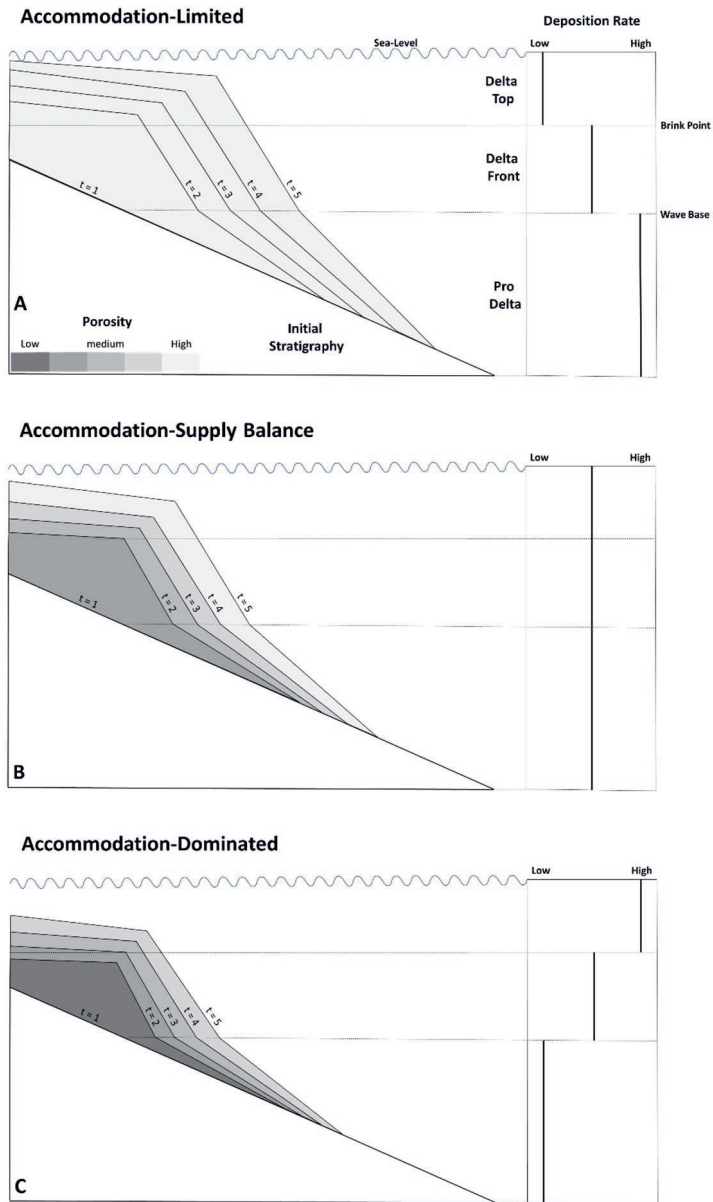


Figure 2.12. Down-dip topography of the delta top-limited-accommodation, delta top-accommodation-supply balance, and delta top-accommodation-dominated deltas (A, B, and C). The deltas respond to the increasing accommodation by promoting deposition at the delta top, limiting sediment delivery to the delta front and pro delta. This slows down the delta top expansion rate, which is mainly the case in the accommodation-dominated delta. The size of additional accommodation depends on the compaction rate of the deposited sediment, indicated by porosity values. Larger compaction resulted in thinner, denser and less porous deposited sediment. The method for classifying delta sub-environments can be seen in Text A4.

2.7. Discussion

This study, for the first time, has been able to show the impact of syn-depositional compaction on a geological timescale evolution of delta morphodynamics. This is because the interaction between sedimentation and compaction cannot be understood by only studying the end product: the preserved sediments. In addition, experimental studies in a flume lack the sediment volume required for compaction. As compaction evolves slowly over geological timescales, its impacts on delta morphodynamics are often overlooked in observations that typically cover much shorter timescales. Therefore, it is essential to assess how compaction and delta morphodynamics interact over a longer timescale ($> 10^3$ years), which is an advantage in studying compaction using simulation models.

The simulations were conducted using simplified boundary conditions, such as time-invariable fluvial discharge and tides, while waves are absent in these simulations. Waves will remove the sediment from the delta top edge. The sediment is then redeposited and recompact along the direction of wave propagation or carried offshore. This mechanism is particularly important in sediment distribution in sand-rich deltas (van der Vegt et al., 2020). Moreover, this model does not consider the second-order impact of compaction, which decreases sediment erodibility, allowing the sediment to withstand erosion (Grabowski et al., 2011; Winterwerp et al., 2012, 2018; Wu et al., 2018; Zhou et al., 2016). Nevertheless, the simulated deltas teach us that syn-depositional compaction is an important process that influences the morphology and preserved sediment trends. Therefore, we should be aware of the fundamental impact of this process on delta morphodynamics and preserved sediment as a whole.

The delta simulations presented in this chapter are simplified versions of reality because many aspects of natural deltas are not represented, such as vegetation. Vegetated delta top tends to slow down flow velocity in the water column, allowing the sediment to settle out of suspension (Fagherazzi et al., 2012; Nardin & Edmonds, 2014). This mechanism is particularly important in mud-rich deltas exposed to strong waves, which contributes to retaining fine-grained sediment at the delta top rather than being transported offshore (e.g., the Mahakam delta) (Storms et al., 2005). Incorporating the vegetation algorithm in the simulation will enhance compaction impact by enhancing sediment retention in the delta top, which is required for land building, allowing the delta top to develop. This is an exciting topic for future studies. The simplification of the modelled deltas is also shown by using two grain-size compositions (mud-rich and sand-rich) supplied to the basin, which are considered very fine-grained compared to natural and previously modelled deltas. Therefore, this study should be used to help interpret the deltas with similar supplied

compositions, and additional work would need to be done to understand any influence of compaction on coarse-grained deltas.

The strength of this study is to show that syn-depositional compaction that occurs at different rates does affect delta evolution, which can be placed in the context of previous grain-size studies (Caldwell & Edmonds, 2014; van der Vegt et al., 2020). The previous studies show an elongated delta top shape with a rugose coastline developed in very-fine-grained deltas. Had the compaction been considered, the delta top would have been more semi-circular with a smoother coastline as the deltas respond to compaction by distributing sediment more evenly across the delta top. In the context of previous compaction modelling studies (Liang et al., 2016a, 2016b), this study corroborates earlier findings that increasing compaction rate enhances sediment trapping efficiency in the delta top, leading to a smaller delta top area. Therefore, this study can help unravel the controlling processes in ancient delta deposits and predict the evolution of modern systems.

The compaction algorithm resulting from this study can also be applied to predict the morphological evolution of non-deltaic coastal environments (e.g., lagoon and estuary), where long-term empirical data is unavailable. As these areas are exposed to a rising sea level, amplified by compaction (Nicholls & Cazenave, 2010), an accurate relative sea-level rise prediction is essential. This prediction relies on compaction-induced subsidence estimation of the subsurface coastal deposits, mainly consisting of mixed clastic sediments (sand and mud). This compaction algorithm allows for such prediction, combined with process-based forward modelling, which can reconstruct the coastal morphodynamic changes in response to sea-level rise. The ability to estimate the long-term evolution of the coastal regions, where millions of people reside, is a powerful tool to help regulators make better policy and management decisions.

2.8. Conclusion

New compaction formulas were derived for primary and secondary compaction, validated using laboratory data, and implemented into Delft3D. The updated Delft3D code was used to generate prograding deltas with varying sediment supply compositions (mud-rich and sand-rich) and maximum allowed compaction rates (0 - 10 mm y⁻¹). The simulated deltas were analysed by post-processing Delft3D outputs to derive the delta top geometry, delta-wide sediment distribution, and delta top accommodation metrics. It is concluded based on the analysis that:

- The interaction between compaction-influenced accommodation and delta top dynamics drives the observed morphology trends.

- The increase in the maximum allowed compaction rate to 10 mm y^{-1} imposed to simulated deltas leads to more significant additional accommodation creation, resulting in more sediment deposition in the delta top, which occurs more evenly alongshore, leading to a more semi-circular delta top with a smoother coastline. The increasing deposition in the delta top also leads to lower sediment delivery downdip, slowing the delta top expansion, resulting in a smaller area.
- The influence of compaction on morphological trends (e.g., area increase, aspect ratio and rugosity) in mud-rich deltas is more significant than in sand-rich deltas. This occurs due to more considerable volume reduction, leading to greater accommodation than sand-rich deltas.

2.9. Data Availability

Simulation input and post-processed code used in this study are available at:

- https://data.4tu.nl/private_datasets/C7RajntOv9MXW3luCKxdeB8Odf6vP11_1WSrGBRG68s
- <https://surfdrive.surf.nl/files/index.php/s/8xy8PEah9bhYuuW>

Chapter 3: The influence of syn-depositional compaction on clastic sediment distribution in river-dominated deltas: a modelling study

3

This chapter has been published in The Depositional Record Journal in 2024

Abstract

Syn-depositional compaction or consolidation is an important process in deltaic environments because it affects both the local morphodynamics and hydrodynamics as well as the delta-scale accommodation space. However, the impact of syn-depositional compaction on the sediment distribution and the interdependency between different delta areas related to the sediment budget are not fully understood. This chapter simulates syn-depositional compaction using improved 1D grain-size compaction formulations, integrated into hydrodynamic and morphodynamic modelling software Delft3D. The updated code is used to model sedimentation in mud-rich deltas under various compaction rate scenarios, which represents the maximum compaction rate potential of sediment that experiences the highest overburden stress in the delta. The simulated deltas are analysed by first classifying their plan-view area development into depositional elements: distributary channel, underfilled channel, delta plain, mouth bar, delta front, and pro delta depositional elements. Then, sedimentation by mass, accommodation space and depositional segment metrics are calculated using the interpreted depositional elements. The results for zero compaction rate scenarios (0 mm y^{-1}) show that limited space-varying and temporal-varying accommodation is available to deposit sediment in the delta plain depositional element. Therefore, the sedimentation mainly occurs in the mouth bar depositional element. For low-mid compaction rate scenarios ($0.01 - 1 \text{ mm y}^{-1}$), the additional syn-depositional accommodation space in the delta plain depositional element increases sedimentation in this area, limiting sedimentation in the mouth bar depositional element. For high compaction rate scenarios ($> 1 \text{ mm y}^{-1}$), a further increase in the accommodation space in the delta plain depositional element leads to lateral sedimentation attributed to channel relocation, where the sedimentation mainly occurs in the mouth bar depositional element. This study shows that syn-depositional compaction impacts long-term delta evolution by influencing sediment distribution in the delta.

Keywords accommodation space, depositional elements, river-dominated deltas, sediment budget, sedimentation distribution, syn-depositional compaction

3.1. Introduction

The interaction between sediment supply and accommodation space strongly affects the development of deltas (Colombera & Mountney, 2020; Muto & Steel, 1997). In a marine (or lacustrine) basin, accommodation space is defined as the available space between the water level and the sea floor (bathymetry), which can be regarded as static or dynamic depending on the absence or presence of relative base-level fluctuations (Carlson et al., 2018; Dong et al., 2023; Jerolmack, 2009; Koss et al., 1994; Muto & Steel, 2000, 2001; Syvitski et al., 2009). In addition to basin-scale accommodation space generation due to the change in base level, syn-depositional compaction of sediments will also contribute to local accommodation space at the depositional element (DE) scale. The local variability of accommodation interacts with the morphodynamic behavior of the delta and, therefore, will affect the depositional patterns associated with the delta development. There is currently a lack of morphodynamic understanding related to the impact of the increased local accommodation space in the delta due to syn-depositional compaction in the clastic sediment. In the previous chapter, the impact of syn-depositional compaction on delta development is simulated using a constant supply of fluvial sediments (mass and grain-size distribution is not varied) and a stable relative base level. The result shows that syn-depositional compaction impacts accommodation space and distributary channel mobility, affecting depositional patterns in the simulated deltas by promoting sedimentation updip of the shoreline while limiting sediment transport downdip. This result is comparable in terms of the increasing distributary channel mobility and sedimentation updip of the shoreline to general studies on the relative base-level change (Chadwick et al., 2020, 2022; Hariharan et al., 2022; Posamentier et al., 1988). Similarly, in this chapter, the accommodation space is only affected by syn-depositional compaction.

Compaction is a process of lowering bed level due to pore fluid expulsion over geological timescales ($> 10^3$ years) (Greensmith & Tucker, 1986; Zoccarato et al., 2018). Consolidation is a process of lowering bed level due to pore fluid expulsion over short timescales, which can be studied in the laboratory (e.g., Bjerrum, 1967; Merckelbach & Kranenburg, 2004). This study focusses on compaction. The product of compaction is subsidence, which results in the creation of accommodation space in the basin. For example, many Holocene deltas experience accelerated subsidence due to compaction caused by excessive groundwater and/or hydrocarbon extraction (i.e., Yellow River and Vietnamese Mekong Delta) (Liu et al., 2016; Minderhoud et al., 2017; Zoccarato et al., 2018). Compaction of sediment can occur in an area with/without potential for deposition (syn-depositional and post-depositional compaction). For example, syn-depositional compaction occurs in an active delta lobe, whereas post-depositional compaction occurs in an inactive delta lobe. Both compaction types can occur interchangeably when there is a

shift in the active deltaic sedimentation area due to the abandonment of an active delta lobe in preference to other locations. This study focusses on the impact of syn-depositional compaction on the active deltaic depositional area.

The active deltaic depositional area can be divided into several DEs, such as distributary channel DE, underfilled channel DE, delta plain DE, mouth bar DE, delta front DE and pro delta DE. Each DE represents a particular part of the surface extent of the depositional area. The interaction between sedimentation and erosion occurs across the boundaries of the DEs. This leads to a complex sediment dispersal system with interdependencies of DE's sediment budget. Over time, this leads to complex sedimentation patterns at the surface, which additionally impacts sediment preservation beneath the surface and generates associated heterogeneity by locally and vertically variable accumulation of sand, silt and clay. As different grain size mixtures in the sediment compact at different rates, local syn-depositional compaction is induced, affecting the bathymetry. In turn, this affects local erosion, transport and sedimentation dynamics in DEs, illustrating a dependency loop. However, how local syn-depositional compaction impacts the distribution of deltaic sediment deposition across DEs is not yet fully understood for the following reasons: (1) compaction occurs at spatial and temporal scales that are beyond our ability to observe and measure ($>10^3$ km² and $>10^3$ years). (2) The preserved deltaic sediment in outcrop analogues is not complete due to erosion, leading to missing information on sedimentation and compaction history. Therefore, this dataset is difficult to use if we want to analyse the relationship between compaction and sedimentation in the delta (van der Vegt et al., 2020). Therefore, the impact of syn-depositional compaction will be addressed using a numerical simulation model.

This chapter aims to better comprehend the interdependencies of sedimentation (by mass) between DEs under the influence of syn-depositional compaction using a numerical simulation method. The focus is only on the distributary channel DE, delta plain DE and mouth bar DE because the accommodation space in these areas can be influenced by syn-depositional compaction. The delta front DE and pro delta DE are excluded from the analysis because the additional accommodation space generated by syn-depositional compaction is small compared to the overall accommodation provided by the basin water depth. This chapter differs from the previous one in three main aspects. First, it focusses on analysing the distribution of sedimentation by mass in the simulated deltas developed under the influence of compaction, whereas the previous chapter focusses on analysing morphodynamic changes in simulated deltas due to compaction. Second, an improved algorithm is employed to classify delta areas into DEs, consisting of distributary channel, underfilled channel, delta plain, mouth bar, delta front and pro delta, compared to a more general spatial definition of delta area, such as delta top, front and pro delta used in the

previous chapter. Third, an upgrade formulation for the secondary compaction is implemented to prevent accelerated thickness reduction trend, aligning better with laboratory observations (Merckelbach & Kranenburg, 2004; Mesri, 2003).

This study is performed in several steps: (1) the compaction formulations presented in the previous chapter are improved. (2) The improved compaction formulations are implemented into Delft3D code, which simulates river-dominated deltas where sedimentation actively occurs. (3) The simulated deltas are then analysed to understand the impact of syn-depositional compaction on the interdependencies of sedimentation (by mass) between DEs. This work builds on previous studies using Delft3D that simulate the impact of hydrodynamic forcings, supplied sediment properties and compaction on delta development (Burpee et al., 2015; Caldwell & Edmonds, 2014; D. Edmonds et al., 2010; D. A. Edmonds et al., 2011; D. A. Edmonds & Slingerland, 2007, 2008, 2010; Geleyse et al., 2010, 2011; Hillen et al., 2014; Nardin et al., 2013; Nardin & Fagherazzi, 2012; Porcile et al., 2023; Storms et al., 2007; van der Vegt et al., 2016, 2020).

3.2. Methodology for Compacting Simulated Delta Deposits

Several formulations have been developed to simulate compaction in unconsolidated sediments in a deltaic domain, which focus on short-timescale sedimentation ($< 10^3$ years) (Winterwerp et al., 2012; Xotta et al., 2022; Zhou et al., 2016). This subchapter describes compaction formulations for long-timescale sedimentation in a deltaic depositional environment ($> 10^3$ years). Laboratory studies show thickness reduction of a sediment bed initially occurs at a quicker rate after deposition, called primary compaction, followed by a slower rate, called secondary compaction (Kaliakin, 2017; Merckelbach & Kranenburg, 2004; Mesri, 2003; Terzaghi, 1923). In this study, both compaction types will occur while deltas are evolving. Both primary and secondary compaction are therefore considered to be syn-depositional. The compaction formulations are described in the following subsections.

Four important assumptions are made in deriving compaction formulas that are applied in this study: (1) the sediment porosity is sufficiently high to always allow the expulsion of pore fluid. Consequently, an overpressured condition due to trapped pore fluid will not occur. (2) The pore fluid disappears after the expulsion, which does not affect the dewatering in neighboring pores. This simplification means that the fluid flow path has no impact on long-timescale compaction ($> 10^3$ years). (3) Compaction does not affect the erodibility of sediment. (4) Compaction is only applied to clastic sediment (sand and mud), as organic materials are not modelled.

3.2.1. Primary Compaction

Primary compaction results in a significant local thickness reduction at short timescales (order of days to years) (e.g., van Asselen et al., 2009), which occurs due to grain rearrangements as pore pressures reduce (Alberts, 2005). While the structure of the formulation is similar, the algorithm to calculate primary compaction is improved from the previous chapter. It is computed not only using the load imposed by overburden weight but also by self-weight, allowing for compaction of the whole model stratigraphy, including near-surface sediment, which was previously not compacted because the weight of overlying water or air was considered insignificant. The primary compaction formula is shown by Equation 3.1.

$$\frac{\Delta H_p}{\Delta t} = C_p \cdot \frac{1}{E} \cdot H_{t-1} \cdot (\sigma_t - \sigma_{t-1}) \quad (3.1)$$

where $\frac{\Delta H_p}{\Delta t}$ is the subsidence per simulated time due to primary compaction (m y^{-1}), C_p represents the proportional rate of subsidence due to primary compaction (y^{-1}), E indicates the oedometric modulus (Pa), H_{t-1} expresses the bed thickness at the previous simulation time (m), and $\sigma_t - \sigma_{t-1}$ is net increase in load (self-weight and overburden weight) between two successive simulation time interval (Pa). $\frac{\Delta H_p}{\Delta t}$ has a unit of m y^{-1} , which represents compaction rate. $\frac{\Delta H_p}{\Delta t}$ can be expressed as ΔH_p within a time step in the calculation. Under the simulated conditions with relatively thick sediment layers, the subsidence is assumed small relative to the total thickness, and the largest subsidence can be estimated in proportion to the rate as it is limited by sediment permeability. A practical approach adopted here is that C_p values are used as a limit to the primary compaction rates (with a change unit to m y^{-1}). (See also Subchapter 2.2.1). The primary compaction occurs in sand and mud if the load is larger than that at the end of the previous simulation time. Otherwise, secondary compaction takes place, as described in the next subchapter.

3.2.2. Secondary Compaction

Secondary compaction was first explained by Taylor & Merchant (1940), who observed that compaction still occurred for conditions where there was very limited or no sedimentation occurring, yet at a much lower rate than primary compaction. This indicates that secondary compaction occurs at no/limited change in load and pore pressure (Mesri & Castro, 1987). This process is characterised by small local thickness reduction per time step that occurs over a long timescale ($>10^3$ years) (Bjerrum, 1967). Secondary compaction includes processes such as plastic adjustment of sediment structure, local particle crushing, and reduced absorbed water in the sediment. This compaction type occurs primarily in mud

due to its low permeability, which prevents rapid expulsion of pore water compared to sand (Zoccarato et al., 2018). The computation of local thickness reduction induced by secondary compaction is based on the following approximation:

$$\frac{\Delta H_s}{\Delta t} = C_s \cdot H_{t-1} \cdot (\log(t - t_p + \Delta t) - \log(t - t_p)) \quad (3.2)$$

where $\frac{\Delta H_s}{\Delta t}$ is the subsidence per simulated time interval due to secondary compaction (m y^{-1}), C_s represents the proportional rate of subsidence due to secondary compaction (y^{-1}), H_{t-1} expresses the bed thickness at the previous simulation time (m), t indicates the simulation time (minutes), t_p is the simulation time at which primary compaction occurs (minutes), and Δt represents the simulation time step (minutes). $\frac{\Delta H_s}{\Delta t}$ has a unit of m y^{-1} , which also indicates compaction rate. $\frac{\Delta H_s}{\Delta t}$ can be expressed as ΔH_s within a time interval in the calculation. Consistent with C_p (See also Subchapter 3.2.1), C_s values are used as a limit to the secondary compaction rates (m y^{-1}).

Equation 3.2 is an improved version from the previous chapter because now the reference time t_p is updated each time primary compaction occurs. This prevents accelerated subsidence due to secondary compaction as the simulation time increase, which is consistent with a previous laboratory study (Merckelbach & Kranenburg, 2004). The reasoning and derivation of the improved secondary compaction formula is explained in Text B1 (see also Figure B1). Note that the simulation output time is in hydrodynamic time, which can be converted to morphodynamic and realistic time. The different time definitions and conversion method are explained in Subchapter 3.3.

3.2.3. Subsidence

The primary and secondary compaction (Equations 3.1 and 3.2) leads to subsidence and porosity reduction of sediment bed. Porosity is calculated by first updating the solid volume fraction of sediment bed due to compaction using Equation 3.3, and subsequently converting it to porosity using Equation 3.4. The bed thickness after primary or secondary compaction is calculated using Equation 3.5.

$$\phi_t = \phi_{t-1} \cdot \frac{H_t}{H_{t-1}} \quad (3.3)$$

$$\eta_t = 1 - \phi_t \quad (3.4)$$

$$H_t = H_{t-1} - \Delta H_{p/s,t} \quad (3.5)$$

here, the solid volume fraction (ϕ_t , dimensionless) is calculated for each simulation time by multiplying the solid volume fraction at the previous simulation time (ϕ_{t-1} , dimensionless) with the ratio of bed thickness between two successive simulation time intervals ($\frac{H_t}{H_{t-1}}$, dimensionless). The bed porosity (η_t , dimensionless) is calculated as one minus the solid fraction (ϕ_t). The bed porosity will decrease from an initial to a minimum value. The initial porosity represents the porosity of newly deposited sediment, whereas the minimum porosity represents the porosity of fully compacted sediment (Text B2).

The compaction formulations (Equations 3.1 - 3.5) are implemented into Delft3D code version 6.02.08.62644, which is embedded in Delft3D GUI version 4.04.01 (Deltares, 2021). The implementation procedures can be seen in Figure B2. This Delft3D version differs from the one used in the previous chapter because it includes a new sediment erosion formula, allowing a more stable simulation (Text B3 and Figure B3). For a detailed explanation of the processes in Delft3D, please refer to the Delft3D FLOW manual, which is available online (Deltares, 2025).

3.3. Modelling Parameters and Scenarios

The updated Delft3D code is tested by simulating prograding river-dominated deltas under a stable regional relative base level. The parameters and scenarios used in the simulations are described in this subchapter.

3.3.1. Modelling Parameters

The model setup consists of a discharge boundary representing a fluvial channel supplying water and sediments to a sloped basin with a 0.1^0 gradient (Figure 3.1). A similar setup has also been used by previous modelling studies using Delft3D (Geleynse et al., 2010, 2011; van der Vegt et al., 2016, 2020). The initial substrate of the model domain is sand ($100 \mu\text{m}$), which is set to fully compact by adjusting the porosity of the substrate to its minimum porosity. The sediment supplied by the fluvial channel consists of three grain-size classes (sand, $100 \mu\text{m}$, cohesive fluvial mud, 50 and $20 \mu\text{m}$). Oedometric modulus of sand and mud are set to $25 \times 10^6 \text{ Pa}$ and $5 \times 10^6 \text{ Pa}$, respectively. Relevant modelling parameters are shown in Table 3.1

The initial substrate sand and the fluvial sand can be traced separately, even though they have identical sediment properties, such as porosity. The initial porosity for mud and sand was set to 80% and 40% respectively, while the minimum porosity for mud and sand was set to 5% and 25%, respectively (Table 3.1) (Alberts, 2005; Revil et al., 2002).

The initial and minimum porosity of sand and mud are used to determine the initial and minimum porosity of sediment mixtures based on their proportion in the mixture (Text B2).

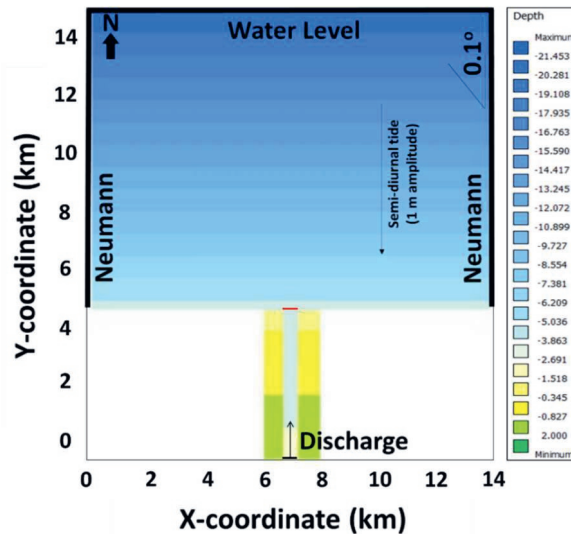


Figure 3.1. The model setup has a width and length of 14 x 15 km, consisting of a fluvial channel debouching into a sloped basin with a 0.1° gradient. The boundary condition at the channel inflow (short horizontal thin black line) is water and sediment discharge. The open boundaries in the basin (long horizontal and vertical thick black lines) are the Neumann at the west and east combined with the water level along the north boundary. The initial water depth ranges from 4 m at the delta apex (short horizontal thin red line) to 21.5 m at the basin edge

Table 3.1. User-defined parameters used in all Delft3D simulations

No	User-Defined Model Parameter	Value	Unit
1	Grid Cell Dimension in x and y	50 x 50	m x m
2	Number of Compacting Layers	76	-
3	Initial Bed Thickness	4	m
4	Water Discharge	1600	m ³ /s
5	Sediment Discharge	0.15	kg/s
6	Total Hydrodynamic Time	57	day
7	Morphological Scaling Factor	120	-
8	Spin-up Interval Before Morphological Updating Begins	720	min
9	Maximum Allowed Erosion Rate of Sediment	0.00067	s/m
10	Critical Bed Shear Stress for Erosion of Sediment	0.18	N/m
11	Critical Bed Shear Stress for Deposition of Sediment	1000	N/m
12	Grain Sizes (Sand and Two Mud Fractions)	1E-04, 5E-05, and 2E-05	m
13	Specific Density of Sand and Mud	2650	kg/m ³
14	Dry Bed Density of Sand and Mud	500 and 1600	kg/m ³
15	Settling Velocity of Mud Fractions	0.0022 and 0.00056	m/s
16	Sand Concentration in Sediment Supply	0.0225	kg/m ³
17	Mud Concentration in Sediment Supply	0.1275	kg/m ³

18	Amplitude of Semi-Diurnal Tide	0.02	m
19	Initial Porosity of Sand	0.4	-
20	Initial Porosity of Mud	0.8	-
21	Minimum Porosity of Sand	0.25	-
22	Minimum Porosity of Mud	0.05	-
23	Oedometric Modulus for Mud	5E+06	Pa
24	Oedometric Modulus for Sand	25E+06	Pa

The model boundary representing a fluvial channel conveys a constant discharge of $1600 \text{ m}^3 \text{ s}^{-1}$, with a sediment concentration of 0.15 kg s^{-1} (van der Vegt et al., 2020), which allows the simulated deltas to prograde and locally aggrade during the simulation time (Text B4). As the fluvial discharge is constant over the simulation time, it is interpreted to represent a bankfull (channel forming) discharge. A low semi-diurnal tidal wave with 1 m amplitude arriving perpendicular to the initial shoreline is included in the simulations. Previous studies show that in order to simulate sedimentation similar to natural deltas, some small tidal wave activity is required to stir up the sediment deposited in the basin (van der Vegt et al., 2016, 2020). Small wind-generated waves are not included in the model setup to reduce the computation time.

The simulation time step used in this study is 0.5 minutes in hydrodynamic time. However, to better observe the changes in the delta development, the simulated deltas are outputted using a simulation output time step of 1 day in hydrodynamic time (Figure 3.2). The total simulation output time is 57 days of hydrodynamic time. This time equals 18.74 years of morphodynamic time obtained by multiplying the hydrodynamic time with the morphological scaling factor (MORFAC) of 120 as used in the model setup (Li et al., 2018). As the simulations were run using bankfull discharge, which is assumed to occur two days a year (Li et al., 2018), the morphodynamic time can be extended to a realistic time of 3373 years. For this study, both primary and secondary compaction operates in realistic time because: (1) the simulated deltas are formed during the flooding period (bankfull discharge) when sedimentation is active in the delta. This will activate primary compaction and, subsequently, secondary compaction if sedimentation ceases. (2) Secondary compaction occurs at a longer timescale because it has a slower compaction rate than primary compaction.

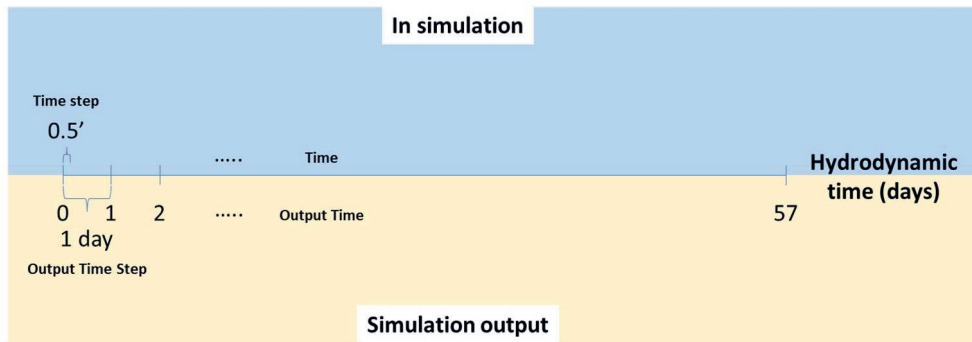


Figure 3.2. In Delt3D simulation, the calculation of delta development is conducted using a simulation time step of 0.5 minutes in hydrodynamic time. The calculation result is outputted using a simulation output time step of 1 day in hydrodynamic time. The total simulation output time is 57 days in hydrodynamic time. To better observe the changes in the delta development due to compaction over a geological timescale, the deposited sediment thickness at each simulation output time is multiplied by a morphological scaling factor of 120. This leads to a total simulation output time of 19 years of delta development in morphodynamic time. The timescale can be further extended by simulating the delta development over the flooding period (bankfull discharge), which results in a total simulation output time of 3373 years in realistic time. Simulating delta development over a flooding period means sedimentation actively occurs in the delta. This triggers the primary compaction, followed by the secondary compaction if sedimentation ceases. Therefore, primary and secondary compaction operate over the realistic time during delta development

It is important to note that computed realistic time is an approximation due to the assumption that the simulation fluvial discharge is the channel-forming bankfull discharge that statistically occurs only two days per year and is absent during the rest of the year (363 days), which is not explicitly modelled. This means that in this model, delta dynamics are only associated with bankfull flood conditions, while in reality, sediment lower stage flow conditions will also affect the delta. In addition, bankfull discharge and its frequency in real-world systems will vary over time. Therefore, the calculated realistic time used in this study should be seen as a first-order approximation to real-world time.

3.3.2. Modelling Scenarios

Simulated deltas represent mud-rich deltas (85% fluvial mud and 15% fluvial sand), subjected to a range of user-defined primary and secondary compaction rates (C_p and C_s in Equations 3.1 and 3.2). The primary compaction rate is the maximum expulsion rate of pore fluid due to the largest load imposed by self-weight and overburden weight, which represents compaction potential in the simulation. This parameter depends on the overall

permeability of sediment mixtures, which differs in deltaic systems. The primary compaction rates are obtained from published syn-depositional compaction rates of active Holocene deltas, such as the Nile and Ganges-Brahmaputra ((Aly et al., 2012; Becker & Sultan, 2009; Gebremichael et al., 2018; Higgins et al., 2014; Saleh & Becker, 2018; Stanley, 1990; Steckler et al., 2022)). The primary compaction rates were set to 0 - 10 and 0 - 100 mm y^{-1} in morphodynamic time for mud and sand, respectively (Table 3.2). Sand compacts faster because it has higher permeability than mud, resulting in the repacking of sand grains from loose to compact packing (Alberts, 2005).

Table 3.2. Eight modelling scenarios (MS01 - MS08) represent mud-rich deltas (85% mud and 15% sand) with varying primary and secondary compaction rates (C_p and C_s)

Run ID	Cp Mud (mm/year)	Cp Sand (mm/year)	Cs Mud (mm/year)
MS01	0	0	0
MS02	0.01	0.1	0.000003
MS03	0.05	0.5	0.000015
MS04	0.1	1	0.00003
MS05	0.5	5	0.00015
MS06	1	10	0.0003
MS07	5	50	0.0015
MS08	10	100	0.003

As the environmental factor influencing the secondary compaction rate is still unknown (van Asselen et al., 2009), this parameter was determined by sensitivity analysis based on two criteria: (1) the secondary compaction rate should be lower than the primary compaction rate (Taylor & Merchant, 1940). (2) The determination of the secondary compaction rate is based on the modelling stability criterion. Mesri (2003) shows that the ratio secondary to primary compaction rate varies for different sediment types, for example, granular soil has a larger ratio than peat and muskeg (0.02 vs 0.06). Different C_s/C_p values were tested, including from Mesri for shale and mudstone sediment type (0.03). The ratio values from Mesri (2003) are considered to be high, which often leads to model error because thickness reduction occurs abruptly at each simulation time. This results in a large bathymetry lowering that cannot be handled by the model. The optimum ratio value was found to be 0.0003. Therefore, the secondary compaction rate is varied from 0 to 0.003 mm y^{-1} in morphodynamic time (Table 3.2).

Sedimentation and erosion vary in the model domain, leading to local net sedimentation rates (positive or negative) depending on local sediment accumulation rates (positive or negative). Local sediment accumulation rates cause local compaction rates. The

local rates are mainly slower than the primary compaction rates (Text B5), which can be considered as the compaction potential in the model. In this study, compaction rate scenarios are defined based on the primary compaction rate for mud (0 to 10 mm y⁻¹). Compaction rate scenarios can be converted to hydrodynamic and realistic time by considering the ratio of total simulation output time between different time definitions. For example, 1 mm y⁻¹ in morphodynamic time equals 120 mm y⁻¹ in hydrodynamic time (18.74 years / 57 / 365 years is multiplied by 1 mm y⁻¹) and 0.0056 mm y⁻¹ in realistic time (18.74 years / 3373 years is multiplied by 1 mm y⁻¹) (Table 3.3).

Table 3.3. Compaction rate scenarios in relative and absolute terms. The absolute term of compaction rate scenarios is defined in morphodynamic time, which can be converted into hydrodynamic and realistic time.

No	Compaction Rate Scenarios (mm/year)			
	Relative Scenarios	Absolute Scenarios		
		Hydrodynamic Time	Morphodynamic Time	Realistic Time
1	Zero Compaction Rate	0	0	0
2	Low-Mid Compaction Rates	1.2	0.01	5.47945E-05
3		6	0.05	0.000273973
4		12	0.1	0.000547945
5		60	0.5	0.002739726
6		120	1	0.005479452
7	High Compaction Rates	600	5	0.02739726
8		1200	10	0.054794521

While the simulation using compaction rate scenarios results in realistic deltas, the absolute values of compaction rate scenarios cannot be directly compared to real-world compaction measurements because: (1) they depend on assumptions used in the model (i.e., MORFAC and frequency of bankfull discharge). (2) The local compaction rates in the simulations are lower than the compaction rate scenarios (Figure B5). However, within the model domain, the zero-compaction rate scenario reveals a different delta behavior than low-mid to high compaction rate scenarios, which are analysed in the subchapter below. It is argued here that the relative differences between the compaction rate scenarios bear important insights that do translate to real-world deltas. Compaction rate scenarios in absolute and relative terms are shown in Table 3.3. Bathymetry development for all compaction rate scenarios is shown in Text B6 (Figures B6 - B14).

3.4. Description of Metrics Used to Analyse the Impact of Syn-depositional Compaction on Sediment Distribution in Simulated Deltas

Several metrics are developed to analyse the impact of syn-depositional compaction on the temporal evolution of simulated deltas and the distribution of sediment deposited on their surface. This allows for objective comparisons of simulated deltas' characteristics between imposed compaction rate scenarios. It is important to note that the computation of metrics is conducted for each simulation output time step starting from 15 days (in hydrodynamic time), at which the simulated deltas reach dynamic equilibrium.

3.4.1. Depositional Elements

The first metric classifies the 2D plan-view area of simulated deltas into DEs: distributary channel DE, underfilled channel DE, delta plain DE, mouth bar DE, delta front DE and pro delta DE. These elements are identified using water depth, flow properties and deposited sediment mass (Text B7 - B9 and Figures B15 - B27). Over time, the accumulation of sediment in these areas will form a 3D geometry of preserved deposits called architectural elements (AE). However, the sedimentation in DEs is not equivalent to the preserved AEs due to post-depositional erosion (van der Vegt et al., 2020). The preservation of AEs is not the focus of this study.

3.4.2. Distribution of Sedimentation in Depositional Elements

In the previous chapter, syn-depositional compaction is shown to impact the sedimentation in various delta areas. To track the distribution of sedimentation across the delta in more detail, two metrics are used. The first metric is the percentage of sediment by mass deposited in each DE (Equation 3.6). This metric represents the contribution of each DE to the total sedimentation by mass in the delta. The second metric is the percentage of sediment by mass deposited in each DE for each grain-size class (Equation 3.7). This metric indicates the grain-size distribution of sediment deposited in DEs.

$$M_{DE,t} = \frac{Totmass_{DE,t}}{Totmass_{Delta,t}} \quad (3.6)$$

$$M_{GS,DE,t} = \frac{Totmass_{GS,DE,t}}{Totmass_{Delta,t}} \quad (3.7)$$

here, the percentage of sediment by mass in DEs during a simulation output time step ($M_{DE,t}$) is calculated as a ratio of total sedimentation by mass in each DE ($Totmass_{DE,t}$ in kg) to total sedimentation by mass in the delta ($Totmass_{Delta,t}$ in kg) during a simulation output time step. The percentage of sediment by mass deposited in DEs for each grain-size class during a simulation output time step ($M_{GS,AE,t}$) is quantified as the ratio of total sedimentation by mass for each grain-size class in each DE ($Totmass_{GS,DE,t}$ in kg) to the total sedimentation by mass for all grain-size classes in the delta ($Totmass_{Delta,t}$ in kg) during a simulation output time step.

To better show the influence of syn-depositional compaction on the distribution of sedimentation in DEs, the output time series of mass fractions ($M_{DE,t}$ and $M_{GS,DE,t}$ in Equations 3.6 and 3.7) are also collapsed into box plots. Note that the calculation of mass fractions also includes the mass eroded from the initial basin substrate. However, the contribution of eroded mass is assumed minimal as simulated deltas are actively aggrading (Figure B4).

3.4.3. Accommodation

In the previous chapter, syn-depositional compaction is shown to reduce the thickness of simulated deposited sediments, lowering the bathymetry and leading to an increase in water depth and, therefore, accommodation space. The accommodation space represents the space available for potential sedimentation (Jervey, 1988; Posamentier et al., 1988). Muto & Steel (2000) further elaborates this concept by defining the accommodation space as the water depth in which the sediment can be deposited. The water depth is defined by subtracting the bathymetry from the water level. Both bathymetry and water level are measured from sea level. The water depth calculation is performed at each grid location for each simulation output time step.

The negative average bathymetry means the majority of DEs are above the water level or less, or no accommodation is available for sedimentation. The sediment can be above the water level if the accretion exceeds the available accommodation space in the delta plain DE. In contrast, the positive average bathymetry indicates that most DEs are below the water level, and accommodation space is available for sedimentation.

3.4.4. Depositional Segments

Each distributary channel acts as a conduit in delivering sediments across the delta plain. Once it reaches the shoreline, the sediments are released from the channel mouths,

deposited as mouth bars close to the channel mouths, or travel further downdip. Therefore, the distributary channel dynamics influence the distribution of sedimentation in simulated deltas.

The change in the location of sedimentation due to distributary channel relocation is quantified using the depositional segment metric (Equation 3.8). Plan-view simulated deltas are divided into radial segments centering at the delta apex, consisting of central (-30° to 30°) and lateral (-90° to -30° and 30° to 90°) segments (Figure 3.3). The depositional segment represents the areal extent of sedimentation in the distributary channel DE and mouth bar DE, which is compared between radial segments. The main distributary channel with a well-developed mouth bar mainly influences this metric. Therefore, the mouth bar is included to amplify the contribution of the main distributary channel in the metric calculation.

$$Dep_{segment,t} = \frac{2*(A_{CH}+A_{MB})_{C,t}}{(A_{CH}+A_{MB})_{L,t}} \quad (3.8)$$

The depositional segment during a simulation output time step ($Dep_{segment,t}$) is quantified as the ratio of two times the total area of distributary channel DE and mouth bar DE in the central segment ($(A_{CH} + A_{MB})_{C,t}$ in m^2) to their total area in the lateral segment ($(A_{CH} + A_{MB})_{L,t}$ in m^2) during a simulation output time step. Ratio values higher than two indicate that sedimentation mainly occurs in the central segment. In contrast, ratio values lower than two mean that sedimentation is primarily in the lateral segments. Note that the radial segments are fixed over the simulation output time step. Therefore, the number of distributary channels and mouth bars does not impact the metric calculation if they are located in the same segment.

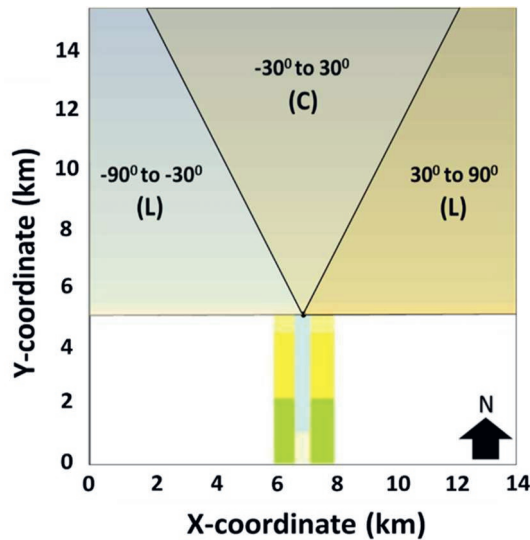


Figure 3.3. The basin area is divided into fixed radial segments centering at the delta apex: the central (-30° to 30°) and lateral (30° to 90° and -90° to -30°) segments

3.5. Delta Simulation Results Analysis

This subchapter reports the results and analyses of the computed metrics designed to understand the impact of compaction for various compaction scenarios. The distribution of sedimentation (by mass) in DEs will be described first, which is then linked to the accommodation and depositional segment. Only the distributary channel DE, delta plain DE and mouth bar DE are analysed and compared. The delta front DE and pro delta DE are excluded because the accommodation space in these areas is mainly influenced by the basin gradient. The underfilled channel DE is also not analysed because it has a limited contribution to the total sedimentation (by mass) in the simulated deltas.

3.5.1. Distribution of Sedimentation in Depositional Elements

The distribution of sedimentation in simulated deltas is analysed using the percentage of sediment by mass deposited in the system per simulation output time step, as shown in Figure 3.4. The result shows that the influence of syn-depositional compaction is not apparent in the temporal sedimentation trend in the distributary channel DE, delta plain DE, and mouth bar DE, shown by fluctuated values of the percentage sediment by mass over the simulation output time (Figures 3.4A, C, E). Temporal variability of the percentage sediment by mass can be removed by collapsing the output time series into a box plot per compaction rate scenario (Figures 3.4B, D, F). The distributary channel DE has a minimal response to compaction rate scenarios (Figure 3.4D). From zero to low-mid compaction rate scenarios ($0 - 1 \text{ mm y}^{-1}$), the sedimentation (by mass) in the delta plain DE increases (Figure 3.4D). The opposite occurs for the mouth bar DE, where sedimentation (by mass) decreases with compaction rate scenarios (Figure 3.4F). In contrast, there is a negative correlation between high compaction rate scenarios ($>1 \text{ mm y}^{-1}$) and the sedimentation (by mass) in the delta plain DE, while a positive trend is observed in the mouth bar DE (Figures 3.4D, F).

The grain-size distribution of sediment deposited in DEs is also compared between compaction rate scenarios using the box plots, which shows the trend better, whereas the temporal plots are in Figures B28 - B30. For the distributary channel DE, the deposited mass consists of sand with lower mud content (Figures 3.5A, D, G). There is an increase in sand and mud sedimentation (by mass) in the delta plain DE from zero to low-mid compaction rate scenarios ($0 - 1 \text{ mm y}^{-1}$) (Figures 3.5B, E, H). Consequently, the sedimentation (by mass)

for these grain size classes decreases in the mouth bar DE (Figures 3.5C, F, I). High compaction rate scenarios ($> 1 \text{ mm y}^{-1}$) show a reversed trend. For these scenarios, more compaction leads to higher sand and mud sedimentation (by mass) in the mouth bar DE. Overall, the contribution of fluvial sand to the sedimentation (by mass) in all DEs is higher than the substrate sand, which is eroded from initial basin sediment (Text B10).

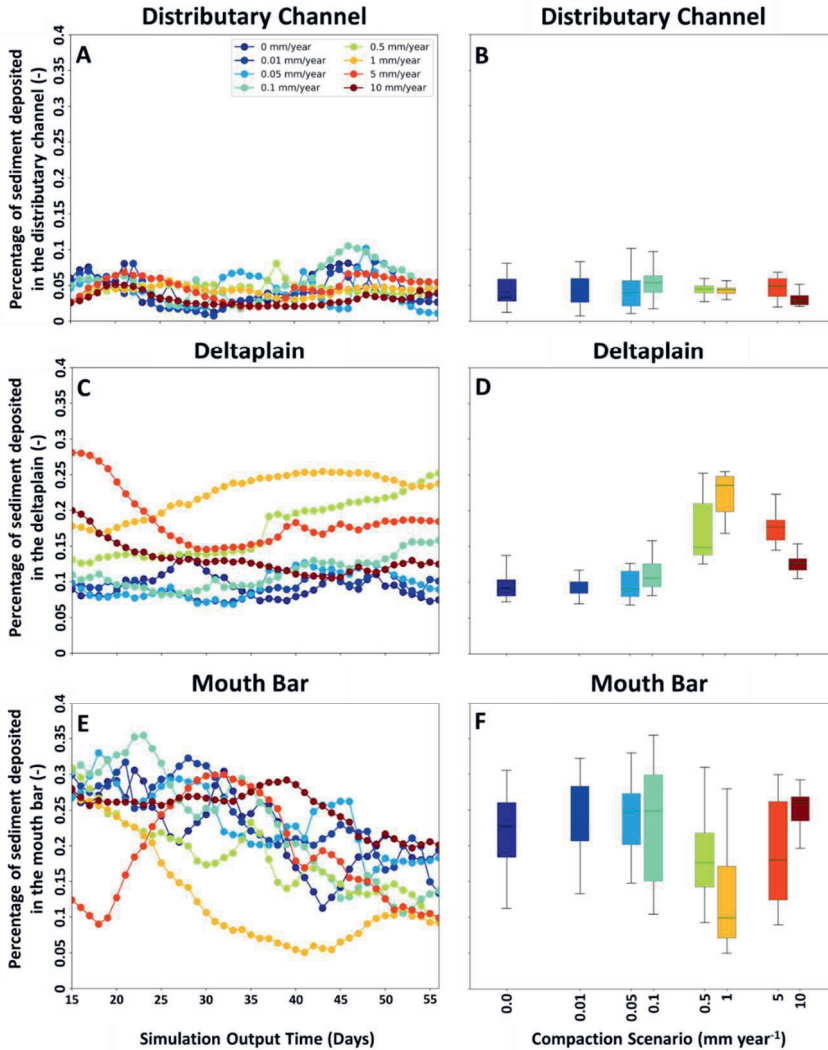


Figure 3.4. The percentage of sediment by mass deposited in the distributary channel DE, delta plain DE and mouth bar DE over the simulation output time step, starting from 15 days in hydrodynamic time (A, C and E). In the second column, the time series of the percentage sediment is collapsed by mass into box plots (B, D, F). Each box plot shows a median value (second quartile, horizontal green lines) between the first and third quartiles (interquartile range, grey boxes). The vertical black lines indicate the maximum and minimum range of data. The x-axis of the box plot is on a log scale. The color indicates compaction scenarios from 0 to 10 mm y^{-1} .

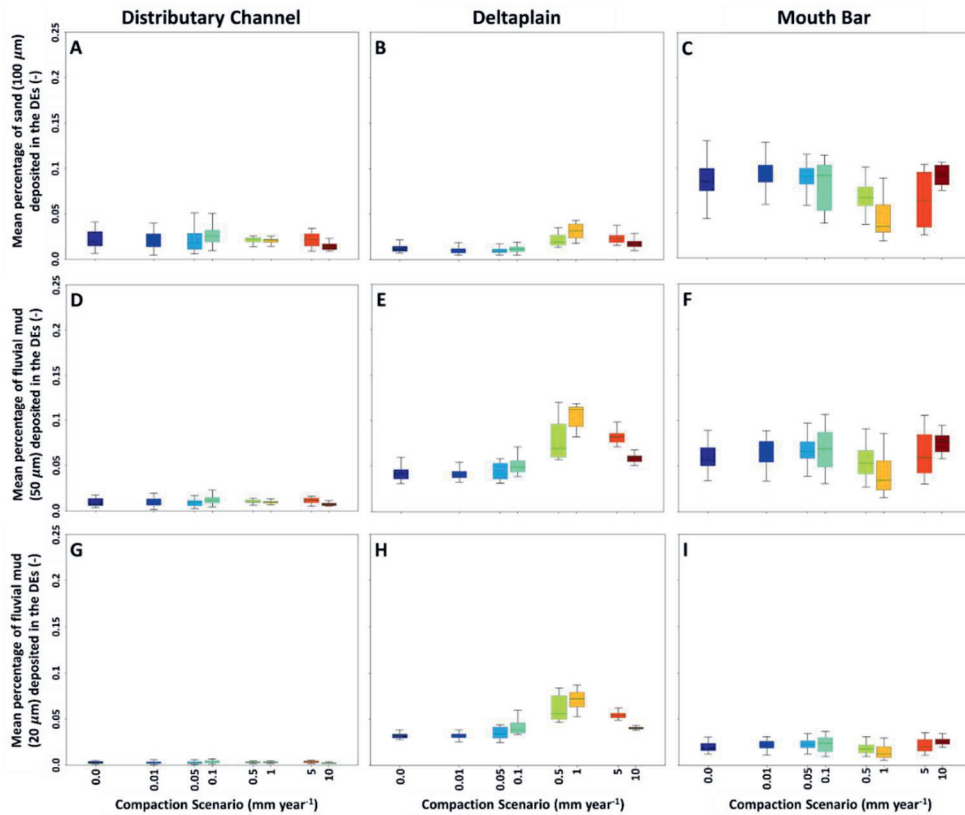


Figure 3.5. The collapsed time series of the percentage of sand and mud (by mass) deposited in distributary channel DE, delta plain DE, and mouth bar DE for all compaction scenarios (A - I). Each box plot shows a median value (second quartile, horizontal green lines) between the first and third quartiles (interquartile range, grey boxes). The vertical black lines indicate the maximum and minimum range of data. The x-axis of the box plot is on a log scale. The color indicates compaction rate scenarios. Note that sand consists of fluvial and substrate sand (Text S10).

The analyses of modelling results also show that the grain-size distribution of sediment deposited in DEs is not representative of the grain-size distribution of supplied sediment. For example, sand is preferentially deposited in the mouth bar DE for all compaction rate scenarios (Figure 3.5C). The over-representation of sand in the mouth bar DE can be attributed to the preferential sedimentation of certain grain size classes in each DE, which is also shown in a previous study on grain size fractionation (van der Vegt et al., 2020). Syn-depositional compaction influences this behavior, which leads to more sedimentation of sand updip at the delta plain DE (Figure 3.5B). In addition, sedimentation of mud also increases in the delta plain DE than in the mouth bar DE (Figures 3.4E, F, H, and I).

3.5.2. Accommodation

Syn-depositional compaction influences the available accommodation space in the simulated deltas (Figure 3.6). The accommodation space increases over the simulation output time step in the distributary channel DE for all compaction rate scenarios (Figure 3.6A). For the same scenarios, the opposite trend occurs in the delta plain DE (Figure 3.6B). In contrast, compaction does not affect the temporal accommodation trend in the mouth bar DE (Figure 3.6C).

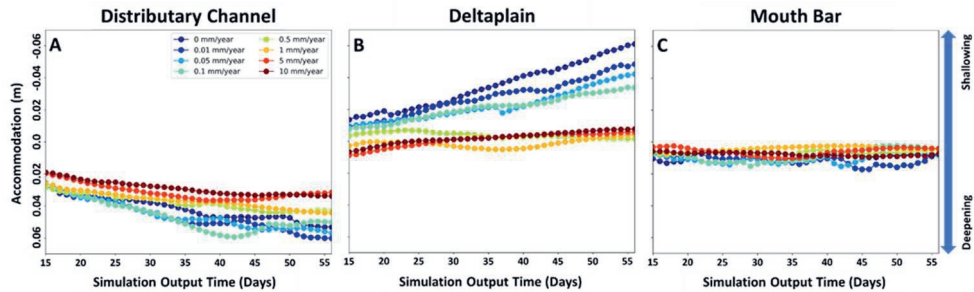


Figure 3.6. Accommodation space is represented by the relative position of bathymetry to water level in the distributary channel DE, delta plain DE, and mouth bar DE, which is averaged for each simulation output time step, starting from 15 days in hydrodynamic time (A, B and C). More positive accommodation means deepening, whereas more negative accommodation means shallowing. The color indicates different compaction rate scenarios, ranging from 0 to 10 mm y^{-1} .

Comparison between compaction rate scenarios shows that the change from zero to high compaction rate scenarios (0 - 10 mm y^{-1}) leads to a shallowing trend in the distributary channel DE (Figure 3.6A). In contrast, the change from zero to low-mid compaction rate scenarios (0 to 1 mm y^{-1}) results in a deepening trend in the delta plain DE, whereas higher compaction rate scenarios (> 1 mm y^{-1}) do not lead to greater accommodation in this area (Figure 3.6B). No correlation is found between the accommodation trend in the mouth bar DE and compaction rate scenarios (Figure 3.6C).

The analyses of the results also indicate that compaction rate scenarios higher than 0.5 mm y^{-1} have a comparable accommodation space, which is near zero. This happens because the accommodation space keeps being created due to syn-depositional compaction, which is then filled by sedimentation due to adequate supplied sediment. The accommodation creation updip in the distributary channel DE and delta plain DE (Figures 3.6A, B) influences the sedimentation (by mass) trend in the delta plain DE and mouth bar DE (Figures 3.4D, F). In addition, the knickpoint of 1 mm y^{-1} at which the trend changes in

the accommodation plot (Figures 3.6B, C) is consistent with the distribution of sedimentation trend (Figures 3.4 and 3.5).

3.5.3. Depositional Segment

The change in the main sedimentation location due to distributary channel development is analysed using the depositional segment (Figure 3.7). The depositional segment has increasing values during the first half of the simulation period for all compaction rate scenarios, which indicates that sedimentation increasingly occurs in the central segment (Figure 3.7A). The trend changes for several compaction rate scenarios (particularly $> 1 \text{ mm y}^{-1}$) during the second half of the simulation period, which shows a decrease in depositional segment values due to increased sedimentation in the lateral segments (Figure 3.7A).

A change in depositional segment from central to lateral can be attributed to distributary channel relocation (Figures 3.7B, C). The channel relocation changes the main sedimentation area to a new path (lateral), which can occur due to the creation of additional accommodation space in the delta plain DE due to syn-depositional compaction (Figure 3.6B). However, the mechanism for the channel relocation is not quantified in this study.

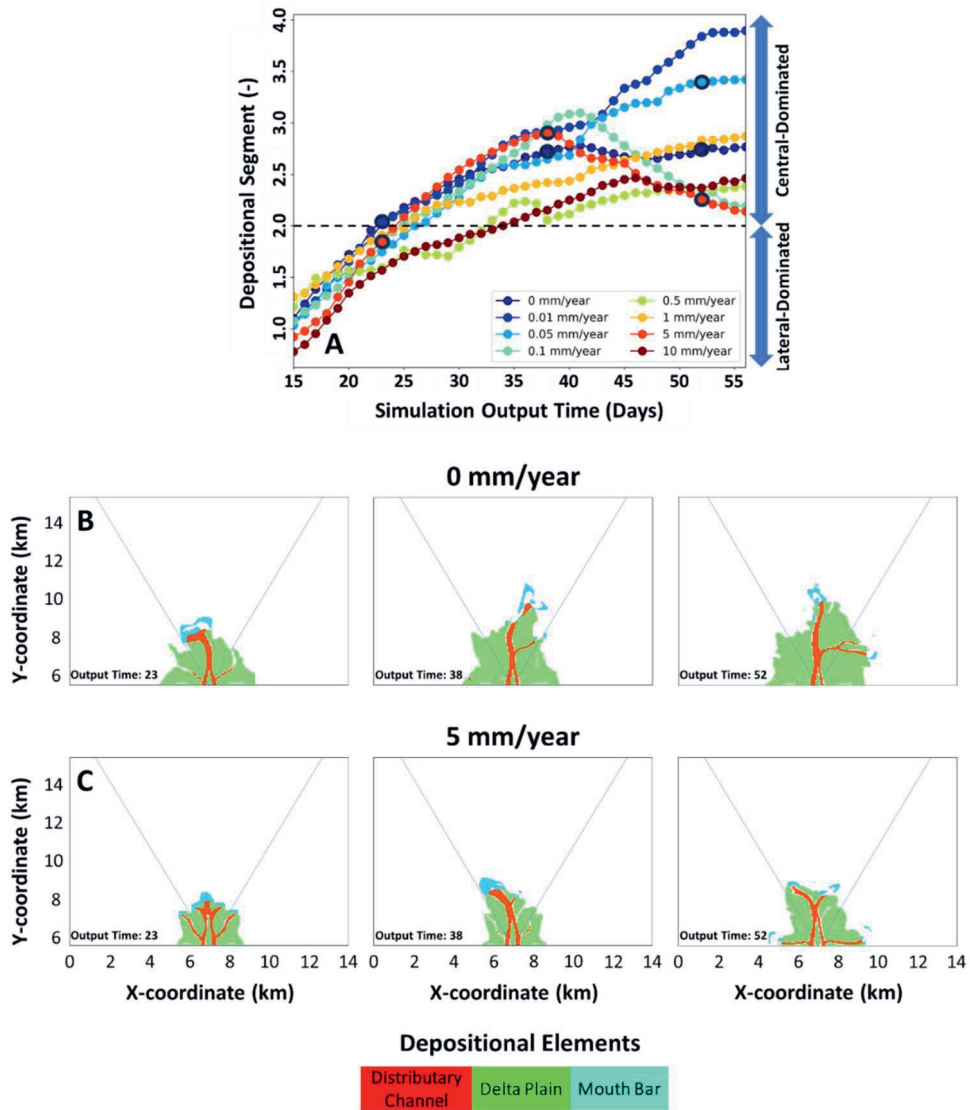


Figure 3.7. The change in the main sedimentation location due to distributary channel development is estimated using the depositional segment metric, calculated for each simulation output time step starting from 15 days in hydrodynamic time (A). The depositional segment values higher than two (marked by a black horizontal dashed line in A) indicate that the sedimentation mainly occurs in the central segment. In contrast, sedimentation primarily occurs in the lateral segments if the depositional segment values are lower than two. The plan-view depositional elements at selected simulation output times (marked by empty black dots in A) are shown for compaction scenarios 0 and 5 mm y^{-1} (B and C). The diagonal blue lines in B and C are boundaries between the central and lateral segments.

3.6. Interpretation of Sediment Distribution in Delta Simulation under the Influence of Syn-Depositional Compaction

In this subchapter, the distribution of sedimentation (by mass) in simulated deltas experiencing syn-depositional compaction is linked to the morphodynamic response using conceptual models that show how DEs are arranged in space for zero, low-mid and high compaction rate scenarios (Figure 3.8). These conceptual models are derived from qualitative observation of DEs over the simulation output time step (Figures B16 - B24), which is then used to draw the typical location of DEs. It is important to note that no relative base-level changes occur during the simulations.

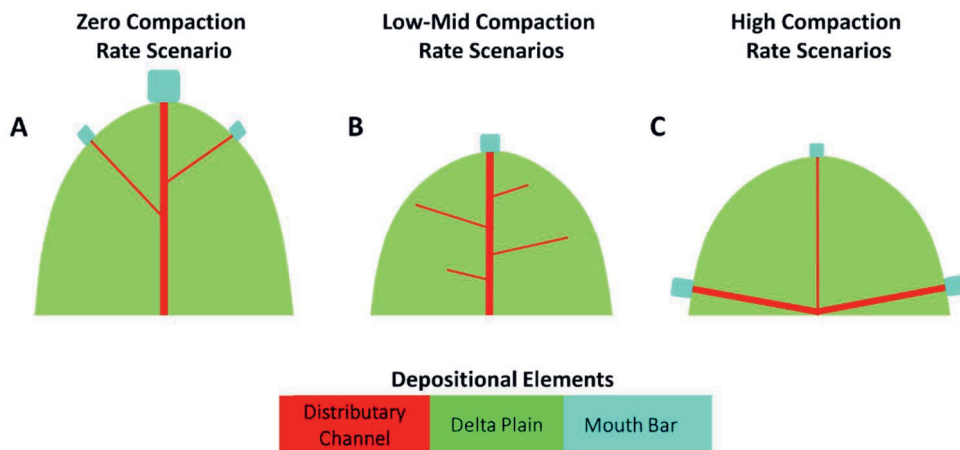


Figure 3.8. The conceptual models show depositional elements (distributary channel DE, delta plain DE, and mouth bar DE) arranged in space for zero, low-mid, and high compaction rate scenarios (A, B, and C).

For zero compaction rate scenario (0 mm y^{-1}), a restricted accommodation in the delta plain DE is available for sedimentation (Figure 3.6B). As a result, of the sediments that are captured in the delta (excluding the simulated delta front and pro delta sediments), the highest proportion of the sediment mass is deposited in the mouth bar DE, whereas a smaller proportion of sediment mass is deposited in the delta plain DE and distributary channel DE (Figures 3.4D, F). Sand is preferentially deposited in the mouth bar DE, leading to over-representation of this grain-size class in this area compared to other DEs (Figure 3.5). The depositional focus area is located in the central segment of the delta (Figures 3.7A, B), where the distributary channel DE and mouth bar DE are mainly situated (Figure 3.8A). Therefore, the land building in the delta primarily occurs in this segment.

From low to mid compaction scenarios ($0.01 - 1 \text{ mm y}^{-1}$), syn-depositional compaction creates additional accommodation space in the delta plain DE (Figure 3.6B). This leads to more sedimentation in the delta plain DE, consisting of sand and mud (Figures 3.4D and 3.5B, E, H). Consequently, less sediment for the same grain-size classes is available for the mouth bar DE (Figures 3.4F and 3.5C, F, I). The depositional focus area is more towards the lateral segments of the deltas due to the development of small distributary channels DE in these segments (Figure 3.8B). The small channels supply sediment to the delta plain DE to compensate for the compaction-induced additional accommodation space in this area. The highest sedimentation in the simulation occurs at compaction rate scenarios of 1 mm y^{-1} (a mid-compaction scenario). This means that the highest compaction scenario does not lead to the largest sedimentation in the delta plain, which contrasts with the findings from Nienhuis et al. (2018).

For high compaction scenarios ($> 1 \text{ mm y}^{-1}$), significant accommodation space is created in the delta plain DE (Figure 3.6B). Locally, this will lead to drowning when the local sediment supply is insufficient to compensate for the increase in accommodation space (Figure 3.6B). The depositional focus area shifts towards the lateral segments of the deltas (Figures 3.7A, C), where sedimentation mainly takes place in the mouth bar DE (Figures 3.4D, F). The shift can occur due to channel relocation (Figure 3.8C) in response to accommodation space creation in the lateral segments. However, the relationship between channel dynamics and compaction-induced accommodation space is not specifically analysed in this study.

3.7. Discussion

In the previous subchapter, the directional shift in the depositional focus for high compaction rate scenarios is attributed to distributary channel relocation (Figure 3.8C), which is linked to compaction-induced accommodation space. However, previous studies also show that an upstream increase in the water level in the channel (the backwater effect) can be an important factor affecting the channel relocation (Chadwick et al., 2022; Zheng et al., 2019). The backwater occurs when the channel discharge approaches the standing body of water. The channel flow interacts with the water body at the outlet, which is, in this study, affected by the incoming tide. In general, the flow gradually adjusts its water level and velocity, which can increase the water level in the channel (Chadwick et al., 2022). To assess whether the backwater affects the channel relocation in simulated deltas, the mean water level is calculated for areas that fall in different radii from the delta apex (Text B11 and Figure B31). The results show that the water level in all areas has a small variation (up

to 25 cm) over the simulation output time, suggesting that the backwater is not responsible for the channel relocation in simulated deltas.

In this study, the simulated delta plain is not vegetated, which differs from all but arctic Holocene deltas. In addition, contemporary deltas are influenced by human activity (Bussi et al., 2021; Day & Giosan, 2008; Liu et al., 2016; Syvitski et al., 2009; Syvitski & Saito, 2007). The simulated deltas are, therefore, best represented by natural unvegetated arctic deltas, such as Greenlandic deltas. These deltas grow rapidly due to high sediment supply and sea-level fall, particularly during the spring and summer conditions, when extensive snow and ice sheets melt (Overeem et al., 2017, 2022). In addition, their location in fjords limits deltaic wave reworking, and the sediment is rich in meltwater (Overeem et al., 2022; Syvitski et al., 2022). However, accurate comparison between simulated and Greenlandic deltas may be difficult because key processes that influence the development of these deltas are different. The Greenlandic deltas experience relative base-level fall due to isostatic rebound triggered by ice-sheet melt (Wake et al., 2016), whilst no relative base-level change occurs in this study. In addition, the supply sediment of Greenlandic deltas is mainly coarse-grained (Syvitski et al., 2022), which contrasts with fine-grained in this study. Therefore, the insight from this study is used to interpret real-world deltas. Syn-depositional compaction will impact the depositional nature of the Greenlandic deltas, leading to more sediment retention in the delta plain, depending on syn-depositional compaction rates and associated accommodation space created in this area. This will influence the amount of sediment (and associated nutrients) flux transported to the ocean.

van der Vegt et al. (2020) studied the distribution of preserved sediment (by mass) in simulated deltas using Delft3D. The results show that the delta plain deposits contribute to less than 5% of the total mass preserved in the deltas, which is attributed to very little sedimentation in this area. The relationship between sedimentation and sediment preservation was not specifically analysed. However, this study indicates that limited sedimentation in the previous study can occur because the processes that are responsible for capturing sedimentation in the delta plain, such as syn-depositional compaction and vegetation, are not simulated. Compaction in the delta plain area results in subsidence of the sediment bed, lowering the delta plain surface elevation and creating additional accommodation space to deposit more sediment in this area. Albernaz et al. (2020) showed that vegetation influences the number of crevasses that act as passages to transport sediment from the distributary channel to the delta plain. Coarse-grained sediment is mainly deposited within the crevasse channel, whilst fine-grained sediment is transported across the delta plain (Cazanacli & Smith, 1998), which defines the area of crevasse splays. Vegetation alters the critical bed shear stress and the roughness of the delta plain sediment, which reduces erosion by the crevasse channel. This leads to intricate crevasse channel

patterns (Albernaz et al., 2020). Vegetation also reduces the flow velocity, retaining more sediment in the delta plain (Albernaz et al., 2020; Cazanacli & Smith, 1998; Nienhuis et al., 2018). Therefore, if vegetation is combined with compaction in this study, a further increase in sedimentation in the delta plain area is expected.

Understanding the link between compaction and vegetation in delta settings is important but it is not well studied. Positive and negative feedback loops can occur due to interaction between compaction and vegetation during the growth and decay period. During the growth period, the stems and leaves increase the roughness, reducing flow velocity and promoting sedimentation (Albernaz et al., 2020; Baustian et al., 2018), which complements the compaction impact on retaining sediment due to additional accommodation space (positive feedback loop). However, a decrease in porosity of the sediment bed due to compaction also restricts root penetration to reach water and nutrients, which affects vegetation growth (negative feedback loop) (Kozlowski, 1999). During the decay period, the plant debris increases the bed level, reducing accommodation space created by compaction, which contrasts with the impact compaction has on increasing accommodation space (negative feedback loop). In addition, plant debris influences bed composition, which affects compaction (i.e., overburden stress, initial porosity and minimum porosity of sediment bed). Simulating complex interactions between compaction and vegetation in the delta would help to predict land reclamation and restoration projects and should, therefore, be a key direction of Delft3D code development in the future.

3.8. Conclusion

A new compaction algorithm was successfully implemented into Delft3D and used to generate seaward prograding and aggrading deltas with varying compaction rate scenarios ($0 - 10 \text{ mm y}^{-1}$). Based on the analysis of simulated deltas, it is possible to conclude:

- Syn-depositional compaction influences the location of sedimentation (by mass), driven by the change in accommodation space in DEs. This leads to interdependency of sediment budget between DEs.
- For zero compaction rate scenario (0 mm y^{-1}), no additional accommodation space is created. Therefore, the sediment quickly fills the available accommodation space in the delta plain DE, while the majority of sediment bypasses towards the mouth bar DE.
- For low-mid compaction rate scenarios ($0.01 - 1 \text{ mm y}^{-1}$), more sedimentation (by mass) occurs in the delta plain DE due to additional accommodation created in this area, resulting in less sedimentation (by mass) in the mouth bar DE.

- For high compaction rate scenarios ($> 1 \text{ mm y}^{-1}$), extensive accommodation leads to a change in the main sedimentation area to the lateral side of the delta due to channel relocation, where the main sedimentation mainly occurs in the mouth bar DE.

3.9. Data Availability

Simulation input and post-processed code used in this study are available at:

- https://data.4tu.nl/private_datasets/e84MSRCtH4as0Z9MI3kVVR137EGF99PNc8IIS8nYXwWs
- <https://surfdrive.surf.nl/files/index.php/s/LHVoddfD1EmwwSI>

Chapter 4: The Effect of Compaction-Influenced Sediment Erodibility on Simulated Levee Breaching

This chapter is prepared to be submitted to Nature Communications in 2026

4

Abstract

Distributary channels are key conduits for sediment transport in deltas, confined by natural levees—elevated ridges that slope toward the delta plain. While levees are critical for directing flow, they can breach, creating new sediment pathways and triggering flooding, driving rapid landscape change. Breach mechanisms are commonly analysed using two hydro- and morphodynamic indicators: superelevation (channel bankfull depth relative to levee thickness) and gradient advantage (levee slope relative to channel slope). However, the effects of levee deposit susceptibility to erosion, expressed by Erodibility Index (EI), on levee breaching remains poorly understood. This study uses Delft3D 4-Flow, incorporating compaction and its associated effects on the critical bed shear stress for erosion, to assess the influence of EI on levee breaching under a range of compaction-rate scenarios (0 – 5 mm y⁻¹). These rates represent maximum values under the greatest overburden, while local compaction rates may vary. Simulation results show that the breach initiation coincides with peaks superelevation and gradient advantage. However, the breach progression depends on local EI—a balance between flow-induced shear stress and critical bed shear stress for erosion. The erosion resistance of levee deposits is not uniform, as compacted fine-grained sediments exhibit higher critical bed shear stress for erosion than compacted coarse-grained sediments. As a result, grain-size successions respond differently to flow-induced shear stress, leading to variability in breach deepening and its effectiveness to capture the main flow. For instance, In a coarsening-upward succession, upper layers erode rapidly, causing EI to increase. This erosion exposes underlying, more compacted fine-grained sediments, which suppress further erosion and reduce EI. This finding highlights how compaction and consequential erodibility changes in stratified levee materials govern breach dynamics.

Keywords: levee breaching, superelevation, gradient advantage, erodibility index, grain size-dependent compaction, delta models, Delft3D.

4.1. Compaction and Erodibility of Sediment in Delft3D

Fluvial-dominated deltas are dynamic landforms shaped by sediment transport through distributary channel networks. These channels are confined by natural levees—elevated ridges of sediment that build up along channel banks and slope towards the delta plain (Brierley et al., 1997). Over time, repeated overflows increase the levee height and width, restricting sediment delivery to the delta plain except during major flood events (Cazanacli & Smith, 1998; Perez-Arlucea & Smith, 1999). When a levee breaches, flow and sediment can be diverted through a new pathway, either temporally or permanently, altering hydrodynamic and sediment distribution in the delta. While levee breaches can trigger rapid topographic changes and pose flood risks to nearby communities (Syvitski & Brakenridge, 2012), factors controlling their initiation and progression remain poorly understood.

Previous studies suggest that levee breaching is influenced by two key geometric factors: superelevation ($\beta_s = \frac{H_{LV}}{H_{DC}}$)—the ratio of levee height (H_{LV} in m) to channel bankfull depth (H_{DC} in m) and gradient advantage ($\gamma = \frac{S_{LV}}{S_{DC}}$)—the ratio of levee slope (S_{LV} in degree) to channel slope (S_{DC} in degree). Both factors affect topography and hydrodynamics around the breach sites (Figure 4.1) (Ganti et al., 2016; Gearon et al., 2024; Hoyal & Sheets, 2009; Slingerland & Smith, 1998; Törnqvist & Bridge, 2002). Using field and satellite data, Gearon et al. (2024) demonstrated that both factors interact to determine breach likelihood ($\Lambda = \beta_s \gamma$), with gradient advantage playing a larger role in low-lying deltas. However, observed levee breach likelihood values (Λ) vary widely across conceptual, laboratory, and field studies (0.2–14) (Ganti et al., 2016; Gearon et al., 2024; Gearon & Edmonds, 2025; Slingerland & Smith, 1998), suggesting that additional controls are at play.

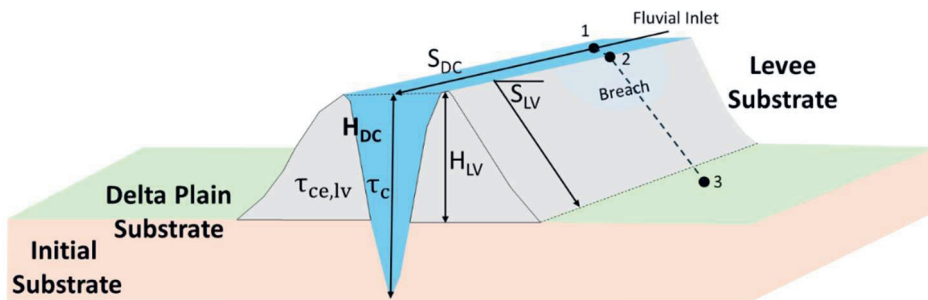


Figure 4.1. Schematic topography of around the breach site. Parameters H_{LV} , H_{DC} , S_{LV} , S_{DC} , τ_c , and $\tau_{ce,lv}$ represent levee thickness, bankfull channel depth, levee slope, distributary channel slope, bed shear stress imposed by flow, and critical bed shear stress for erosion of the sediment. They are measured at three observation points—distributary channel, levee, and delta plain (points 1 - 3)—and are used to compute superelevation, gradient advantage, and levee erodibility.

Nienhuis et al. (2018) demonstrated that sediment erodibility, influenced by root density, plays a key role in levee breach evolution. However, compaction can also alter both levee geometry affecting flow conditions and erodibility, yet its effect on levee breach development remains poorly understood. Here, we quantify this effect using erodibility index ($EI = \tau_c - \tau_{ce}$), which couples flow-induced shear stress (τ_c in Pa) with critical bed shear stress for erosion (τ_{ce} in Pa). Higher EI values indicate greater susceptibility of levee deposits to local erosion. τ_{ce} increases with compaction (Grabowski et al., 2011; van Rijn et al., 2020), a grain size-dependent process whereby pore-water drainage induces bed subsidence and creates additional accommodation space (Chapters 2 and 3). We hypothesize that EI will better characterize breach development than commonly used proxies such as superelevation and gradient advantage. To test this, we conducted numerical simulation using Delft3D 4 - Flow framework developed in previous chapters, across a range of compaction scenarios. The results enable evaluation of flow, elevation, and EI changes at breach sites, providing new insights into compaction's role in breach dynamics

4.2. Compaction and Erodibility of Sediment in Delft3D

We simulate delta development using an open-source hydro- and morphodynamic model Delft3D 4 - Flow, widely used in fluvial, lacustrine, and shallow marine environments (Lesser et al., 2004; Storms et al., 2020; van der Vegt et al., 2020; Zăinescu et al., 2024). The 1D grain-size dependent compaction and its associated critical bed shear stress for erosion formulations are implemented into Delft3D 4 - Flow source code version 6.02.08.62644, embedded into Delft3D 4 GUI version 4.04.01 (Deltares, 2021), as detailed below.

4.2.1. Compaction

The implementation of compaction as a syn-depositional process in Delft3D has been described in detail in Chapters 2 and 3 and is therefore only briefly summarized here. The modelled compaction behavior is grain-size dependent and occurs in two phases based on laboratory studies: primary and secondary (Merckelbach & Kranenburg, 2004; Mesri, 2003; Taylor & Merchant, 1940; von Terzaghi, 1923). Primary compaction is triggered by an increasing overlying sediment load, which includes self-weight and overburden. In contrast, secondary compaction occurs with a stagnant or reduced load associated with hiatus or erosion. Both compaction phases ultimately cause decreased elevation and reduced porosity of simulated stratigraphy.

4.2.2. Critical Bed Shear Stress for Erosion

In previous versions of Delft3D 4 - Flow, compaction was not linked to sediment properties affecting resuspension. Cohesive sediment resuspension occurs when flow-induced shear stress (τ_c) exceeds critical bed shear stress for erosion (τ_{ce}), serving as an erosion threshold (Text C1) (Partheniades, 1965). Typically, this threshold is assumed static, relying on published values dependent on mud content in sediment mixtures (Edmonds & Slingerland, 2010; Winterwerp et al., 2012). Field and laboratory studies indicate that higher compaction and mud content increases τ_{ce} (Dunne, 2019; Jacobs, 2011; Kamphuis & Hall, 1983; Lafren & Beasley, 1960; Lim, 2006; Mostafa et al., 2008; Smerdon & Beasley, 1959; L. van Rijn et al., 2019, 2020; L. C. van Rijn et al., 2025; Winterwerp et al., 2012; Xu et al., 2022; Yao et al., 2022). To account for variable τ_{ce} due to compaction and mud content, we modified Delft3D's erosion formula for cohesive sediments. τ_{ce} is the critical bed shear stress for erosion ($\text{kg m}^{-1} \text{s}^{-2}$ or Pa), calculated as:

$$\tau_{ce} = \alpha \cdot \left(\frac{\eta_{dep}}{\eta_t} \right) \cdot \left(\frac{P_m}{P_{m,ref}} \right) \cdot \tau_{ce,ref} \quad (4.1)$$

where $\tau_{ce,ref}$ is the reference critical bed shear stress for erosion from the literature ($\text{kg m}^{-1} \text{s}^{-2}$ or Pa), P_m is the mud content at a given output time (%), $P_{m,ref}$ is the reference mud content over which sediment is considered cohesive type (%), and η_{dep} is the initial porosity of newly deposited sediment (%), η_t denotes the sediment porosity at a given output time (%), which will be smaller than η_{dep} if compaction occurs, and α is site-specific tuning parameters (–). The validation of τ_{ce} formula is described in Text C2. When the resuspension occurs ($\tau_c - \tau_{ce} > 0$), the amount of sediment removed from the bed is defined by the erosion rate (M_{ce}) ($\text{kg m}^{-2} \text{s}^{-2}$) (Houwing, 2000; van Rijn et al., 2020), calculated as:

$$M_{ce} = \beta \cdot \left(\frac{\eta_t}{\eta_{dep}} \right) \cdot \left(\frac{P_{m,ref}}{P_m} \right) \cdot M_{ce,ref} \quad (4.2)$$

where $M_{ce,ref}$ is the reference erosion rate from the literature ($\text{kg m}^{-2} \text{s}^{-2}$), β is site-specific tuning parameter (–). For erosion of non-cohesive sediments, Delft3D uses default source and sink terms acting near the bed: sediment entering the flow is handled implicitly via the advection-diffusion equation, while settling is treated explicitly (Text C1). Resuspension is based on deviations of sediment concentration due to source and sink process from a reference concentration near the bed (Deltares, 2025). Additional factors influencing τ_{ce} , such as grain size, sphericity, biological activity, and chemical composition, are not included but may play important roles beyond the scope of this study (Grabowski et al., 2011; Yang et al., 2019).

4.3. Model Setup and Scenario

To investigate the effect of sediment resistance to resuspension on levee-breach development, we simulate prograding, fluvial-dominated deltas over 100 hydrodynamic days, with morphodynamic changes accelerated using a scaling factor of 120, equivalent to 33 morphodynamic years. Under the assumption of continuous bankfull discharge, the simulation output time is approximately ~ 5900 years in realistic time, representing a first-order approximation of real-world time. Erosion parameters include a reference critical bed shear stress for erosion ($\tau_{ce,ref} = 0.18$ Pa) and reference maximum erosion rate ($M_{e,ref} = 0.00067$ kg m⁻² s⁻²) (van Rijn et al., 2020; Winterwerp et al., 2012). Other modeling parameters align with simulations in Chapters 2 and 3 (Table 4.1).

Table 4.1. User-defined parameters used in Delft3D simulations.

No	User-Defined Model Parameter	Value	Unit
1	Grid Cell Dimension in x and y	50 x 50	m x m
2	Number of Compacting Layers	76	-
3	Initial Bed Thickness	4	m
4	Water Discharge	1600	m ³ /s
5	Sediment Discharge	0.15	kg/s
6	Total Hydrodynamic Time	100	day
7	Morphological Scaling Factor	120	-
8	Spin-up Interval Before Morphological Updating Begins	720	min
9	Maximum Allowed Erosion Rate of Sediment	0.00067	s/m
10	Critical Bed Shear Stress for Erosion of Sediment	0.18	N/m
11	Critical Bed Shear Stress for Deposition of Sediment	1000	N/m
12	Grain Sizes (Sand and Two Mud Fractions)	1E-04, 5E-05, and 2E-05	m
13	Specific Density of Sand and Mud	2650	kg/m ³
14	Dry Bed Density of Sand and Mud	500 and 1600	kg/m ³
15	Settling Velocity of Mud Fractions	0.0022 and 0.00056	m/s
16	Sand Concentration in Sediment Supply	0.0225	kg/m ³
17	Mud Concentration in Sediment Supply	0.1275	kg/m ³
18	Amplitude of Semi-Diurnal Tide	0.02	m
19	Initial Porosity of Sand	0.4	-
20	Initial Porosity of Mud	0.8	-
21	Minimum Porosity of Sand	0.25	-
22	Minimum Porosity of Mud	0.05	-
23	Oedometric Modulus for Mud	5E+06	Pa
24	Oedometric Modulus for Sand	25E+06	Pa

Simulation scenarios are defined by varying the primary compaction rates, representing the maximum allowed rates due to the largest overburden, while local rates typically lower depending on local overburden. Primary compaction rates are 0 - 5 mm y⁻¹ for mud and 0 - 50 mm y⁻¹ for sand in morphodynamic time, based on published rates in Holocene deltas, such as the Nile, Mississippi, and Ganges-Brahmaputra (Aly et al., 2012; Becker & Sultan, 2009; Gebremichael et al., 2018; Higgins et al., 2014; Morton & Bernier,

2010; Saleh & Becker, 2018; Stanley, 1990; Steckler et al., 2022). Secondary compaction rates are determined through stability criteria by comparing model response and ratios secondary to primary compaction rates. While higher ratios—such as 0.02 (granular soil) and 0.06 (peat)—are reported (Mesri, 2003), these often lead to model instability due to rapid elevation lowering. An optimal ratio of 0.0003 is identified for this study, yielding 0 to 0.0015 mm γ^{-1} in morphodynamic time, applied only to mud due to its lower hydraulic permeability than sand (Zoccarato et al., 2018). The plan-view elevation of simulated deltas and breach sites are depicted in Figures 4.2 & 4.3.

4.4. Metrics for Analysing Simulation Results

Simulation results are analysed using a methodology akin to field studies, relying on 1D stratigraphic sections at observation points. To accurately position observation points at the distributary channel, levee, and delta plain, the simulated delta area is classified into depositional elements (DE). Levee DE is defined based on four geometric and hydrodynamic conditions informed by field studies in the Mississippi Delta, Saskatchewan Rivers, and Rhine-Meuse Delta (Brierley et al., 1997; Perez-Arlucea & Smith, 1999; Pierik et al., 2017) (for details, see Text C3). Other depositional elements—distributary channel, underfilled channel, delta plain, mouth bar, delta front, and pro delta—are identified using the framework established by the previous chapter, as shown in Figure 4.4.

The observation points are positioned along the cross-levee flow direction when the breach initiates, encompassing distributary channel, levee, and delta plain. These observation points may move over time following breached channel migration (Figures 4.3 & 4.4). At these points, data on flow velocity, flow-induced bed shear stress (τ_c), critical bed shear stress for erosion (τ_{ce}), elevation, and water depth are obtained to calculate superelevation (β_s), gradient advantage (γ), and erodibility index (EI) at each simulation output time. Formulations of β_s , γ , and EI are shown in Subchapter 4.1. In general, EI > 0 means potential sediment erosion at a levee observation point, whereas EI \leq 0 suggests erosion is unlikely. However, because sediment resistance to resuspension is represented by the median critical bed shear stress for erosion of \sim 0.8 m layers most susceptible to erosion, EI \leq 0 may still lead to erosion when flow-induced shear stress exceeds the resistance of uppermost layers (see also Text C1).

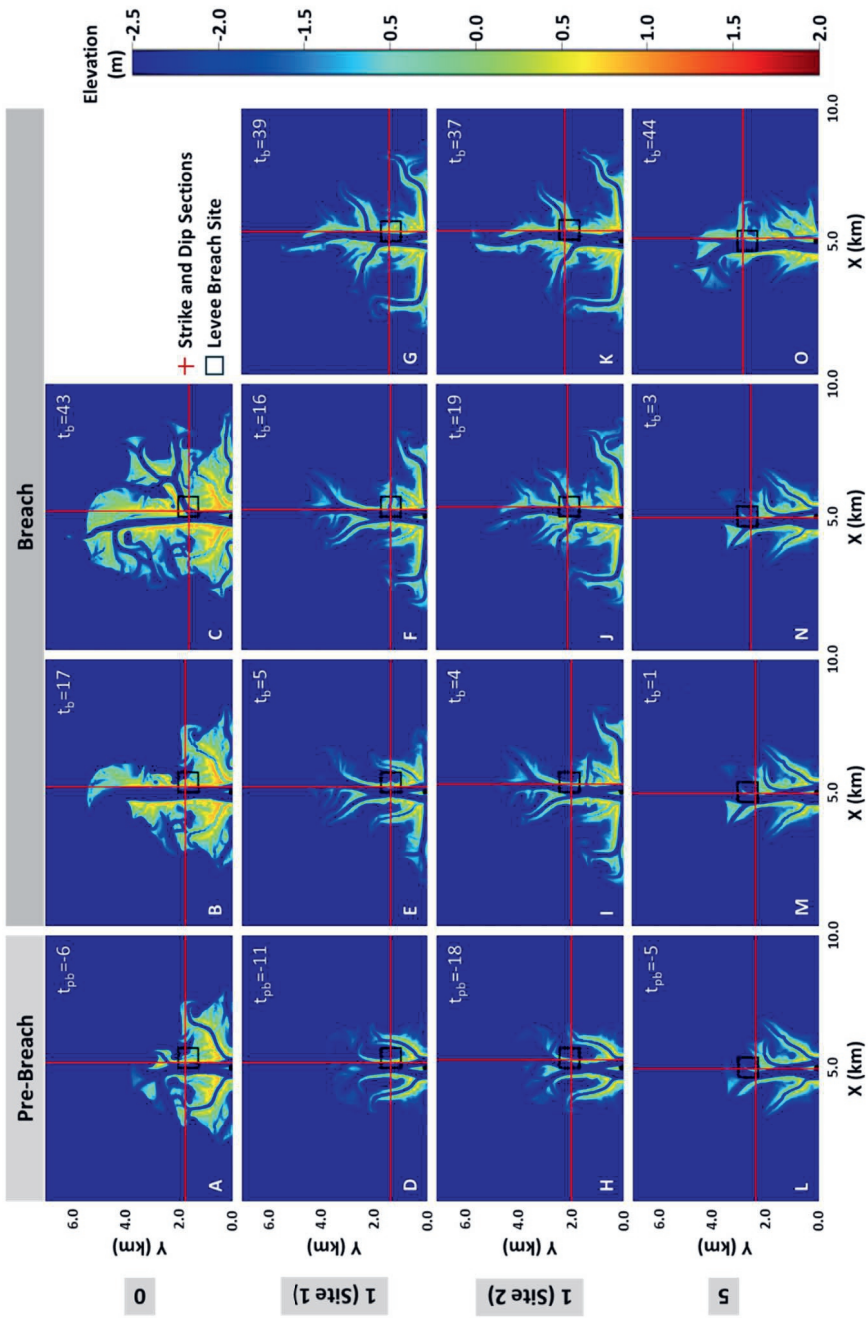


Figure 4.2. Elevation maps at key simulation output times during pre-breach (pb) and breach (b) phases across all compaction rate scenarios (A – O). Black squares indicate breach locations, and red lines show cross-sections along dip and strike directions traversing levee observation points. Note that the simulation output time is relative to the breach initiation.

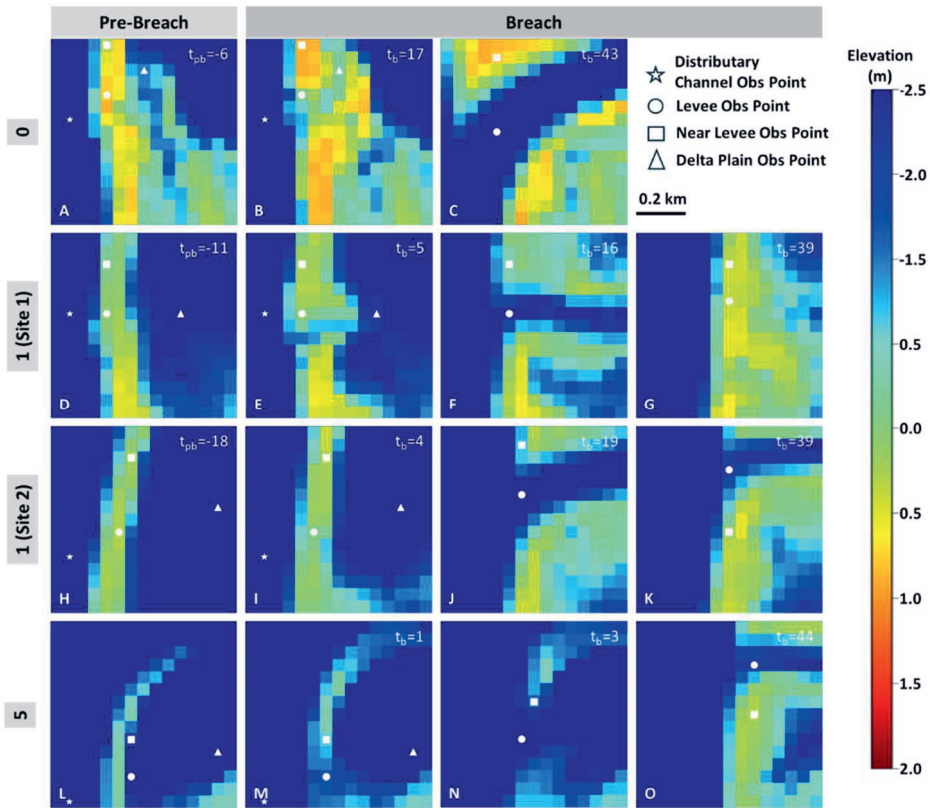


Figure 4.3. Zoomed-in elevation maps around breach sites at key simulation output times during pre-breach (pb) and breach (b) phases across all compaction rate scenarios (A – O). White stars, circles, squares, and triangles indicate distributary channel, levee at breach sites, levee near breach sites, and delta plain observation points, respectively. Corresponding interpreted depositional elements at these sites are shown in Figure 4.4.

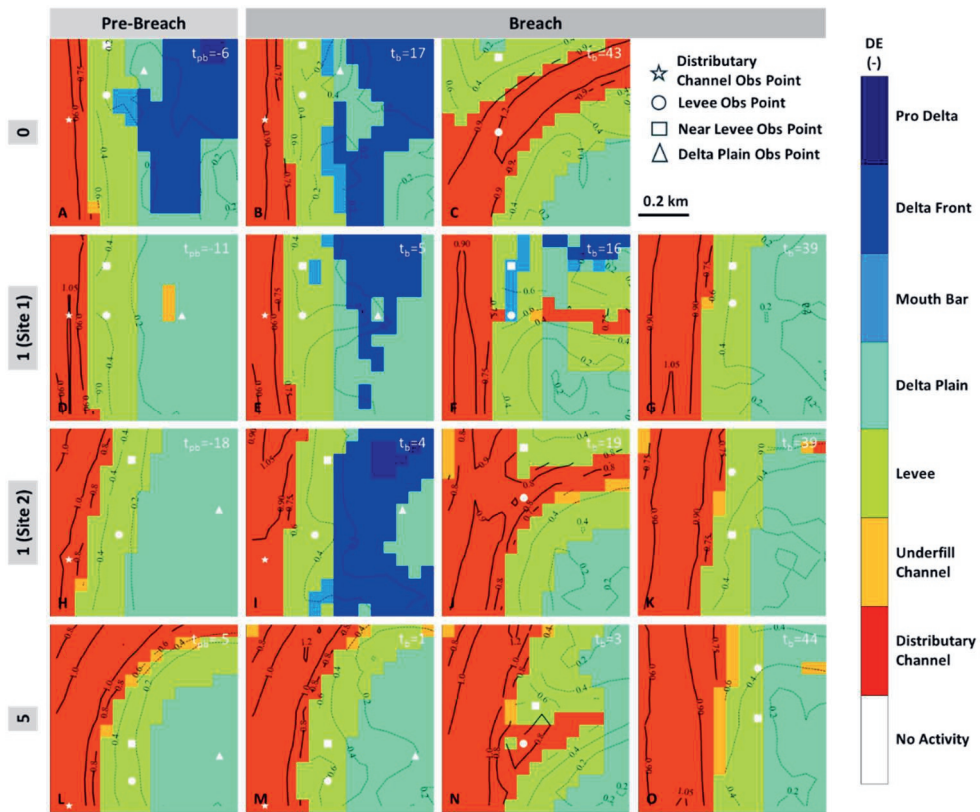


Figure 4.4. Depositional element (DE) maps around breach sites at key simulation output times during pre-breach (pb) and breach (b) phases across all compaction rate scenarios (A – O). DEs include distributary channel, underfill channel, levee, delta plain, mouth bar, delta front, and pro delta. White stars, circles, squares, and triangles indicate observation points at the distributary channel, levee at breach sites, levee near breach sites, and delta plain, respectively.

4.5. Analysis of Simulation Results

4.5.1. Description of Levee Breaching

Levee breaching is characterised using flow velocity, elevation, and erodibility index (EI), which combines flow-induced shear stress (linked to flow velocity) with critical bed shear stress for erosion at levee observation points (Figure 4.5). The breaching process is divided into two phases: pre-breach and breach. During the pre-breach phase, flow velocity remains relatively low across all compaction rate scenarios (Figures 4.5A - D), resulting in flow-induced shear stress ($\tau_{c,lv}$) insufficient to exceed critical bed shear stress for erosion of levee deposits ($\tau_{ce,lv}$). Consequently, EI values are negative (Figures 4.5E - H), promoting deposition that increases levee elevation (Figures 4.5I - L).

The breach phase initiates when cross-levee flow velocity increases (Figures 4.5A - D), coinciding with peaks superelevation and gradient advantage (for details, see Text C4). While EI remains negative (Figures 4.5E - H), this initiates erosion that decreases levee elevation (Figures 4.5I - L). The full breach occurs as flow velocity rises rapidly (Figures 4.5A - D), accompanied by increasing EI (Figures 4.5E - H). EI is positive for all compaction rate scenarios, except 5 mm γ^{-1} . For all scenarios, the full breach leads to rapid elevation loss (Figures 4.5I - L). Flow decelerates once flow-induced shear stress becomes insufficient to erode deeper, more resistive levee deposits (Figures 4.5A - D), shown by reversed EI trend (Figures 4.5E - H), promoting deposition that increases levee elevation (Figures 4.5I - L).

Levee Observation Point

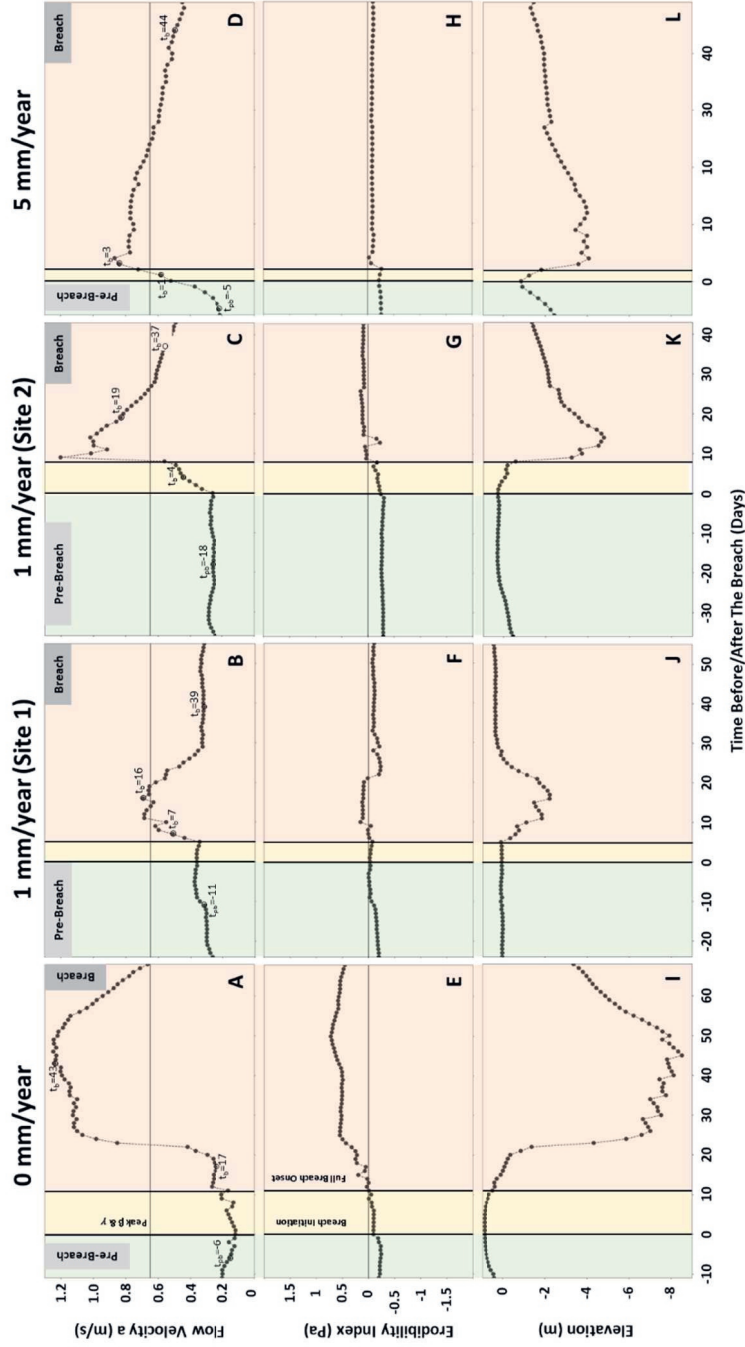


Figure 4.5. Time series plots of flow velocity, erodibility index (EI), and elevation from levee observation points at breach sites during pre-breach (pb) and breach (b) phases for all compaction rate scenarios (A - L). Small open circles indicate selected simulation output times corresponding to plan-view maps in Figures 4.2 - 4.4. A horizontal line at a flow velocity of 0.65 m s^{-1} is included in plots (A - D) to indicate the threshold used to identify distributary channel. Vertical lines indicate: (1) The breach initiation, corresponding to peak superlevation (β_s) and gradient advantage (γ); (2) the onset of full breach. All simulation output times are relative to the breach initiation. Shaded green, yellow, and orange represent periods of pre-breach, initial breaching, and full breach.

4.5.2. Interpretation of Levee Breaching

The transition from pre-breach to breach phase marks a hydrodynamic tipping point, driven by cross-levee flow acceleration, leading to a local regime shift from aggradational to degradational. Degradation is caused by both erosion and compaction-induced subsidence. Previous studies indicate that cross-levee flow acceleration corresponds to channel aggradation at the breach site, yet we did not analyse that explicitly (see also Text C5) (Han et al., 2025; Jones & Schumm, 1999; Prasojo et al., 2025). Unlike the previous view of levee breaching as a “sudden” event (Slingerland & Smith, 2004; Törnqvist & Bridge, 2002), our results reveal gradual process, initiated by localised levee erosion that capture the flow. This triggers a feedback loop that increases flow velocity, enhancing erosion, which in turn captures more flow and enlarges the breach, leading to a full breach.

However, the breach progression is governed by erodibility index (EI), a balance between flow-induced shear stress ($\tau_{c,lv}$) and critical bed shear stress for erosion ($\tau_{ce,lv}$) at levee observation point. In non-compacted levees represented by relatively low and uniform $\tau_{ce,lv}$ values, EI increases as flow accelerates. However, in compacted levees with high and depth-increasing $\tau_{ce,lv}$ values, EI increases slightly despite flow acceleration. Interestingly, EI remains negative in 5 mm γ^{-1} scenario, reflecting the use of a median $\tau_{ce,lv}$ over ~ 0.8 m levee thickness, which includes more compacted layers compared to lower rate scenarios. Here, erosion still occurs but is limited to upper, less compacted layers (see also Text C1), evidenced by continued elevation loss during the full breach (Figures 4.5I - L). For all scenarios, breaching influences local water depth, excluding possible effects from backwater (Text C6).

EI trend reverses once flow-induced shear stress ($\tau_{c,lv}$) is insufficient to erode deeper, more compacted layers, thereby hindering further breach deepening and its ability to capture the main flow. In this case, flow decelerates that leads to a regime shift from degradational back to aggradational, which promotes sedimentation, thereby restoring the breach in the levee. This highlights the role of stratigraphic heterogeneity in controlling $\tau_{ce,lv}$ variability, discussed further in the next subchapter.

4.5.3. Critical Bed Shear Stress for Erosion in Modelled Stratigraphy

Zoom-in strike-sections traversing levee observation points show that the simulated stratigraphy with compaction has higher critical bed shear stress for erosion (τ_{ce}) than without compaction (Figure 4.6). Full strike and dip sections showing critical bed shear stress for erosion and sand fractions are shown in Text C7. Shallow sediment layers in the levee typically have low τ_{ce} values associated with un- or poorly compacted sediment.

However, τ_{ce} values increase with depth as well as with increasing mud content (Figure 4.6). The highest τ_{ce} values occur in mud-rich and well compacted sediments (Figures 4.6D - O). This indicates that the distribution of τ_{ce} values in the stratigraphy is related to grain-size succession (coarsening and fining upwards) and compaction history.

The distribution of τ_{ce} values show a bimodal pattern, clustering around lower (<5 Pa) and higher (≥ 5 Pa) values (Figure 4.6). This pattern results from classifying subsurface layers as either cohesive or non-cohesive based on 10% mud content ($P_{m,ref}$ in Equations 4.1 and 4.2) (Houwing, 1999; Panagiotopoulos et al., 1997; Torfs, 1995; van Ledden et al., 2004; van Rijn et al., 2020). Abrupt τ_{ce} transition contrasts laboratory evidence suggesting a gradual increase with clay content (Torfs, 1995). Furthermore, clay mineralogy also affects τ_{ce} ; different clay types (e.g., kaolinite vs. montmorillonite) exhibit distinct erosion behaviors even at comparable proportions in sediment mixtures (Torfs, 1995; van Ledden et al., 2004). These complexities warrant further investigation into the rheology of sand-mud mixtures.

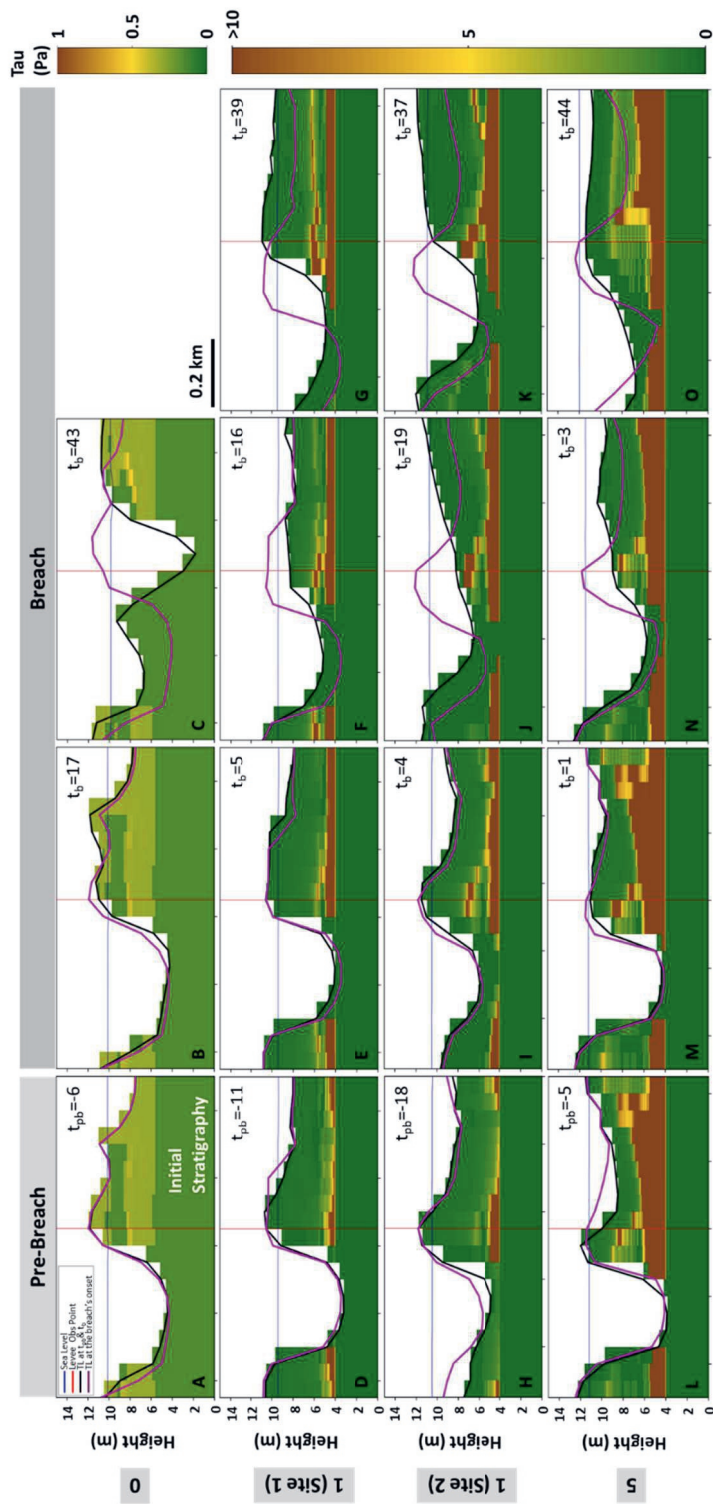


Figure 4.6. Zoom-in strike sections of critical bed shear stress for erosion (t_{ce}) traversing levee observation points at breach sites, shown for selected simulation output times during pre-breach (pb) and breach (b) across all compaction rate scenarios (A – O). Cross-section locations are indicated in Figure 4.2. Black lines denote timelines at selected simulation output times, while purple lines mark timelines at the breach initiation. Vertical red lines indicate breach locations, and blue horizontal lines represent sea level. The t_{ce} color scheme reflects different value ranges for non-compacted and compacted scenarios. Note that simulations include initial 4-m thick sediment layer assumed in compaction equilibrium; therefore, no EI variation occurs within this interval (not interpreted).

4.5.4. Conceptual Model of Levee Breaching

Based on simulation results, we developed a conceptual model of levee breaching under three stratigraphic scenarios based on compaction and grain-size successions: (1) non-compacted, (2) compacted coarsening-upward, and (3) compacted fining-upward (Figures 4.7A, E, I). In all these scenarios, breaching begins with cross-levee flow acceleration, initiating erosion, which corresponds to peaks superelevation and gradient advantage (Figures 4.7B, F, J). Breached channel formation causes a local increase of flow depth, leading to positive feedback between flow-induced shear stress and erosion rate, leading to full breach. However, breach progression is controlled by erodibility index (EI), defined as the balance between flow strength across levee ($\tau_{c,lv}$) and levee resistance to resuspension ($\tau_{ce,lv}$), rather than superelevation and gradient advantage.

Un- or poorly compacted layers near the levee surface typically have lower $\tau_{ce,lv}$. EI increases when these layers are eroded during full breach ($EI > 0$) (Figures 4.7C, G, K). As erosion deepens, grain size trends become increasingly important. A compacted fining-upward sequence leads to shallower incision than coarsening upward sequence ($EI < 0$) (Figures 4.7G, K). However, once upper resistive layers are eroded, erosion may accelerate ($EI > 0$), potentially leading to deeper scours. These dynamics influence breach deepening, affecting its ability to capture the main flow. Once flow-induced shear stress is insufficient to drive further breach deepening, flow decelerates as flood stage diminishes, promoting sedimentation and levee beach restoration (Figures 4.7D, H, L).

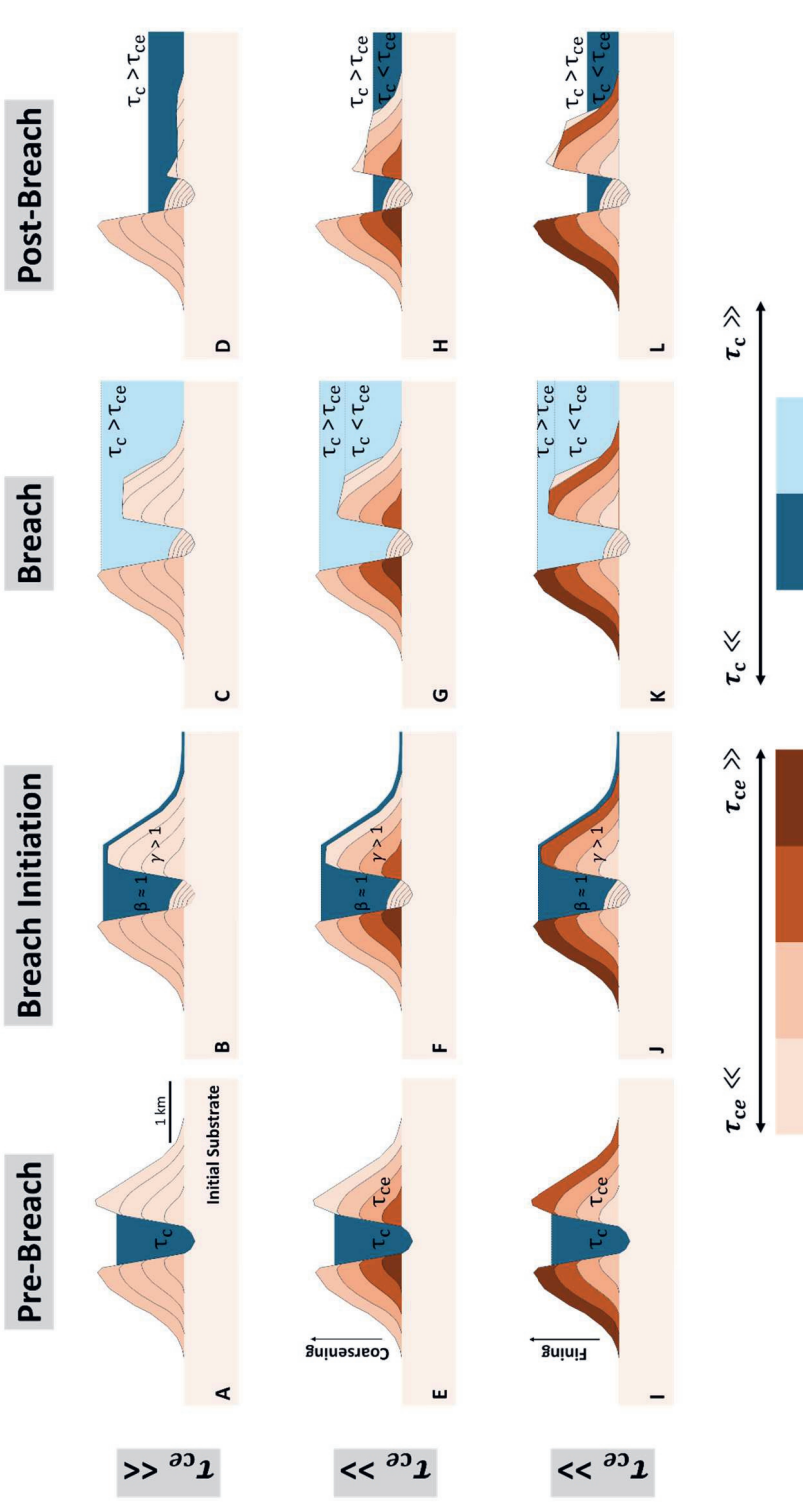


Figure 4.7. Conceptual model of levee breaching under three stratigraphic scenarios—uncompacted homogeneous, compacted coarsening-upward, and compacted fining-upward (A–I). Breach starts when cross-levee flow accelerates that initiates erosion, corresponding to peak superlevation (β) and gradient advantage (γ) (B, F, J). This increases flow depth to capture more flow, increasing erosion and breach depth. The breach progression depends on a balance between flow strength (τ_c) and sediment property (τ_{ce}), influenced by grain-size trends and compaction history. Compacted levees undergo less erosion than uncompacted ones, which influences the breach depth and its ability to capture the main flow (C, G, K). This leads to flow deceleration, which promotes sedimentation and levee rebuilding (D, H, L).

4.6. Discussion

Although compaction always occurs in natural deltas, we study this process using simulations, which allow us to selectively activate or deactivate this process, enabling comparison of its impact in simulated deltas. Our simulations show that incorporating compaction and the associated increase in sediment resistance to resuspension yields a more realistic representation of delta development for three reasons. First, the period between breach initiation and full breach occurs shorter in simulations with compaction than without compaction (Figure 4.5). This is consistent with field and remote sensing data, indicating that breach initiation precedes full breach by a short period (few years) (Gearon & Edmonds, 2025). Second, elevation and levee resistance to resuspension change over time and space due to sedimentation and compaction. Therefore, predicting the breach initiation should not rely solely on geometry-based proxies such as superelevation (β_s) and gradient advantage (γ), but also account for sediment property. This limitation is exemplified in the Mississippi Delta, where breaches are rare despite extreme gradient advantage ($\gamma > 100$) (Aslan et al., 2005). Third, while flow in combination with a topographic low are essential for breach initiation, the subsequent breach development is primarily governed by local erodibility index (EI)—direct interaction between flow-induced bed shear stress and local stratigraphic property. Because EI varies with depth due to differences in grain size and compaction history, breach progression depends on these subsurface characteristics. These reasons expose a gap in previous morphodynamic modelling studies, which lacks formulations accounting for compaction-driven sediment's resistance to resuspension. This property is fundamental to sediment transport models, which serve as the building blocks of delta simulations. As such, previous models that exclude compaction should be interpreted with caution, because it neglects an essential process in delta development

Improving our understanding on sediment property affecting breach dynamics requires a clearer understanding of intermediate processes—specifically how flow interacts with erodibility index (EI), how EIs translate to erosion rates, and how erosion rates affect breach depth. Without resolving these steps, the connection between sediment properties and breach outcomes remains incomplete and speculative. The next step is to better understand stratigraphic and compaction control on critical bed shear stress for erosion of levee deposits ($\tau_{ce,lv}$). This can be achieved by evaluating $\tau_{ce,lv}$ values at depths in natural systems, since levee thickness can reach several meters, such as in the Saskatchewan and Columbia Rivers, Canada (Cazanacli & Smith, 1998; Filgueira-Rivera et al., 2007). Depth-resolved τ_{ce} measurements are costly, relying on core data to access deeper layers (Lianqiang et al., 2007; Xu et al., 2022). Low-cost Cone Penetration Tests (CPT), commonly used for site assessment to design foundations of constructions or buildings and

increasingly for predicting stratigraphic units (Amorosi & Marchi, 1999; Satriyo & Soebowo, 2018; Styllas, 2014), offer promising methods for measuring soil strength, a proxy for τ_{ce} at depths. The Rhine-Meuse delta provides publicly available subsurface data; CPTs located in paleo-levee deposits when paired with nearby core data, allowing immediate comparison of modelled and field-based $\tau_{ce,lv}$ based on: (1) grain size successions of levee deposits, (2) porosity–grain density to evaluate compaction effects, and (3) spatial variation across the delta.

Vegetation commonly covers natural levees and influences their critical bed shear stress for erosion ($\tau_{ce,lv}$) (Albernaz et al., 2020; Nienhuis et al., 2018). Root systems enhance soil drainage, accelerating dewatering and compaction, thereby increasing $\tau_{ce,lv}$ (Osman & Barakbah, 2006), while stems and leaves increase surface roughness, which reduces flow-induced shear stress across levee ($\tau_{c,lv}$) (Albernaz et al., 2020). Despite these dual effects on both flow strength and sediment resistance to resuspension—key factors to the erodibility index—vegetation is not yet incorporated into the current workflow assessing levee breach dynamics. Future studies should integrate vegetation, which requires understanding how factors such as flow conditions and water-depth fluctuations affect species-specific traits related to growth and mortality, which in turn shape spatiotemporal vegetation density (Baustian et al., 2018). Such an integrated approach is essential for supporting sustainable delta management in the face of environmental change.

4.7. Conclusion

We have analysed the impact of erodibility index (EI), defined as the balance between flow strength and sediment resistance to resuspension, on levee breach development. EI is a reliable proxy for characterizing breach development. Breaching is initiated when flow accelerates on the levee, resulting in initial erosion and deepening, while EI remains negative. This coincides with peaks superelevation and gradient advantage. Full breach occurs when flow velocity increases rapid, accompanied by a corresponding increase in EI. As erosion progresses, the flow encounters deeper, more compacted and resistant layers, which limits further breach deepening that reduce the breach's ability to capture the main flow. This shifts EI trend, promoting sedimentation and breach restoration. The simulations emphasize the necessity of incorporating sediment resistance to resuspension into delta models to better simulate levee breaching, a key process in delta development.

4.8. Data Availability

Simulation input, output and post-processed data can be accessed at:

- https://data.4tu.nl/private_datasets/6fwEU0Zr8Myg52x5OLt8Nw-pYLSIUNCAgeYnXyjLQDc
- <https://surfdrive.surf.nl/s/L356fRcSTCBkgAm>

Chapter 5: Synthesis

Syn-depositional compaction always occurs in active natural deltas. Here, we investigate its role solely using numerical simulations in which compaction of deposited sediment can be switched on and off within model-land framework. The resulting response of delta formation and dynamics therefore constitutes model-land behavior, not direct representations of field-based behavior. Any implications for field-based behavior therefore must be interpreted with caution, acknowledging model limitations and the potential for processes not represented in the model. Extensive field observations remain essential to assess the extent to which these model-land insights can be used to explain observed field-land behavior.

The impact of syn-depositional compaction on delta development is assessed in this dissertation through several steps. First, developing compaction formulations using readily obtainable parameters, designed for Delft3D 4 - FLOW integration with minimal modifications to existing modules; Second, defining quantitative metrics to compare the impact of syn-depositional compaction in simulated deltas; Third, examining how compaction-induced volume reduction influences local accommodation, which alters delta morphodynamics and sediment distribution; Lastly, assessing the role of compaction-induced volume reduction and its effects on sediment resistance to resuspension to key deltaic processes, such as levee breaching.

In this Chapter, we address the research questions by presenting key findings, synthesized and contextualized within the broader literature (Subchapter 5.1). This work establishes a foundation to systematically investigate compaction using Delft3D 4 – FLOW and compare model insights with field observations. In addition, the methodologies developed here open new opportunities to explore the interconnections between compaction and other deltaic processes across a wide range of depositional environments. These potential directions for future research are discussed in Subchapter 5.2.

5.1. Answer to Research Questions

5.1.1. How does syn-depositional compaction impact simulated delta morphodynamics?

To assess the impact of syn-depositional compaction on delta development at large spatial ($>10^3$ m²) and temporal ($>10^3$ years) scales, we integrated new compaction formulations into the Delft3D-FLOW code to allow dynamic coupling between compaction,

sedimentation & erosion, and morphodynamics. However, simulating compaction presents several challenges. First, it requires solving the 3D Darcy equation for fluid flow under pore pressure gradients, which is computationally intensive and difficult to validate at delta scales. We therefore adopted a 1D compaction approach in which fluid flow is not explicitly simulated but implicitly represented by relating porosity reduction directly to overburden pressure. Although this simplifies computations, compaction becomes localized to grid cells experiencing stress changes, as lateral fluid flow between cells is neglected. As a result, the spatial distribution of porosity reduction, and thus subsidence, may be affected. Second, compaction always reduces porosity from initial (freshly deposited sediment) to minimum values (compaction equilibrium). In reality, pore pressure builds up during burial, and if exceeding overburden pressure, can generate overpressure zones that prevent further porosity reduction (Wangen, 2001). Third, the mechanisms governing secondary compaction remain poorly understood. Previous studies showed that bed-surface lowering due to secondary compaction decreases over time (Bjerrum, 1967; Merckelbach & Kranenburg, 2004; Taylor & Merchant, 1940). Accordingly, secondary compaction is represented here as a time-dependent process. Finally, several modelling choices affect the results. The model setup represents river-dominated deltas with minimal tidal and negligible wave influence, thereby excluding tide- and wave-dominated environments. This configuration isolates the influence of compaction under conditions where fluvial processes dominates delta development.

Simulation results reveal that syn-depositional compaction of underlying delta-front and pro-delta deposits enhances local accommodation at the delta top, driving variability in delta planform morphology. This effect is more pronounced in mud-rich deltas than sand-rich deltas. Increasing compaction rate scenarios results in additional local accommodation, which amplifies feedback on sedimentation patterns and emergent delta morphology. This shifts depositional focus laterally, yielding more spatially uniform sedimentation. As a result, mud-rich deltas exhibit smaller increases in delta area, smoother shoreline, and higher aspect ratio (delta-top width over length). These outcomes diverge from previous simulations, which typically produce rugose shoreline and lower aspect ratio (Burpee et al., 2015; Caldwell & Edmonds, 2014; Edmonds & Slingerland, 2010; van der Vegt et al., 2020), underscoring the impact of syn-depositional compaction on delta morphology.

Several assumptions may influence the impact of syn-depositional compaction on simulated deltas. First, the 1D vertical approach neglects lateral fluid flow, while fixed initial and minimum porosities ignore grain-size variability in sediment mixtures. These simplifications can lead to over- or underestimation of local porosity reduction and the resulting local additional accommodation. Second, omitting explicit pore-pressure modelling may exclude the development of overpressured zones that inhibit further

compaction, thereby affecting local accommodation. Third, secondary compaction remains poorly understood, introducing additional uncertainty regarding its representation and relative contribution to local additional accommodation. Finally, by excluding tidal and wave influences, the model is tailored to river-dominated deltas, a subset of possible deltaic settings, and results should be interpreted within this context.

5.1.2. How does syn-depositional compaction affect sediment distribution in the simulated delta?

Simulated syn-depositional compaction is 1D, grain-size-dependent process that operates independently within each grid cell. These grid cells collectively form larger depositional areas, such as distributary channels, levees, delta plains, mouth bar, delta front, and pro delta. As each grid cell compacts differently depending on overburden pressure, simulated time, and grain sizes, spatiotemporal magnitude of compaction varies across the delta, creating localized accommodation within and between depositional areas. However, how this localized accommodation affects sedimentation by mass across the delta remains poorly understood, which is addressed using numerical simulation.

Two improvements were implemented in simulating compaction within Delft3D 4 – FLOW compared to the version used in Subchapter 5.1.1: First, porosity reduction during compaction was previously applied over a single range from initial to minimum values, regardless of grain-size composition in sediment mixtures. Because the porosity range controls the amount of subsidence, this simplification could lead to under- or overestimate local additional accommodation. By assigning initial and minimum porosity values according to grain-size composition, the amount of subsidence of different sediment mixtures is better represented; Second, the secondary compaction formulation is updated to prevent accelerated subsidence with increasing simulated time, aligning more closely with laboratory observation and data (Bjerrum, 1967; Merckelbach & Kranenburg, 2004; Taylor & Merchant, 1940).

Simulation results show that syn-depositional compaction of underlying delta-front and pro-delta deposits modifies local accommodation on the delta plain, thereby altering sediment budgets across depositional areas, compared to simulations without compaction. Although compaction also occurs in the delta front and pro delta, the accommodation change in these areas is minor due to inherently greater water depth. Under low to moderate compaction rate scenarios ($0 - 1 \text{ mm yr}^{-1}$), increased accommodation on the delta plain enhances sedimentation by mass, reducing sediment delivery to the mouth bar and beyond. At higher rates ($>1 \text{ mm yr}^{-1}$), excessive accommodation on the delta

plain promotes distributary channel relocation and increases sediment delivery to the mouth bar. Although channel dynamics are not explicitly analysed, compaction affects relative topography (elevation and slope) among distributary channel, levee, and delta plain, potentially influencing relocation events (Gearon et al., 2024; Jerolmack & Paola, 2007; Slingerland & Smith, 1998).

Our findings highlight syn-depositional compaction as a key process in simulated delta development. Excluding it risks overlooking a key driver in accommodation and sedimentation. For instance, our result differs from van der Vegt et al. (2020), who reported limited sedimentation by mass on the delta plain, likely due to the absence of syn-depositional compaction. Despite these insights, limitations are acknowledged: First, the link between sedimentation and preservation is not analysed in this study. Natural delta-plain deposits are commonly partially reworked by subsequent channel activity, such as migration or avulsion. Outcrops, flume, and satellite data provide evidence for the preservation of channelized delta plain deposits (Feng et al., 2019; Fielding, 1985; Syvitski et al., 2012); (2) The simulations in this subchapter do not account for the effect of syn-depositional compaction on sediment resistance to resuspension (Grabowski et al., 2011; van Rijn et al., 2020), which may influence channel dynamics and associated sedimentation across depositional areas. This will be addressed in the next subchapter.

5.1.3. How does syn-depositional compaction influence simulated levee breaching?

Levee breaching diverts flow and sediment pathways, driving rapid topographic change and posing flood risk to nearby communities. Previous studies have relied on superelevation and gradient advantage as proxies for topographic control on flow diversion to predict the location and timing of breach initiation (Ganti et al., 2016; Gearon et al., 2024; Hoyal & Sheets, 2009; Slingerland & Smith, 1998; Törnqvist & Bridge, 2002). The role of syn-depositional compaction on breach initiation and progression through its effects on local elevation, slope, and sediment resistance to resuspension remains underexplored. To address this, we adjusted the Delft3D 4 - FLOW code by coupling compaction with sediment resistance to resuspension via critical bed shear stress for erosion. This parameter is combined with flow-induced shear stress to derive an erodibility index (EI) that represents levee susceptibility to resuspension. Erodibility index enables a quantitative assessment of syn-depositional compaction's role on levee breaching.

Simulation results show that levee breaching occurs in two phases. In pre-breach phase, cross-levee flow velocity remains low across all compaction rate scenarios (0 – 5 mm

γ^{-1}), generating flow-induced shear stress (τ_c) below critical bed shear stress for erosion (τ_{ce}). This yields a negative erodibility index, promoting sedimentation that increases levee elevation. Breaching initiates when cross-levee flow velocity increases, coinciding with peaks in superelevation and gradient advantage. This triggers erosion of levee deposits, marking a shift from an aggradational to a degradational regime. Erodibility index remains negative as flow-induced shear stress is still below critical bed shear stress for erosion, calculated as a median value over ~ 0.8 m erosion-prone levee deposits. This confines erosion to upper, less compacted layers, decreasing levee elevation and increasing flow depth to capture more flow. Full breach develops as flow velocity enhances rapidly, accompanied by increasing erodibility index, leading to significant erosion that substantially lowers levee elevation. Positive erodibility index emerges in all compaction rate scenarios except $5 \text{ mm } \gamma^{-1}$, where it remains negative because critical bed shear stress for erosion incorporates more compacted layers than in lower-rate scenarios.

Full-breach progression is governed by erodibility index, controlled by compaction history and grain-size succession in levee deposits. In a coarsening-upward succession, upper layers erode rapidly (erodibility index > 0), exposing underlying, more compacted fine-grained sediment. This shift suppresses further erosion (erodibility index < 0). Conversely, in a fining upward succession, upper layers initially resist erosion (erodibility index < 0), but once these compacted fine-grained sediments are eroded, rapid erosion ensues (erodibility index > 0). This shows that compaction and subsurface characteristics influence breach depth. When flow-induced shear stress cannot sustain further breach deepening, which affects the breach's ability to divert the main flow, flow velocity decreases and sedimentation resumes as river flood stage diminishes. This resumes the regime back from degradational to aggradational, thereby restoring the breach in the levee.

This study exhibits a representative framework for modelling and assessing levee breaching for two reasons. First, the period between breach initiation and full breach is shorter in simulations with compaction than without compaction. This is consistent with field and remote sensing observations which indicate that breach initiation precedes full breach over a short duration (Gearon & Edmonds, 2025). Second, we employ erodibility index to evaluate breach initiation and progression, as it captures the combined effects of compaction on topography and sediment resistance to resuspension. In contrast, superelevation and gradient advantage mainly describe breach initiation and only depend on topography, overlooking sediment resistance to resuspension. Superelevation and gradient advantage should therefore be applied with caution. This is evident in the Mississippi Delta, where breaches are rare despite extreme gradient advantages (Aslan et al., 2005). Together these two arguments highlight that compaction is an essential process that must be included in delta simulations.

5.2. Future Work

This subchapter provides practical recommendations for research and applications to improve our understanding of how syn-depositional compaction affects delta development.

5.2.1. Improving Compaction Formulations in Delft3D 4 – FLOW Code Integrating 3D Groundwater Flow with Compaction Formulations

In this dissertation, the compaction formulations incorporate both primary and secondary phases, driven by overburden pressure and simulated time. These phases reduce sediment volume and enhance sediment resistance to resuspension, implicitly linked to 1D pore-fluid expulsion. This approach overlooks a more realistic, explicit representation of 3D pore-fluid expulsion governed by pressure gradients. Additionally, expulsion is assumed to occur continuously during compaction, without considering the development of overpressure that may inhibit further compaction (You et al., 2020; Zhao et al., 2018). These model limitations can be addressed by coupling the stratigraphy module of Delft3D 4–FLOW with iMOD (Interactive Modelling), which integrates the MODFLOW code developed by the U.S. Geological Survey (USGS) for 3D groundwater flow simulation.

iMOD computes the 3D hydraulic head (m), defined as the total mechanical energy per unit weight of water. As groundwater flows from higher to lower hydraulic head, the 3D hydraulic head gradient (m) is derived. This parameter is exported to Delft3D 4 - FLOW to drive 3D fluid expulsion during compaction. However, coupling Delft3D 4 - FLOW with iMOD introduces several technical challenges. First, the 3D hydraulic head gradient must be converted to 3D pore pressure gradient (Pa) for compaction calculations, which requires information on water density (Pa m^{-1}) and elevation differences along the flow path (m). Second, iMOD requires 3D hydraulic conductivity as input, determined from the horizontal and vertical permeabilities of each grid cell. Delft3D 4 – FLOW, however, does not directly provide these parameters, as it assumes uniform grain-size mixing within each grid cell.

The assumption of uniform grain-size mixing also obscures the bounding surfaces between fine- and coarse-grained sediments within each grid cell. Consequently, even when coarse-grained sediments occur at different depths in adjacent cells, the bounding surface is assumed to be horizontal. This introduces artificial discontinuities that can distort permeability and pressure gradient calculations, thereby affecting pore-fluid expulsion and overpressure development. Lastly, in this dissertation, the Delft3D grid uses a horizontal spacing of 50 m and vertical layering of 0.3 m. A sensitivity analysis is therefore necessary

to evaluate whether these resolutions adequately capture locally developed overpressures in the model. These challenges highlight the need for data integration, improved sediment bookkeeping (e.g., how sediment is stored in grid cells), and grid refinements to better couple compaction in Delft3D 4 – FLOW with 3D groundwater flow and improve overpressure prediction.

Integrating The Impact of Vegetation on Flows and Sediment Resistance to Resuspension in Model Simulations

This study applies compaction formulations solely adequate for clastic sediments (e.g., sand and mud) and excludes vegetation interactions. Vegetation enhances bed roughness through roots, stems, and leaves, reducing overbank flow velocity across levees and delta plains (Baustian et al., 2018; Lauzon & Murray, 2018). Previous modelling studies show that sparse to intermediate vegetation densities (plants per square meter) promote sedimentation and retain more sediment in these areas, whereas dense vegetation density causes flow to preferentially remain in the distributary channel (Albernaz et al., 2020; Lauzon & Murray, 2022; Nardin & Edmonds, 2014). Combined field and model results suggest that following a levee breach, high vegetation density retains more sediment in the delta plain than intermediate and sparse vegetation densities (Esposito et al., 2017; Nienhuis et al., 2018).

Previous studies have coupled the impact of vegetation on flow and sediment resistance to resuspension to Delft3D 4 - FLOW by updating the Chézy bed roughness coefficient based on vegetation density and species-specific parameters such as stem diameter and height (Albernaz et al., 2020; Nienhuis et al., 2018). Nienhuis et al. (2018) further linked root density to sediment resistance to resuspension by modifying the critical bed shear stress for erosion. These couplings, however, rely on external Python-based routines, which increase computation time. Additionally, the impact of vegetation is not yet integrated with compaction, which also modulates sedimentation and erosion resistance to resuspension. Such integration may amplify compaction-driven impacts on delta development.

Coupling vegetation and compaction in the Delft3D 4 – FLOW requires several steps: First, variations in water depth (bed level relative to water surface) are linked to species-specific vegetation growth and dieback. Because terrestrial vegetation dies when submerged, compaction-driven changes in water depth affect spatiotemporal vegetation density. Second, the Chézy bed roughness coefficient is updated to account for vegetation density and species, thereby modifying flow velocity and bed shear stress. Third, the

stabilizing effect of vegetation is linked to compaction, as both increase sediment resistance to resuspension. Their combined influence may amplify the overall resistance of sediments to being resuspended. Fourth, vegetation dieback and decay are linked to compaction. Plant debris can locally modify bed roughness and contribute to overburden pressure. Additionally, organic material undergoes microbial decomposition, resulting in organic mass loss (Al-Khafaji & Andersland, 1981; Zain, 2019), after which the remaining material is compacted under overburden pressure. Overall, these proposed steps will enable a coupled representation of vegetation and compaction within Delft3D 4 – FLOW, allowing more realistic simulation of delta development.

5.2.2. Comparing Models to Natural Systems

Simulation results show that changes in the erodibility index values affect levee breaching. Erodibility index is affected by sediment resistance to resuspension via critical bed shear stress for erosion. The extent to which the critical bed shear for erosion in the simulations reflects the natural values and spatial variability remains uncertain. Cone penetration testing (CPT) offers a potential method for estimating critical bed shear stress for erosion and has been widely applied in soil stability assessment for foundation design and lithofacies analysis (Amorosi & Marchi, 1999; Satriyo & Soebowo, 2018; Styllas, 2014). The Rhine-Meuse delta provides publicly available subsurface data suitable for such analysis. CPTs located within paleo-levee deposits, when paired with nearby core data, enable comparison between modeled and field-based critical bed shear stress for erosion based on: (1) grain size successions of levee deposits, (2) porosity–grain density to evaluate compaction effects, and (3) spatial variation across the delta.

Levee breaches also present in natural systems, such as in the Mississippi and St. Claire deltas (Figures 2A-F). These natural breaches are often accompanied by land building, highlighting their importance as sediment conduit to the delta plain (Figures 2B-C). Modelling results show that levee breaching exposes underlying deposits with higher critical bed shear stress for erosion, thereby limiting further vertical erosion and affecting the breach's ability to capture the main flow. This promotes breach restoration in the levee. Healed natural breaches can be observed in the form of small lakes in The Netherlands, around which rivers now flow (Figures 2G - I). These lakes are locally called *wiel*, representing remnants of former breach scours formed when breaching diverted flow and sediment onto the adjacent delta plain. Comparison to natural analogs serves as validation of modeled levee breaching dynamics as well as opportunities to explore long-term morphodynamic consequences of this process.

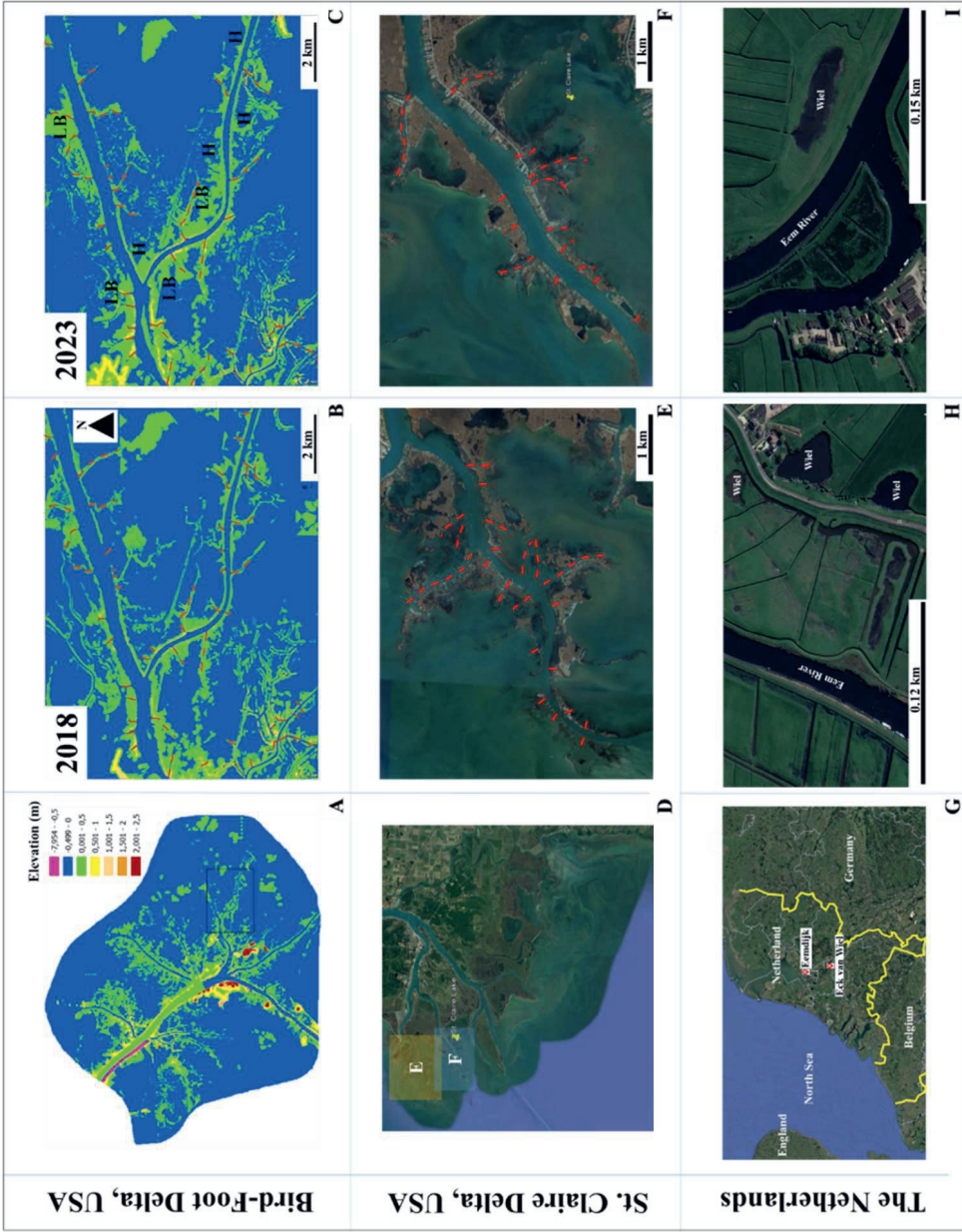


Figure 5.1. (A - C) Timelapse elevation maps of a bird-foot delta branch, taken in 2018 and 2023 Lidar (source: <https://apps.nationalmap.gov/>), located few kilometers downstream from the Neptune Pass (Kolker et al., 2025). (D - F) Elevation maps of St. Clair delta branches (source: <https://earth.google.com>). Breach locations in these deltas are marked by red-dotted lines. Abbreviations LB and H in Figure 2C are land building and healing, respectively. (G - I) The Eem River goes around small lakes south of Eemdijk, The Netherlands (source: <https://earth.google.com>). These lakes are locally called *wiel* or *wielen*, which represent remnants of past levee breaches that later healed. Today, some *wielen* are located far from the present River (> 100 m), indicating that the river has migrated away from the original breach sites (H). As the river shifted, the once-adjacent scour lakes now appear far from the present river course.

5.2.3. Assessing The Impact of Syn-Depositional Compaction on Delta Plain and Mouth Bar Processes

The Impact of Syn-Depositional Compaction on Sedimentation and Preservation of Sediment in The Delta Plain

This study demonstrates that syn-depositional compaction affects the initiation and progression of levee breaching in model simulations. As an inherent process in deltaic systems, syn-depositional compaction also affects processes in other depositional areas, such as the delta plain and mouth bar. The delta front and pro delta are excluded from this analysis, as syn-depositional compaction contributes minimally to accommodation in these deeper-water areas. In natural deltas, syn-depositional compaction dynamically changes delta plain elevation together with sedimentation and erosion associated with overbank flow, crevasse splays, and avulsion. In anthropogenically influenced deltas such as the Yellow River and Mekong, delta plains are densely populated and increasingly vulnerable to relative sea-level rise driven by sea-level rise and compaction-induced subsidence. Here, the subsidence is further accelerated due to hydrocarbon and groundwater extraction (Liu et al., 2016; Minderhoud et al., 2020; Nienhuis et al., 2023). The accelerated subsidence is uncompensated by sedimentation due to embanked channels that restrict overbank flow and crevasse splay formation, instead promoting channel lengthening. This increases the susceptibility of delta plain to drowning.

Levee breaching causes flooding in populated delta plains, but in unpopulated areas it can serve as a natural or human-induced mechanism that reintroduces fresh water and sediment to sediment-starved delta plains. In the Mississippi Bird-Foot Delta, breaches redirect sediment-laded flow into adjacent interdistributary bays, increasing land area (Figures 2B-C). Similar increase in land area have been observed in Bay Denesse after breaching along Neptune Pass within the same delta system (Kolker et al., 2025). Our modelling results show that syn-depositional compaction influences sediment distribution across depositional areas. Levee breaching as a key sediment delivery mechanism has also

been investigated, which shows consistent behavior to real-world breaching. However, the subsequent transport, deposition, and preservation processes in the delta plain continue to be modified by compaction through changes in bed elevation and sediment resistance to resuspension. This interaction remains poorly understood and provides an opportunity for future work with implications for delta restoration and resilience under environmental change.

The Impact of Syn-Depositional Compaction on Mouth Bar Formation

Mouth bars form as a sediment-laden flow decelerates when exiting channel mouths into standing body of water, which play a key role in channel bifurcation. Modelling studies using Delft3D 4 – FLOW have elucidated key controls on mouth bar formation. In simulations without waves and tides, the distance of the mouth bar from river mouth scales with jet momentum and inversely with grain size (Edmonds & Slingerland, 2007). Simulated waves enhance bottom shear stress and resuspension, thereby suppressing mouth bar growth and channel network development (Geleynse et al., 2011; Jerolmack & Swenson, 2007; Nardin et al., 2013; Nardin & Fagherazzi, 2012). Simulated oblique tidal oscillations generate residual currents that laterally redistribute sediment, producing wider and less shallow mouth bars (Hoitink et al., 2017; Leonardi et al., 2013).

The above-mentioned modelling studies did not consider syn-depositional compaction as a key process in mouth bar formation. Although mouth bars are typically sand-dominated, field studies show that they contain interbedded cohesive muds (Ainsworth et al., 2016; Storms et al., 2005). Sand compacts faster than mud due to its higher hydraulic permeability. In our simulations, mouth bars consist of rapidly depositing sediment mass (800 - 1000 kg per output interval). Such high deposition rates may drive initial rapid mouth bar growth. Compaction of mouth bar deposits, particularly sand, is also rapid, causing subsidence of the deposits. This can potentially reduce the rate of mouth bar growth relative to what the deposition rate alone would suggest. Additionally, compacting mud layers increase resistance to resuspension, potentially shielding sandy layers from erosion and enhancing mouth bar growth. These competing effects of compaction on mouth bar formation remain poorly constrained and warrant further study.

Supplementary Materials

Generating synthetic deltas serves as a valuable data source for sedimentological studies. Utilizing established datasets and information from the literature, computer simulations are conducted using the open-source software Delft3D. These simulated deltas are employed to investigate the impact of compaction on delta development, with a focus on morphodynamic changes, sediment budget partitioning, and sediment preservation within the delta system. To analyse the effects of compaction in the simulated deltas, the simulation results must undergo post-processing to facilitate comparisons between different scenarios. This chapter provides an extended explanation of the compaction and erosion resistance formulations and assumptions, the numerical methods employed in delta modeling, and the post-processing metrics used to compare simulation outcomes.

Supplementary Materials A

This sub-chapter provides supplementary materials for chapter 2. First, validation of compaction formulas using laboratory data and the implementation of these formulas into Delft3D is provided (A1 and A2). In addition, A3 and A4 report the temporal bathymetry development of simulated deltas and methods to interpret the deltas' sub-environments, respectively. Finally, A5 describes the morphology plots in time series.

A1. Validation of Compaction formulas

The compaction formulas (Equations 2.4 and 2.5 in the main text) were validated by datasets obtained from a settling column experiment using well-mixed slurry mud (Merckelbach & Kranenburg, 2004b). The sediment settled for 95 days, forming a sediment bed at the base of the column. The changes in the sediment bed thickness were measured during this period. The result shows a rapid decrease in bed thickness from 1.53 m to 0.54 m in the first ten days due to primary compaction. Subsequently, the bed thickness decreases at a more gradual rate due to secondary compaction.

The bed thickness changes due to compaction were modelled using Equations 2.4 and 2.5 by incorporating the initial bed thickness and duration of primary and secondary compaction obtained from the laboratory study. As the compaction formulas were designed for a longer timescale than the laboratory study duration, a few adjustments need to be made to the formulas: (1) As the primary compaction depends on overburden stress, it is assumed that 1.53 m of clay sediment was deposited on top of the bed in the first ten days

to trigger the primary compaction. No deposition occurs afterwards to activate the secondary compaction.

(2) The primary and secondary compaction rates (parameters C_p and C_s in Equations 2.4 and 2.5) were modified to the laboratory scale, which occurs at a much higher rate than in natural systems. The C_p and C_s were set to 87 and 0.03 m y^{-1} . The comparison between the laboratory and modelling results indicates a similar compaction trend (Figure A1).

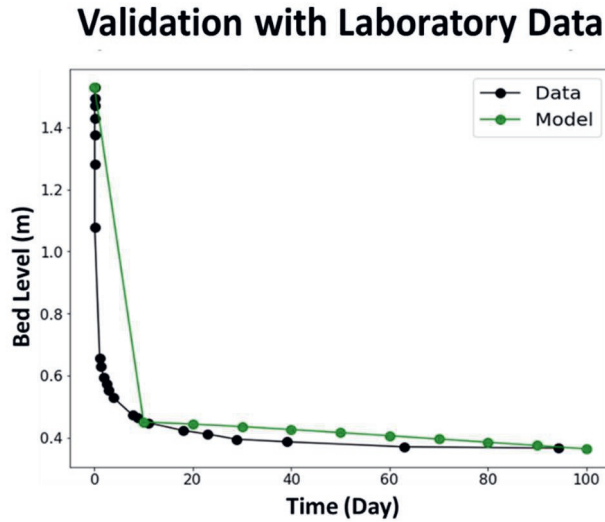


Figure A1. The graph compares bed level changes over time obtained from laboratory data (settling column experiment) and numerical modelling.

A2. Compaction Implementation in Delft3D

The stratigraphic layer in Delft3D consists of a transport layer, underlayers, and a base layer (Figure A2). The transport layer has a fixed thickness of 0.2 m, moving up and down in response to deposition and erosion. The transport layer moves upward during the deposition, meaning that the newly deposited sediment is registered on top of the existing sediment in the transport layer. The excess thickness from the lower part of the transport layer with the same thickness as the newly deposited sediment is stored in the underlayers situated below the transport layer, starting from the lowermost underlayer. Seventy-five underlayers were used, and each can reach a maximum thickness of 0.3 m. The base layer has a flexible thickness and stores the excess sediment once all underlayers have been filled. If the transport layer is partly or entirely eroded, the stored sediment will be used to restore

the top layer to its initial thickness. The stored sediment is taken from the uppermost filled underlayer. If the underlayers are empty, then the sediment from the base layer will be used. This way, the sediment is administered at each grid cell throughout the simulation period.

The primary and secondary compaction (Equations 2.4 and 2.5 in the main text) were implemented in underlayers. It is assumed that the initial bed stratigraphy (base layer) is fully compacted before the simulation (Figure A2). Moreover, no compaction occurs at the transport layer as it is assumed that the loading from the overlying water or air is negligible. It is also assumed that compaction does not impact the transport layer's erodibility (cf. critical bed shear stress for erosion and maximum erosion rate). The compaction algorithm quantifies the overburden stress in each underlayer imposed by the overlying layers. The primary compaction occurs in an underlayer when overburden stress is larger than previously experienced by the underlayer. In contrast, secondary compaction takes place after the onset of the primary compaction and if the overburden stress is equal to or smaller than previously experienced by the underlayer.

An example of how the stratigraphic layer behaves under compaction influence is shown in Figure A2. At the initial condition ($t = 0$), the empty underlayers are subjected to the overburden stress from the transport layer. During deposition ($t = 1 - 6$), the deposited sediment at the transport layer is stored in underlayers starting from the lowermost underlayer (UL 75). At $t = 6$, Primary compaction occurs at layer UL 75 because the overburden stress imposed by overlying layers (TL and UL 74) is larger than the historical largest stress experienced by this layer. During erosion ($t = 7$), the eroded transport layer is replenished to its original thickness using the stored sediments taken from the uppermost filled underlayer (UL 74), decreasing the overburden stress imposed on UL 75. As a result, UL 75 undergoes secondary compaction because the overburden stress imposed on UL 75 is now smaller than previously experienced by this layer. During hiatus ($t = 8$), UL 75 also experiences secondary compaction because the overburden stress is the same as the previous simulation time ($t = 7$). No secondary compaction occurs at UL 74 as the primary compaction has not started.

The newly deposited sediment in each underlayer is assigned a bed porosity, which decreases from initial to minimum value over the simulation time due to compaction (Figure A2). The initial value of bed porosity is determined by weighted averaging of the depositional porosity of mud and sand based on their proportion in the supplied sediment. For example, mud and sand have a depositional porosity of 0.8 and 0.4, respectively (Revil et al., 2002; Alberts, 2005, whilst their proportion in the supply is 85%:15% and 30%:70% for mud-rich and sand-rich deltas, respectively. Therefore, the initial porosity of the

deposited sediment is set to 0.75 and 0.52 for mud-rich and sand-rich deltas, respectively. Similarly, the minimum porosity is also determined by weighted averaging of the compacted porosity of mud and sand, following their proportion in the supplied sediment. As mud and sand have a compacted porosity of 0.05 and 0.25, respectively (Revil et al., 2002; Alberts, 2005), the minimum porosity of the deposited sediment is set to 0.08 and 0.18 for mud-rich and sand-rich deltas, respectively.

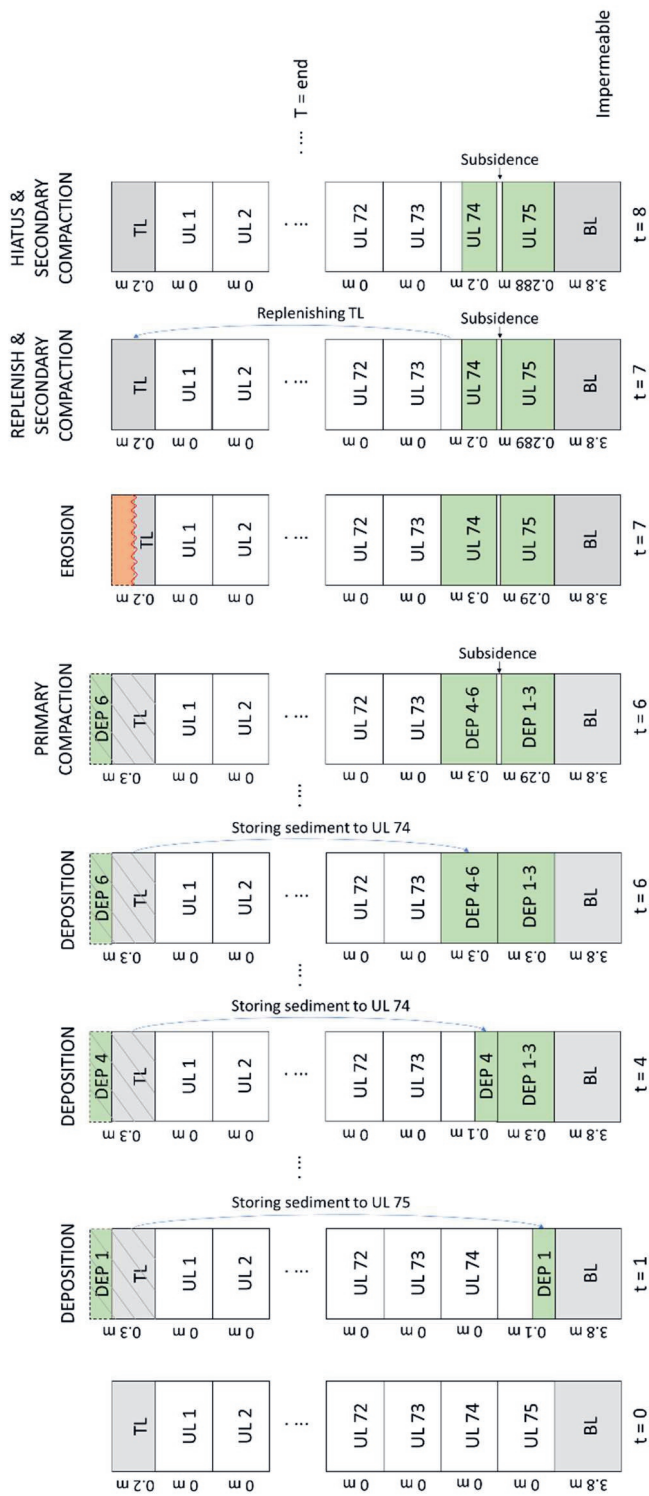


Figure A2. The sketch provides a schematic overview of how compaction interacts with the stratigraphic layers of Delft3D. These layers consist of a transport layer (TL), underlayers (UL 1 - UL 75), and a base layer (BL), subjected to hypothetical deposition, erosion, and hiatus.

A3. Temporal Bathymetry Development of Simulated Deltas

The temporal bathymetry development of each mud-rich delta for selected simulation output times is shown in Figures A3 to A13, whilst the bathymetry for all mud-rich deltas at the end of the simulation is shown in Figure A14. Plan-view observation indicates that the delta top dynamics in compaction scenarios 0 - 0.1 mm y⁻¹ are dominated by channel avulsion, directing the main deposition towards the avulsion direction. This results in uneven land building alongshore. As the compaction scenario increases to 1 mm y⁻¹, the influence of avulsion decreases. The channel tends to prograde seaward, migrating laterally with smaller branches developed parallel to the initial shoreline. As a result, the land building focuses on the delta centerline. In compaction scenarios 5 - 10 mm y⁻¹, the main channels and smaller branches distribute the sediment across the delta top and rarely reach the coastline. This leads to more evenly land building alongshore.

The temporal bathymetry development of each sand-rich delta for selected simulation output times is shown in Figures A15 to A25, whilst the bathymetry for all sand-rich deltas at the end of the simulation is shown in Figure A26. Plan-view observation indicates that the delta top dynamics are dominated by channel avulsion, which occurs more frequently than in mud-rich deltas. The increasing compaction scenario does not significantly reduce avulsion frequency, resulting in an unevenly distributed sediment alongshore for all compaction scenarios, mainly towards the direction of avulsion. This leads to a less significant decrease in the delta top area than in mud-rich deltas

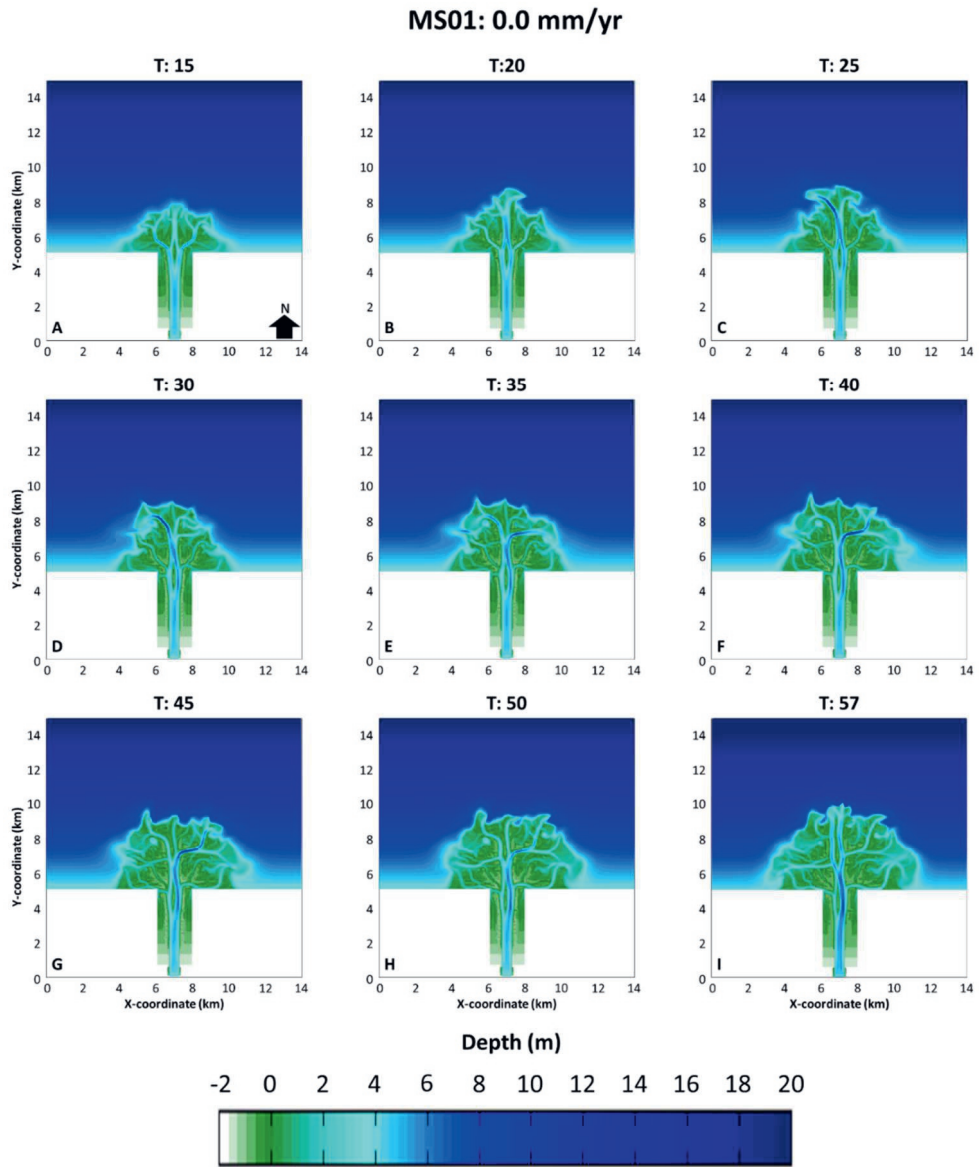


Figure A3. Plan-view bathymetry of a mud-rich delta with compaction scenario 0 mm yr^{-1} for selected simulation output times (A - I).

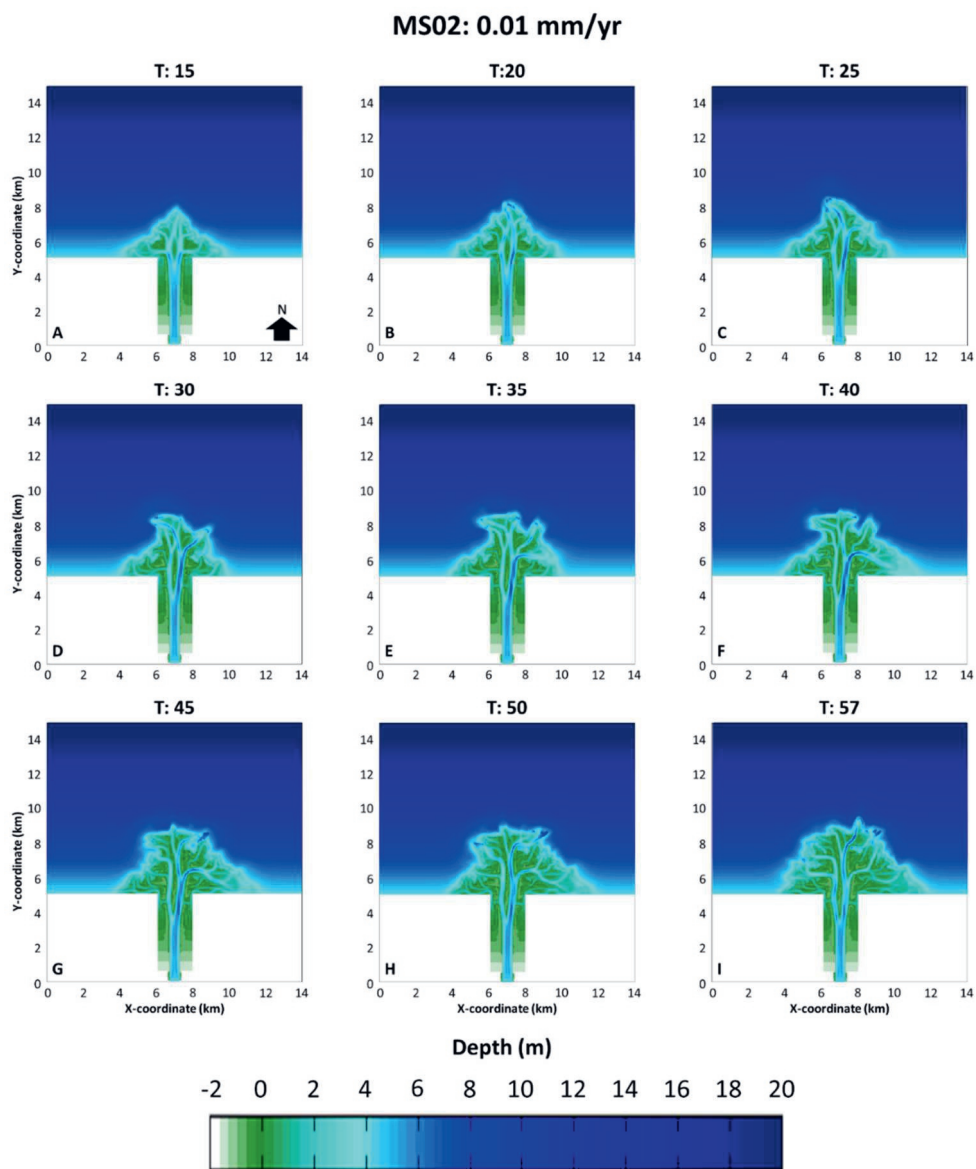


Figure A4. Plan-view bathymetry of a mud-rich delta with compaction scenario 0.01 mm yr^{-1} for selected simulation output times (A - I).

MS03: 0.05 mm/yr

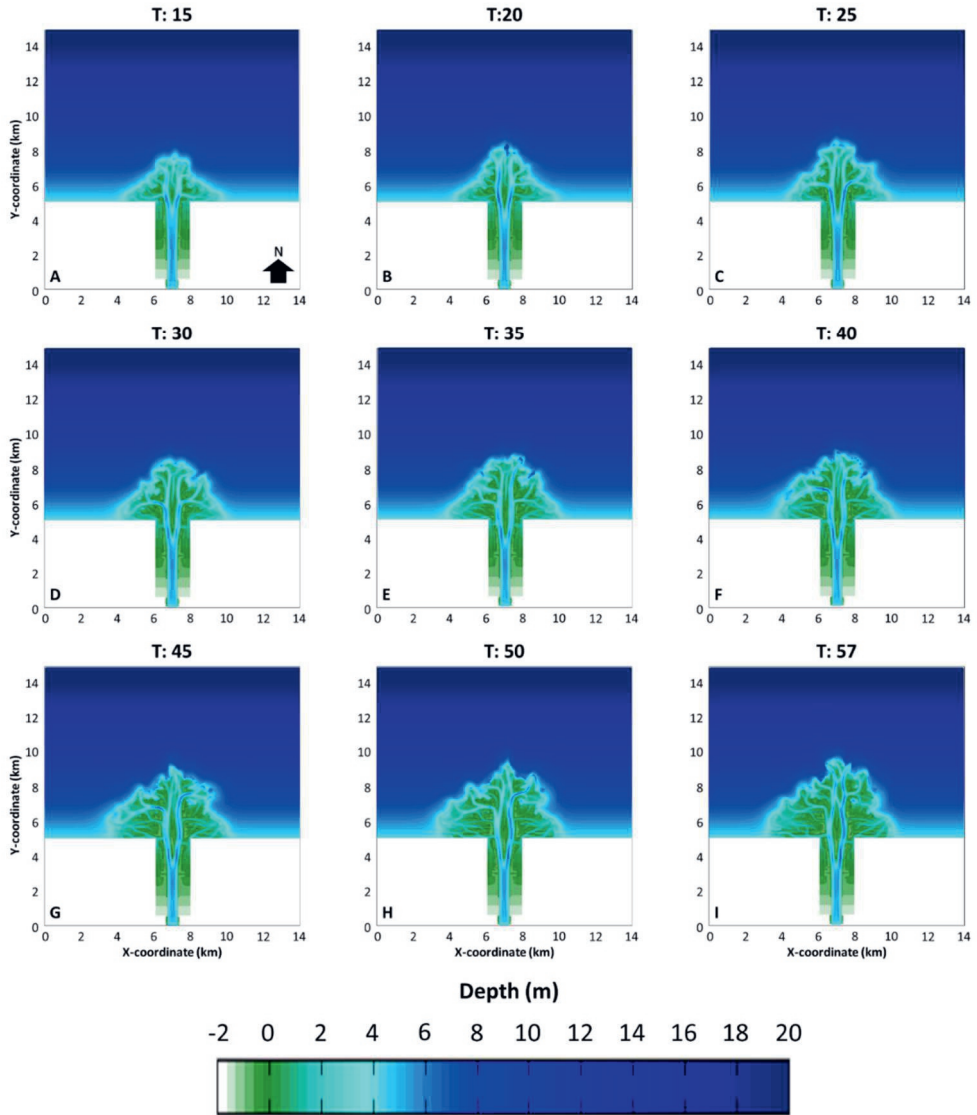


Figure A5. Plan-view bathymetry of a mud-rich delta with compaction scenario 0.05 mm y^{-1} for selected simulation output times (A - I).

MS04: 0.075 mm/yr

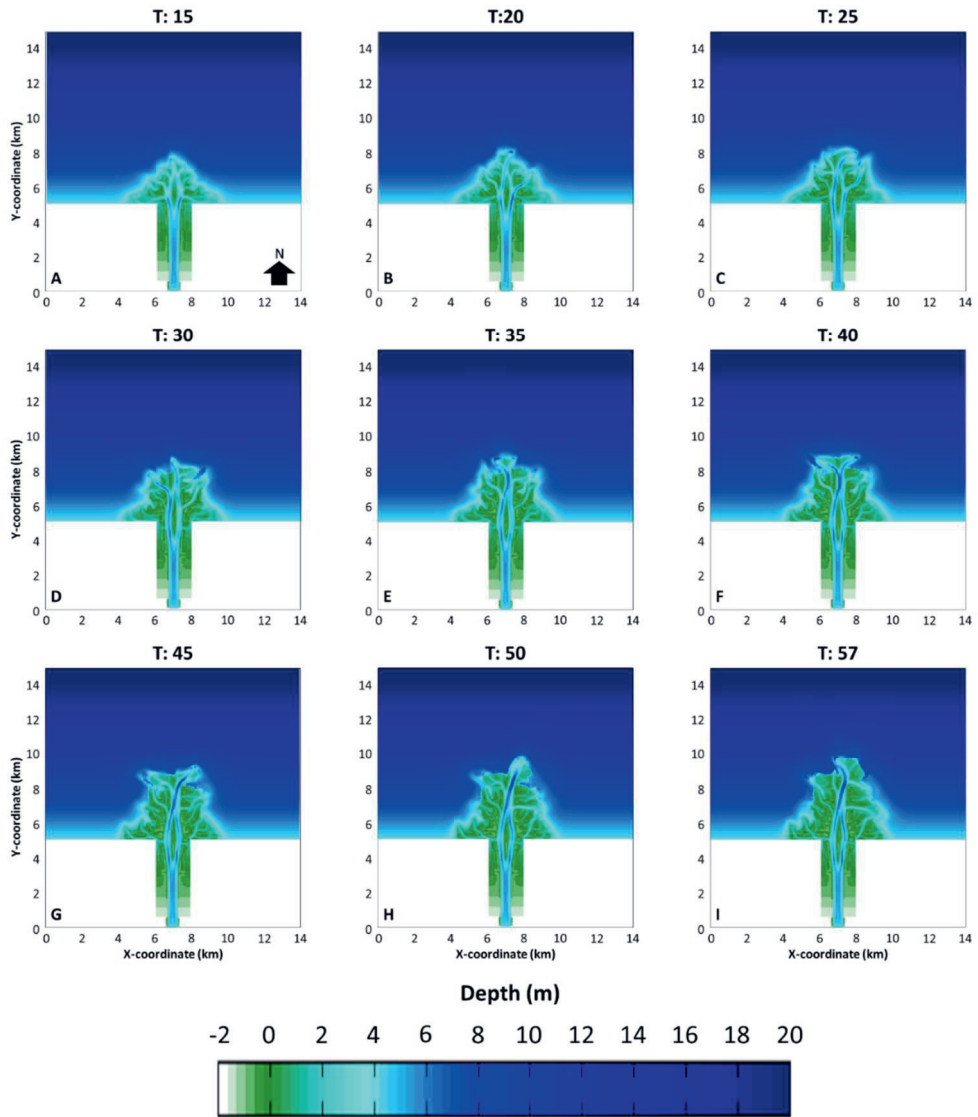


Figure A6. Plan-view bathymetry of a mud-rich delta with compaction scenario 0.075 mm y^{-1} for selected simulation output times (A - I).

MS05: 0.1 mm/yr

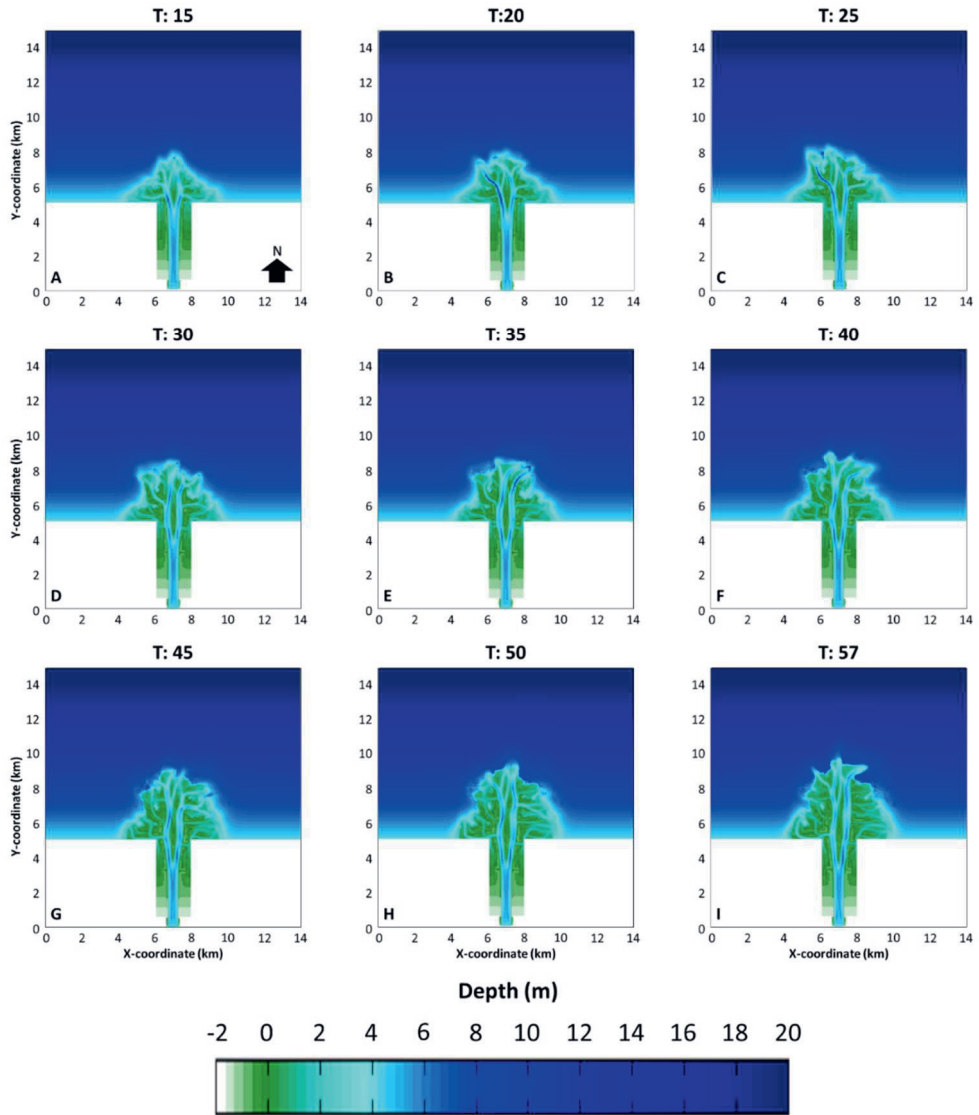


Figure A7. Plan-view bathymetry of a mud-rich delta with compaction scenario 0.1 mm yr^{-1} for selected simulation output times (A - I).

MS06: 0.5 mm/yr

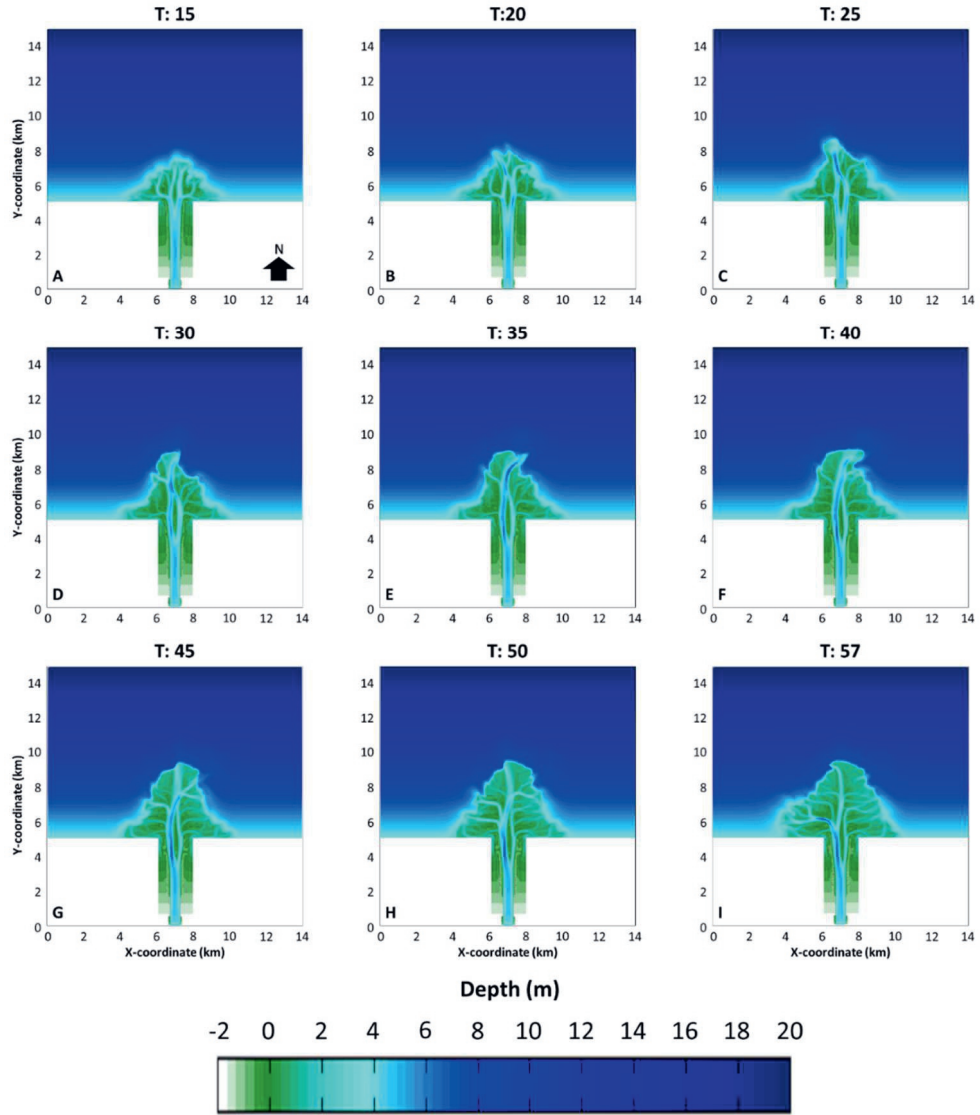


Figure A8. Plan-view bathymetry of a mud-rich delta with compaction scenario 0.5 mm y^{-1} for selected simulation output times (A - I).

MS07: 0.75 mm/yr

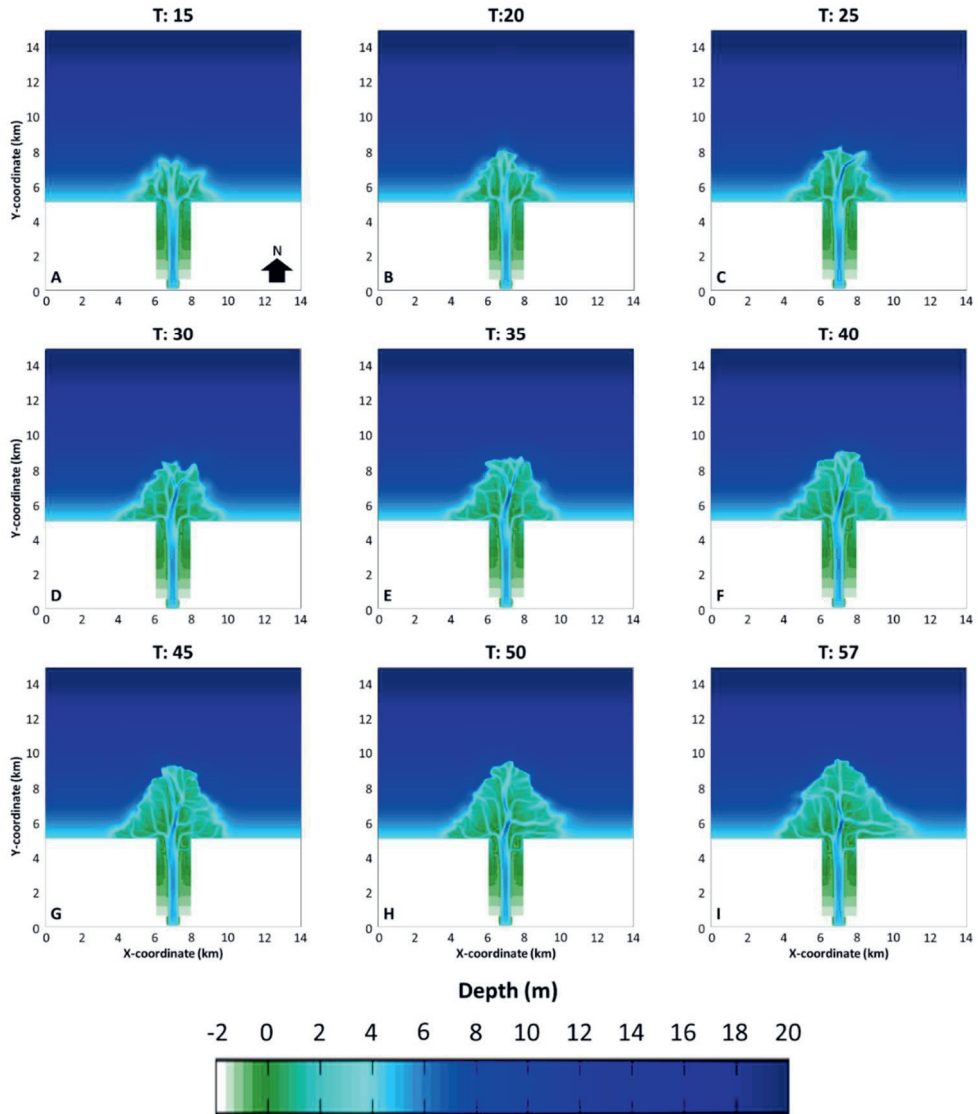


Figure A9. Plan-view bathymetry of a mud-rich delta with compaction scenario 0.75 mm yr^{-1} for selected simulation output times (A - I).

MS08: 1 mm/yr

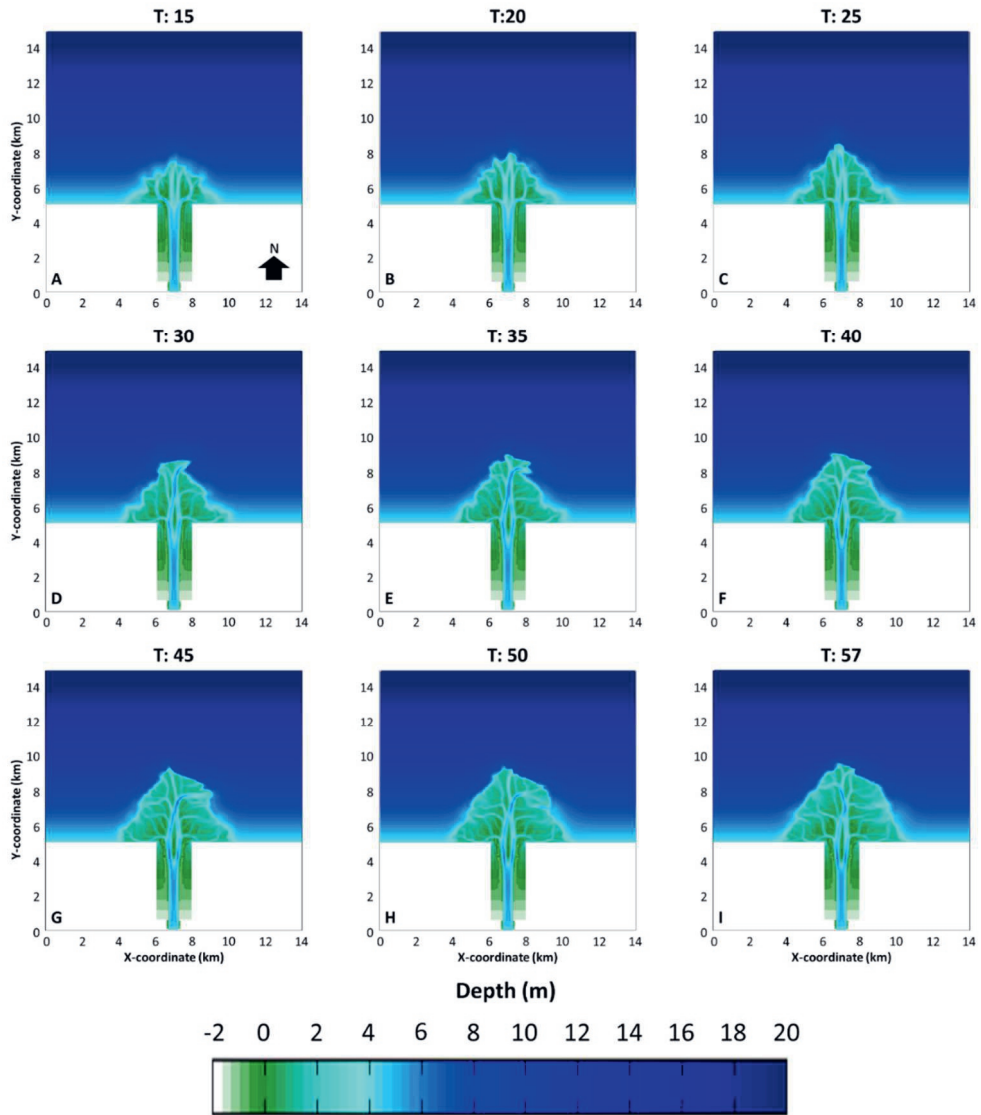


Figure A10. Plan-view bathymetry of a mud-rich delta with compaction scenario 1 mm y^{-1} for selected simulation output times (A - I).

MS09: 5 mm/yr

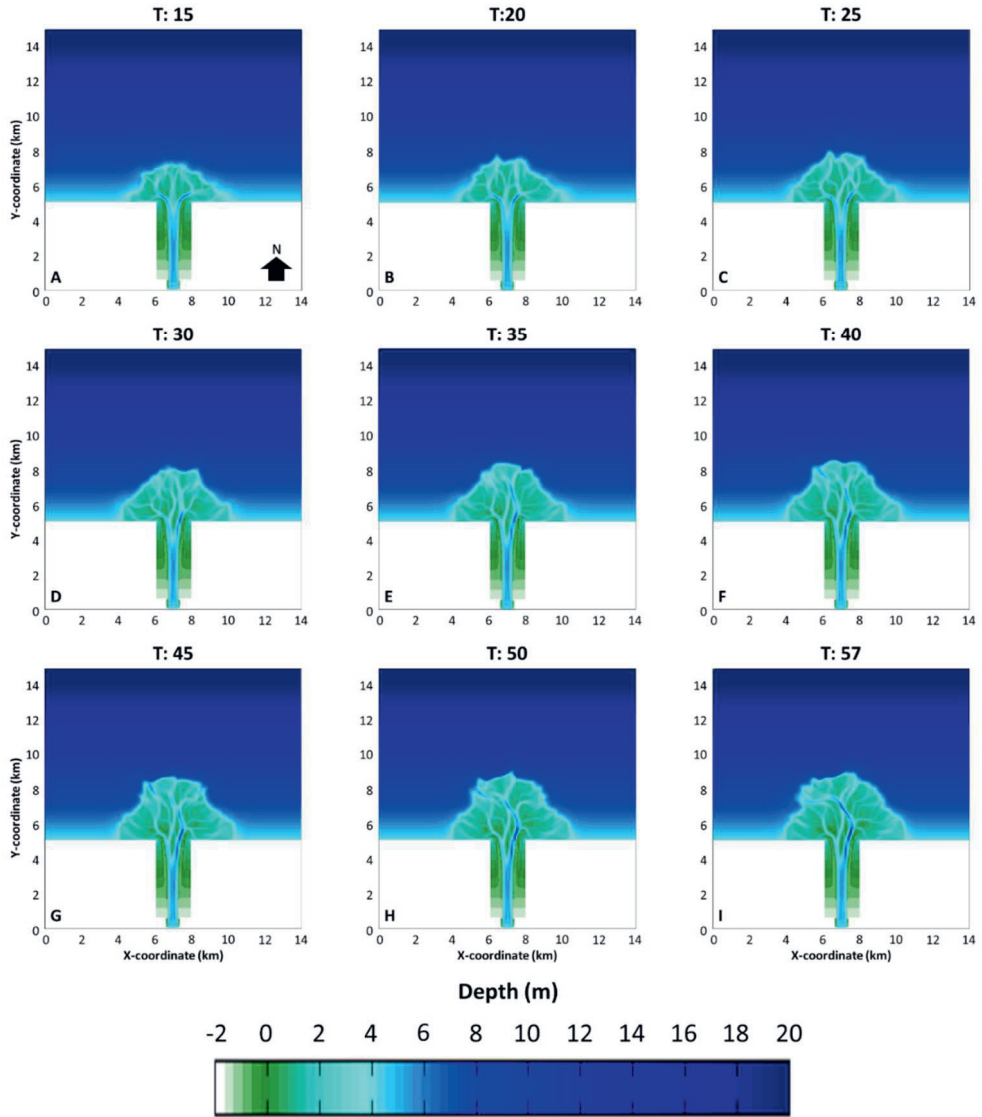


Figure A11. Plan-view bathymetry of a mud-rich delta with compaction scenario 5 mm y^{-1} for selected simulation output times (A - I).

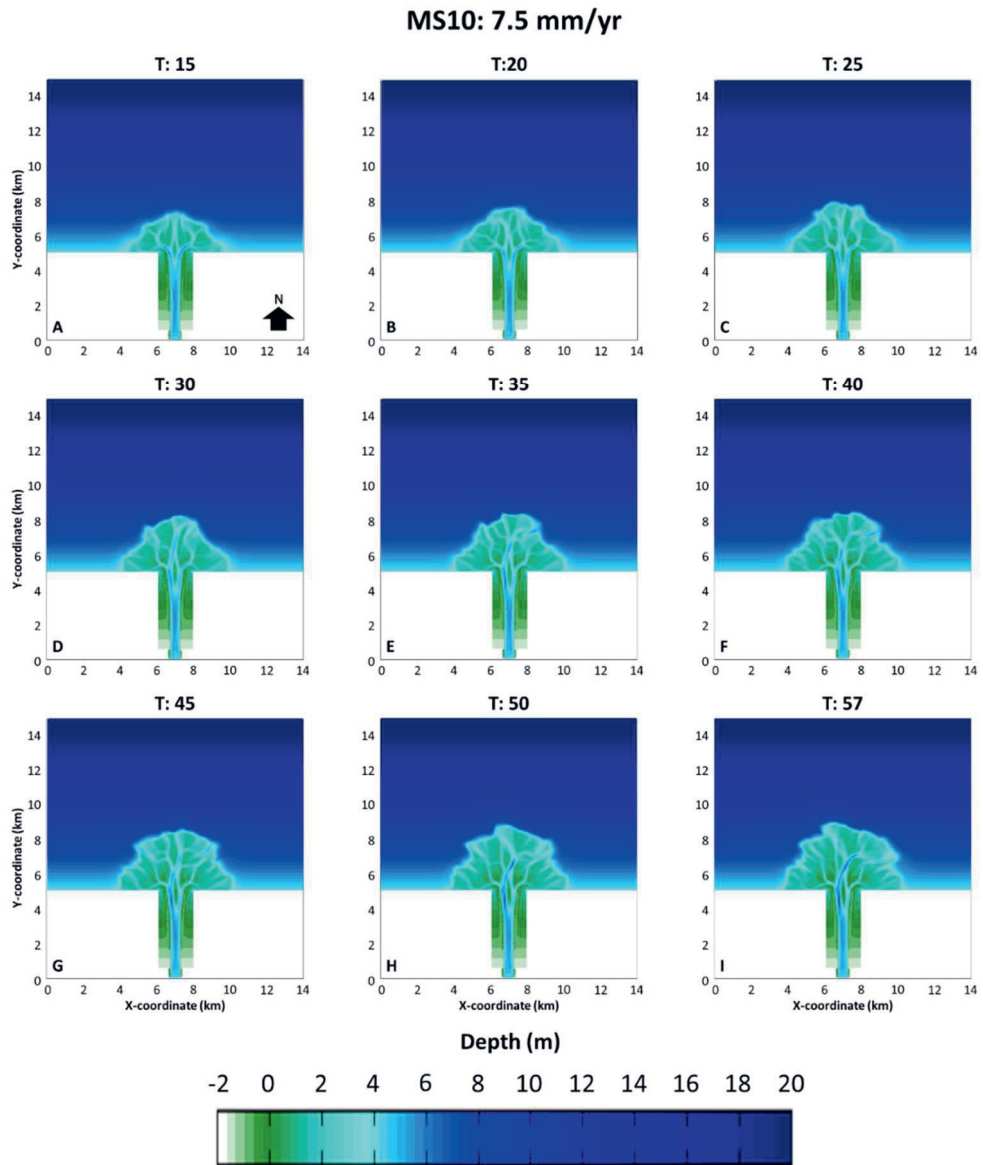


Figure A12. Plan-view bathymetry of a mud-rich delta with compaction scenario 7.5 mm yr^{-1} for selected simulation output times (A - I).

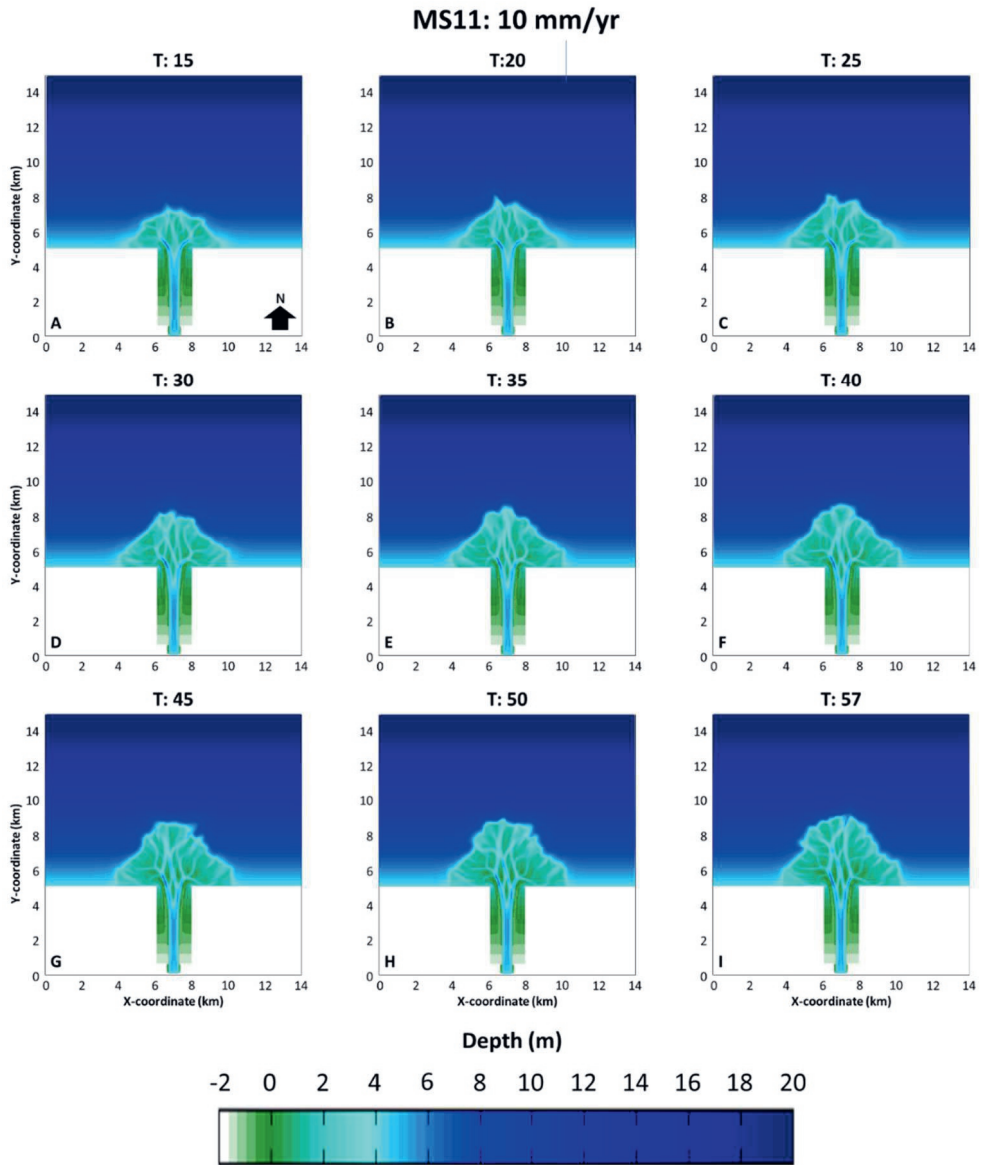


Figure A13. Plan-view bathymetry of a mud-rich delta with compaction scenario 10 mm yr^{-1} for selected simulation output times (A - I).

Mud-rich Deltas

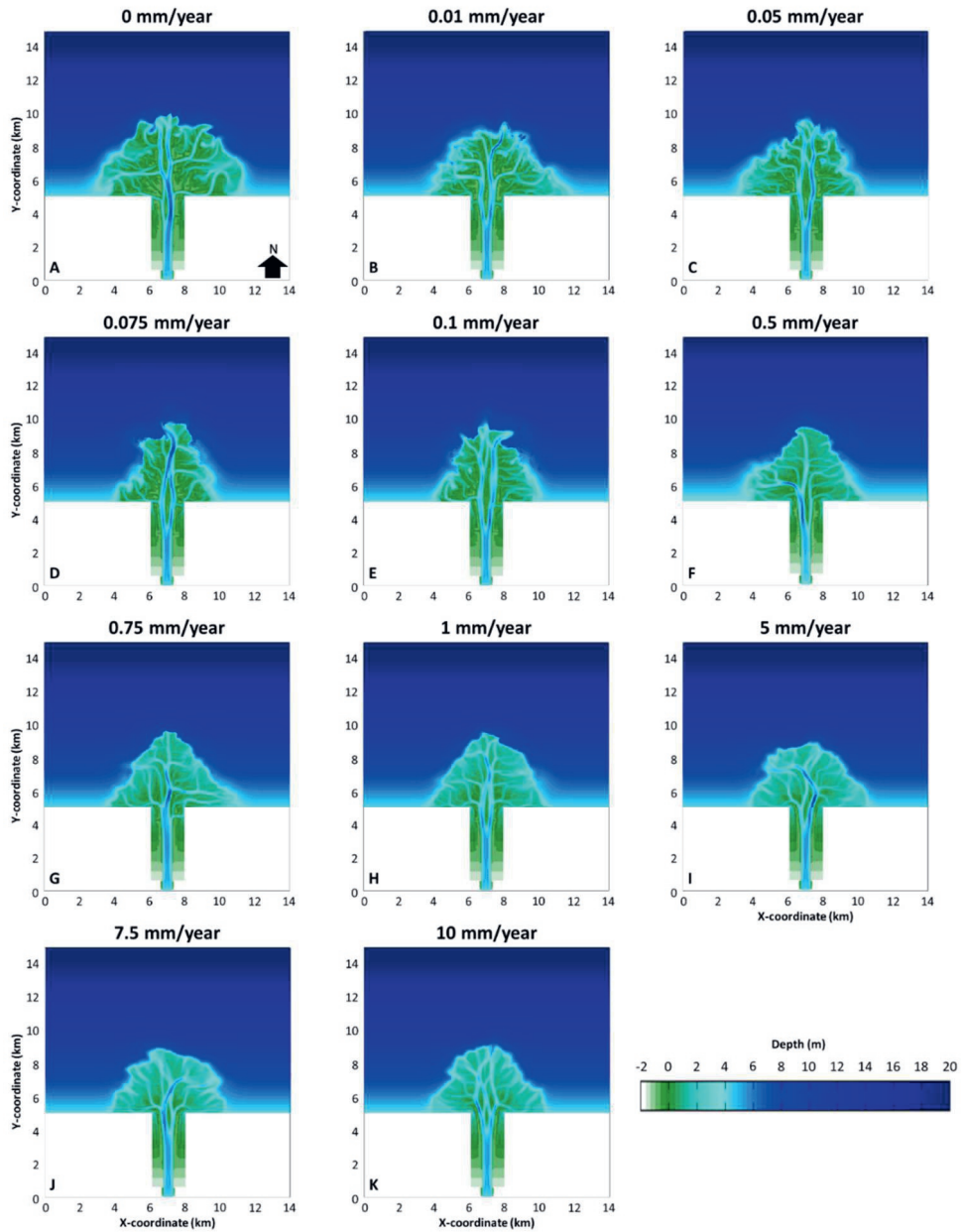


Figure A14. Plan-view bathymetry for all compaction scenarios ($0 - 10 \text{ mm y}^{-1}$) of mud-rich deltas at the end of the simulation (A - K).

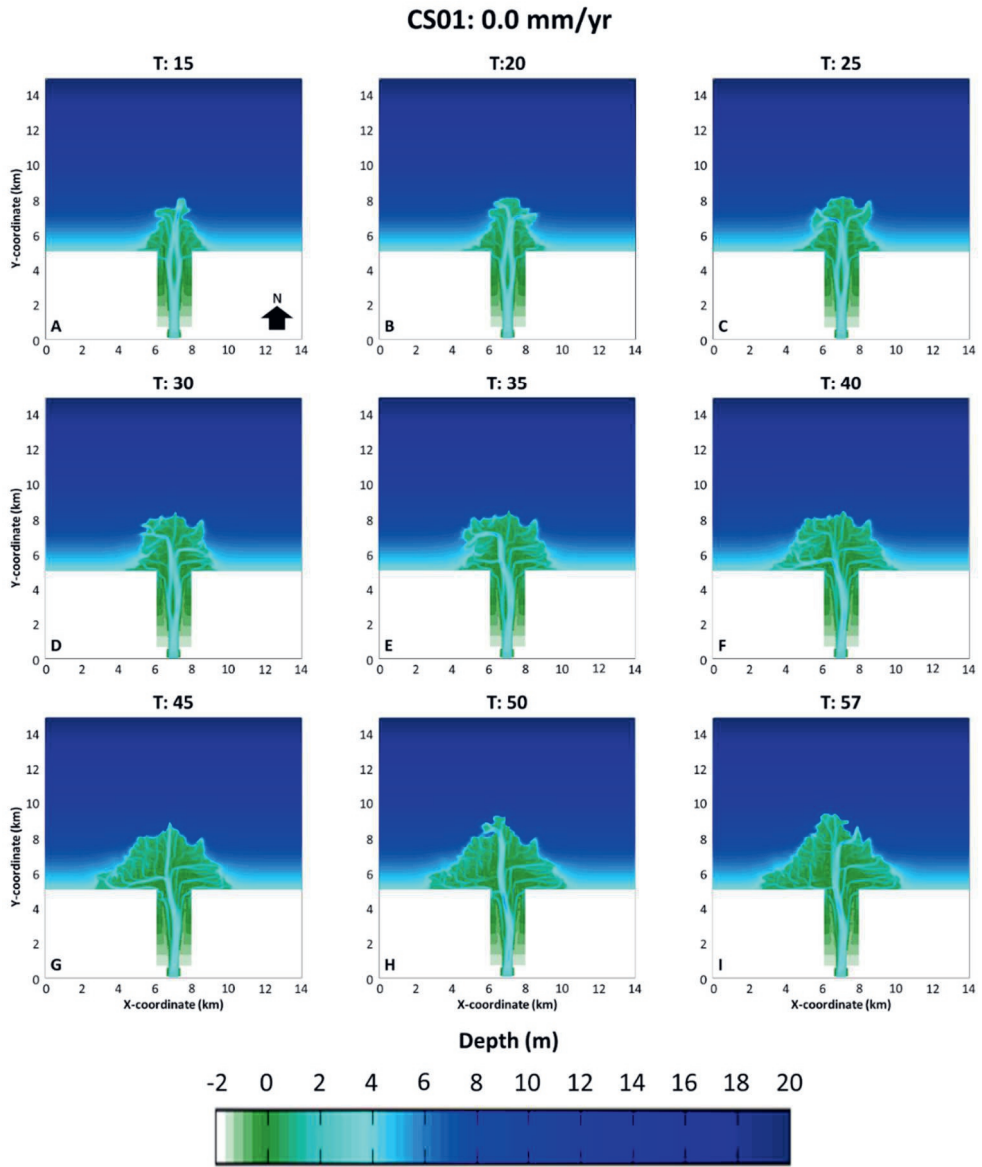


Figure A15. Plan-view bathymetry of a sand-rich delta with compaction scenario 0 mm yr^{-1} for selected simulation output times (A - I).

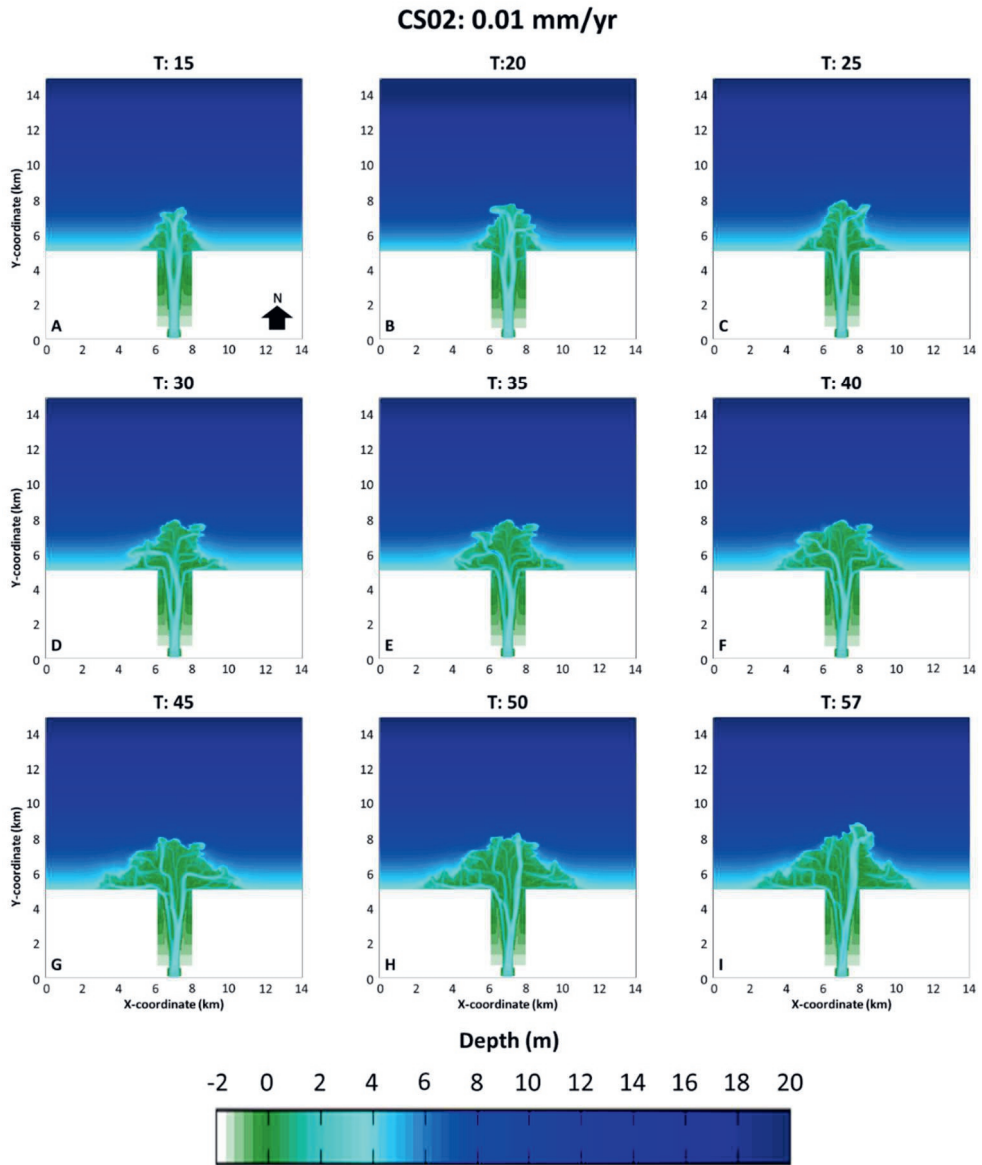


Figure A16. Plan-view bathymetry of a sand-rich delta with compaction scenario 0.01 mm y⁻¹ for selected simulation output times (A - I).

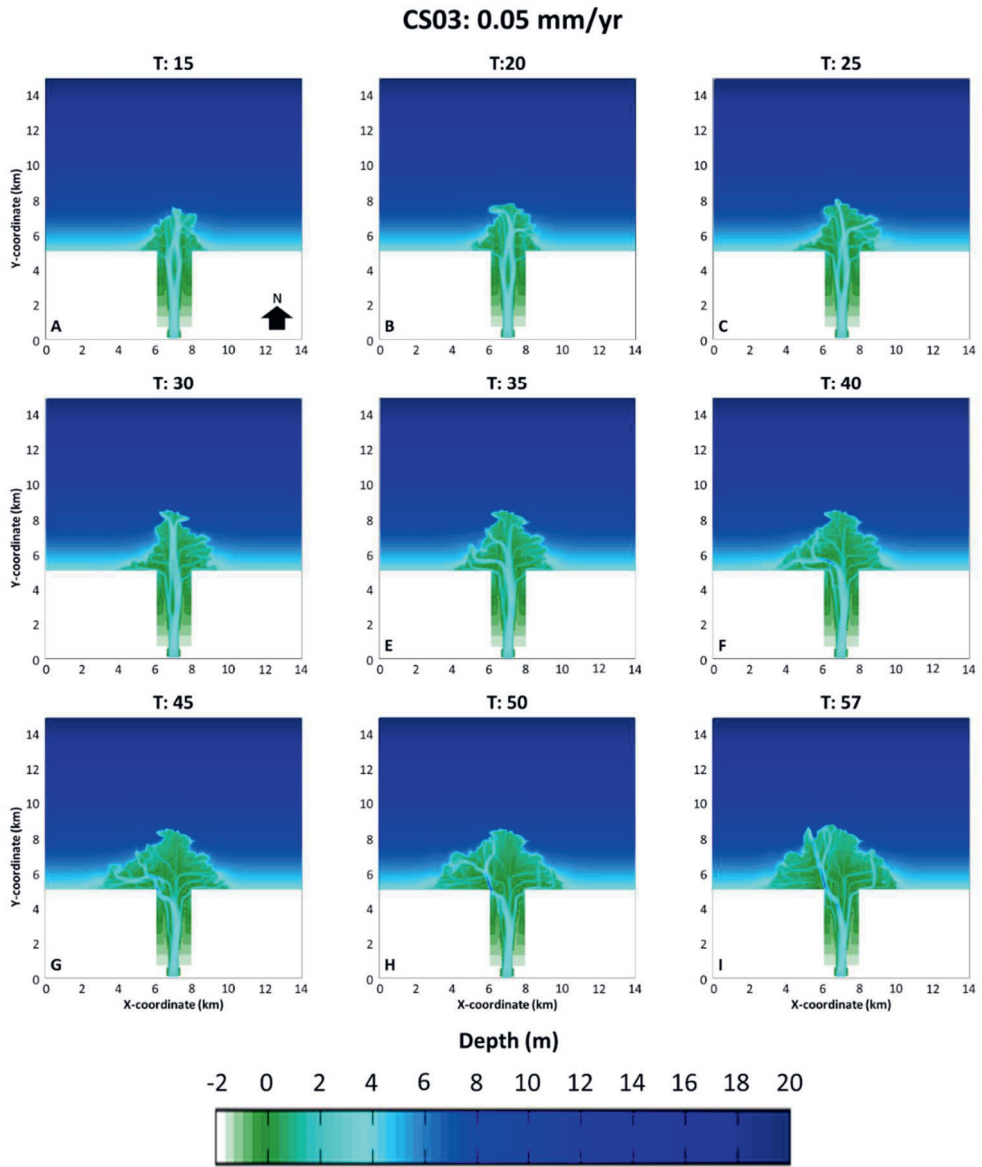


Figure A17. Plan-view bathymetry of a sand-rich delta with compaction scenario 0.05 mm y^{-1} for selected simulation output times (A - I).

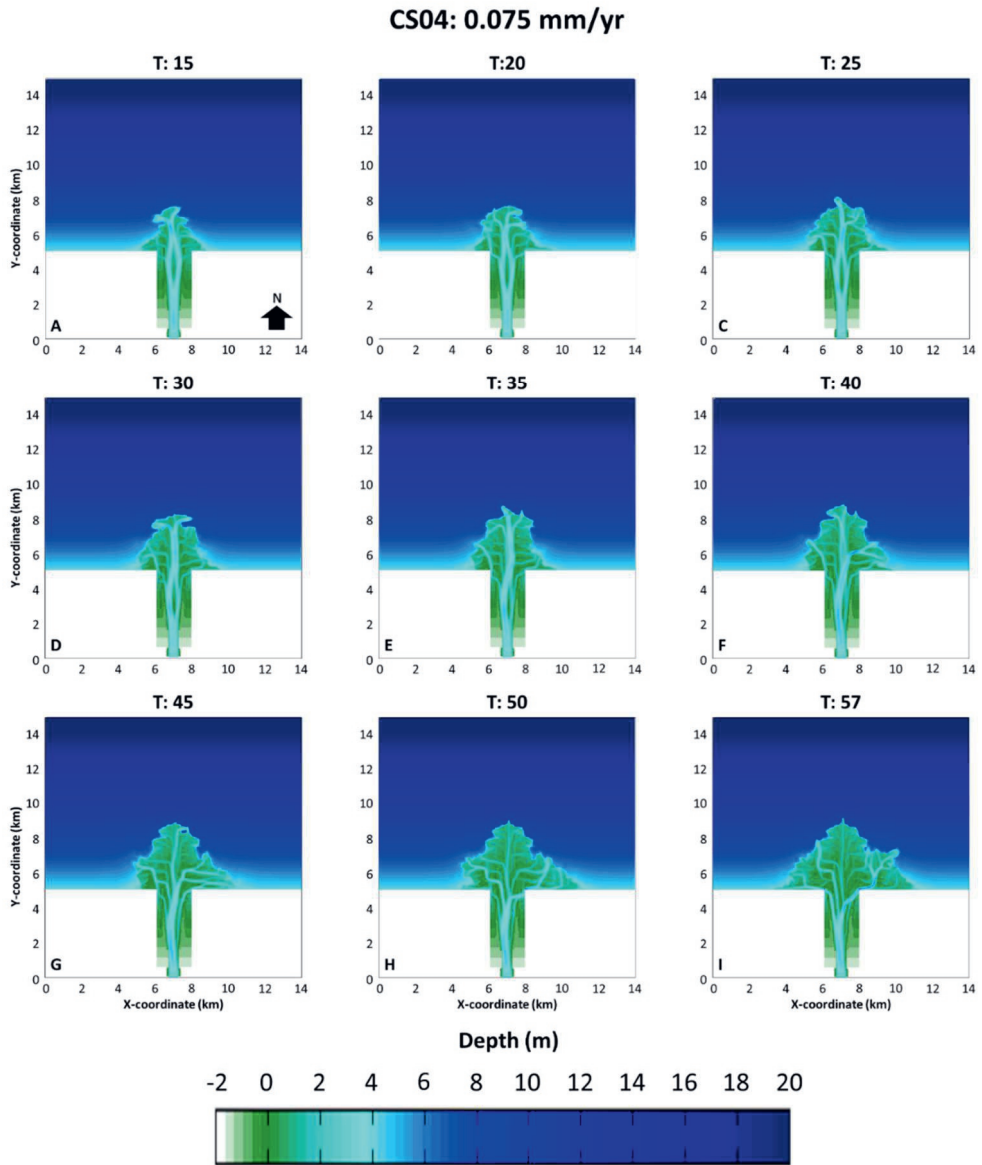


Figure A18. Plan-view bathymetry of a sand-rich delta with compaction scenario 0.075 mm yr^{-1} for selected simulation output times (A - I).

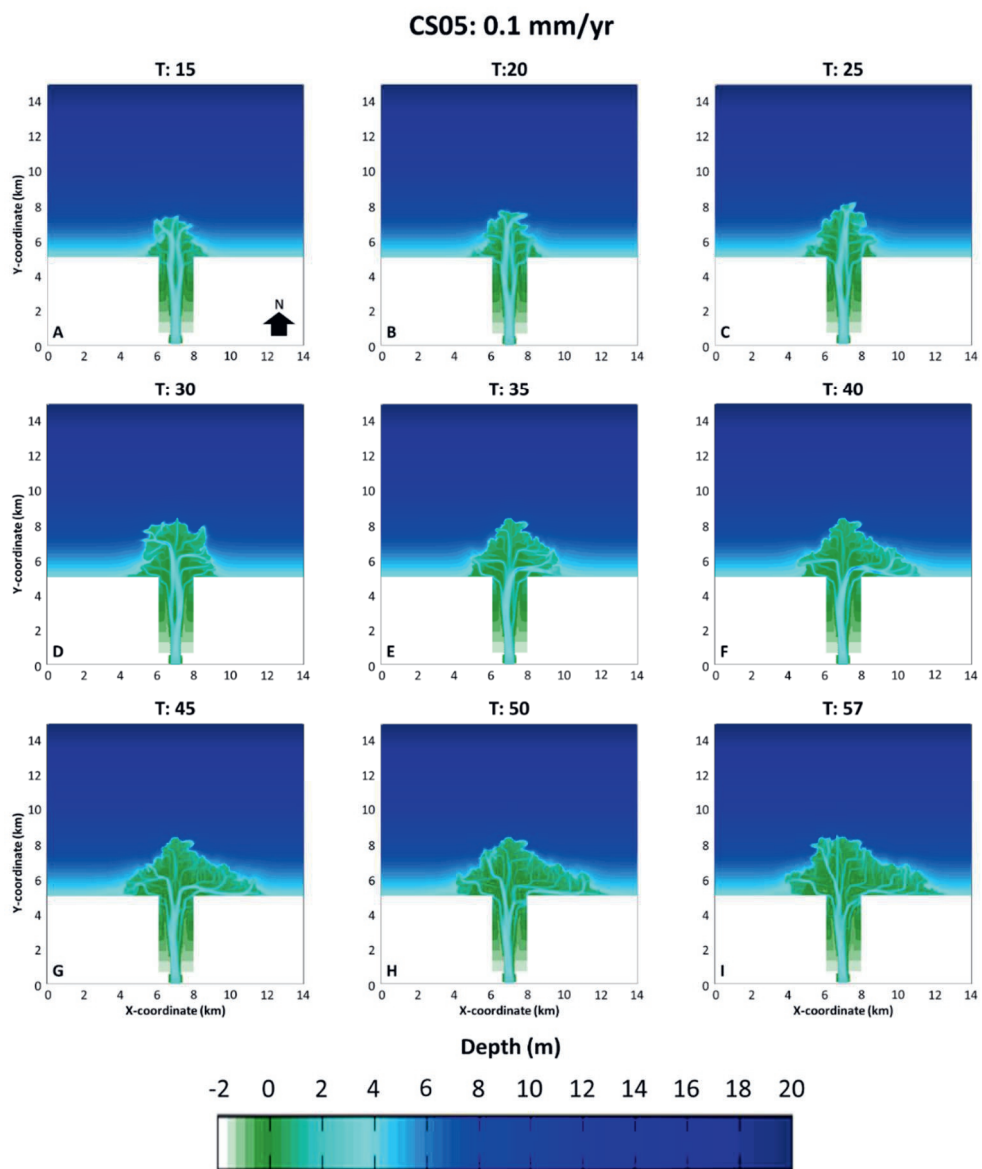


Figure A19. Plan-view bathymetry of a sand-rich delta with compaction scenario 0.1 mm y^{-1} for selected simulation output times (A - I).

CS06: 0.5 mm/yr

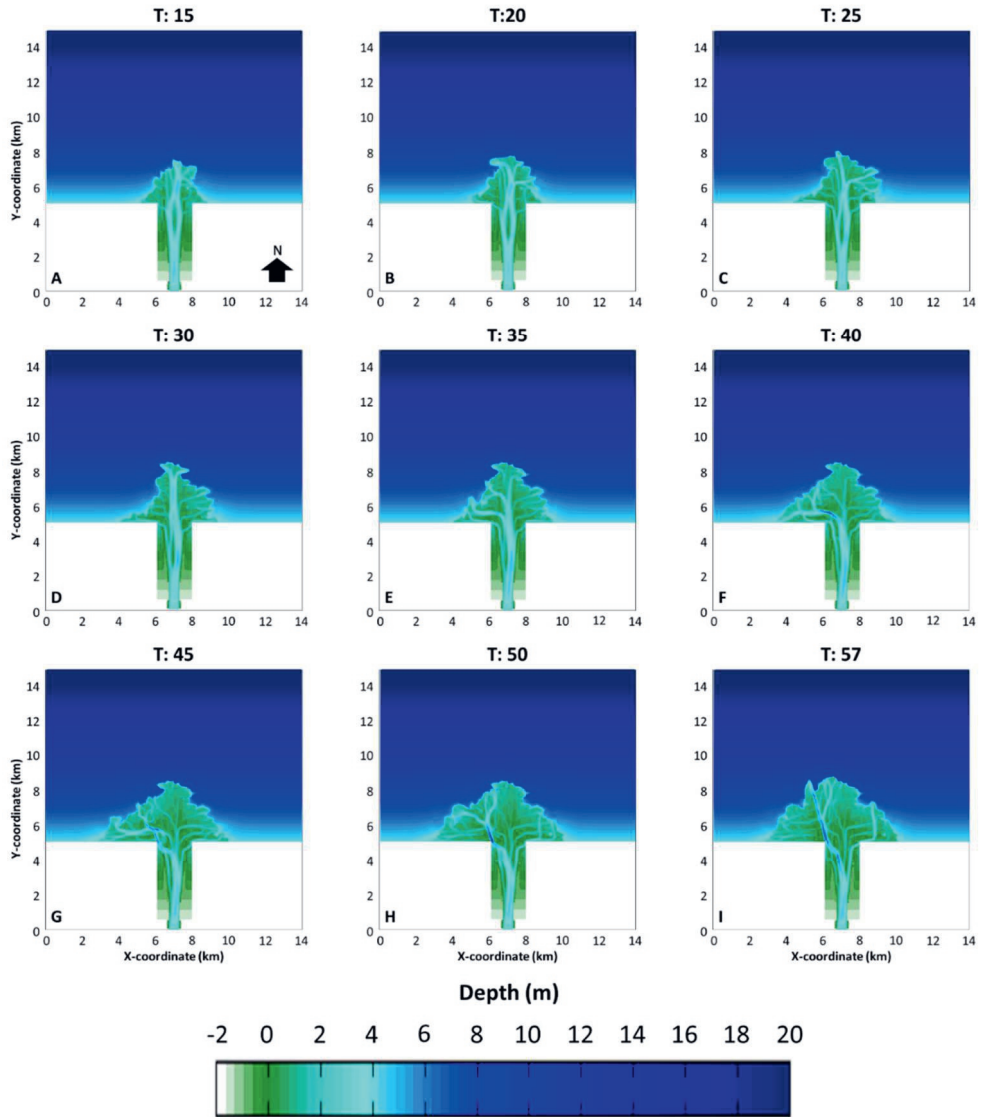


Figure A20. Plan-view bathymetry of a sand-rich delta with compaction scenario 0.5 mm y^{-1} for selected simulation output times (A - I).

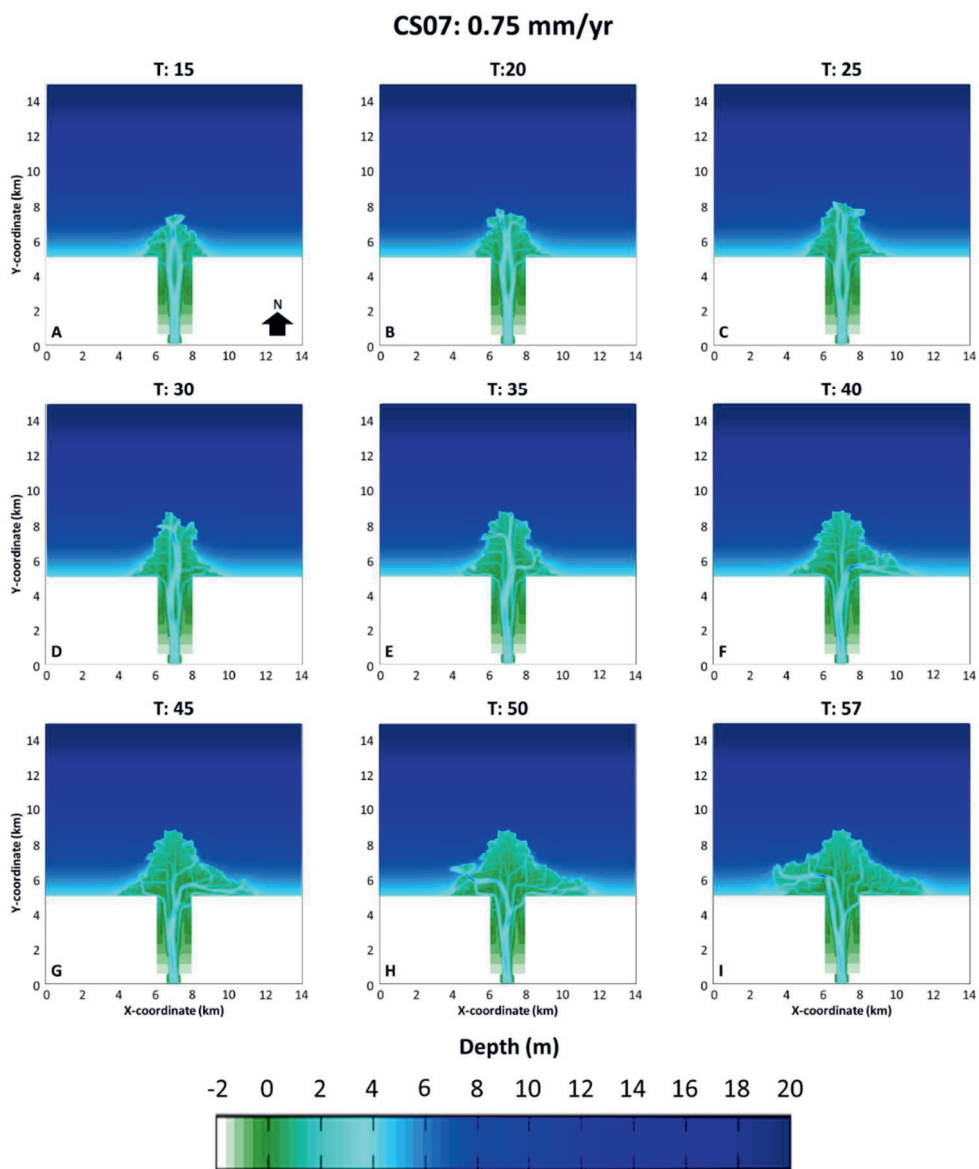


Figure A21. Plan-view bathymetry of a sand-rich delta with compaction scenario 0.75 mm y^{-1} for selected simulation output times (A - I).

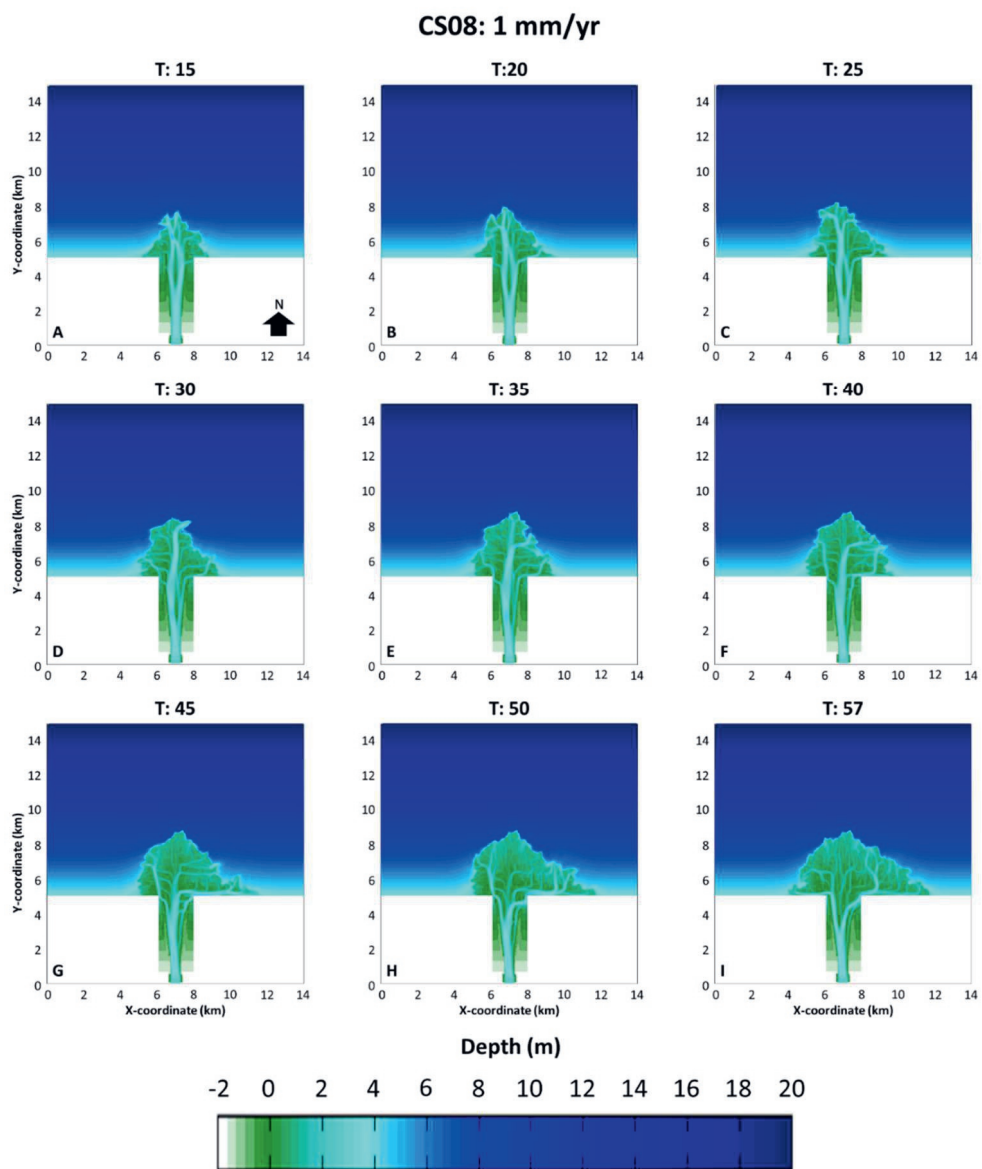


Figure A22. Plan-view bathymetry of a sand-rich delta with compaction scenario 1 mm y^{-1} for selected simulation output times (A - I).

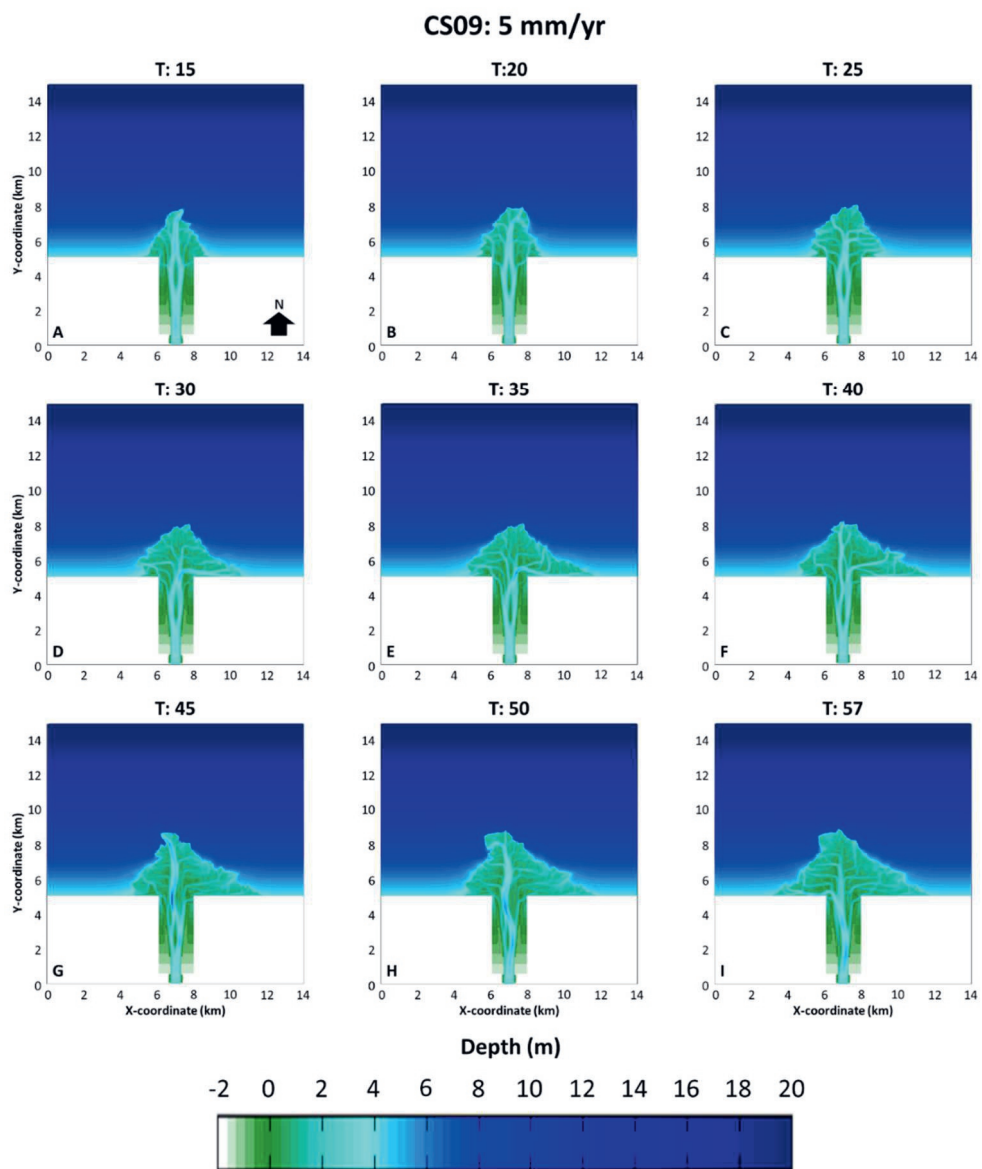


Figure A23. Plan-view bathymetry of a sand-rich delta with compaction scenario 5 mm y^{-1} for selected simulation output times (A - I).

CS10: 7.5 mm/yr

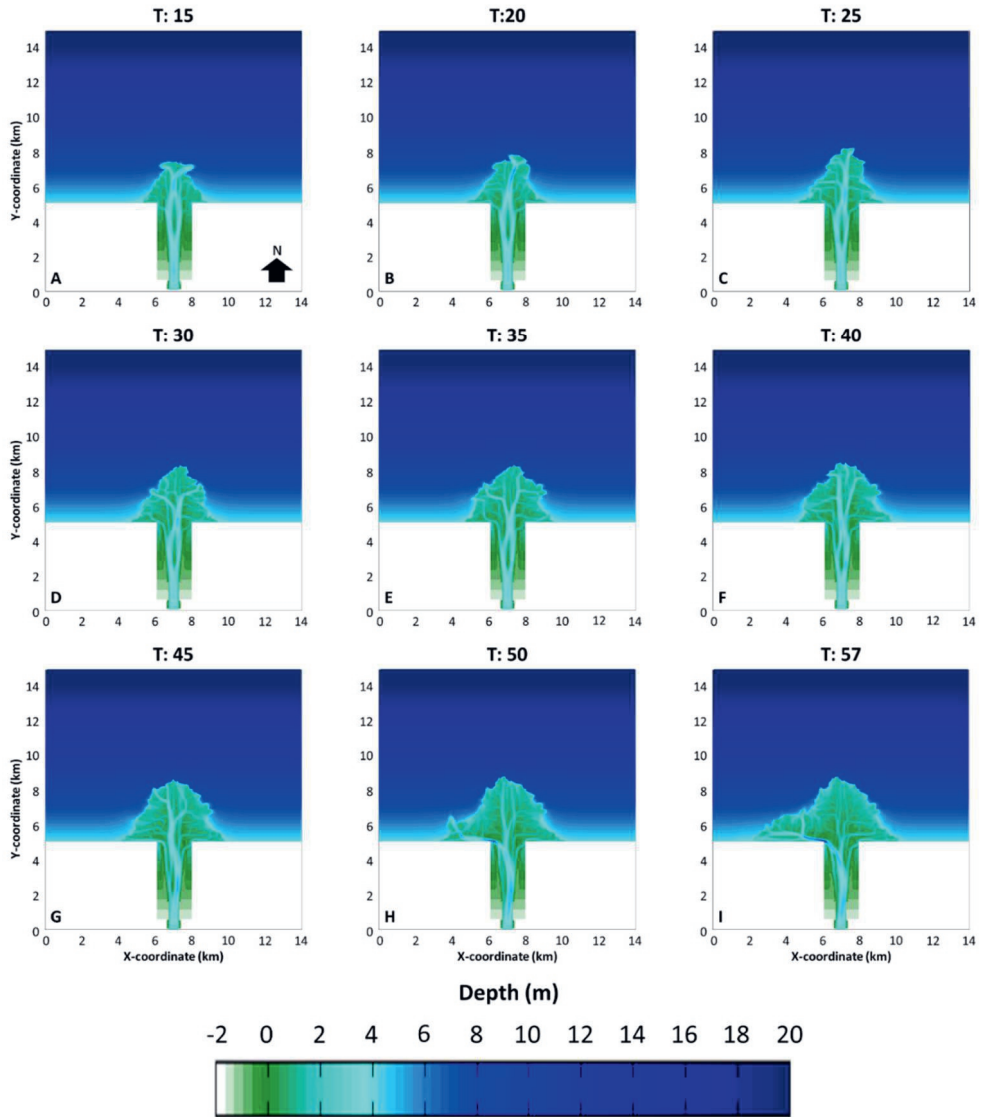


Figure A24. Plan-view bathymetry of a sand-rich delta with compaction scenario 7.5 mm yr^{-1} for selected simulation output times (A - I).

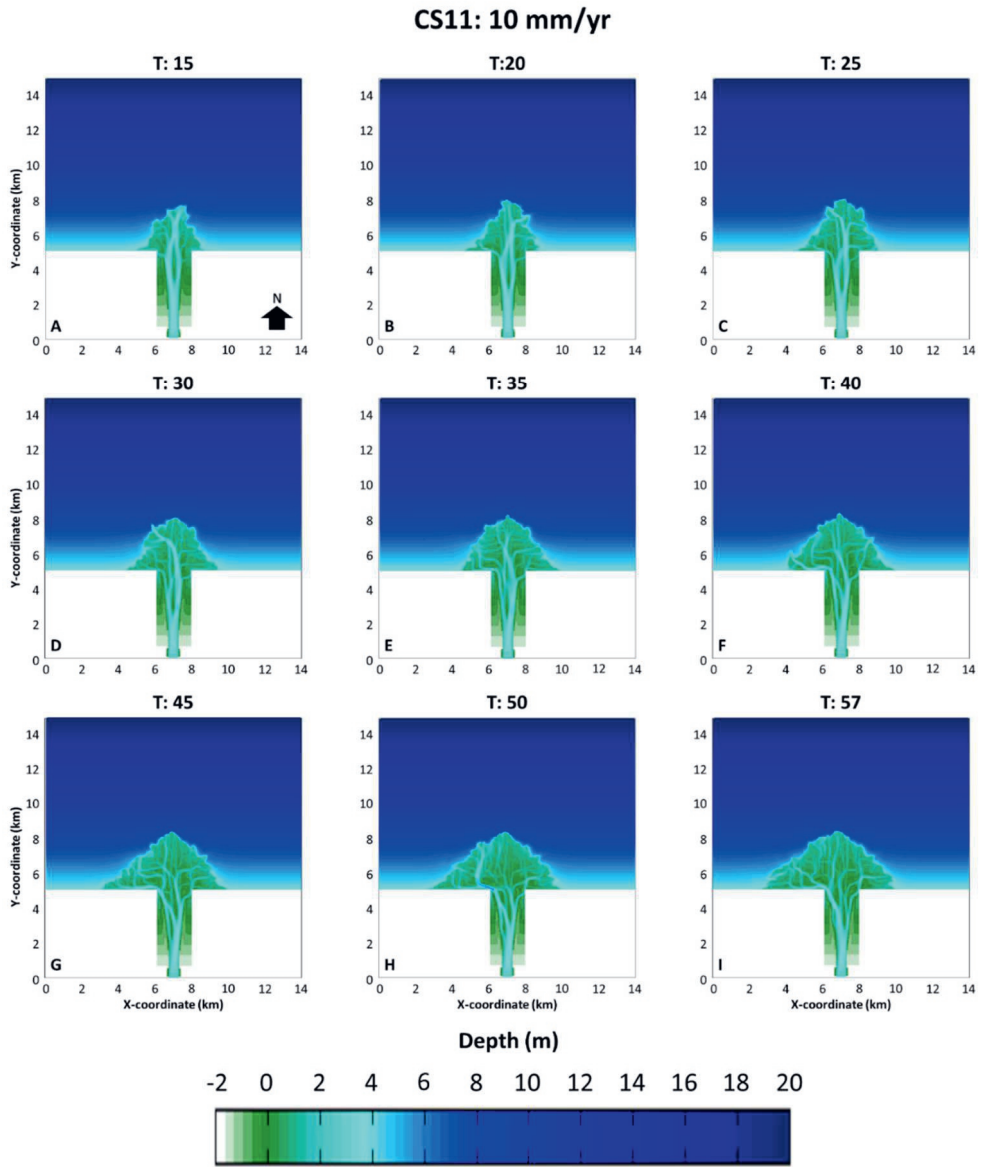


Figure A25. Plan-view bathymetry of a sand-rich delta with compaction scenario 10 mm y^{-1} for selected simulation output times (A - I).

Sand-rich Deltas

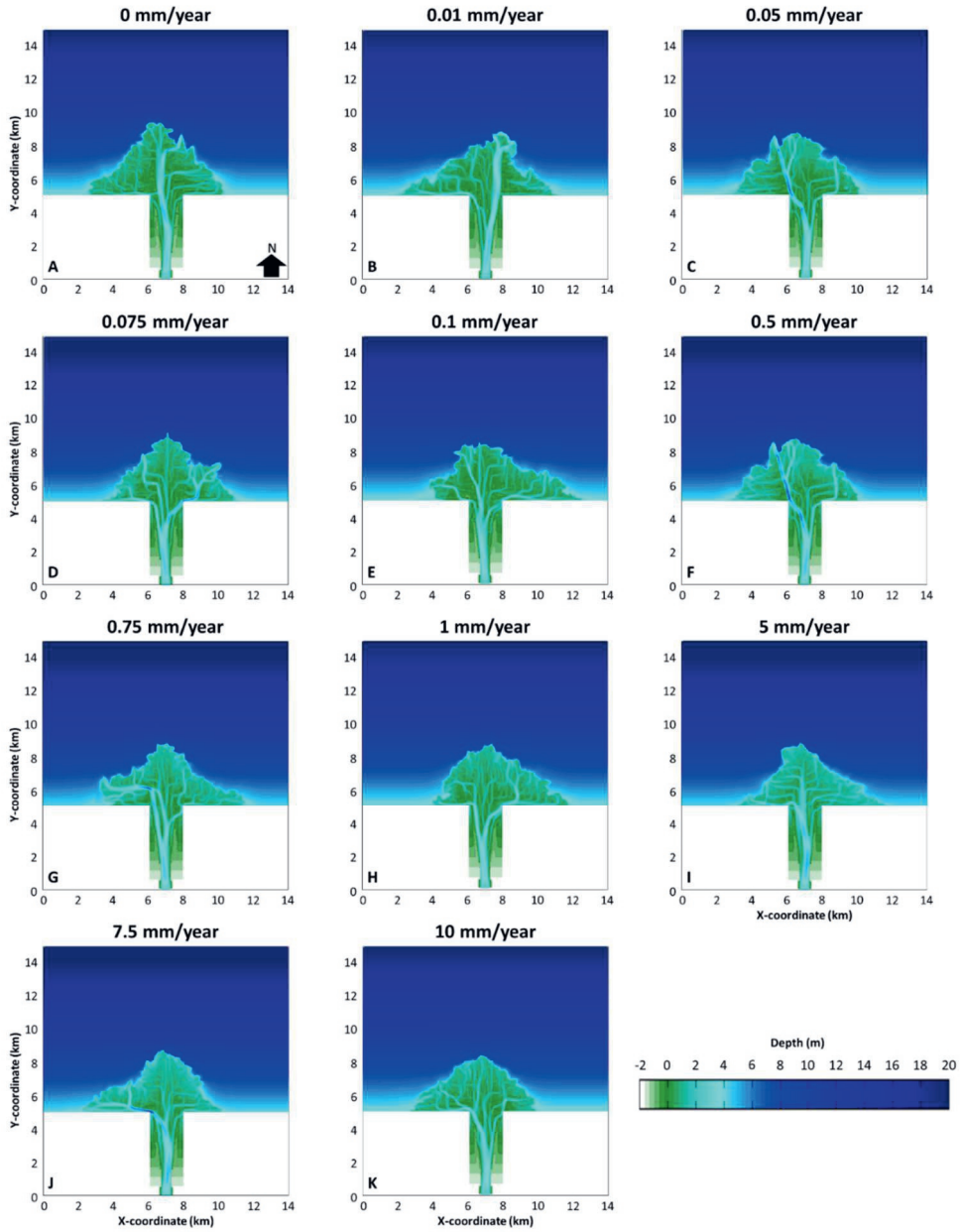


Figure A26. Plan-view bathymetry for all compaction scenarios ($0 - 10 \text{ mm y}^{-1}$) of sand-rich deltas at the end of the simulation (A - K).

A4. Identification of Simulated Deltas' Sub-environments

The delta sub-environments consist of delta top, delta front and pro delta identified based on elevation. The grid cells with an elevation higher than the brink point depth were classified as the delta top. The brink point depth indicates the depth at which the slope breaks from upstream to downstream of the delta (van der Vegt et al., 2016, 2020). The brink point depth of 1.9 m below sea level was identified through a sensitivity analysis.

The channel is an erosive feature in the delta top, which can have a bathymetry lower than the brink point elevation. An additional criterion was used to identify the channel based on a cutoff velocity, which was set to 0.65 and 0.85 m s⁻¹ for mud-rich and sand-rich deltas, respectively. Any grid cells with a velocity larger than the cutoff velocities were identified as the delta top

The delta front was located between the brink point depth and wave base, with at least 1% sand content in the sediment mixture. In this study, the wave base was set at 5 m below sea level. Lastly, the pro delta was characterised as an area below the wave base. Grid cells with a deposition below 15 mm were considered inactive. The computed sub-environments for mud-rich and sand-rich deltas at the last interval are shown in Figures A27 and A28.

Mud-rich deltas

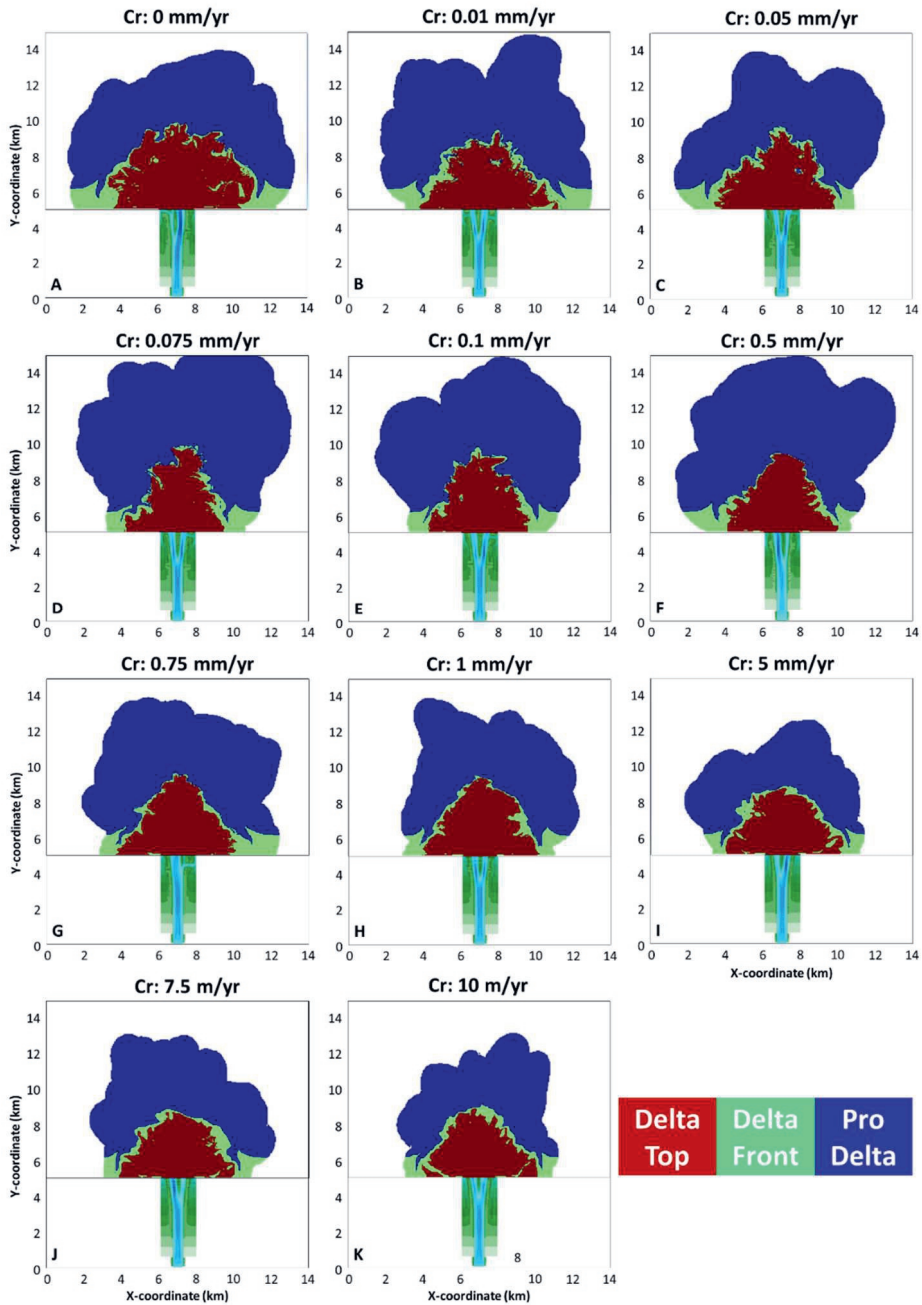


Figure A27. The computed delta sub-environments for mud-rich deltas at the end of the simulation (A - K). The red, green, and blue areas represent delta top, delta front, and pro delta, respectively. The compaction scenario ranges from 0 to 10 mm y⁻¹.

Sand-rich deltas

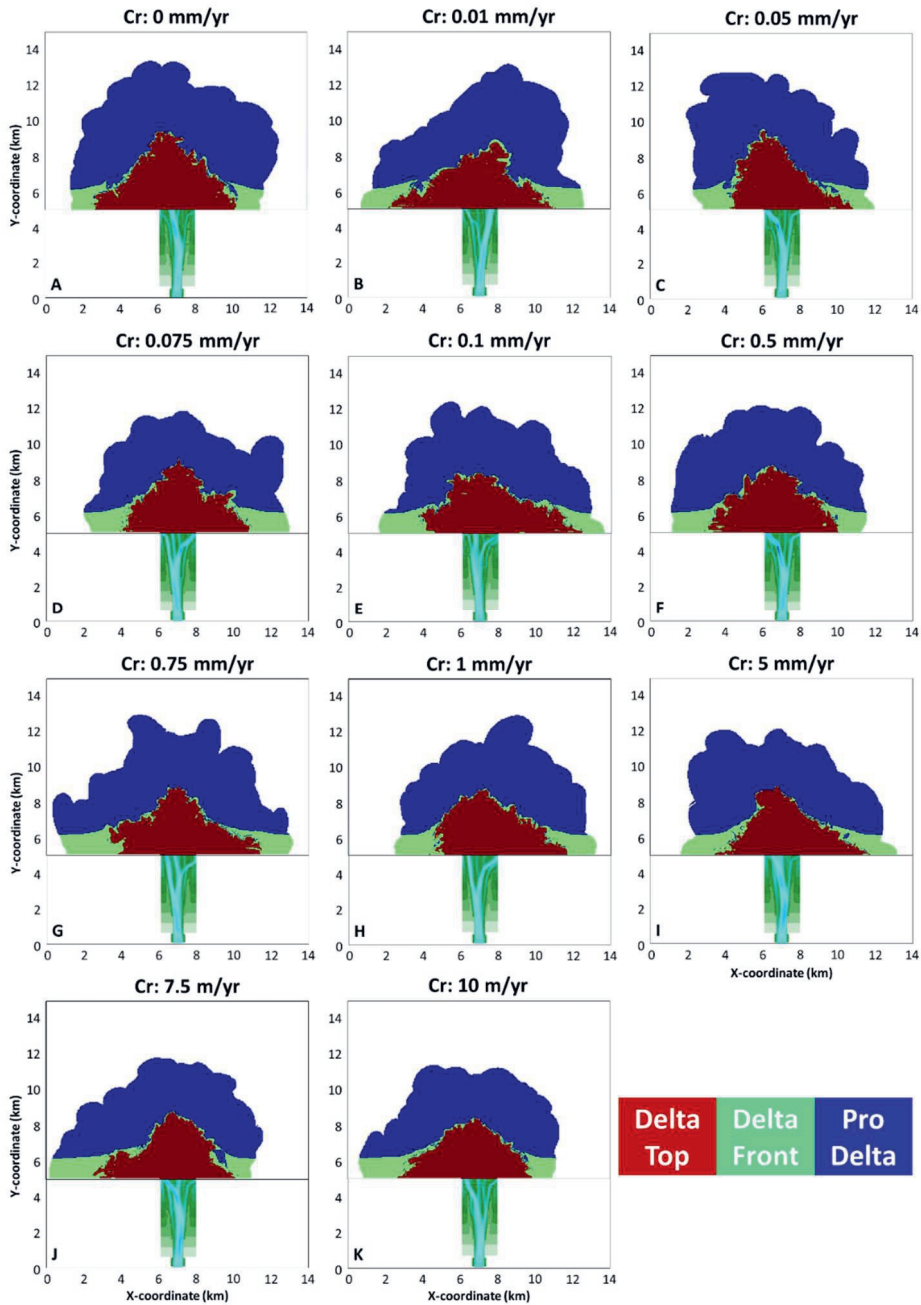


Figure A28. The computed delta sub-environments for sand-rich deltas at the end of the simulation (A - K). The red, green, and blue areas represent delta top, delta front, and pro delta, respectively. The compaction scenario ranges from 0 to 10 mm y^{-1} .

A5. Morphology Plots in Time Series

To improve the clarity of morphology trends, trendlines were calculated for morphology plots (area increase, rugosity, and aspect ratio) for each compaction scenario developed under compaction influence. The trendlines were used to estimate linear equations, which were then used to compute area increase, rugosity, and aspect ratio at the end of the simulation output time (Figure A29).

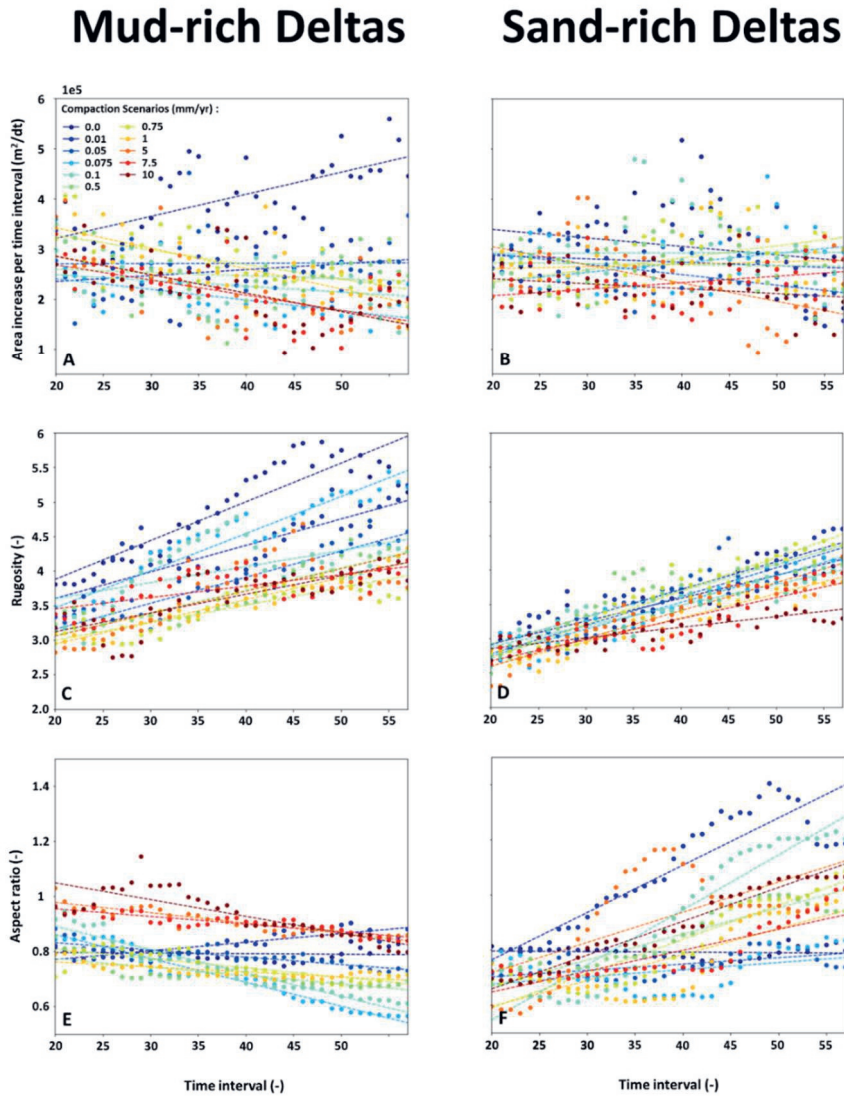


Figure A29. The plots indicate area increase, rugosity, and aspect ratio for mud- and sand-rich deltas with compaction scenarios ranging from 0 to 10 mm y⁻¹ (A - F). Trendlines are calculated for all compaction scenarios and used to estimate linear equations. The area increase, rugosity, and aspect ratio at the end of the simulation are then calculated using linear equations.

Supplementary Materials B

This sub-chapter describes supplementary materials for chapter 3, which includes the derivation of improved secondary compaction formula, implementation of compaction formulations into Delft3D 4 - FLOW, implementation of new erosion formula into Delft3D 4 - FLOW, ratio of sedimentation and erosion in simulated deltas, and compaction realization and compaction potential in simulated deltas (B1 – B5). In addition, bathymetry development of the simulated deltas, identification of depositional elements, fringe areas, and validation of depositional elements are explained (B6 – B9). Finally, sediment distribution plots and backwater effects will be described (B10 and B11).

B1. Derivation of Improved Secondary Compaction Formula

Mesri (2003) shows that the vertical strain of a sediment bed due to primary and secondary compaction can be computed as:

$$[\varepsilon_v]_t = [\varepsilon_v]_{t_p} + \frac{C_c}{1+e_0} \frac{C_\alpha}{C_c} \ln\left(\frac{t}{t_p}\right) \quad (\text{B1})$$

or equivalently

$$[\varepsilon_v]_t = [\varepsilon_v]_{t_p} + \frac{C_c}{1+e_0} \frac{C_\alpha}{C_c} \ln(t) - \frac{C_c}{1+e_0} \frac{C_\alpha}{C_c} \ln(t_p) \quad (\text{B2})$$

where $[\varepsilon_v]_t$ is the vertical strain during a simulation time (m), $[\varepsilon_v]_{t_p}$ represents the vertical strain when primary compaction occurs (m), C_c is the coefficient of primary compaction ($C_c = \Delta e / \Delta \sigma'_v$), C_α indicates the coefficient of secondary compaction ($C_\alpha = \Delta e / \Delta \ln t$), e_0 is the initial void ratio (-), t is a simulation time (minutes), t_p represents a simulation time at which the secondary compaction occurs (minutes), Δe indicates the change of void ratio (-), and $\Delta \sigma'_v$ is the change in vertical effective stress (Pa). The change in vertical strain due to secondary compaction can be calculated using Equation B3 below.

$$[\varepsilon_v]_t - [\varepsilon_v]_{t_p} = \frac{C_c}{1+e_0} \frac{C_\alpha}{C_c} (\ln(t + \Delta t - t_p) - \ln(t - t_p)) \quad (\text{B3})$$

where Δt is the simulation time step (minutes). The change in vertical strain on the left-hand side of Equation 10 can be rewritten as the change in void ratio, as shown by Equation B4.

$$\frac{e_{t+\Delta t} - e_t}{1+e_0} = \frac{C_c}{1+e_0} \frac{C_\alpha}{C_c} (\ln(t + \Delta t - t_p) - \ln(t - t_p)) \quad (\text{B4})$$

Removing $1 + e_0$ on both sides of Equation 11, cancelling the implicit reference e_0 . Cancelling C_c on the right-hand side gives:

$$\Delta e_{t+\Delta t} - \Delta e_t = C_\alpha (\ln(t + \Delta t - t_p) - \ln(t - t_p)) \quad (B5)$$

The change in the void ratio (Equation B5) can be converted into subsidence using this relationship $\Delta H = H\Delta e$, which gives:

$$\Delta H_{s,t} = C_s \cdot H_{t-1} \cdot (\log(t - t_p + \Delta t) - \log(t - t_p)) \quad (B6)$$

where $\Delta H_{s,t}$ is the subsidence due to secondary compaction during a simulation time (m), C_s represents the secondary compaction rate (mm y^{-1}), and H_{t-1} indicates the sediment thickness at the end of the previous simulation time (m)

Three different equations for secondary compaction are tested against synthetic data of a sediment bed consisting of clay with a thickness of 1 m: (1) Equation 2.5 from Chapter 2, (2) an exponent function, and (3) Equation B6. The simulation output time step is 1 day in hydrodynamic time, whereas the total simulation output time is 200 days in hydrodynamic time. MORFAC is assumed to be 1 and no bankful discharge is applied to the simulations. Therefore, the total simulation output time will be the same in morphodynamic and realistic time. The secondary compaction has a rate of 40 mm y^{-1} , which will reach equilibrium when bed thickness is 0.6 m. The simulation output time at which the primary compaction (t_p) occurs is 5 and 10 days in hydrodynamic time (Figure B1).

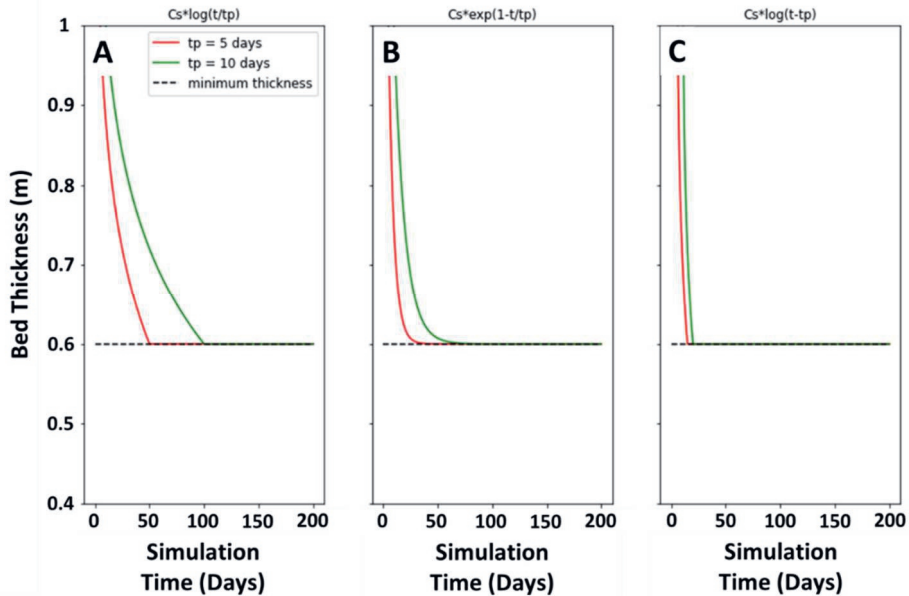


Figure B1. The thickness profile of a sediment bed is simulated using three secondary compaction formulas. (A) Equation 2.5 from Chapter 2, (B) secondary compaction formula using an exponent function, and (C) Equation 13 from this study. The initial thickness of the sediment bed is 1 m. The simulation output time is 200 days in hydrodynamic time. The secondary compaction rate used in all simulations is 40 mm y^{-1} .

The results show that Equation B6 yields a consistent subsidence trend for $t_p = 5$ days and 10 days (Figure B1C), whereas other Equations result in a different trend (Figures B1A and B1B). The subsidence trend for secondary compaction should be consistent regardless of when primary compaction occurs (Mesri, 2003). Therefore, we implement Equation B3 into the Delft3D 4 - FLOW code.

B2. Implementation of Compaction Formulations into Delft3D

The sediment bookkeeping in Delft3D is governed by the stratigraphy module, which schematizes the simulated sediment column into multilayers consisting of, from top to bottom, a transport layer, multiple underlayers, and a base layer (Ribberink, 1987). Compaction was implemented in the transport layer and underlayers, whereas the base layer, which indicates the initial sediment bed, was assumed compacted prior to delta progradation. A conceptual example of how the compaction algorithm operates in the stratigraphy module is shown in Figure B2. During deposition, the newly deposited sediment is assigned an initial porosity (Figure B2), calculated by weight-averaging the depositional porosity of sand and mud based on their proportion in the sediment (Equation B7). Then, the transport layer's porosity is updated due to deposition by weight-averaging the porosity of the transport layer at the end of the previous simulation time and the porosity of newly deposited sediment based on their thickness (Equation B8) (Figure B2).

$$\eta_{dep} = p_m \cdot \eta_{m,dep} + p_s \cdot \eta_{s,dep} \quad (B7)$$

$$\eta_{tl} = \frac{H_{tl,t-1} \cdot \eta_{tl,t-1} + H_{dep} \cdot \eta_{dep}}{H_{tl,t-1} + H_{dep}} \quad (B8)$$

where η_{dep} is the porosity of newly deposited sediment, p_m indicates the mud content in the newly deposited sediment, p_s represents the sand content in the newly deposited sediment, $\eta_{m,dep}$ expresses the depositional porosity of mud (user-defined), $\eta_{s,dep}$ is the depositional porosity of sand (user-defined), η_{tl} indicates the transport layer's porosity, $\eta_{tl,t-1}$ represents the transport layer's porosity at the end of the previous simulation time, H_{dep} is the deposited sediment's thickness (m), and $H_{tl,t-1}$ expresses the transport layer's thickness at the end of the previous simulation time (m).

It is assumed that the maximum thickness of the transport layer is 0.2 m. Consequently, the excess sediment in the transport layer due to deposition is stored in underlayers, starting from the lowermost empty/partially filled underlayer (Figure B2). In the partially filled underlayer, the porosity is updated by weight-averaging the porosity at the end of the previous simulation time with the transport layer's porosity (Equation B9). This sediment-storing procedure is repeated until all underlayers reach maximum thickness,

which is assumed to be 0.3 m. The sediment will be stored in the base layer if all underlayers are filled.

$$\eta_{ul} = \frac{H_{ul,t-1} \cdot \eta_{ul,t-1} + (H_{tl} - 0.2) \cdot \eta_{tl}}{H_{ul,t-1} + (H_{tl} - 0.2)} \quad (B9)$$

where, η_{ul} is the underlayer's porosity, $H_{ul,t-1}$ represents the underlayer's thickness at the end of the previous simulation time (m), $\eta_{ul,t-1}$ is the underlayer's porosity at the end of the previous simulation time, $(H_{tl} - 0.2)$ indicates the excess sediment thickness calculated by subtracting the transport layer's thickness (H_{tl}) after deposition with the maximum transport layer's thickness (0.2 m) (m), and η_{tl} expresses the excess sediment porosity, which equals the transport layer's porosity.

The primary compaction decreases the porosity of the transport layer and underlayers (η_{tl} and η_{ul}) due to total stress imposed by self-weight and overburden weight (Equations 3.1, 3.3, 3.4, and 3.5 (Figure B2)). During erosion, the deposited sediment in the transport layer is partially or entirely removed. The transport layer is then replenished to its original thickness (0.2 m) using the stored sediment from the uppermost fully/partially filled underlayers (Figure B2). If the underlayers are empty, the sediment from the base layer is used. This replenishing step does not change the porosity of the stratigraphic layers. However, erosion decreases the overburden weight experienced by the sediment. As a result, the primary compaction is deactivated, while the secondary compaction is active (Equations 3.2, 3.3, 3.4, and 3.5) (Figure B2). Compaction is in equilibrium once the porosity of sediment layers reaches a minimum value. The minimum porosity of fully compacted sediment can be calculated as the weight-averaged compacted porosity of sand and mud based on their proportion in the layers (Equation B10).

$$\eta_{min} = p_m \cdot \eta_{m,comp} + p_s \cdot \eta_{s,comp} \quad (B10)$$

where, η_{min} is the minimum porosity of the stratigraphic layer, p_m represents the mud content in the sediment layer, $\eta_{m,comp}$ is the compacted porosity of mud (user-defined), p_s indicates the sand content in the sediment layer, and $\eta_{s,comp}$ is the compacted porosity of sand (user-defined). The porosity calculation presented in this chapter is an update from the previous one to incorporate various sediment compositions in the sediment layers.

Notably, the porosity calculation assumed a homogeneous mixing of grain sizes in sediment layers, which differs from natural systems as finer mud grains tend to fill the space between coarser sand grains (Revil et al., 2002). Improving the porosity calculation to account for sand and mud interaction is an exciting topic for future study.

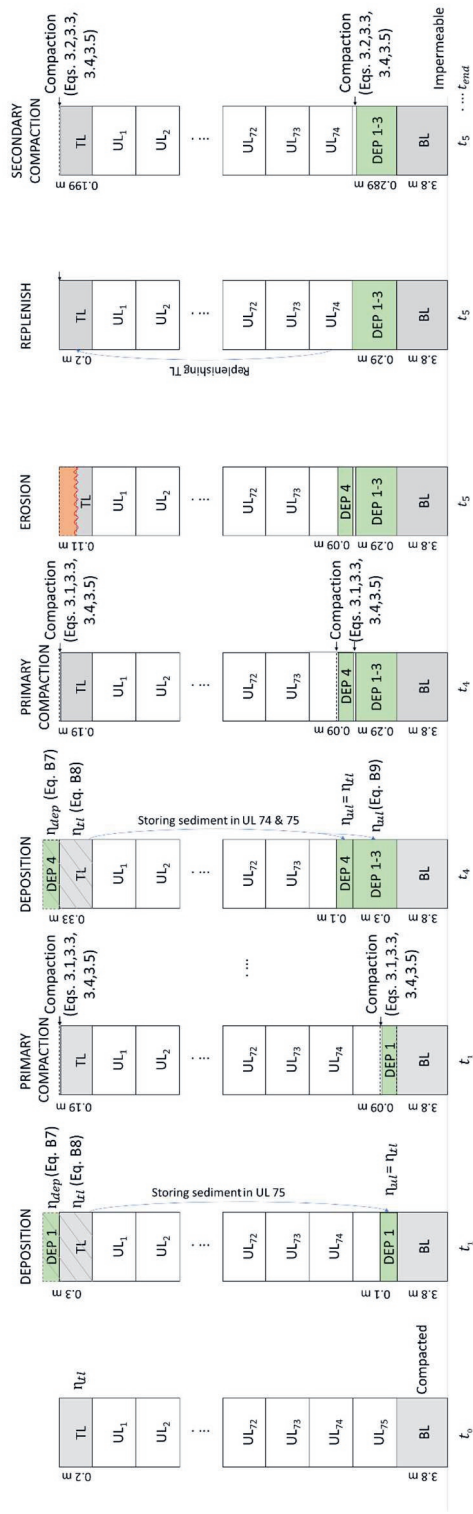


Figure B2. The schematic drawing of a model stratigraphy in Delft3D, consisting of a top layer, 75 underlayers, and a base layer. The white boxes indicate empty spaces, which will be filled or stay empty depending on deposition and erosion trends. Compaction is in equilibrium at t_0 . Deposition occurs from t_1 to t_4 , during which the top layer porosity (η_{TL}) is updated to account for the newly deposited sediment. As the top layer is assumed to have a constant thickness, the excess sediment in the top layer is stored in the underlayers, starting from the lowermost underlayer (UL_{75}). The primary compaction occurs immediately in the transport layer (TL) and underlayers (UL_{74} and UL_{75}) due to load imposed by self-weight and/or overlying weight. The erosion occurs at t_5 , removing sediments from the uppermost filled underlayer (UL_{74}). Consequently, the secondary compaction occurs in the transport layer and underlayer (UL_{75}) because the load imposed by self-weight and overlying weight is smaller than experienced by these layers at the end of the previous simulation time.

B3. Implementation of New Erosion Formula into Delft3D

Sediment erosion in Delft3D is governed by the Partheniades-Krone formula (Partheniades, 1965), shown by Equation B11.

$$E = M_e \left(\frac{\tau_b}{\tau_{ce}} - 1 \right) \quad (\text{B11})$$

where E is erosion rate ($\text{kg m}^{-2} \text{s}^{-1}$), M_e represents the maximum allowed erosion rate (s m^{-1}), τ_b is bottom shear stress induced by hydrodynamic flow (e.g., current, wave, and tide) ($\text{kg m}^{-1} \text{s}^{-2}$), and τ_{ce} expresses critical bed shear stress for erosion ($\text{kg m}^{-1} \text{s}^{-2}$). τ_{ce} indicates sediment resistance against resuspension, influenced by mud content in sediment mixtures.

Equation B11 often causes numerical instability during the simulation if the sediment contains no/very low mud content, leading to a zero/very small value of critical bed shear stress for erosion (τ_{ce}), which acts as a denominator. This results in an unrealistic erosion rate. Therefore, Equation B11 was updated by multiplying it with the parameter τ_{ce} , resulting in a linear relationship between erosion rate and critical bed shear stress for erosion (Equation B12).

$$E = M_e (\tau_b - \tau_{ce}) \quad (\text{B12})$$

Modelling scenarios represent mud-rich deltas (85% mud and 15% sand) with 0, 0.01, 0.1, 1, and 10 mm y^{-1} compaction rates, simulated using Equations B11 and B12. The simulation results were post-processed to derive the delta top area, consisting of distributary channel DE and delta plain DE. We excluded the underfilled channel DE, which has a limited contribution to the total deposited sediment in the simulated deltas, which was assumed to be overprinted by noise (see also Text B9). The results show a decreasing delta top area as the compaction rate increases in simulations run using Equations B11 and B19 (Figure B3). The comparable trend indicates that the updated erosion formula does not affect the modelling results, which is used in this study.

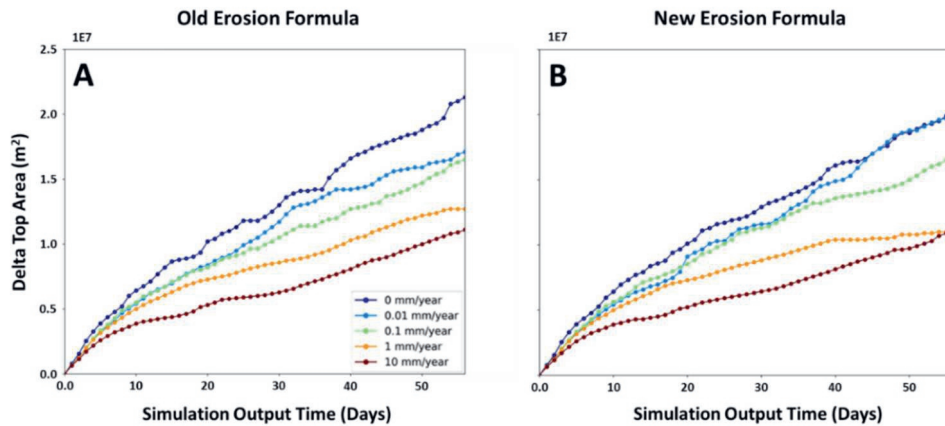


Figure B3. The line plots show the delta top area over the simulation output time for compaction rate scenarios developed using old and new erosion formulas (Equations B11 and B12 in Text B3) (A and B). The modelling scenarios represented mud-rich deltas with compaction rate scenarios of 0, 0.01, 0.1, 1, and 10 mm y^{-1} , indicated by different colored lines.

B4. Ratio of Sedimentation and Erosion in Simulated Deltas

The simulated deltas are produced by supplying bankfull water and sediment discharge to the basin through a fluvial feeder. As a result, the deltas are actively aggrading over the simulation output time, as shown by the ratio of cumulative sedimentation to erosion (by mass) in simulated deltas (Figure B4). The sedimentation and erosion are defined as a temporal difference of the total mass in the model stratigraphy between two successive time steps. A positive difference indicates net sedimentation. Otherwise, net erosion. The results show that the ratio values are positive over the simulation output time, which can reach a value of fifty (Figure B4). This means the sedimentation (by mass) is more dominant than erosion in simulated deltas.

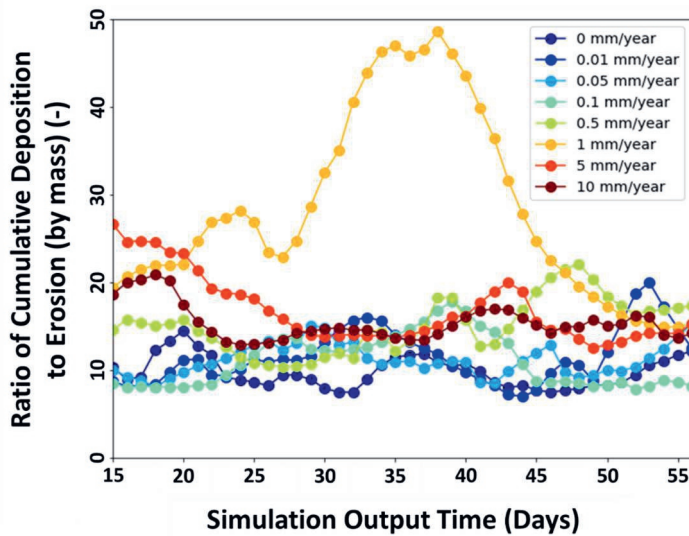


Figure B4. The output time series of the ratio of cumulative deposition to erosion (by mass) in simulated deltas for compaction rate scenarios ranging from 0 to 10 mm γ^{-1} . The total simulation output time is 57 days in hydrodynamic time.

B5. Compaction Realization Vs Compaction Potential in Simulated Deltas

Compaction rate scenarios are defined by varying the primary compaction rate of mud (C_p in Equation 3.1), which is considered compaction potential in the model. However, compaction realization can vary locally depending on local net sedimentation and erosion. The compaction realization is obtained from Delft3D output, which is the result of thickness reduction due to primary and secondary compaction ($\Delta H_{p,t}$ and $\Delta H_{s,t}$ in Equations 3.1 and 3.2). The ratio of compaction realization and potential is calculated for each simulation output time step, shown in Figure B5.

The results show that (1) compaction realization is smaller than compaction potential in all compaction rate scenarios, indicated by the ratio values of less than 1 (Figure B5). (2) The increasing compaction rate scenario leads to higher compaction realization in a relatively small number of grid cells. However, they seem to drive the change in sedimentation trend in simulated deltas. This is indicated by the increasing third quartiles (75th percentiles) and maximum range of ratio values as the compaction rate scenario increases to 1 mm γ^{-1} and decreases for higher compaction rate scenarios (Figure B5). This trend is similar to the distribution of sedimentation trend (Figures 3.4 and 3.5).

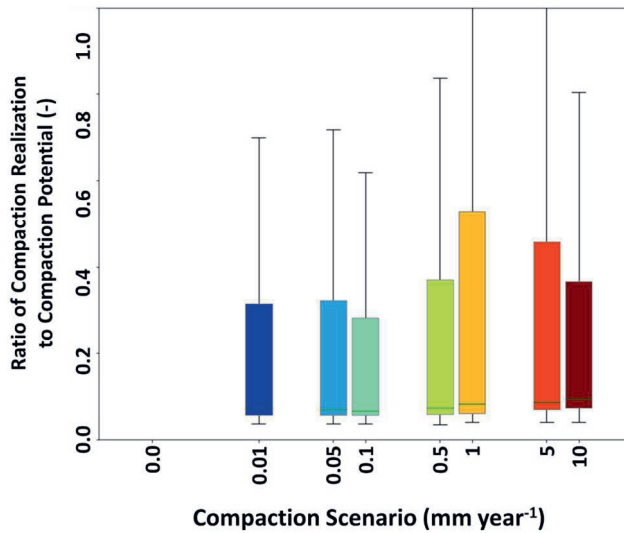


Figure B5. The collapsed output time series of the ratio of compaction realization to compaction potential for all grid cells in compaction scenarios 0 – 10 mm y^{-1} (colored boxes). Each box plot shows a median value (second quartile, horizontal green lines) between the first and third quartiles (interquartile range, grey boxes). The vertical black lines indicate the maximum and minimum range of data. The x-axis of the box plot is on a log scale.

B6. Bathymetry Development of the Simulated Deltas

The plan-view bathymetry development of simulated deltas for selected simulation output times shows a clear channelized and non-channelized area (Figures B6 – B13). Compaction rate scenario 0 mm y^{-1} has a relatively stable distributary channel, prograding in the central segment of the delta through a series of bifurcations (Figure B6). The increasing compaction rate to 10 mm y^{-1} results in more frequent channel relocation, shifting the main flow toward the lateral segment of the delta (Figures B7 – B13). The plan-view bathymetry for all compaction rate scenarios at the last simulation output time is shown in Figure B14.

MS01: 0.0 mm/year

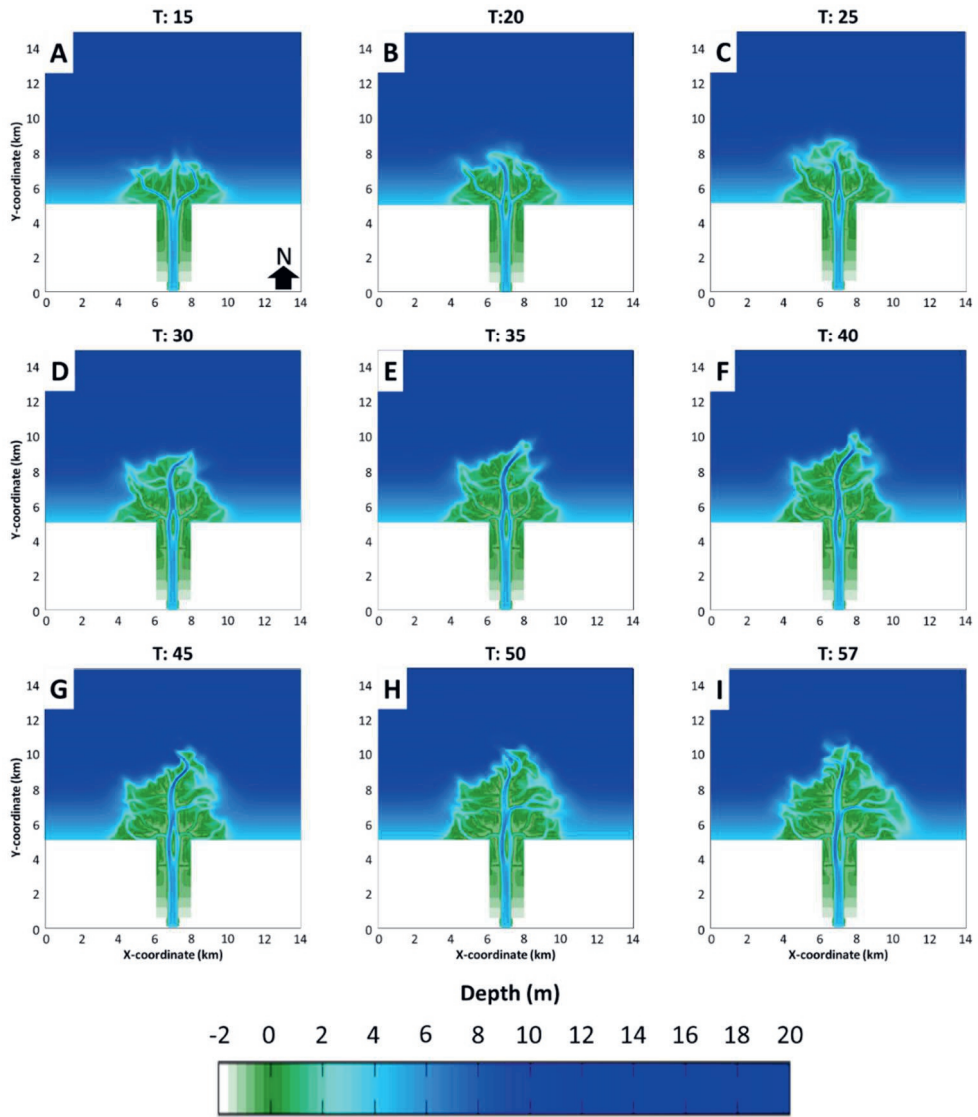


Figure B6. Plan-view bathymetry of compaction rate scenario 0 mm y⁻¹ for selected simulation output times (days) in hydrodynamic time (A – I).

MS02: 0.01 mm/year

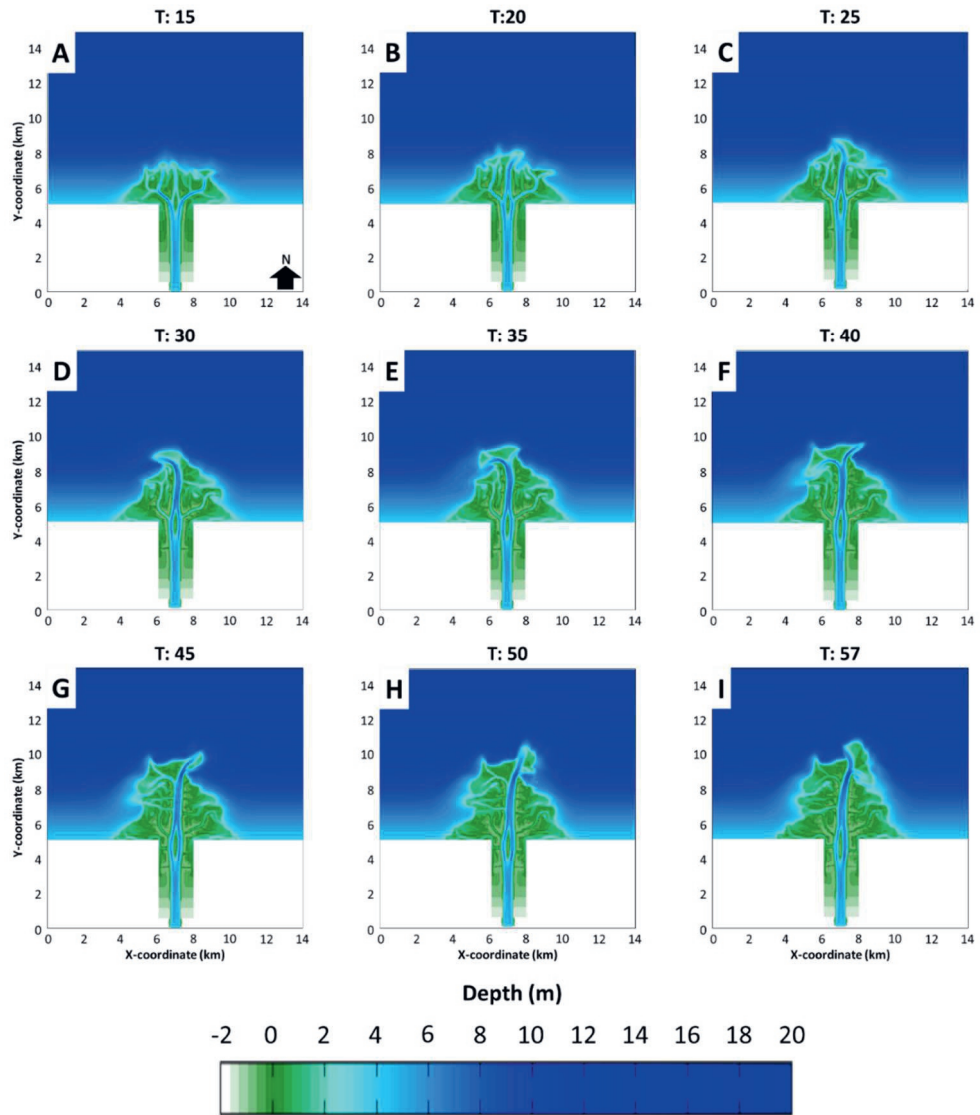


Figure B7. Plan-view bathymetry of compaction rate scenario 0.01 mm y^{-1} for selected simulation output times (days) in hydrodynamic time (A – I).

MS03: 0.05 mm/year

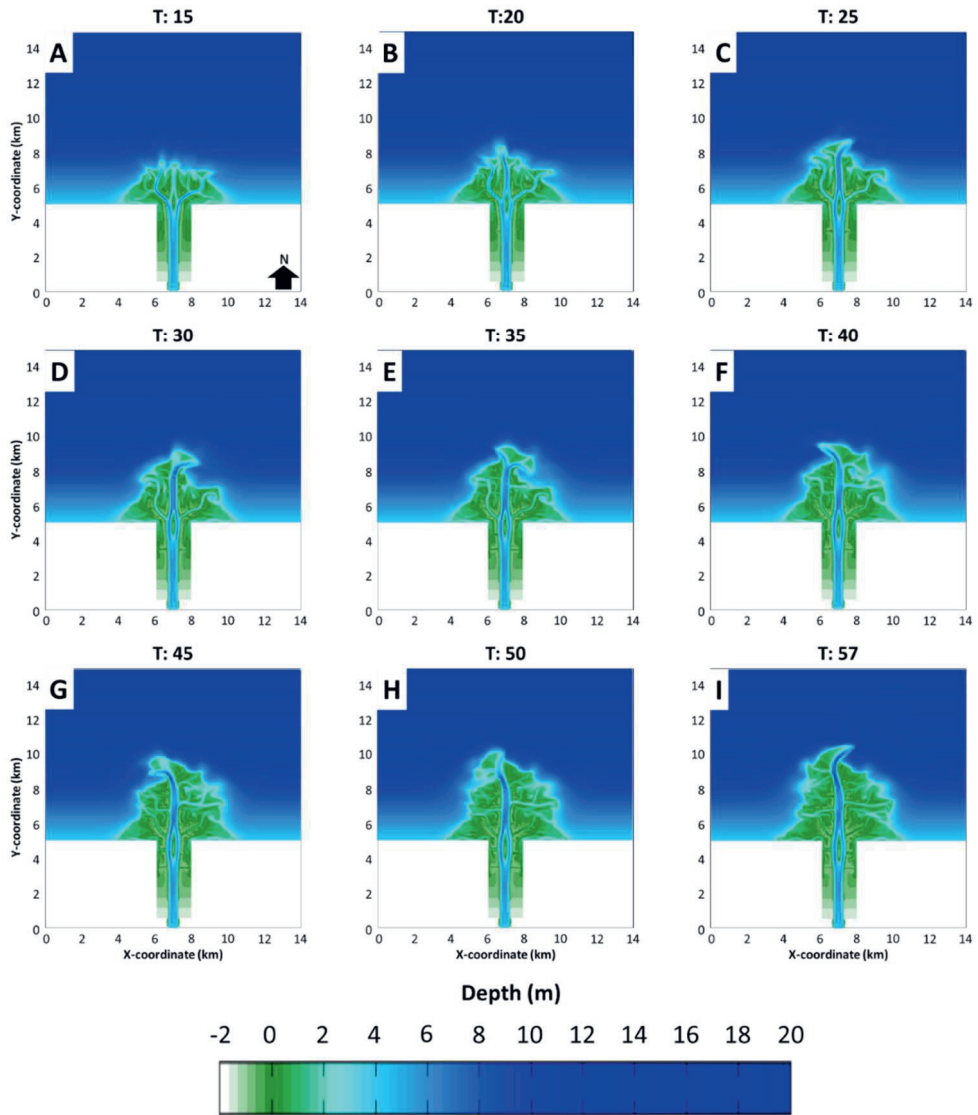


Figure B8. Plan-view bathymetry of compaction rate scenario 0.05 mm y^{-1} for selected simulation output times (days) in hydrodynamic time (A – I).

MS04: 0.1 mm/year

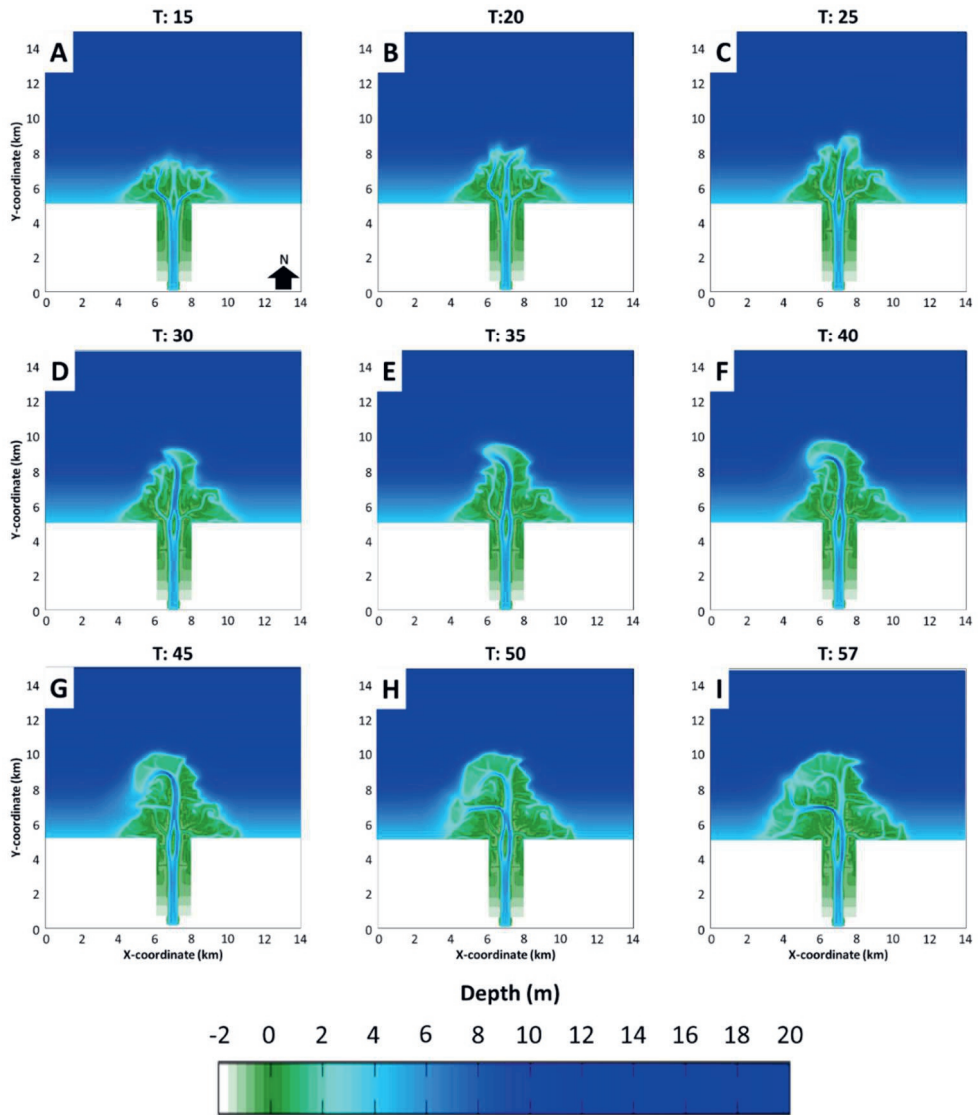


Figure B9. Plan-view bathymetry of compaction rate scenario 0.1 mm y^{-1} for selected simulation output times (days) in hydrodynamic time (A – I).

MS05: 0.5 mm/year

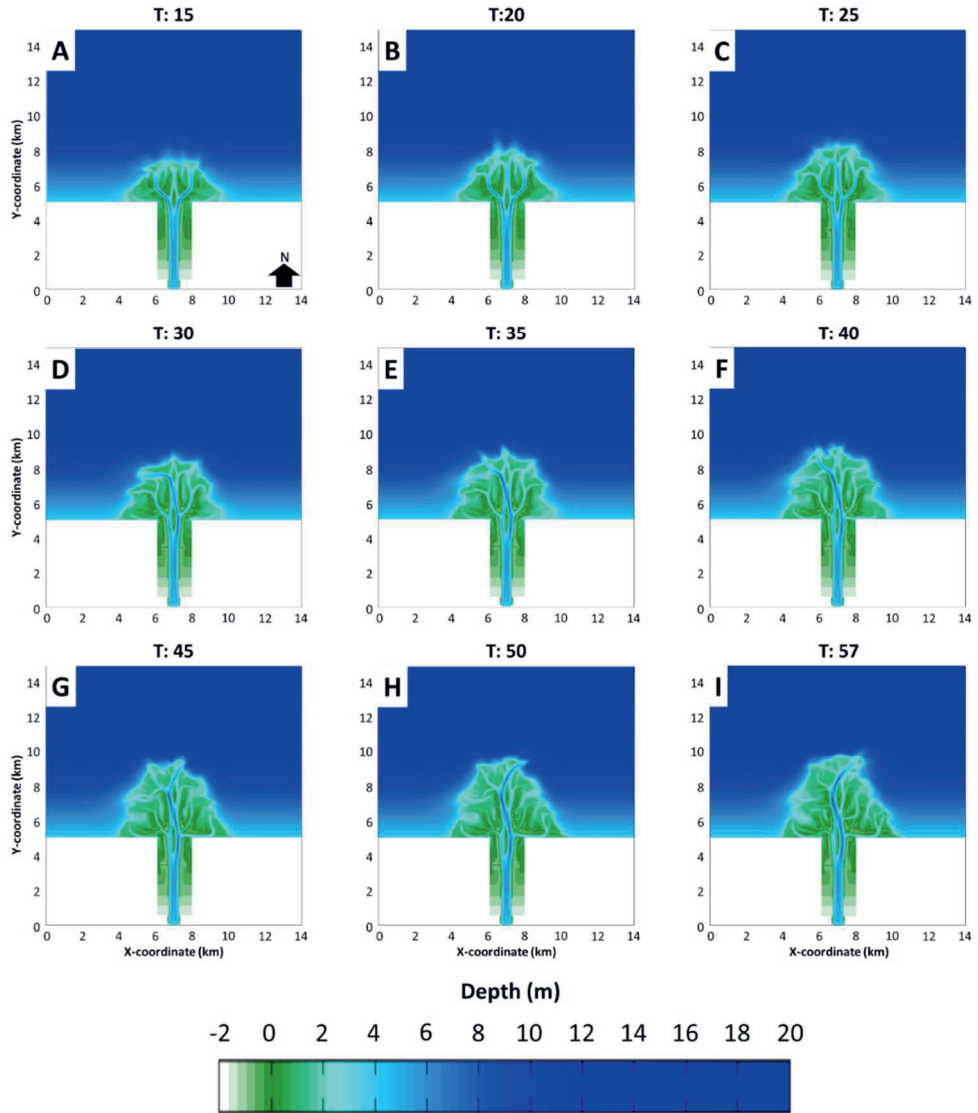


Figure B10. Plan-view bathymetry of compaction rate scenario 0.5 mm y^{-1} for selected simulation output times (days), which are in hydrodynamic time (A – I).

MS06: 1 mm/year

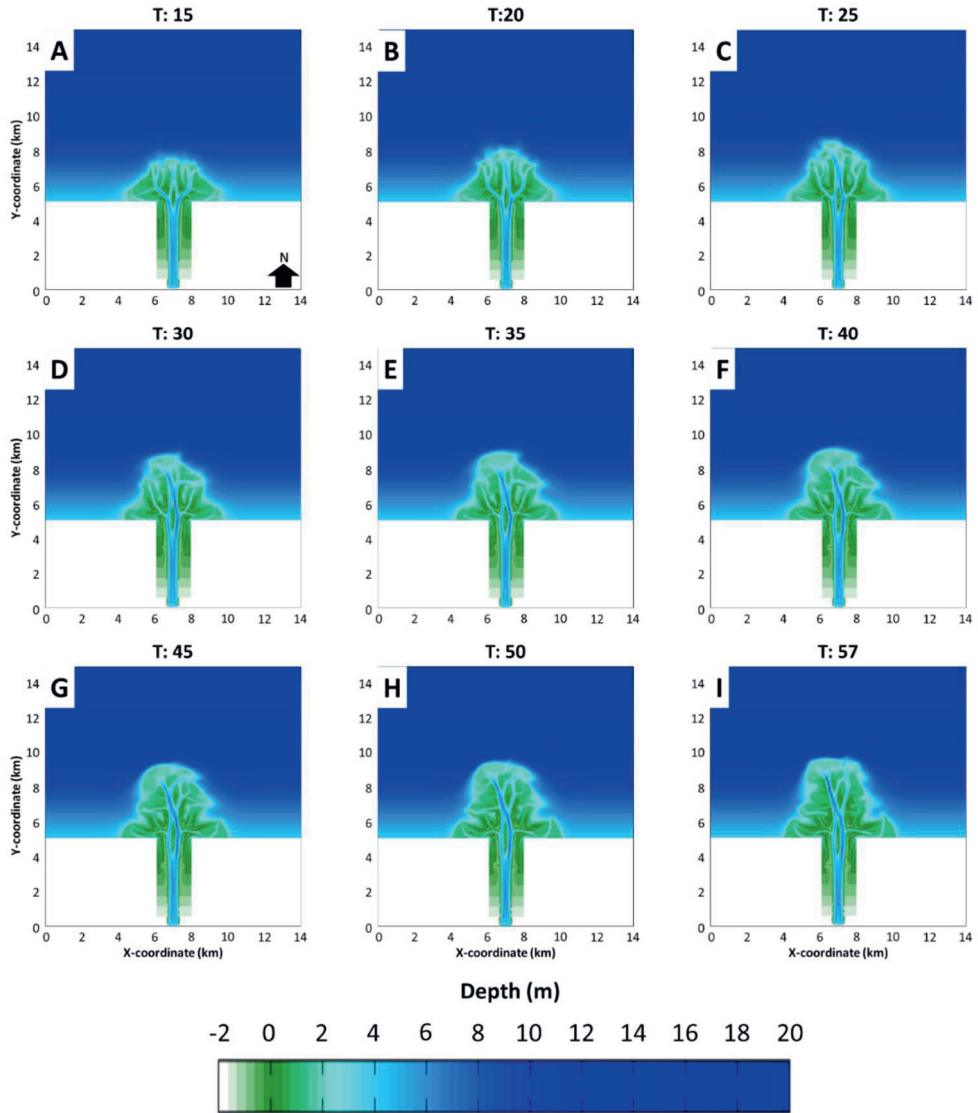


Figure B11. Plan-view bathymetry of compaction rate scenario 1 mm y^{-1} for selected simulation output times (days) in hydrodynamic time (A – I).

MS7: 5 mm/year

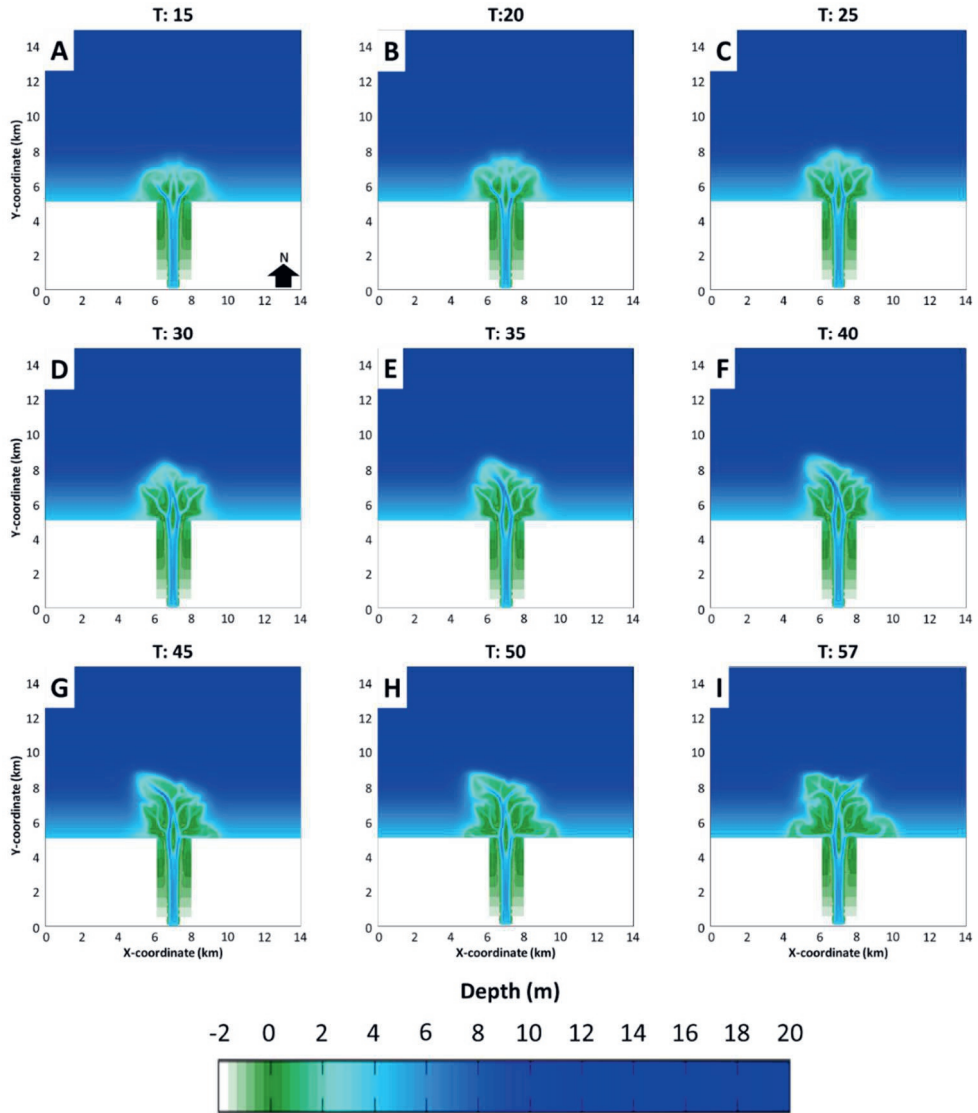


Figure B12. Plan-view bathymetry of compaction rate scenario 5 mm y^{-1} for selected simulation output times (days) in hydrodynamic time (A – I).

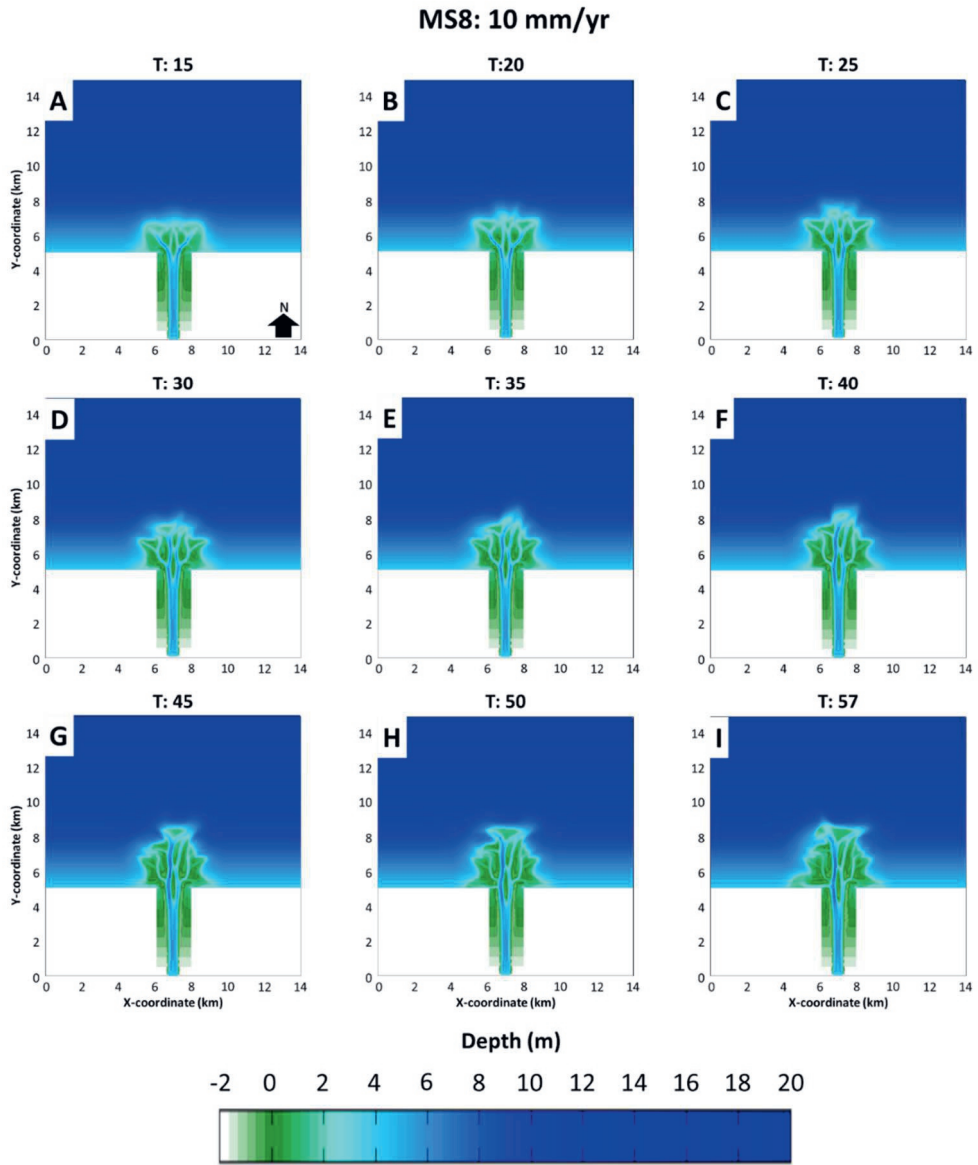


Figure B13. Plan-view bathymetry of compaction rate scenario 10 mm y^{-1} for selected simulation output times (days), which are in hydrodynamic time (A – I).

Mud-rich deltas

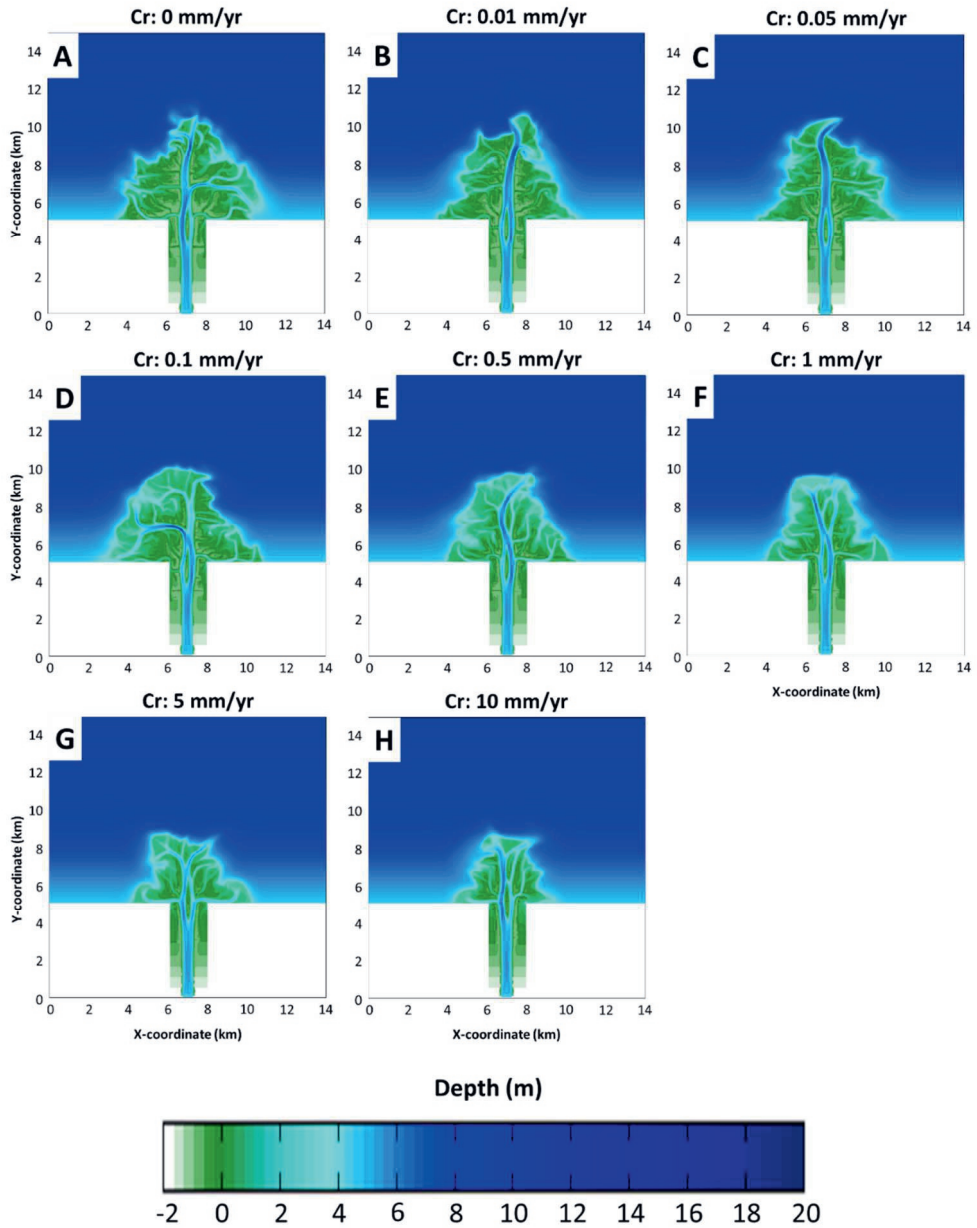


Figure B14. The plan-view bathymetry of all compaction rate scenarios ($0 - 10 \text{ mm yr}^{-1}$) at the end of the simulation output time (A – H).

B7. Identification of Depositional Elements

The plan-view area of simulated deltas is classified into depositional elements consisting of distributary channel DE, underfilled channel DE, delta plain DE, mouth bar DE, delta front DE, and pro delta DE. Depositional elements are calculated in two steps (Figure B15). First, we identify the brink point depth, which marks the transition between the updip and downdip of the delta (van der Vegt et al., 2016, 2020). The brink point was defined at a water depth of 1.9 m based on sensitivity tests using tidal range values (see also Text A4). The area deeper than the brink point depth can be part of the mouth bar DE, delta front DE, and pro delta DE. Otherwise, it is included as part of the distributary channel DE, underfilled channel DE, and delta plain DE. The pro delta DE is below the wave base (7 m). The delta front DE is between the wave base and brink point depth. In addition, the delta front deposits have at least 1% of sand content. The mouth bar DE is located in the delta front DE, characterized by a rapid deposition ($> 800 \text{ kg}$) in front of the distributary channel mouth in a single simulation output time step.

Above the brink point depth is the delta top DE, which contains distributary channel DE, underfilled channel DE, and delta plain DE. In addition, the delta front DE that is part of the delta top DE at the end of the previous simulation output time step and located adjacent to the delta top DE was assigned as the delta top DE. The distributary channel DE is a dynamic feature identified using a cutoff flow velocity of 0.65 m s^{-1} . The underfilled channel DE is a previously distributary channel that becomes underfilled as the flow direction changes. The delta plain DE is an area other than the distributary channel DE and underfilled channel DE. However, estimating the distributary channel DE using a single velocity cutoff causes a problem. If the cutoff value is too small, the distributary channel DE includes the proximal mouth bar DE and delta plain DE. Otherwise, the distal distributary channel network cannot be resolved. Therefore, in the second step, the identification of depositional elements is optimized to overcome this issue using the fringe area concept (Figure B15) (Text B8). The optimized depositional elements for all simulated deltas for selected and at the end of the simulation output time are shown in Figures B16 – B24.

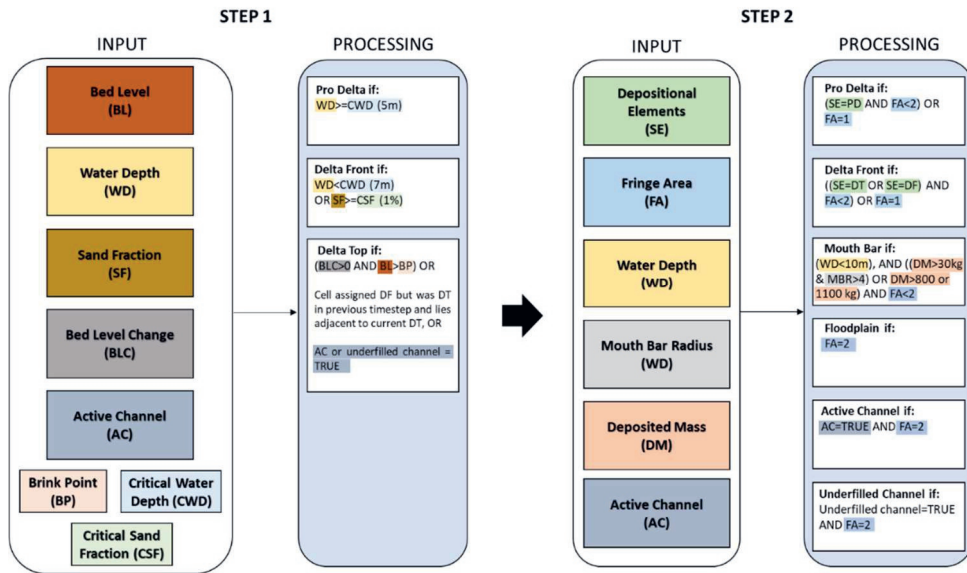


Figure B15. The algorithm computes depositional elements (DE) consisting of distributary channel DE, underfilled channel DE, delta plain DE, mouth bar DE, delta front DE, and pro delta DE. The depositional elements are calculated in two steps. First, the simulated delta regions are classified based on the brink point water depth, which is further optimized using the fringe areas concept.

MS01: 0.0 mm/year

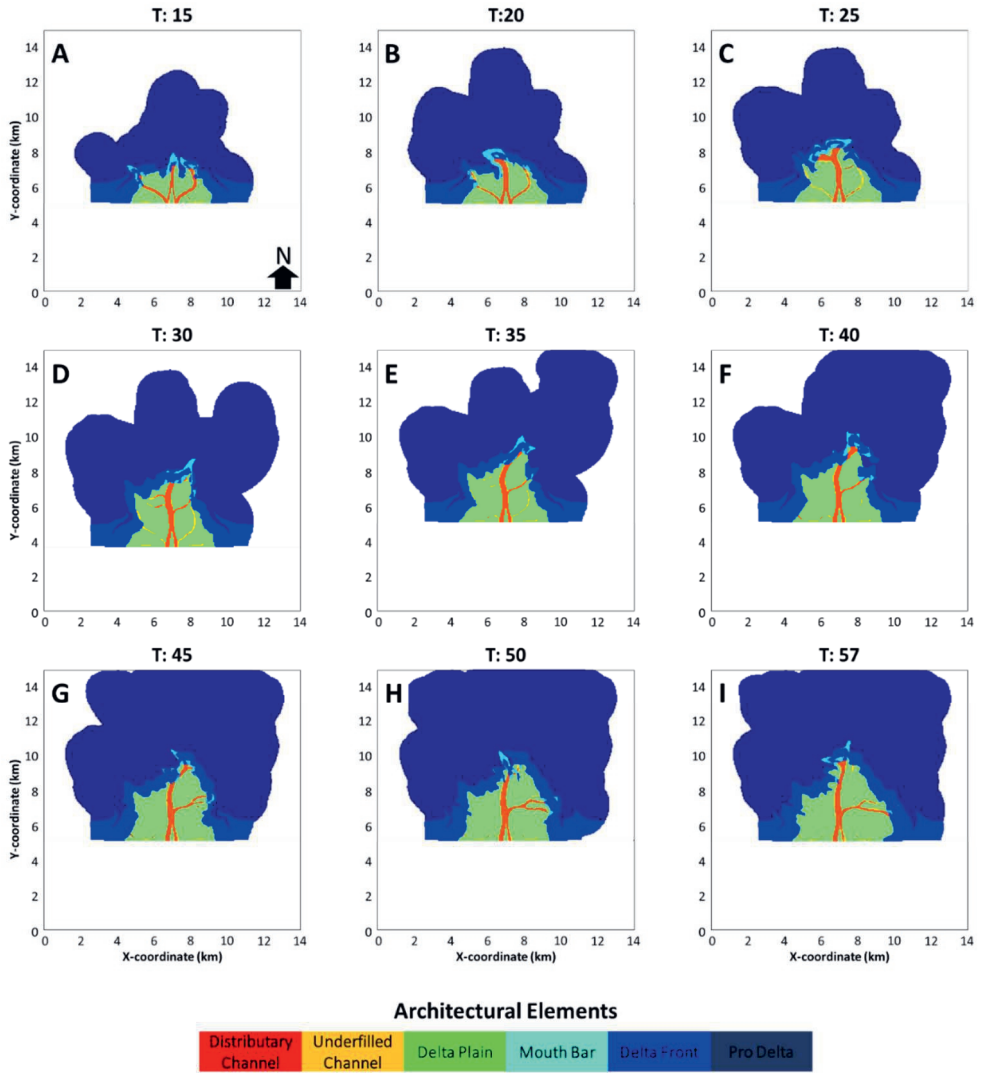


Figure B16. The interpreted depositional elements for compaction rate scenario 0.0 mm y^{-1} at selected simulation output times (days) in hydrodynamic time (A – I).

MS02: 0.01 mm/year

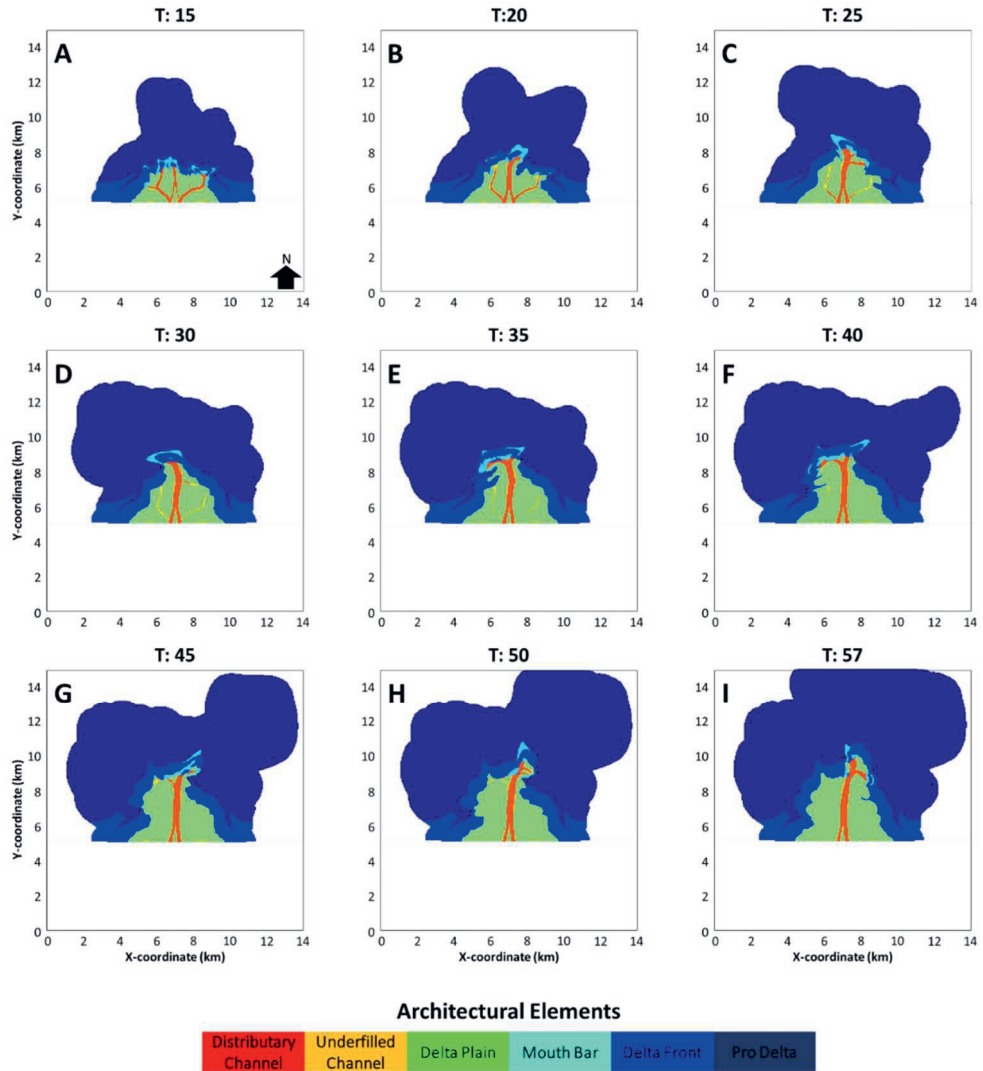


Figure S17. The interpreted depositional elements for compaction rate scenario 0.01 mm y^{-1} at selected simulation output time (days) in hydrodynamic time (A – I).

MS03: 0.05 mm/year

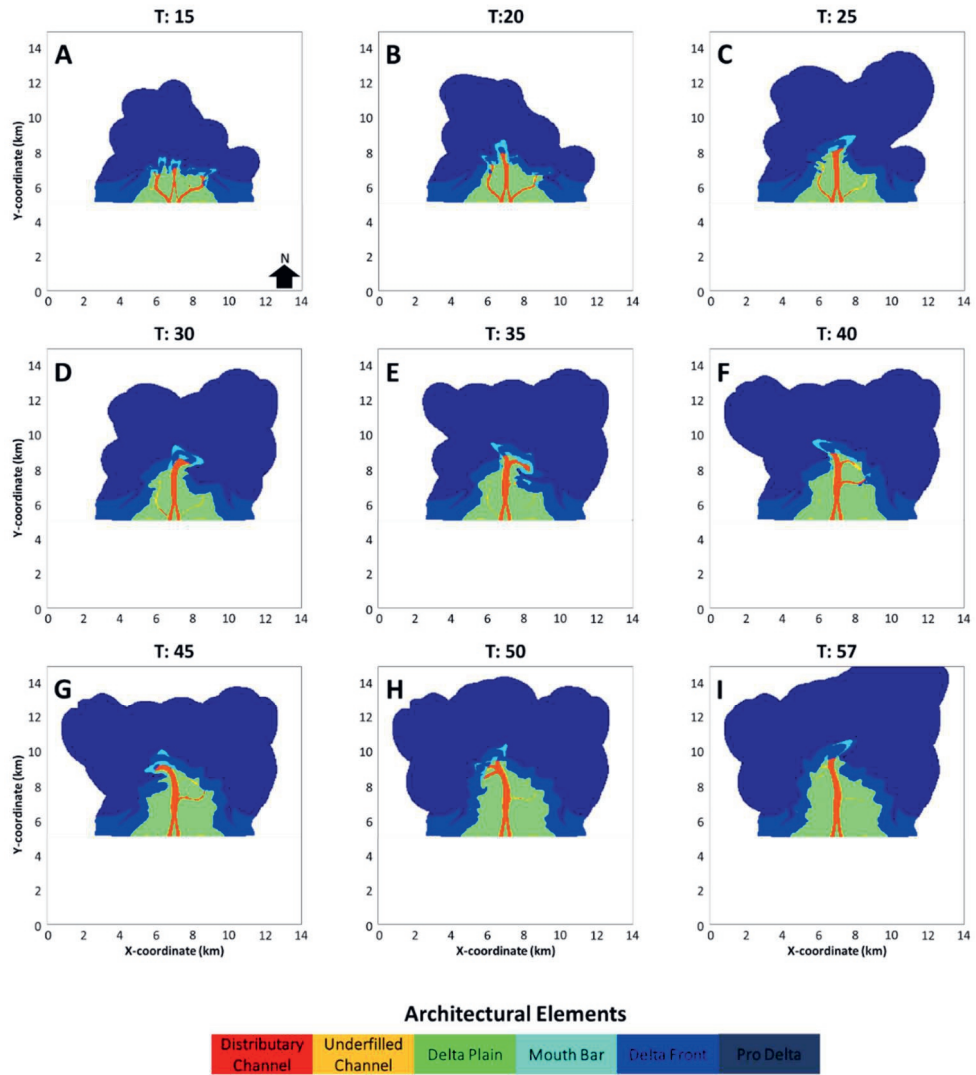


Figure B18. The interpreted depositional elements for compaction rate scenario 0.05 mm y^{-1} at selected simulation output time (days) in hydrodynamic time (A – I).

MS04: 0.1 mm/year

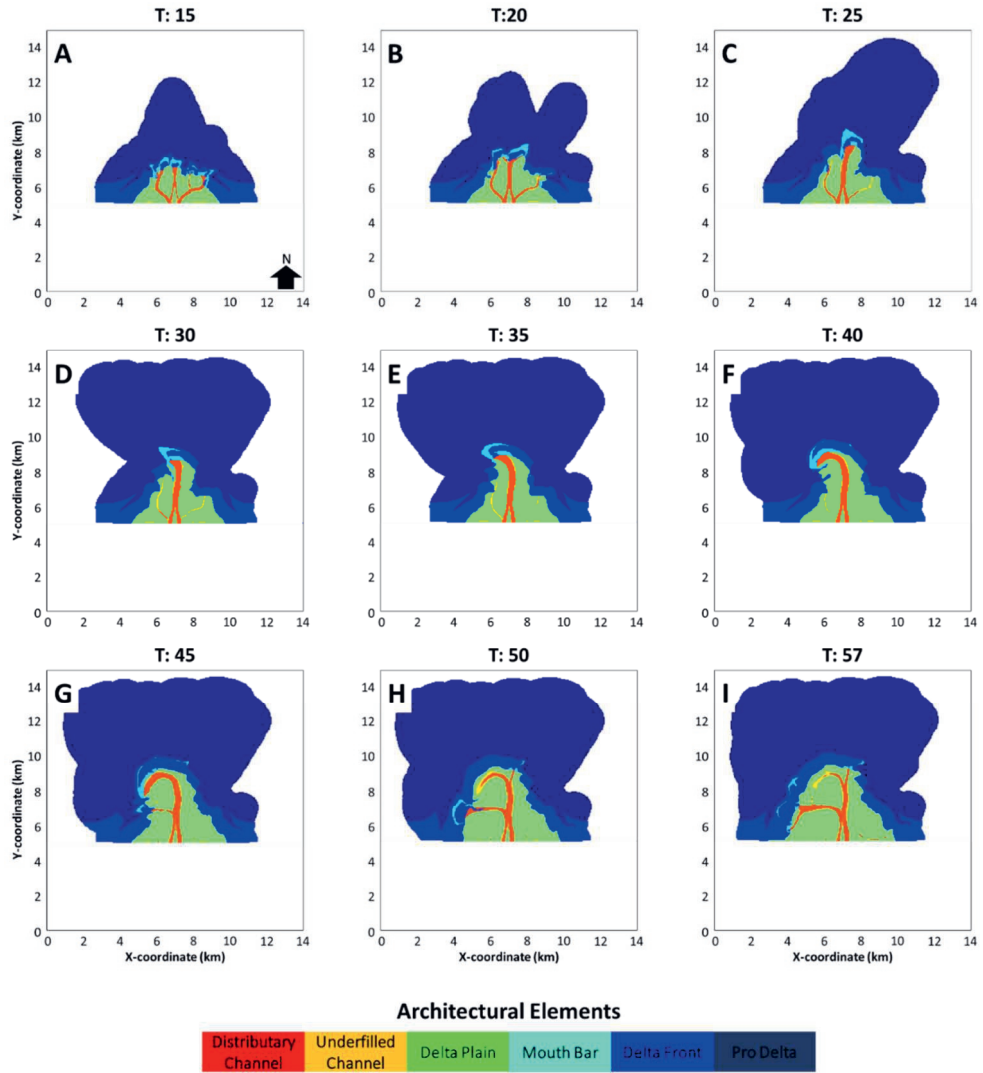


Figure B19. The interpreted depositional elements for compaction rate scenario 0.1 mm y^{-1} at selected simulation output time (days) in hydrodynamic time (A – I).

MS05: 0.5 mm/year

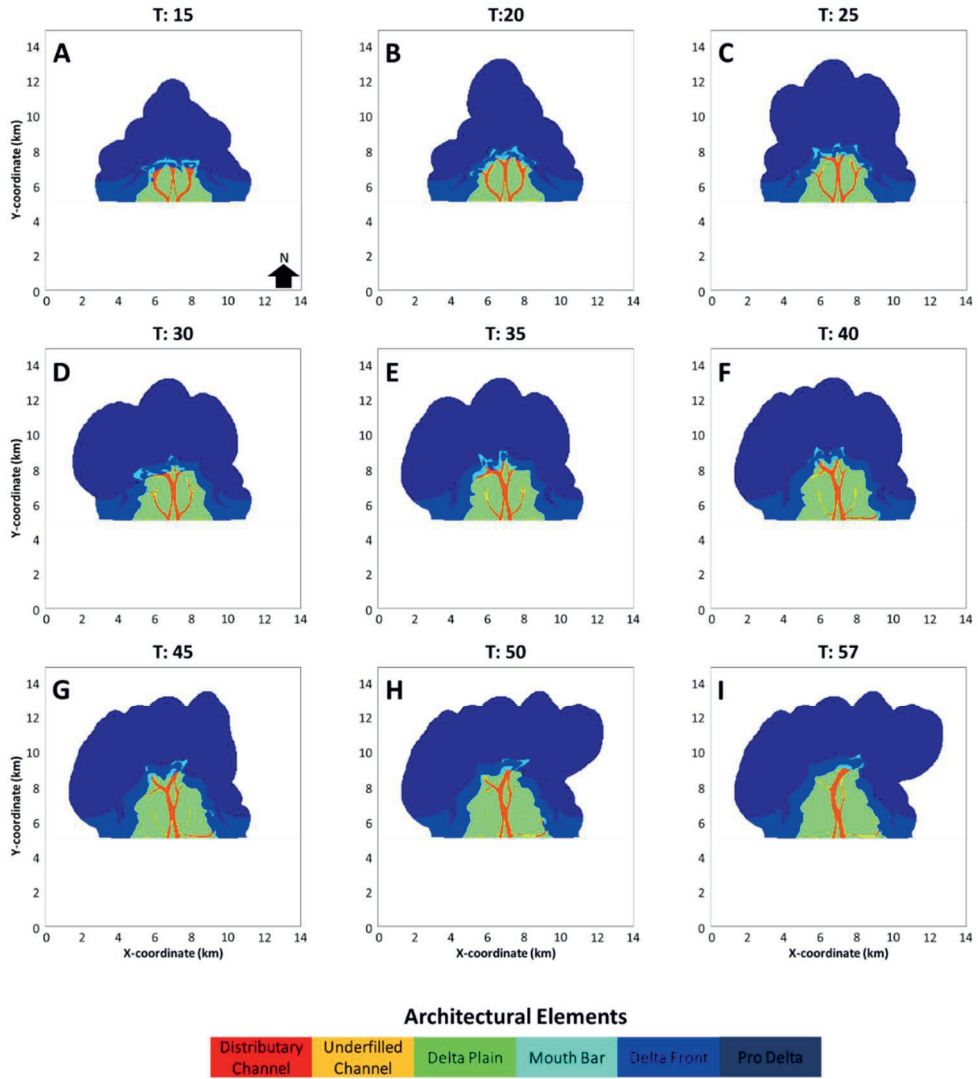


Figure B20. The interpreted depositional elements for compaction rate scenario 0.05 mm y⁻¹ at selected simulation output time (days) in hydrodynamic time (A – I).

MS06: 1 mm/year

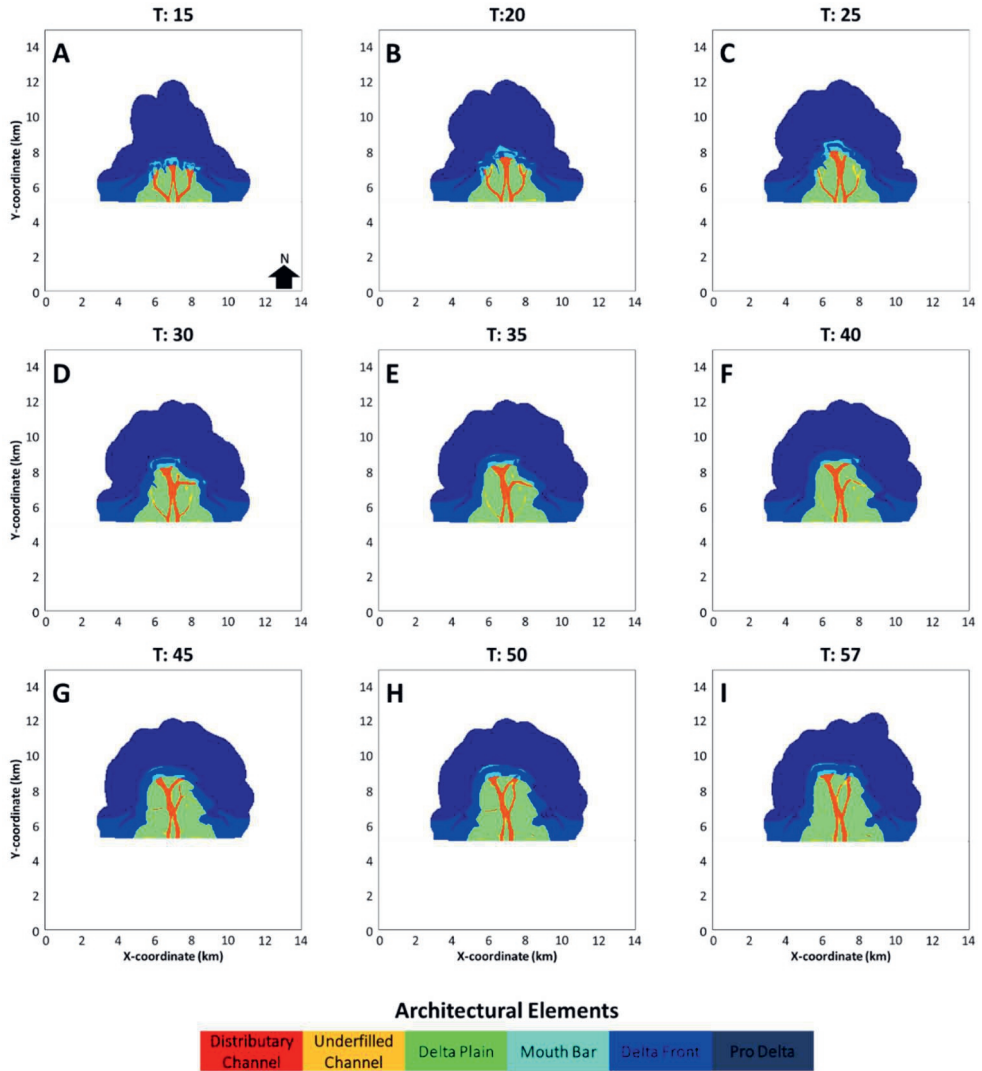


Figure B21. The interpreted depositional elements for compaction rate scenario 1 mm y^{-1} at selected simulation output time (days) in hydrodynamic time (A – I).

MS07: 5 mm/year

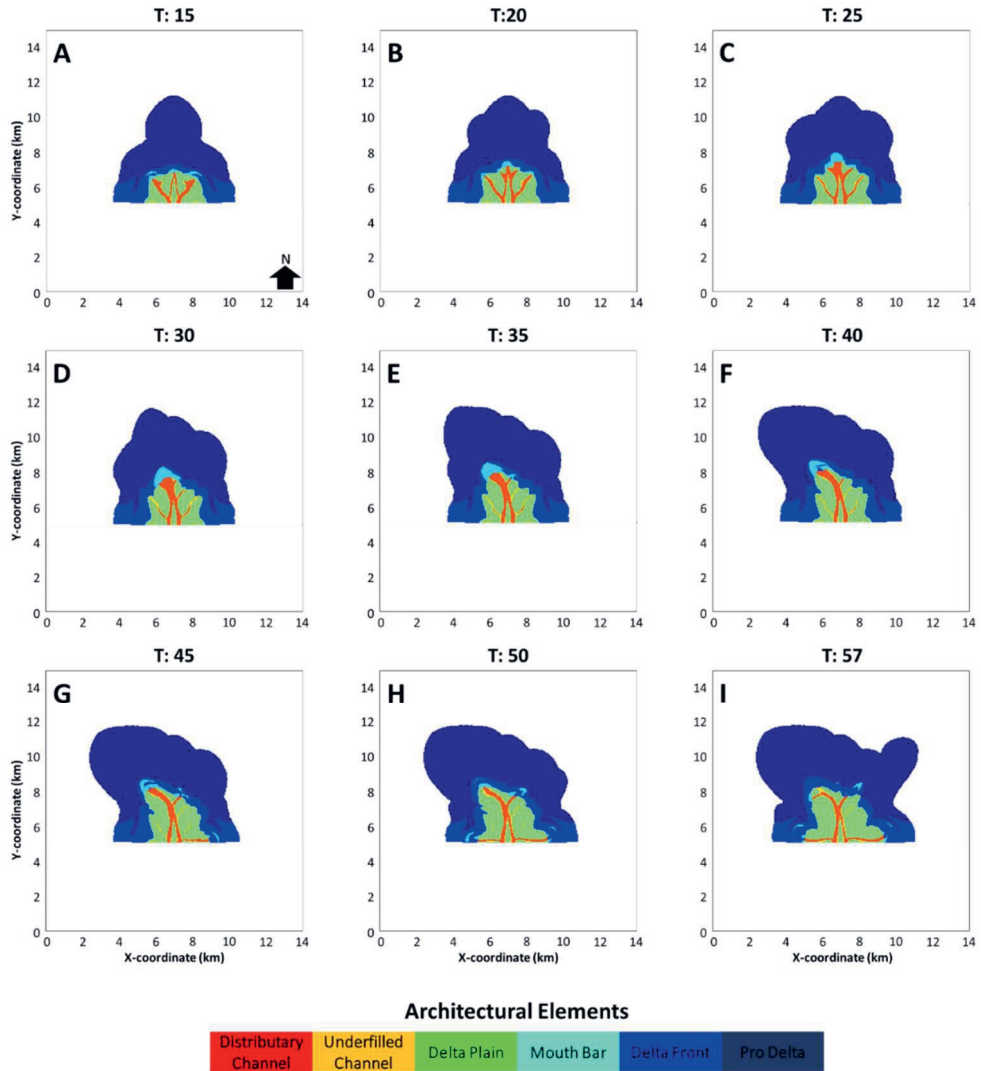


Figure B22. The interpreted depositional elements for compaction rate scenario 5 mm y^{-1} at selected simulation output time (days) in hydrodynamic time (A – I).

MS08: 10 mm/year

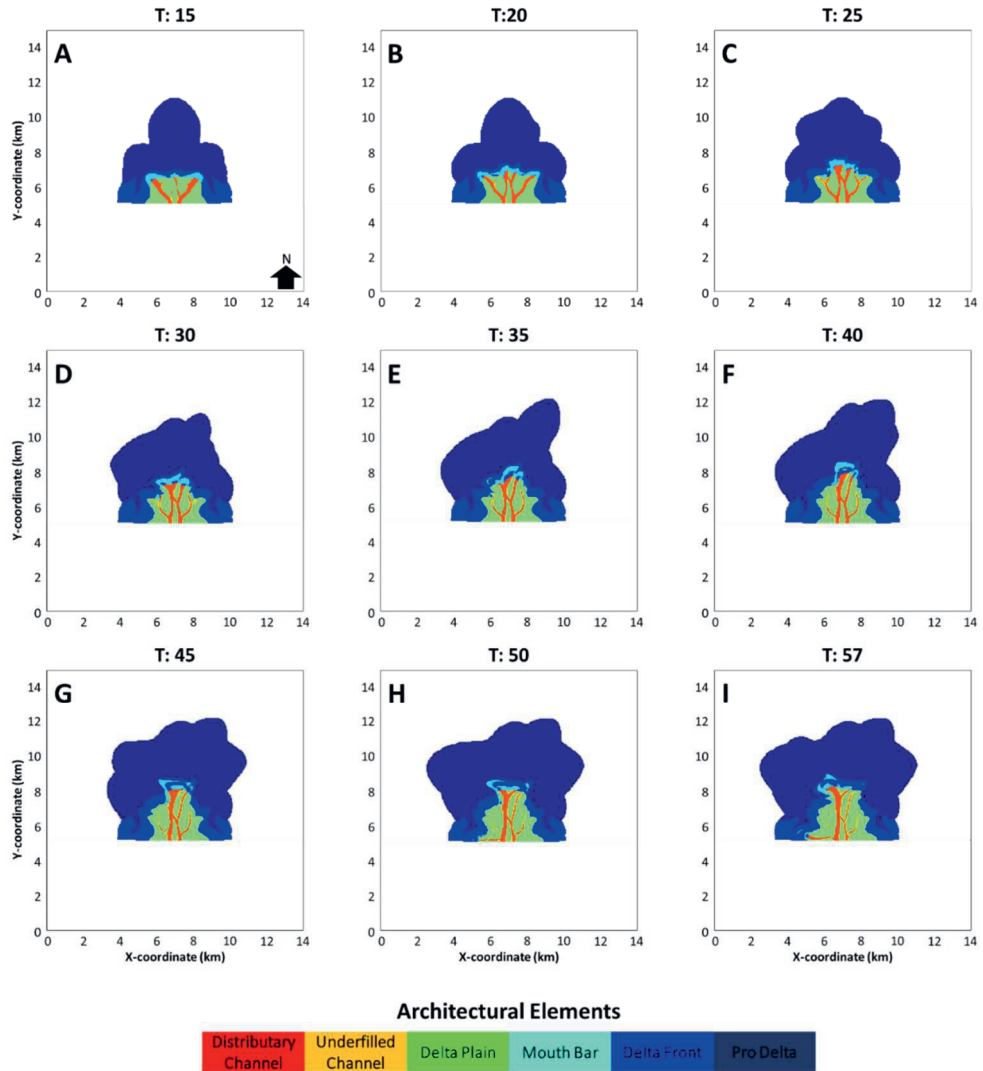


Figure B23. The interpreted depositional elements for compaction rate scenario 10 mm y^{-1} at selected simulation output time (days) in hydrodynamic time (A – I).

Mud-rich deltas

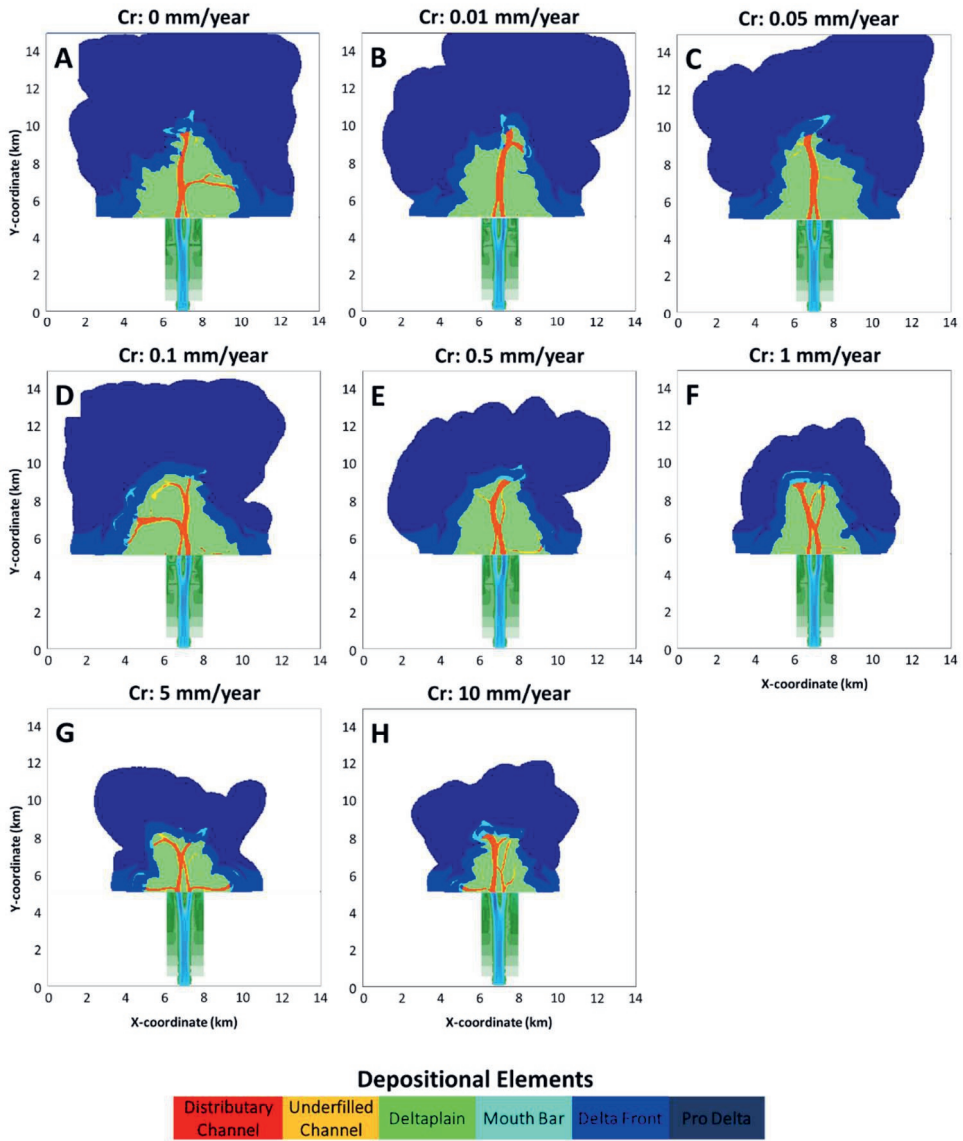


Figure B24. The interpreted deposited elements (DE) for all compaction rate scenarios (0 - 10 mm y⁻¹) at the end of the simulation output time (A – I).

B8. Fringe Areas

The fringe area is a new method to optimize channel identification. This method divides the simulated deltas into three areas based on the fringe lines (Figure B25). The first fringe line is called delta fringe, identified using an isoline of approximately 3 m water depth along the seaward boundary of the simulated deltas. Since the deltas have a roughly semi-circular or pyramid shape, the inner fringe line is estimated by moving the delta fringe radially inward with respect to the delta apex, accounting for the water depth variation along the delta fringe and delta size as weight factors. The inner fringe also has the same functionality as the brink point (Text B7), marking the transition between the updip and downdip of the delta. As the location of the inner fringe line can differ due to interpretation, the tuning parameter alpha was added, with a value ranging from 0 to 1. The alpha influences the inner fringe line by scaling the weight factor of the delta size. The decreasing alpha leads to a less inward inner fringe line. In this study, an alpha value of 0.9 was used. The water depth and alpha values, used to calculate the delta fringe line and inner fringe line, are pragmatic choices based on plan-view observation. The selection of the values can be further researched in the future.

In the simulated deltas with a rugose coastline, the water depth can change rapidly along the delta fringe. As a result, the estimated inner fringe line does not have a shape similar to the delta fringe line. To avoid this issue, the delta fringe line is moved outward by thirty grid cells, determined by sensitivity analysis to find smoother water depth variation along the delta fringe line. This new line is called the outer fringe line, which is then used to estimate the inner fringe. Another problem is that the estimated inner fringe line can be located outside the delta fringe line. Therefore, these locations are filtered out and placed on the delta fringe.

The estimated fringe lines are used to identify the fringe areas (Figure B26). The fringe area 0 indicates the area distal to the delta fringe line (dark blue). Fringe area 1 is between the delta fringe and inner fringe lines (white). The mouth bars are likely to form in this area. Fringe area 2 is the proximal area to the inner fringe line (red) where the distributary channels and delta plain are situated. It is important to note that given the greater offshore water depth, the delta builds up vertically more than laterally. Hence, the area where mouth bars are expected (fringe area 1) is smaller (inner fringe is closer to delta fringe) towards perpendicular to the initial shoreline than if the mouth bars are formed in a shallower area parallel to the initial shoreline. This can be explained by the auto-retreat concept (Muto & Steel, 1997, 2001), where more sediment is required to aggrade due to the increasing water depth as the delta progrades downdip. Eventually, this leads to drowning the delta once the vertical growth can no longer keep up with the increase in

accommodation. This implies that less sediment reaches the distal delta, so the formation of mouth bars will be restricted to a smaller area.

Mud-rich deltas

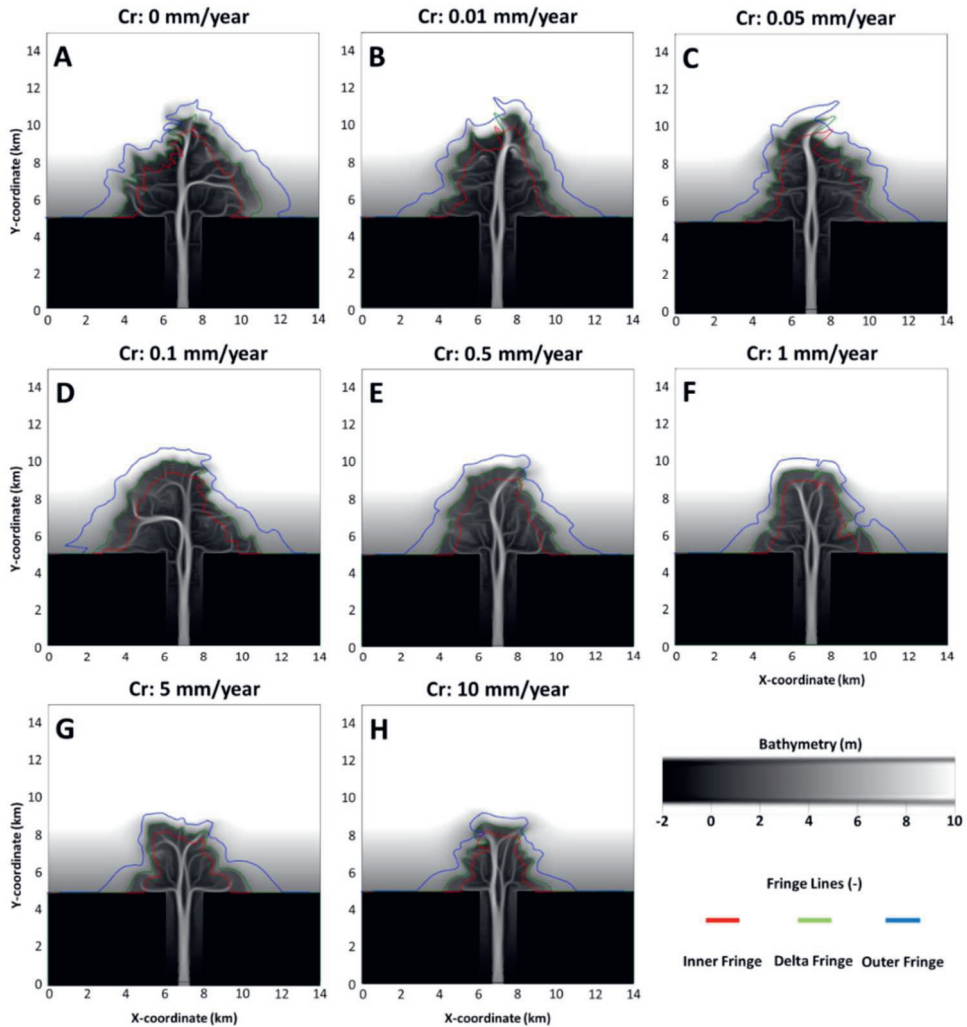


Figure B25. The bathymetry of simulated deltas in greyscale at the end of the simulation output time is superimposed by the fringe lines: inner fringe, delta fringe, and outer fringe (A – H).

Mud-rich deltas

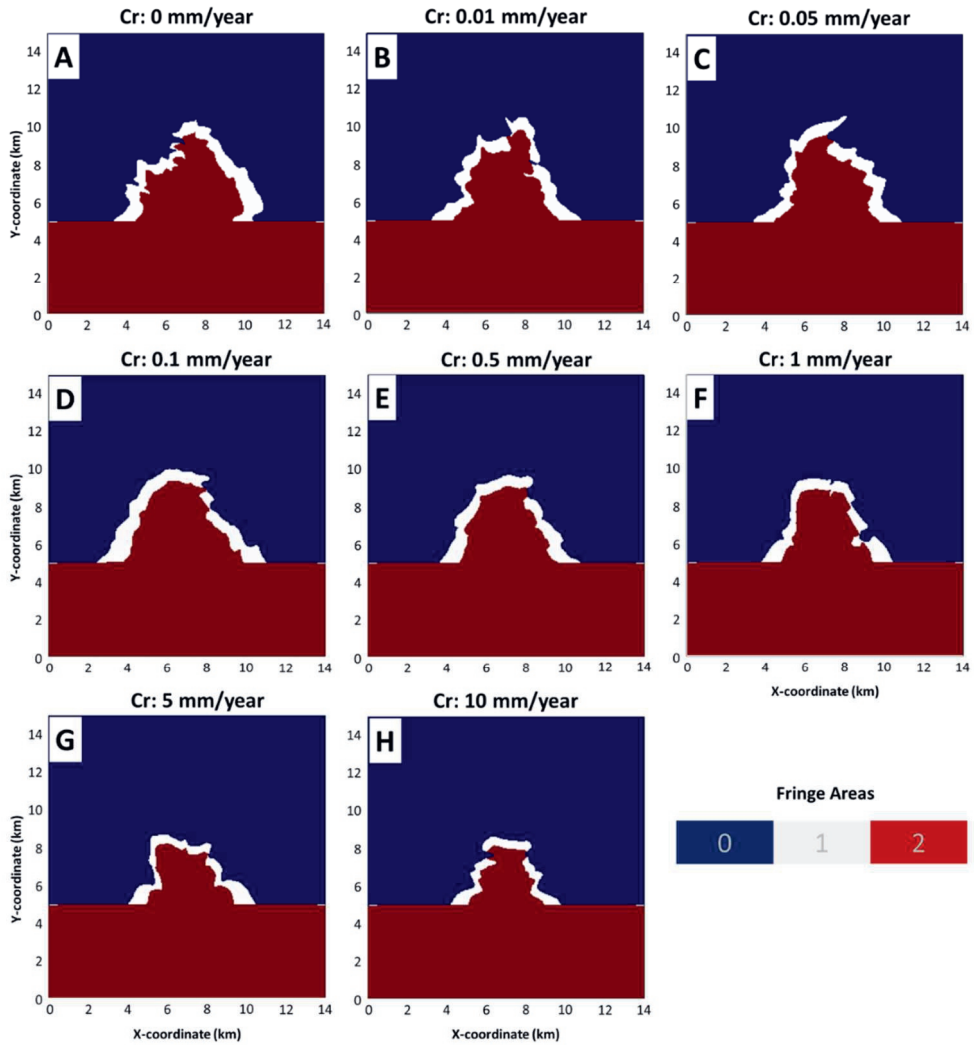


Figure B26. Estimated fringe areas in simulated deltas at the end of the simulation output time, consisting of fringe areas 0, 1, and 2 (A – H).

B9. Validation of Depositional Elements

The computed depositional elements are validated by analysing the sedimentation (by mass) in these areas for all simulation output time steps for compaction scenario 0 mm y^{-1} (Figure B27). The results show that a large quantity of sediment is deposited in the mouth bar DE (Figure B27D), accumulating up to 5500 kg of sediment at a single simulation output time step. This also occurs in natural deltas as the distributary channel reaches the shoreline, releasing substantial sediment from the channel mouth to be deposited in the mouth bar. In addition, considerable sedimentation (by mass) also occurs on the distributary channel DE (Figure B27A).

The delta plain DE, delta front DE, and pro delta DE experience low sedimentation (by mass) (Figures B27C, E, F), which is also the case in natural deltas. Note that the sedimentation (by mass) in the underfilled channel DE is not analysed because the total sedimentation in this area contributes to less than 5% of the total sedimentation in the delta, which is considered overprinted by noise (Figure B27B).

Non-Compacted Mud-rich deltas

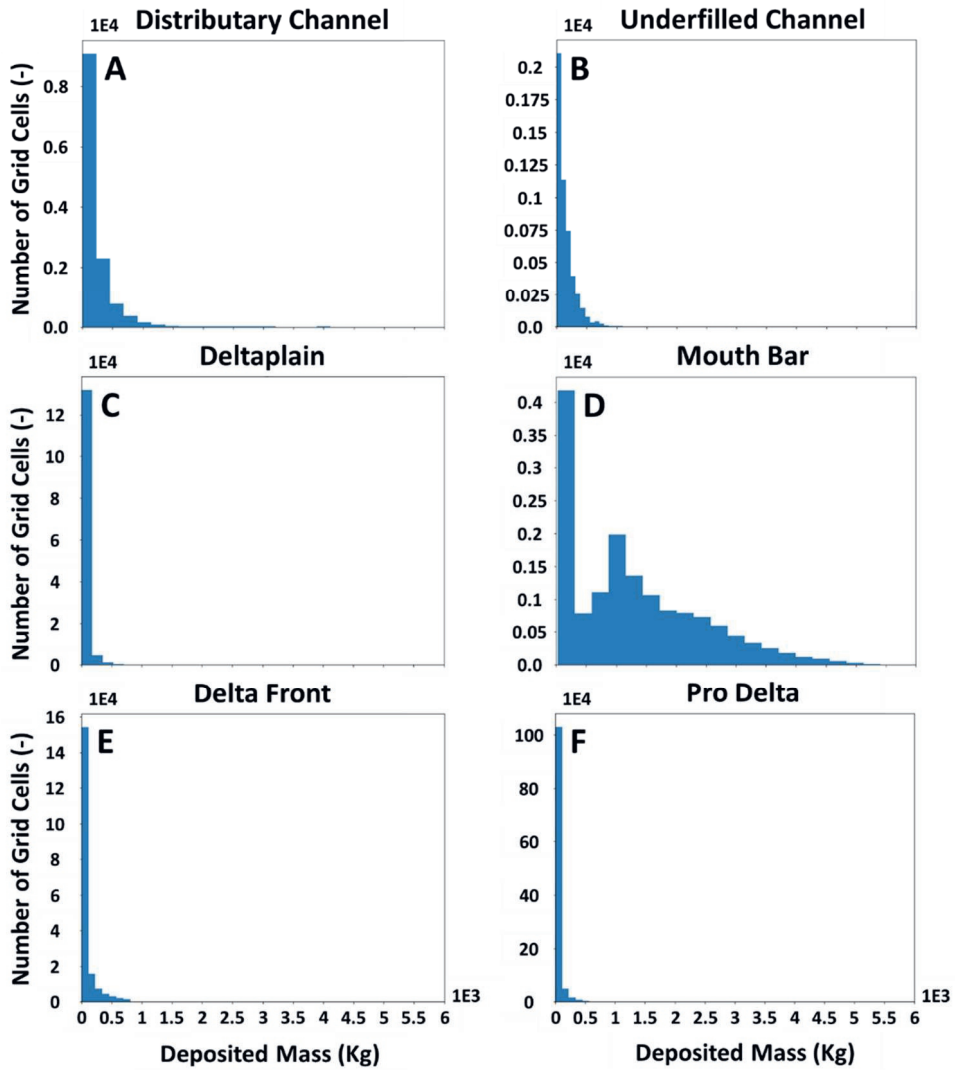


Figure B27. A collapse output time series of the sedimentation (by mass) in all grid cells that falls in each depositional element (A - F) for compaction rate scenario 0.0 mm y^{-1} . Note that the y-axis has a different range of values for each depositional element.

B10. Sediment Distribution Plots

The grain-size distribution of sediment deposited in the distributary channel DE, delta plain DE, and mouth bar DE over the simulation output time step is shown in Figure B28. The result indicates a limited compaction impact on the temporal sedimentation trend in these areas.

Sand consists of fluvial sand and substrate sand eroded from the initial sediment bed. The percentage of these sands in sediment deposited in distributary channel DE, delta plain DE, and mouth bar DE is shown in Figures B29 and B30. The fluvial sand has a higher proportion in deposited sediment than the substrate sand.

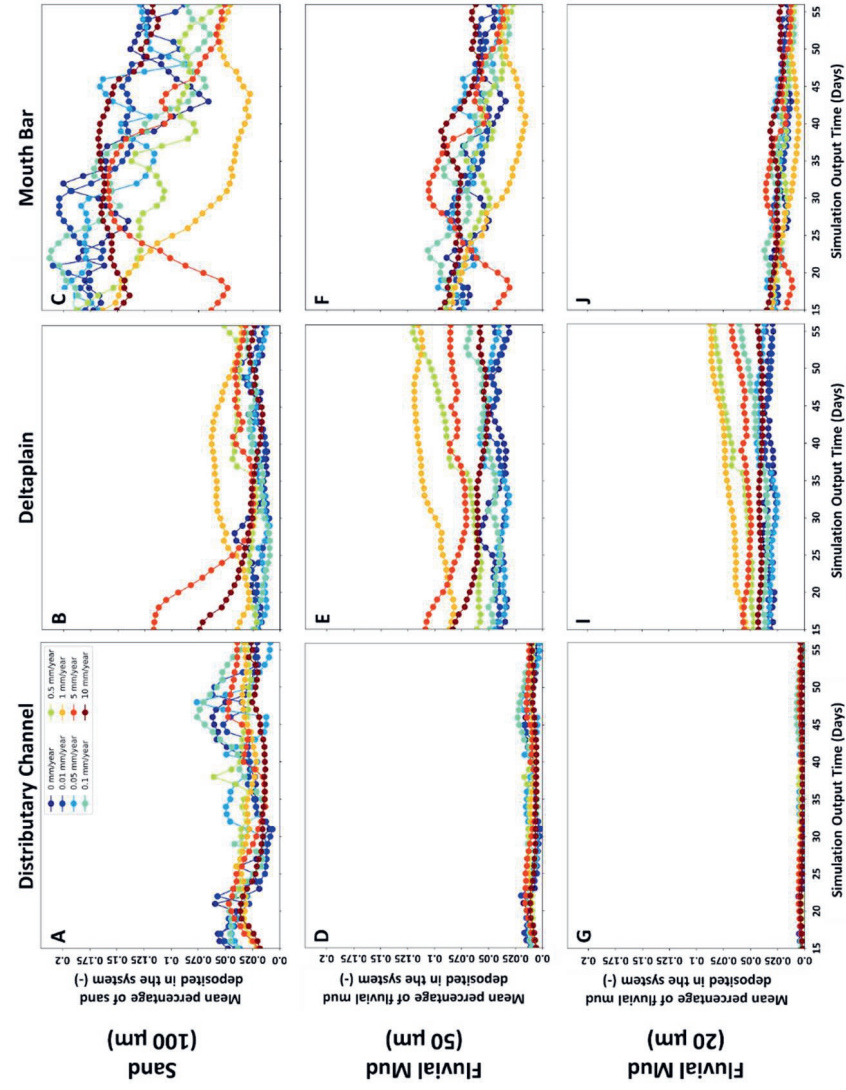


Figure B28. Percentage of sand and fluvial mud deposited in the distributary channel DE, delta plain DE, and mouth bar DE over the simulation output time step (A - I). The colored dots represent compaction rate scenarios, ranging from 0 to 10 mm y^{-1} . Note that sand consists of fluvial sand and substrate sand. Their percentage of deposited mass is shown in Figures B29 and B30.

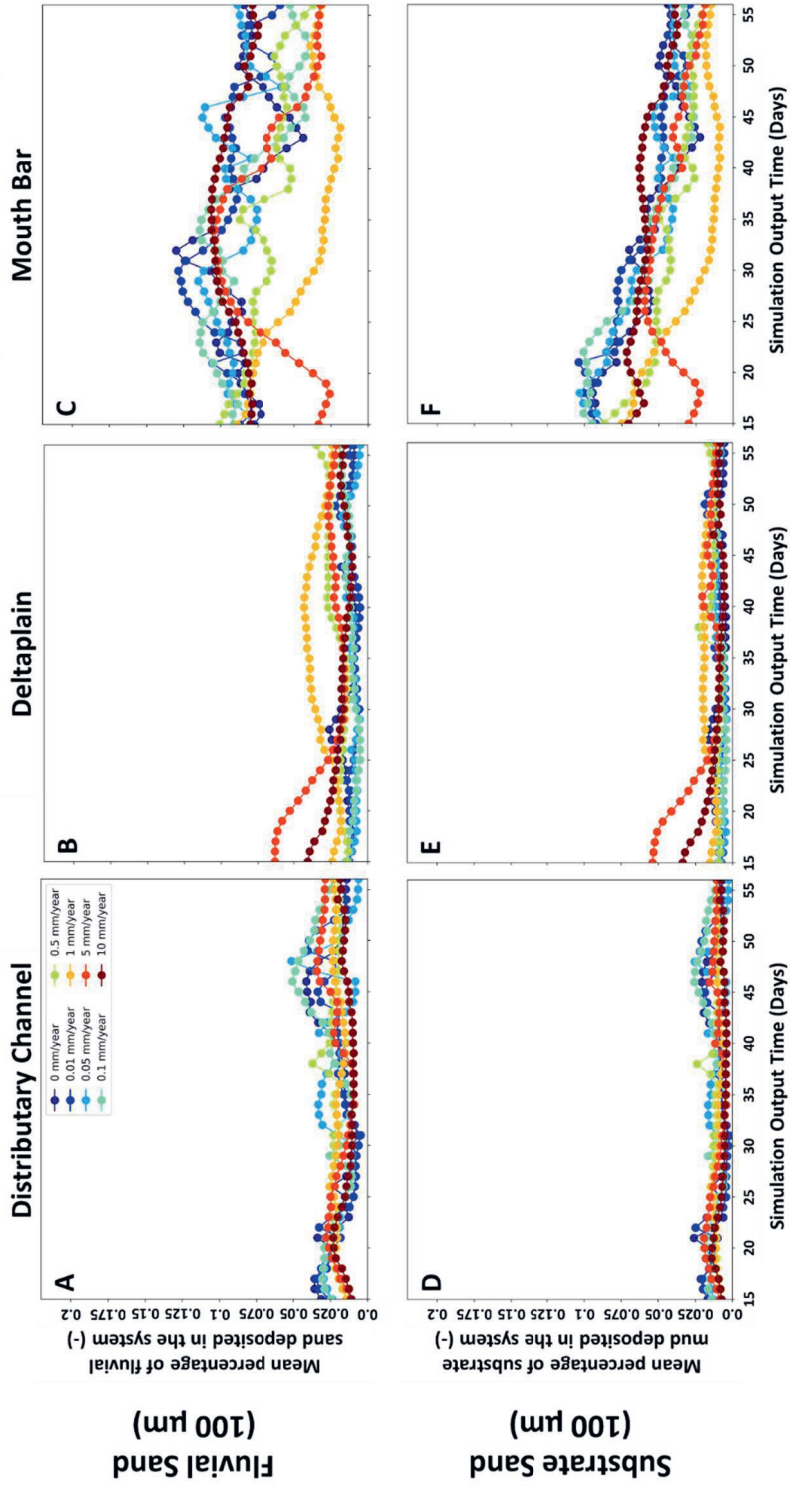


Figure B29. Percentage of fluvial sand and substrate sand deposited in the distributory channel DE, delta plain DE, and mouth bar DE over the simulation output time (A - I). The colored dots represent compaction rate scenarios, ranging from 0 to 10 mm y⁻¹.

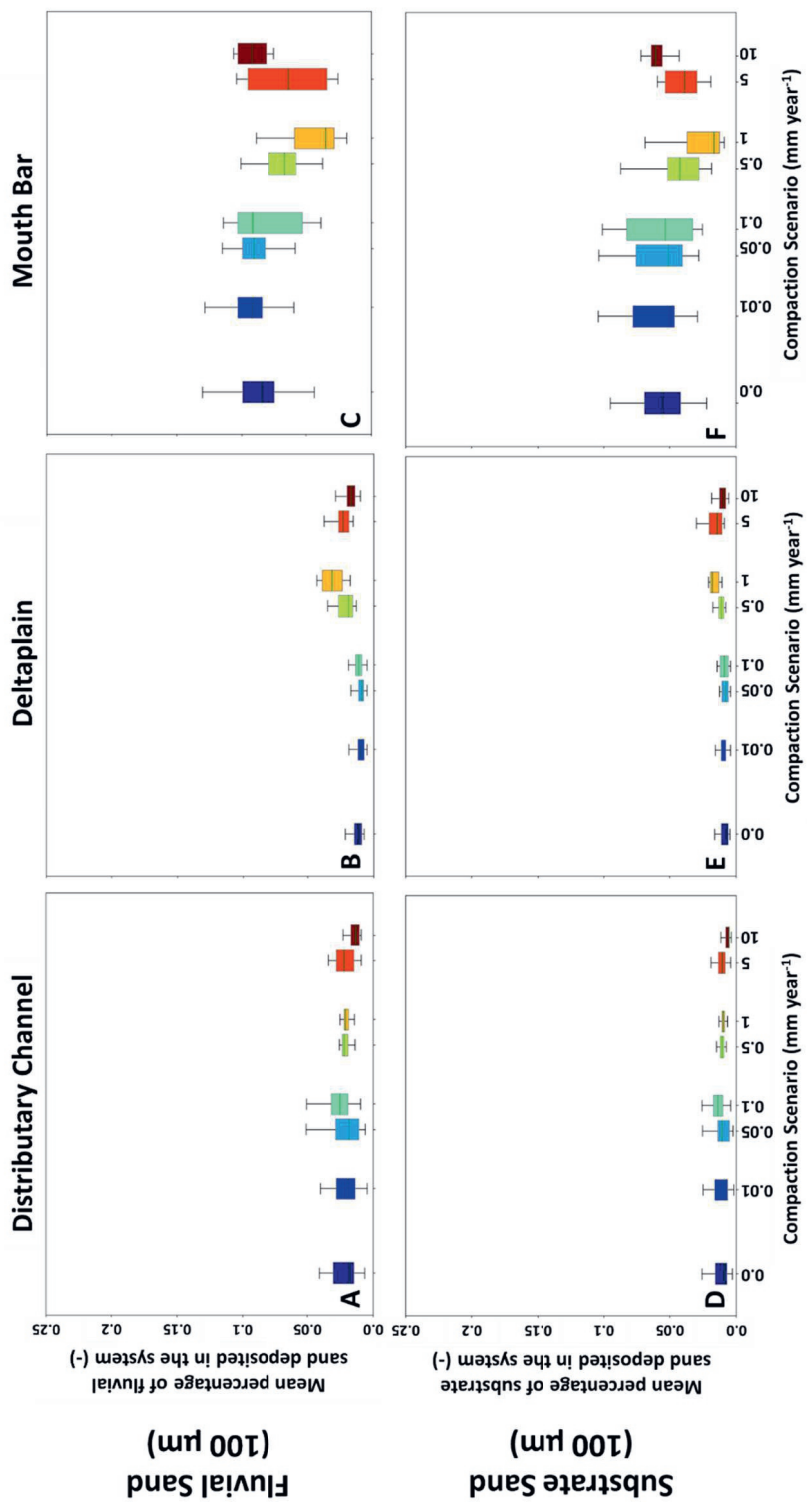


Figure B30. The output time series of the percentage of fluvial sand and substrate sand deposited in the distributary channel DE, delta plain DE, and mouth bar DE is collapsed into boxplots (A – F). The colored dots represent compaction rate scenarios, ranging from 0 to 10 mm y⁻¹.

B11. Backwater Effect

The influence of backwater on channel relocation is assessed by analysing the water level in the distributary channel, which is conducted in several steps. First, the plan-view simulated deltas are divided into several areas by increasing the delta radius for every 511 m (Figure B31A). The delta radius is obtained from sensitivity analysis to avoid local variation in the water level. Then, the average water level is calculated for each area for each simulation output time step for compaction rate scenarios 0.1 and 5 mm y^{-1} , of which the channel relocation is observed from plan-view bathymetry observation (Figures B9 and 12). The water level variation, defined as the difference between the max and min water level in the distributary channel over the simulation output time step, has the maximum values in Area 1, which are 25 cm and 13 cm for compaction rate scenarios 0.1 and 5 mm y^{-1} , respectively (Figures B31B, C). The slight variation indicates the backwater effect has limited influence on the channel relocation in this study.

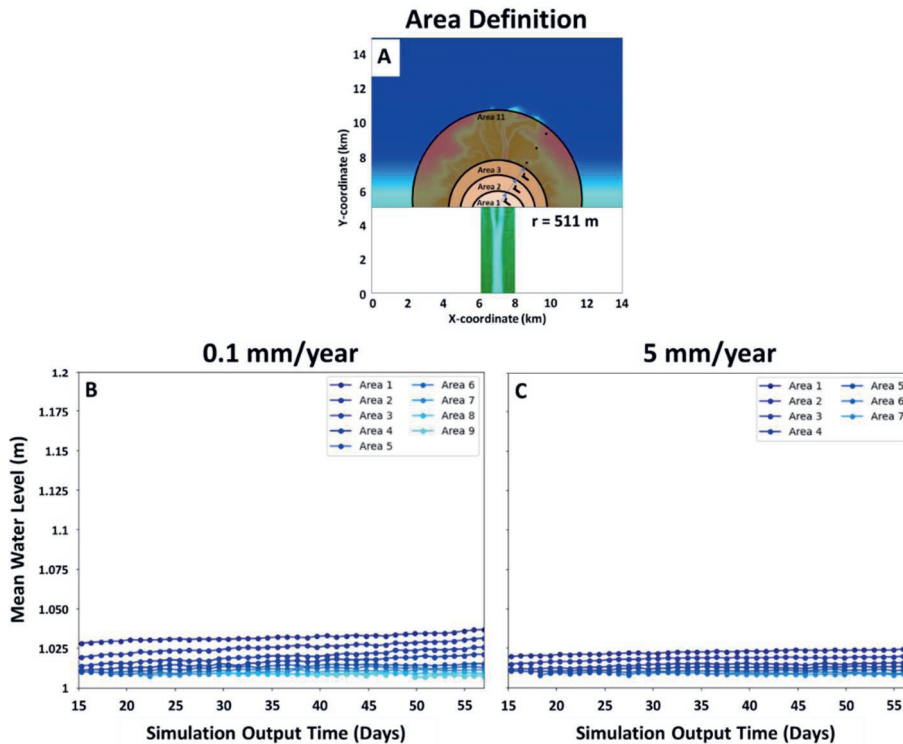


Figure B31. The delta is divided into various areas by increasing the delta radius for every 511 m (A). For all areas, the water level is averaged for each simulation output time step for compaction scenarios 0.1 mm y^{-1} and 5 mm y^{-1} (B and C).

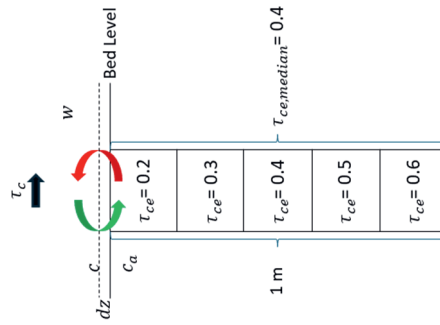
Supplementary Materials C

This sub-chapter shows supplementary materials for chapter 4, which includes the deposition and erosion in simulated deltas (C1), the validation of a new critical bed shear stress formula (C2), levee identification (C3), superelevation and gradient advantage (C4), channel aggradation (C5), water depth at breach sites (C6), strike and dip sections (C7).

C1. Deposition and Erosion in Simulated Deltas

Sediment transport across the model domain is driven by flow, resulting in deposition and erosion at grid cells. Deposition of non-cohesive and cohesive sediments is controlled by their respective settling velocities and near-bed concentrations (Figure C1). Erosion, however, differs between sediment types. For non-cohesive sediments, Erosion is governed by upward diffusion driven by concentration gradients near and at the bed (Figure C1). In contrast, cohesive sediment erosion occurs when flow-induced bed shear stress exceeds a threshold defined by critical bed shear stress for erosion (Figure C1).

Erodibility Index (EI) of cohesive sediment has been used in analysing levee breach dynamics, calculated as the difference between flow-induced bed shear stress and median critical bed shear stress for erosion over ~0.8 m thick levee sediment. Since this median includes more compacted, deeper layers (Figure C1), it may underestimate the resistance of the upper sediment. As a result, erodibility index may appear negative (i.e., flow strength is less than the median threshold), yet erosion still occurs because the upper layers have lower critical shear stress for erosion values. This behavior is evident in Figures 4.5J - L: compacted simulations show negative erodibility values, yet erosion persists, leading to elevation loss.



Deposition

Deposition (D) of non-cohesive and cohesive sediment occurs due to sediment settling near the bed

$$D = c w$$

c : Near-bed concentration (kg m^{-3})
 w : Settling velocity (m s^{-1})

Non-Cohesive Erosion

Erosion (E_{nc}) occurs because upwards diffusion driven by the difference between sediment concentration near and of the bed.

$$E_{nc} = \varepsilon_s (c - c_a) / dz$$

ε_s : Sediment diffusion coefficient ($\text{m}^2 \text{s}^{-1}$)
 c : Near-bed concentration (kg m^{-3})
 c_a : Bed concentration (kg m^{-3})
 dz : Near-bed elevation (m)

Cohesive Erosion

Erosion (E_c) occurs because bed shear stress is larger than critical bed shear stress for erosion of the bed ($\tau_c > \tau_{ce}$)

$$E_c = M_{ce} (\tau_c - \tau_{ce})$$

M_{ce} : Erosion Rate ($\text{kg m}^{-2} \text{s}^{-1}$)
 τ_c : Bed shear stress (Pa)
 τ_{ce} : Critical bed shear stress for erosion (Pa)
 Formulations for M_{ce} & τ_{ce} can be seen in Equations 1 and 2.

Figure C1. Deposition and erosion formulas for non-cohesive and cohesive sediments in simulated deltas.

C2. Validation of Critical Bed Shear Stress Formula

The critical bed shear stress for erosion formula (τ_{ce} in Equation 4.1) is validated using laboratory datasets (Jacobs, 2011; Kamphuis & Hall, 1983; Laflen & Beasley, 1960; Lim, 2006; Mostafa et al., 2008; Smerdon & Beasley, 1959; van Rijn et al., 2019, 2020). These datasets provide measured τ_{ce} from soil samples with varying mud content and dry density (Figure C2). Samples with similar mud content but higher dry density reflect more compaction (van Rijn et al., 2020, 2025). The modelled τ_{ce} is calculated using hypothetical sediment mixtures, defined by increasing mud content and decreasing porosity to indicate more compaction. The results show that modelled τ_{ce} increases with mud content and compaction, aligning with laboratory observations (Figure C2).

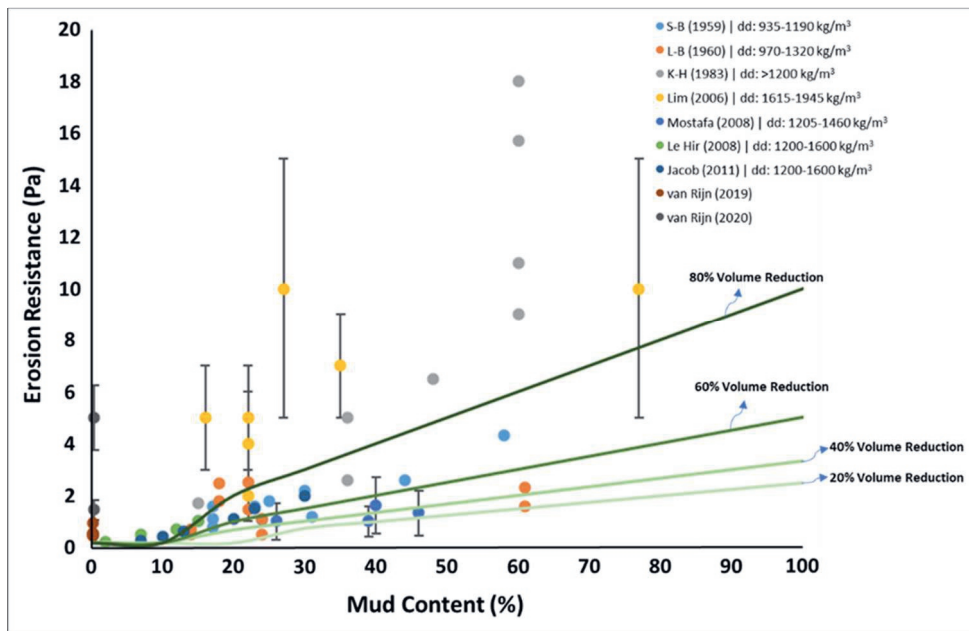


Figure C2. The critical bed shear stress for erosion (τ_{ce}) measured in the laboratory with varying mud content and bulk density is plotted as colored dots. Numerical τ_{ce} is derived from Equation 4.1 using hypothetical samples with varying mud content and porosity, plotted as colored lines. The legend abbreviations S-B, L-B, and K-H refer to datasets from Smerdon & Beasley, Laflen & Beasley, and Kamphuis & Hall, respectively, while 'dd' denotes dry density.

C3. Levee Identification

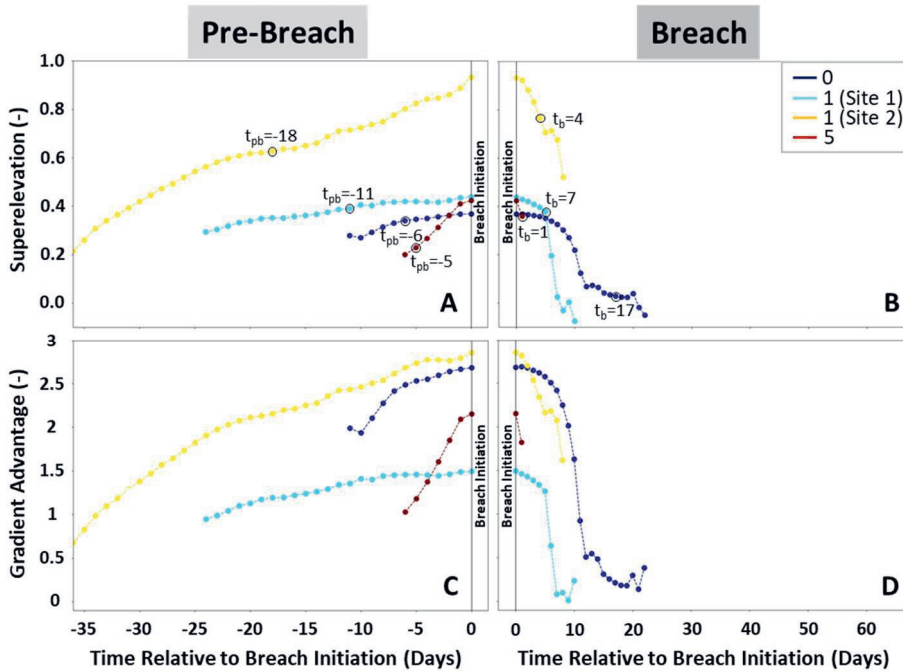
Levee in simulated deltas is identified based on several criteria: (1) A 200 m levee search radius is orthogonal from the distributary channel edge, identified using a flow velocity threshold of 0.65 m/s. (2) Only levees next to delta plain are considered, excluding subaqueous levees (Orton & Reading, 1993). (3) Levee elevation is higher than distributary channel's water level (4) Lastly, levees adjacent to abandoned channels are identified only if they are positioned next to the main channel.

C4. Superelevation & Gradient Advantage

Superelevation (β_s) and gradient advantage (γ) are measured using several parameters—bankfull channel depth (H_{dc}), levee height (H_{lv}), channel slope (S_{dc}), and levee slope (S_{lv}). H_{dc} is determined by subtracting channel base elevation from channel water surface level, whereas S_{DC} is a slope from delta apex to channel observation point. Similarly, S_{lv} is a slope from levee observation point at the breach site to delta plain observation point.

Previous studies indicated that channel bed aggrades to delta plain level at the breach initiation, reducing bankfull channel depth (H_{dc}) relative to the levee height (H_{lv}), resulting in superelevated channel ($\beta_s \sim 1$) (Gearon et al., 2024; Slingerland & Smith, 1998). The breach can also be triggered when the levee slope (S_{lv}) exceeds that of the channel (S_{dc}), leading to a gradient advantage ($\gamma > 1$) (Gearon et al., 2024; Slingerland & Smith, 1998; Törnqvist & Bridge, 2002).

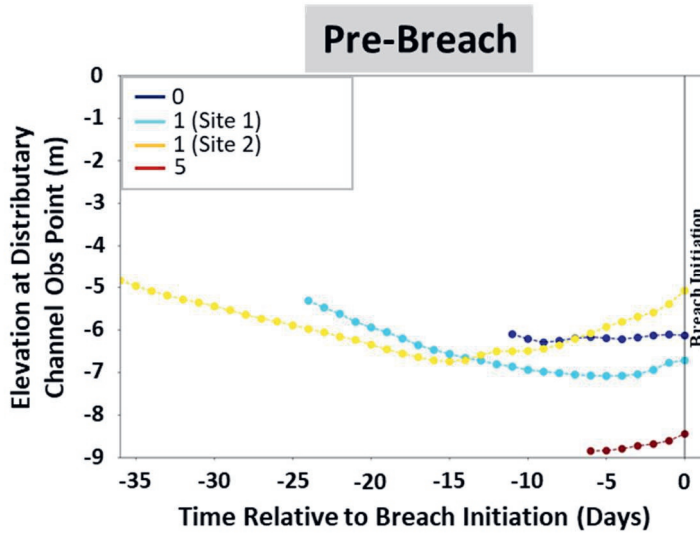
Superelevation (β_s) and gradient advantage (γ) are calculated during pre-breach and initial breaching, while the levee undergoes initial erosion. During the pre-breach stage, β_s increases and peaks at the breach initiation—0.37, 0.44, 0.93, and 0.42 for compaction rate scenarios 0, 1 (Site 1), 1 (Site 2), and 5 mm γ^{-1} , respectively (Figure C3A)—then declines (Figure C3B). γ follows a similar pattern, peaking at 2.68, 1.49, 2.85, and 2.15 (Figures C3C, D).



Figures C3. Time series of superelevation (β_s) and gradient advantage (γ) from levee observation points at breach sites during pre-breach and initial breaching (b) (A – D). Colored lines represent compaction rate scenarios 0, 1 (Site 1), 1 (Site 2), and 5 mm y^{-1} . The vertical lines indicate the breach initiation. Small open circles indicate selected simulation output times, corresponding to plan-view maps in Figures 4.2 – 4.4.

C5. Channel Aggradation

The levee exhibits a local regime shift from degradational to aggradational during the breach phase. This transition precedes by a noticeable increase in channel bed elevation immediately before the breach initiation (Figure C4).



Figures C4. Time series of elevation from distributary channel observation points during pre-breach phase. Colored lines represent compaction rate scenarios 0, 1 (Site 1), 1 (Site 2), and 5 mm γ^{-1} .

C6. Water Depth at Breach Sites

To investigate whether the levee breaching is influenced by backwater effects, we plot water depth at breach sites across all compaction rate scenarios (Figure C5). The results indicate that water depth is affected by breach dynamics (Figures C5E - H), as evidenced by their similar temporal trends to flow velocity (Figures C5A - D). This excludes possible backwater influence on the breach.

C7. Strike and Dip Sections

Strike and dip sections are produced to analyse the variability of critical bed shear stress for erosion (τ_{ce} in Pa) and sand fractions (in %) within the modelled stratigraphy. These sections are presented for selected simulation output times, covering both pre-breach and breach phases, under compaction rate scenarios of 0, 1 (Sites 1 & 2), and 5 mm γ^{-1} (Figures C6 - 9).

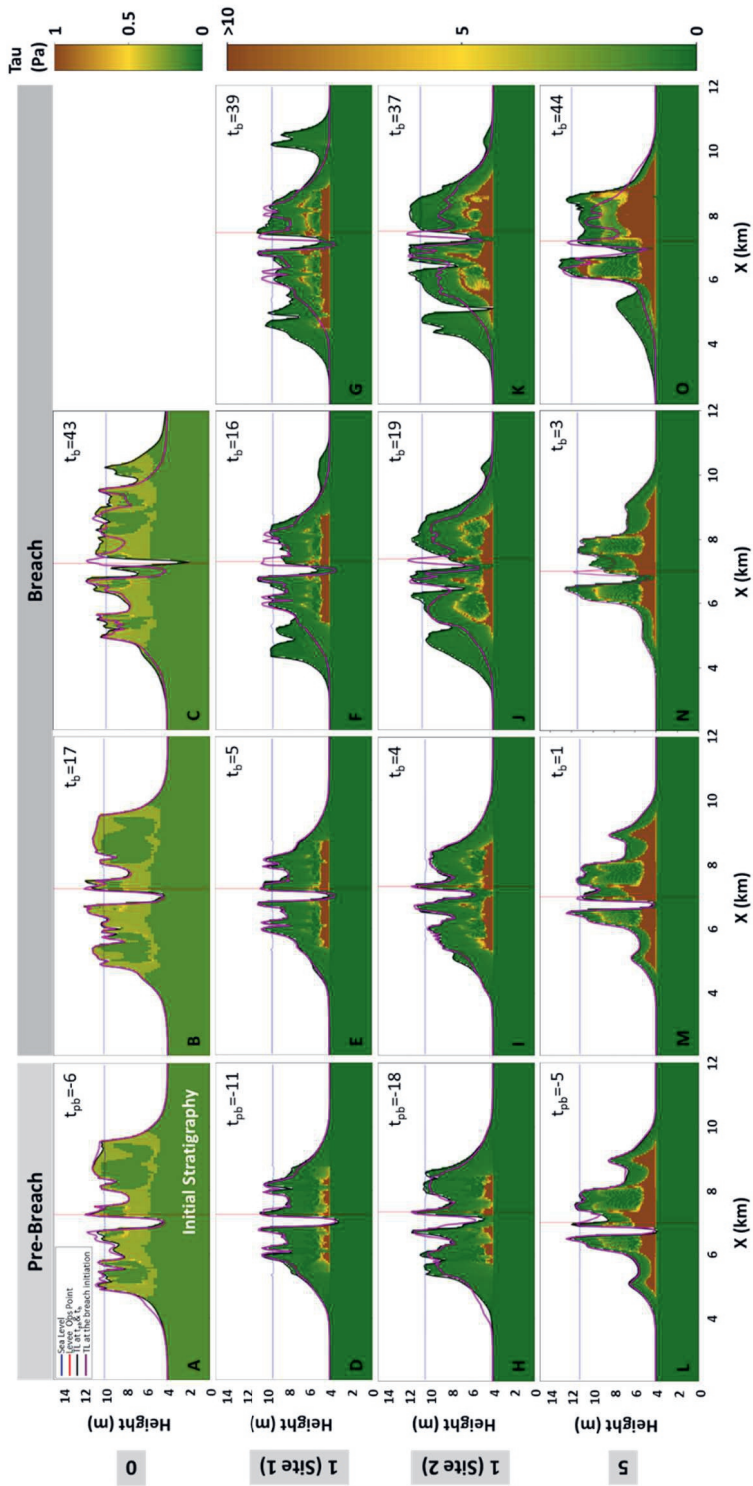


Figure C6. Strike sections of critical bed shear stress for erosion (τ_{ce}) traversing levee observation points at breach sites, shown for selected simulation output times during pre-breach and breach across all compaction rate scenarios (A - O). Cross-section locations are indicated in Figure 4.2. Black lines denote timelines at selected simulation output times, while purple lines mark timelines at the breach initiation. Vertical red lines indicate breach locations, and blue horizontal lines represent sea level. The τ_{ce} color scheme reflects different value ranges for non-compacted and compacted scenarios.

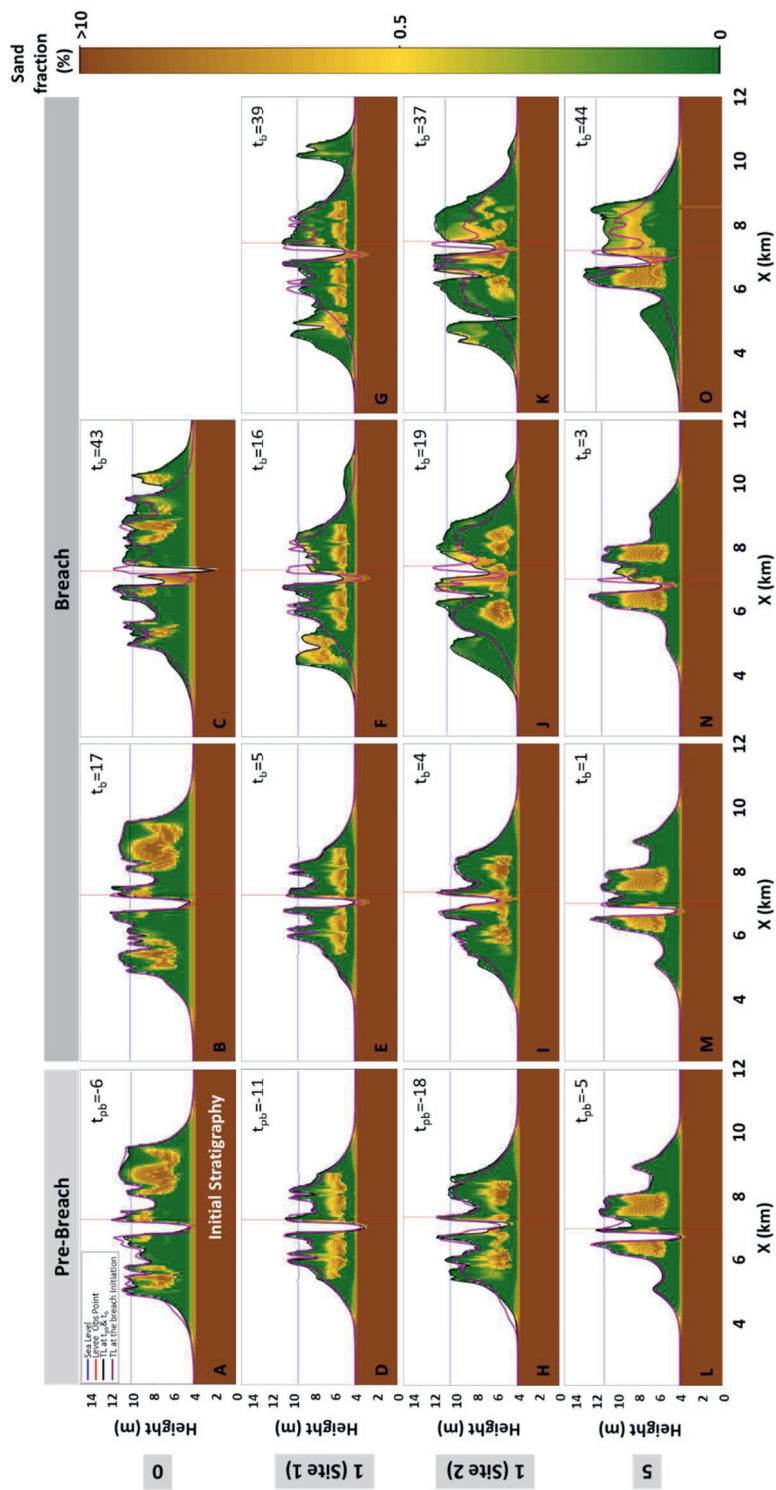


Figure C7. Strike sections of sand fraction traversing levee observation points at breach sites, shown for selected simulation output times during pre-breach and breach across all compaction rate scenarios (A - O). Cross-section locations are indicated in Figure 4.2. Black lines denote timelines at selected simulation output times, while purple lines mark timelines at the breach initiation. Vertical red lines indicate breach locations, and blue horizontal lines represent sea level. The sand fraction color scheme reflects different value ranges for non-compacted and compacted scenarios.

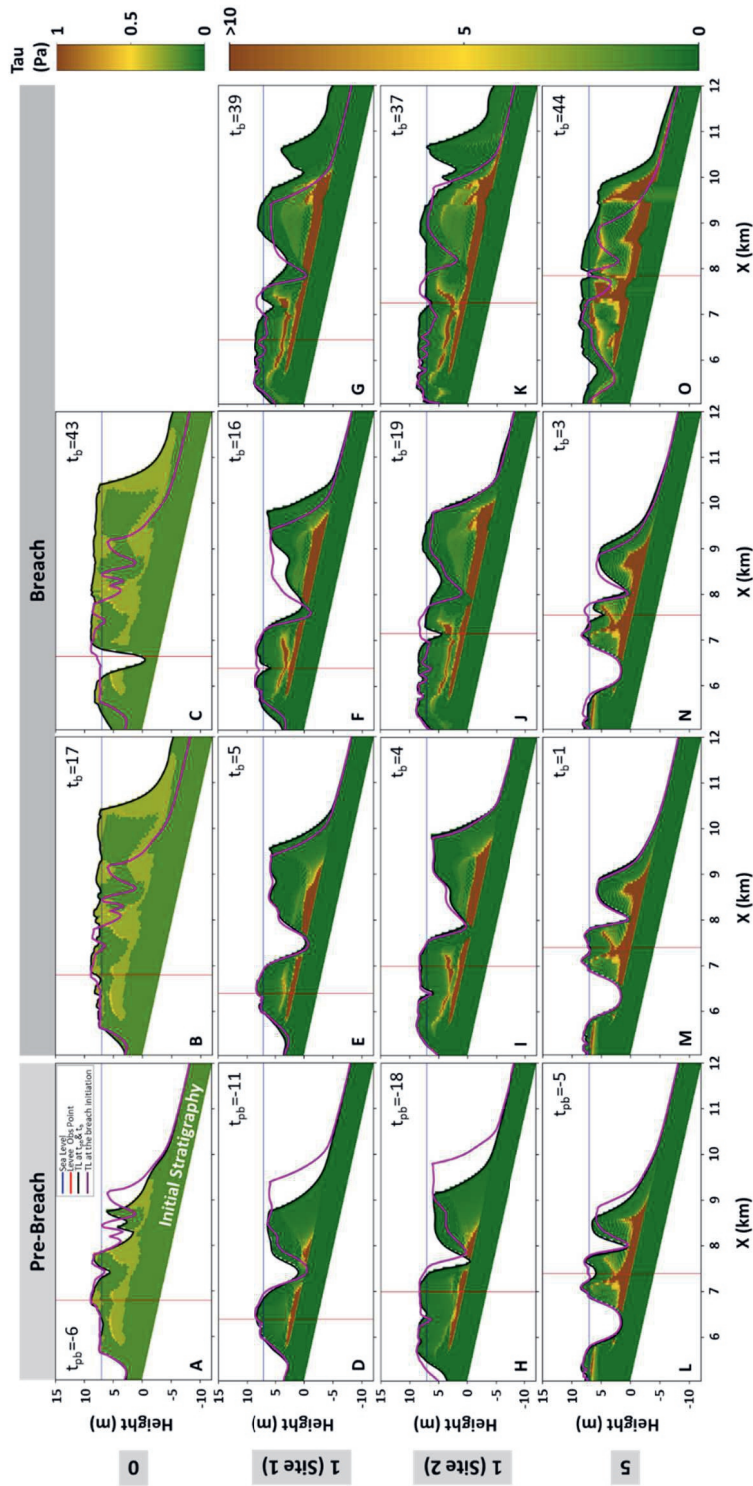


Figure C8. Dip sections of critical bed shear stress for erosion (τ_{ce}) traversing levee observation points at breach sites, shown for selected simulation output times during pre-breach and breach across all compaction rate scenarios (A – O). Cross-section locations are indicated in Figure 4.2. Black lines denote timelines at selected simulation output times, while purple lines mark timelines at the breach initiation. Vertical red lines indicate breach locations, and blue horizontal lines represent sea level. The τ_{ce} color scheme reflects different value ranges for non-compacted and compacted scenarios.

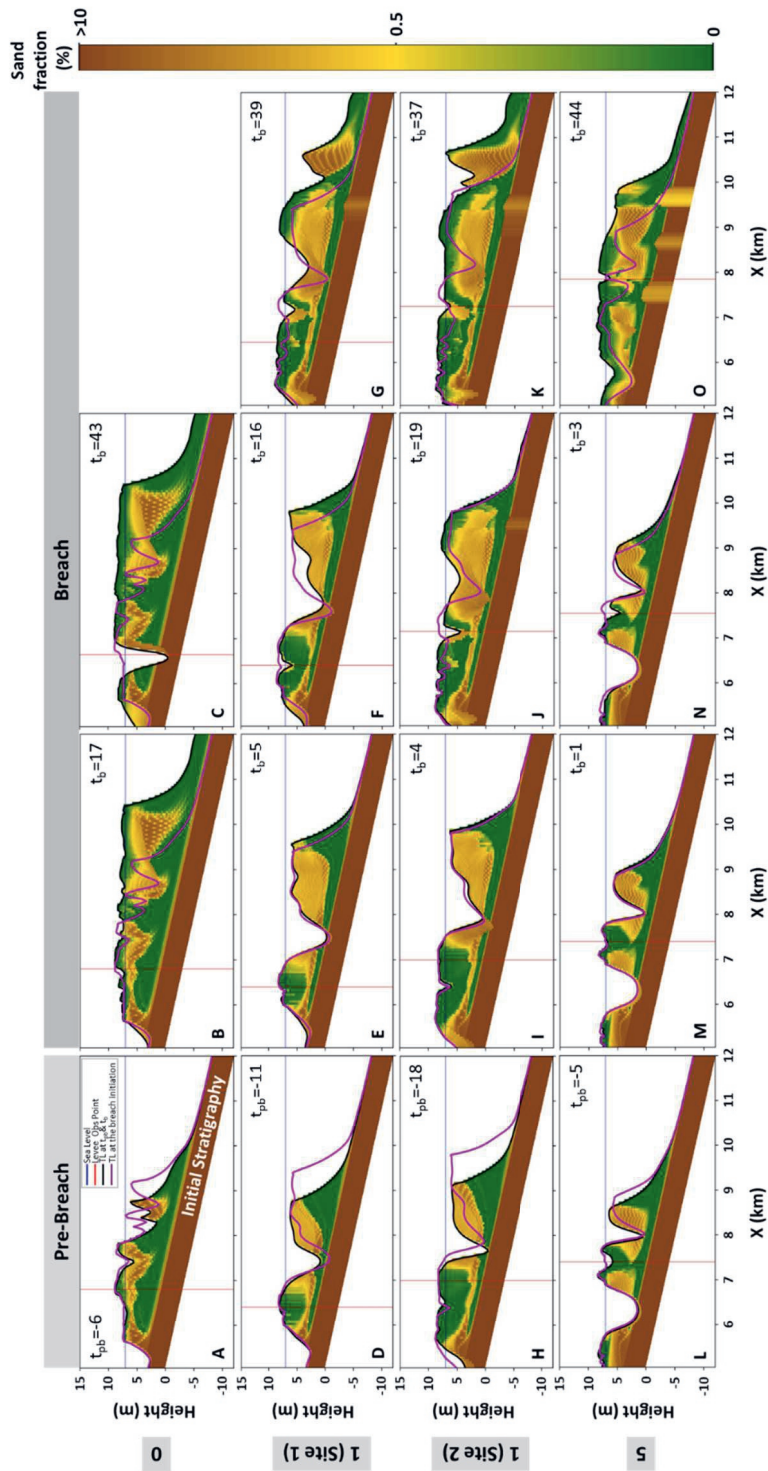


Figure C9. Dip sections of sand fraction traversing levee observation points at breach sites, shown for selected simulation output times during pre-breach and breach across all compaction rate scenarios (A - O). Cross-section locations are indicated in Figure 4.2. Black lines denote timelines at selected simulation output times, while purple lines mark timelines at the breach initiation. Vertical red lines indicate breach locations, and blue horizontal lines represent sea level. The sand fraction color scheme reflects different value ranges for non-compacted and compacted scenarios.

REFERENCES

- Abidin, H. Z., Andreas, H., Gumilar, I., Fukuda, Y., Pohan, Y. E., & Deguchi, T. (2011). Land subsidence of Jakarta (Indonesia) and its relation with urban development. *Natural Hazards*, *59*(3), 1753–1771. <https://doi.org/10.1007/s11069-011-9866-9>
- Ainsworth, R. B., Vakarelov, B. K., MacEachern, J. A., Nanson, R. A., Lane, T. I., Rarity, F., & Dashtgard, S. E. (2016). Process-Driven Architectural Variability In Mouth-Bar Deposits: A Case Study From A Mixed-Process Mouth-Bar Complex, Drumheller, Alberta, Canada. *Journal of Sedimentary Research*, *86*(5), 512–541. <https://doi.org/10.2110/jsr.2016.23>
- Albernaz, M. B., Roelofs, L., Pierik, H. J., & Kleinhans, M. G. (2020). Natural levee evolution in vegetated fluvial-tidal environments. *Earth Surface Processes and Landforms*, *45*(15), 3824–3841. <https://doi.org/10.1002/esp.5003>
- Alberts, L. J. H. (2005). *Initial porosity of random packing: Computer simulation of grain rearrangement* [Doctoral Thesis, Delft University of Technology]. <http://resolver.tudelft.nl/uuid:fa3b8d33-3eda-474a-bebd-87f43dd58873>
- Al-Khafaji, A. W. N., & Andersland, O. B. (1981). Compressibility and strength of decomposing fibre–clay soils. *Géotechnique*, *31*(4), 497–508. <https://doi.org/10.1680/geot.1981.31.4.497>
- Aly, M. H., Klein, A. G., Zebker, H. A., & Giardino, J. R. (2012). Land subsidence in the Nile Delta of Egypt observed by persistent scatterer interferometry. *Remote Sensing Letters*, *3*(7), 621–630. <https://doi.org/10.1080/01431161.2011.652311>
- Amorosi, A., & Marchi, N. (1999). High-resolution sequence stratigraphy from piezocone tests: An example from the Late Quaternary deposits of the southeastern Po Plain. *Sedimentary Geology*, *128*(1), 67–81. [https://doi.org/10.1016/S0037-0738\(99\)00062-7](https://doi.org/10.1016/S0037-0738(99)00062-7)
- Anthony, E. J. (2015). Deltas. In *Coastal Environments and Global Change* (pp. 299–337). <https://doi.org/10.1002/9781119117261.ch13>
- Anthony, E. J., Syvitski, J., Zăinescu, F., Nicholls, R. J., Cohen, K. M., Marriner, N., Saito, Y., Day, J., Minderhoud, P. S. J., Amorosi, A., Chen, Z., Morhange, C., Tamura, T., Vespremeanu-Stroe, A., Besset, M., Sabatier, F., Kaniewski, D., & Maselli, V. (2024). Delta sustainability from the Holocene to the Anthropocene and envisioning the future. *Nature Sustainability*, *7*(10), 1235–1246. <https://doi.org/10.1038/s41893-024-01426-3>
- Aslan, A., Autin, W. J., & Blum, M. D. (2005). Causes of River Avulsion: Insights from the Late Holocene Avulsion History of the Mississippi River, U.S.A. *Journal of Sedimentary Research*, *75*(4), 650–664. <https://doi.org/10.2110/jsr.2005.053>
- Baldan, S., Minderhoud, P. S. J., Xotta, R., Zoccarato, C., & Teatini, P. (2025). Data-driven 3D modelling of long-term Holocene delta evolution and sediment compaction: The Mekong Delta. *Earth Surface Processes and Landforms*, *50*(1), e6046. <https://doi.org/10.1002/esp.6046>
- Bale, A. J., Stephens, J. A., & Harris, C. B. (2007). Critical erosion profiles in macro-tidal estuary sediments: Implications for the stability of intertidal mud and the slope of mud banks. *Continental Shelf Research*, *27*(18), 2303–2312. <https://doi.org/10.1016/j.csr.2007.05.015>
- Bale, A. J., Widdows, J., Harris, C. B., & Stephens, J. A. (2006). Measurements of the critical erosion threshold of surface sediments along the Tamar Estuary using a mini-annular flume. *Continental Shelf Research*, *26*(10), 1206–1216. <https://doi.org/10.1016/j.csr.2006.04.003>
- Baustian, M. M., Meselhe, E., Jung, H., Sadid, K., Duke-Sylvester, S. M., Visser, J. M., Allison, M. A., Moss, L. C., Ramachandiran, C., Maren, D. S. van, Jeuken, M., & Bargu, S. (2018). Development of an Integrated Biophysical Model to represent morphological and ecological processes in a changing deltaic and coastal ecosystem. *Environmental Modelling & Software*, *109*, 402–419. <https://doi.org/10.1016/j.envsoft.2018.05.019>

- Becker, R. H., & Sultan, M. (2009). Land subsidence in the Nile Delta: Inferences from radar interferometry. *The Holocene*, 19(6), 949–954. <https://doi.org/10.1177/0959683609336558>
- Bhattacharya, J. P., & Willis, B. J. (2001). Lowstand Deltas in the Frontier Formation, Powder River Basin, Wyoming: Implications for Sequence Stratigraphic Models. *AAPG Bulletin*, 85(2), 261–294. <https://doi.org/10.1306/8626C7B7-173B-11D7-8645000102C1865D>
- Biot, M. A. (1941). General Theory of Three-Dimensional Consolidation Available to Purchase. *J. Appl. Phys.*, 12, 155–164. <https://doi.org/10.1063/1.1712886>
- Bjerrum, L. (1967). Engineering Geology of Norwegian Normally-Consolidated Marine Clays as Related to Settlements of Buildings. *Géotechnique*, 17(2), 83–118. <https://doi.org/10.1680/geot.1967.17.2.83>
- Bjørlykke, K., & Høeg, K. (1997). Effects of burial diagenesis on stresses, compaction and fluid flow in sedimentary basins. *Marine and Petroleum Geology*, 14(3), 267–276. [https://doi.org/10.1016/S0264-8172\(96\)00051-7](https://doi.org/10.1016/S0264-8172(96)00051-7)
- Bloch, S., Suchecki, R. K., Duncan, J. R., & Bjorlykke, K. (1986). Porosity prediction in quartz-rich sandstones: Middle Jurassic, Haltenbanken area, offshore central Norway. *Am. Assoc. Pet. Geol., Bull. (United States)*, 70:5. <https://www.osti.gov/biblio/5300682>
- Blum, M. D., & Törnqvist, T. E. (2000). Fluvial responses to climate and sea-level change: A review and look forward. *Sedimentology*, 47(s1), 2–48. <https://doi.org/10.1046/j.1365-3091.2000.00008.x>
- Borba, T., Roelvink, T., & Rollnic, M. (2025). Hydrodynamic modelling in the Amazonian Estuary: A flexible mesh approach. *Ocean and Coastal Research*.
- Brierley, G. J., Ferguson, R. J., & Woolfe, K. J. (1997). What is a fluvial levee? *Sedimentary Geology*, 114(1), 1–9. [https://doi.org/10.1016/S0037-0738\(97\)00114-0](https://doi.org/10.1016/S0037-0738(97)00114-0)
- Broadus, C. M., Vulis, L. M., Nienhuis, J. H., Tejedor, A., Brown, J., Foufoula-Georgiou, E., & Edmonds, D. A. (2022). First-Order River Delta Morphology Is Explained by the Sediment Flux Balance From Rivers, Waves, and Tides. *Geophysical Research Letters*, 49(22), e2022GL100355. <https://doi.org/10.1029/2022GL100355>
- Burpee, A. P., Slingerland, R. L., Edmonds, D. A., Parsons, D., Best, J., Cederberg, J., McGuffin, A., Caldwell, R., Nijhuis, A., & Royce, J. (2015). Grain-Size Controls On the Morphology and Internal Geometry of River-Dominated Deltas. *Journal of Sedimentary Research*, 85(6), 699–714. <https://doi.org/10.2110/jsr.2015.39>
- Bussi, G., Darby, S. E., Whitehead, P. G., Jin, L., Dadson, S. J., Voepel, H. E., Vasilopoulos, G., Hackney, C. R., Hutton, C., Berchoux, T., Parsons, D. R., & Nicholas, A. (2021). Impact of dams and climate change on suspended sediment flux to the Mekong delta. *Science of The Total Environment*, 755, 142468. <https://doi.org/10.1016/j.scitotenv.2020.142468>
- Caldwell, R. L., & Edmonds, D. A. (2014). The effects of sediment properties on deltaic processes and morphologies: A numerical modeling study. *Journal of Geophysical Research: Earth Surface*, 119(5), 961–982. <https://doi.org/10.1002/2013JF002965>
- Carlson, B., Piliouras, A., Muto, T., & Kim, W. (2018). Control of Basin Water Depth On Channel Morphology and Autogenic Timescales in Deltaic Systems. *Journal of Sedimentary Research*, 88(9), 1026–1039. <https://doi.org/10.2110/jsr.2018.52>
- Cazanacli, D., & Smith, N. D. (1998). A study of morphology and texture of natural levees—Cumberland Marshes, Saskatchewan, Canada. *Geomorphology*, 25(1), 43–55. [https://doi.org/10.1016/S0169-555X\(98\)00032-4](https://doi.org/10.1016/S0169-555X(98)00032-4)
- Chadwick, A. J., Lamb, M. P., & Ganti, V. (2020). Accelerated river avulsion frequency on lowland deltas due to sea-level rise. *Proceedings of the National Academy of Sciences*, 117(30), 17584–17590. <https://doi.org/10.1073/pnas.1912351117>
- Chadwick, A. J., Steele, S., Silvestre, J., & Lamb, M. P. (2022). Effect of Sea-Level Change on River Avulsions and Stratigraphy for an Experimental Lowland Delta. *Journal of Geophysical Research: Earth Surface*, 127(7), e2021JF006422. <https://doi.org/10.1029/2021JF006422>

- Colombera, L., & Mountney, N. P. (2020). Accommodation and sediment-supply controls on clastic parasequences: A meta-analysis. *Sedimentology*, 67(4), 1667–1709. <https://doi.org/10.1111/sed.12728>
- Dade, W. B., Nowell, A. R. M., & Jumars, P. A. (1992). Predicting erosion resistance of muds. *Marine Geology*, 105(1), 285–297. [https://doi.org/10.1016/0025-3227\(92\)90194-M](https://doi.org/10.1016/0025-3227(92)90194-M)
- Day, J. W., & Giosan, L. (2008). Survive or subside? *Nature Geoscience*, 1(3), 156–157. <https://doi.org/10.1038/ngeo137>
- Deltares. (2021). *Svn repository* (Version 6.02.08.62644) [Computer software]. https://svn.oss.deltares.nl/repos/delft3d/branches/research/Technical%20University%20of%20Delft/20190419_consolidation_compaction_v2/
- Deltares. (2025a). *Delft3D-FLOW, simulation of multi-dimensional hydrodynamic flows and transport phenomena, including sediments, user manual*. Deltares. https://content.oss.deltares.nl/delft3d4/Delft3D-FLOW_User_Manual.pdf
- Deltares. (2025b). *D-Flow Flexible Mesh, computational cores and user interface, user manual*. Deltares. https://content.oss.deltares.nl/delft3d/D-Flow_FM_User_Manual.pdf
- Dong, T. Y., Nittrouer, J. A., Carlson, B., McElroy, B., Il'icheva, E., Pavlov, M., & Ma, H. (2023). Impacts of Tectonic Subsidence on Basin Depth and Delta Lobe Building. *Journal of Geophysical Research: Earth Surface*, 128(2), e2022JF006819. <https://doi.org/10.1029/2022JF006819>
- Drexler, J. Z., de Fontaine, C. S., & Deverel, S. J. (2009). The legacy of wetland drainage on the remaining peat in the Sacramento—San Joaquin Delta, California, USA. *Wetlands*, 29(1), 372–386. <https://doi.org/10.1672/08-97.1>
- Dunne, K. B. J. (2019). *A Sticky Pursuit Of The Threshold Channel: The Effect Of Cohesion On Alluvial River Channel Geometry* [university of pennsylvania]. <https://repository.upenn.edu/handle/20.500.14332/30222>
- Dunnington, H. V. (1967). *Aspects of Diagenesis and Shape Change in Stylolitic Limestone Reservoirs*. WPC-12129.
- Edmonds, D. A., Caldwell, R. L., Brondizio, E. S., & Siani, S. M. O. (2020). Coastal flooding will disproportionately impact people on river deltas. *Nature Communications*, 11(1), 4741. <https://doi.org/10.1038/s41467-020-18531-4>
- Edmonds, D. A., Chadwick, A. J., Lamb, M. P., Lorenzo-Trueba, J., Murray, A. B., Nardin, W., Salter, G., & Shaw, J. B. (2022). 10.09—Morphodynamic Modeling of River-Dominated Deltas: A Review and Future Perspectives. In J. (Jack) F. Shroder (Ed.), *Treatise on Geomorphology (Second Edition)* (pp. 110–140). Academic Press. <https://doi.org/10.1016/B978-0-12-818234-5.00076-6>
- Edmonds, D. A., Paola, C., Hoyal, D. C. J. D., & Sheets, B. A. (2011). Quantitative metrics that describe river deltas and their channel networks. *Journal of Geophysical Research: Earth Surface*, 116(F4). <https://doi.org/10.1029/2010JF001955>
- Edmonds, D. A., & Slingerland, R. L. (2007). Mechanics of river mouth bar formation: Implications for the morphodynamics of delta distributary networks. *Journal of Geophysical Research: Earth Surface*, 112(F2). <https://doi.org/10.1029/2006JF000574>
- Edmonds, D. A., & Slingerland, R. L. (2008). Stability of delta distributary networks and their bifurcations. *Water Resources Research*, 44(9). <https://doi.org/10.1029/2008WR006992>
- Edmonds, D. A., & Slingerland, R. L. (2010). Significant effect of sediment cohesion on delta morphology. *Nature Geoscience*, 3(2), 105–109. <https://doi.org/10.1038/ngeo730>
- Edmonds, D., Slingerland, R., Best, J., Parsons, D., & Smith, N. (2010). Response of river-dominated delta channel networks to permanent changes in river discharge. *Geophysical Research Letters*, 37(12). <https://doi.org/10.1029/2010GL043269>
- Engelund, F., & Hansen, R. L. (1967). *A Monograph on Sediment Transport in Alluvial Streams*. <http://resolver.tudelft.nl/uuid:81101b08-04b5-4082-9121-861949c336c9>
- Esposito, C. R., Shen, Z., Törnqvist, T. E., Marshak, J., & White, C. (2017). Efficient retention of mud drives land building on the Mississippi Delta plain. *Earth Surface Dynamics*, 5(3), 387–397. <https://doi.org/10.5194/esurf-5-387-2017>

- Fagherazzi, S. (2008). Self-organization of tidal deltas. *Proceedings of the National Academy of Sciences*, 105(48), 18692–18695. <https://doi.org/10.1073/pnas.0806668105>
- Fagherazzi, S., Kirwan, M. L., Mudd, S. M., Guntenspergen, G. R., Temmerman, S., D'Alpaos, A., van de Koppel, J., Rybczyk, J. M., Reyes, E., Craft, C., & Clough, J. (2012). Numerical models of salt marsh evolution: Ecological, geomorphic, and climatic factors. *Reviews of Geophysics*, 50(1). <https://doi.org/10.1029/2011RG000359>
- Feng, W.-J., Zhang, C.-M., Yin, T.-J., Yin, Y.-S., Liu, J.-L., Zhu, R., Xu, Q.-H., & Chen, Z. (2019). Sedimentary characteristics and internal architecture of a river-dominated delta controlled by autogenic process: Implications from a flume tank experiment. *Petroleum Science*, 16(6), 1237–1254. <https://doi.org/10.1007/s12182-019-00389-x>
- Fielding, C. R. (1985). Coal depositional models and the distinction between alluvial and delta plain environments. *Sedimentary Geology*, 42(1), 41–48. [https://doi.org/10.1016/0037-0738\(85\)90072-7](https://doi.org/10.1016/0037-0738(85)90072-7)
- Filgueira-Rivera, M., Smith, N. D., & Slingerland, R. L. (2007). Controls on natural levée development in the Columbia River, British Columbia, Canada. *Sedimentology*, 54(4), 905–919. <https://doi.org/10.1111/j.1365-3091.2007.00865.x>
- Galappatti, R. (1983). *A Depth Integrated Model for Suspended Transport*. Delft University of Technology. <http://resolver.tudelft.nl/uuid:2cf67a5b-d2c4-4287-8ed2-16f1b27bdbcc>
- Galloway, W. E. (1975). *Process framework for describing the morphologic and stratigraphic evolution of deltaic depositional systems*.
- Gambolati, G. (1973a). Equation for one-dimensional vertical flow of groundwater: 1. The Rigorous Theory. *Water Resources Research*, 9(4), 1022–1028. <https://doi.org/10.1029/WR009i004p01022>
- Gambolati, G. (1973b). Equation for one-dimensional vertical flow of groundwater: 2. Validity range of the diffusion equation. *Water Resources Research*, 9(5), 1385–1395. <https://doi.org/10.1029/WR009i005p01385>
- Ganti, V., Chadwick, A. J., Hassenruck-Gudipati, H. J., & Lamb, M. P. (2016). Avulsion cycles and their stratigraphic signature on an experimental backwater-controlled delta. *Journal of Geophysical Research: Earth Surface*, 121(9), 1651–1675. <https://doi.org/10.1002/2016JF003915>
- Gearon, J. H., & Edmonds, D. A. (2025). River Avulsion Precursors Encoded in Alluvial Ridge Geometry. *Geophysical Research Letters*, 52(8), e2024GL114047. <https://doi.org/10.1029/2024GL114047>
- Gearon, J. H., Martin, H. K., DeLisle, C., Barefoot, E. A., Mohrig, D., Paola, C., & Edmonds, D. A. (2024). Rules of river avulsion change downstream. *Nature*, 634(8032), 91–95. <https://doi.org/10.1038/s41586-024-07964-2>
- Gebremichael, E., Sultan, M., Becker, R., El Bastawesy, M., Cherif, O., & Emil, M. (2018). Assessing Land Deformation and Sea Encroachment in the Nile Delta: A Radar Interferometric and Inundation Modeling Approach. *Journal of Geophysical Research: Solid Earth*, 123(4), 3208–3224. <https://doi.org/10.1002/2017JB015084>
- Geleynse, N., Storms, J. E. A., Stive, M. J. F., Jagers, H. R. A., & Walstra, D. J. R. (2010). Modeling of a mixed-load fluvio-deltaic system. *Geophysical Research Letters*, 37(5). <https://doi.org/10.1029/2009GL042000>
- Geleynse, N., Storms, J. E. A., Walstra, D.-J. R., Jagers, H. R. A., Wang, Z. B., & Stive, M. J. F. (2011). Controls on river delta formation; insights from numerical modelling. *Earth and Planetary Science Letters*, 302(1), 217–226. <https://doi.org/10.1016/j.epsl.2010.12.013>
- Gibson, R. E., England, G. L., & Hussey, M. J. L. (1967). The Theory of One-Dimensional Consolidation of Saturated Clays: 1. Finite Non-Linear Consolidation of Thin Homogeneous Layers. *Géotechnique*, 17(3), 261–273. <https://doi.org/10.1680/geot.1967.17.3.261>
- Giles, M. R., Indrelid, S. L., & James, D. M. D. (1998). Compaction—The great unknown in basin modelling. *Geological Society, London, Special Publications*, 141(1), 15–43. <https://doi.org/10.1144/GSL.SP.1998.141.01.02>
- Goodbred, S. L., Kuehl, S. A., Steckler, M. S., & Sarker, M. H. (2003). Controls on facies distribution and stratigraphic preservation in the Ganges–Brahmaputra delta sequence. *Sedimentary Geology*, 155(3), 301–316. [https://doi.org/10.1016/S0037-0738\(02\)00184-7](https://doi.org/10.1016/S0037-0738(02)00184-7)

- Grabowski, R. C., Droppo, I. G., & Wharton, G. (2011). Erodibility of cohesive sediment: The importance of sediment properties. *Earth-Science Reviews*, 105(3), 101–120. <https://doi.org/10.1016/j.earscirev.2011.01.008>
- Greensmith, J. T., & Tucker, E. V. (1986). Compaction and consolidation. In O. van de Plassche (Ed.), *Sea-Level Research: A manual for the collection and evaluation of data* (pp. 591–603). Springer Netherlands. https://doi.org/10.1007/978-94-009-4215-8_22
- Hajek, E. A., & Edmonds, D. A. (2014). Is river avulsion style controlled by floodplain morphodynamics? *Geology*, 42(3), 199–202. <https://doi.org/10.1130/G35045.1>
- Han, J., Kim, W., & Edmonds, D. A. (2025). Assessing Channel Bank-Height Adjustments and Flood Frequency Trends in a Dynamic Channel-Levee Evolution Model. *Journal of Geophysical Research: Earth Surface*, 130(3), e2024JF008137. <https://doi.org/10.1029/2024JF008137>
- Hariharan, J., Passalacqua, P., Xu, Z., Michael, H. A., Steel, E., Chadwick, A., Paola, C., & Moodie, A. J. (2022). Modeling the Dynamic Response of River Deltas to Sea-Level Rise Acceleration. *Journal of Geophysical Research: Earth Surface*, 127(9), e2022JF006762. <https://doi.org/10.1029/2022JF006762>
- Higgins, S. A., Overeem, I., Steckler, M. S., Syvitski, J. P. M., Seeber, L., & Akhter, S. H. (2014). InSAR measurements of compaction and subsidence in the Ganges-Brahmaputra Delta, Bangladesh. *Journal of Geophysical Research: Earth Surface*, 119(8), 1768–1781. <https://doi.org/10.1002/2014JF003117>
- Hillen, M. M., Geleynse, N., Storms, J. E. A., Walstra, D. J. R., & Groenenberg, R. M. (2014). Morphodynamic modelling of wave reworking of an alluvial delta and application of results in the standard reservoir modelling workflow. In *From Depositional Systems to Sedimentary Successions on the Norwegian Continental Margin* (pp. 167–185). John Wiley & Sons, Ltd. <https://doi.org/10.1002/9781118920435.ch8>
- Hoitink, A. J. F., Wang, Z. B., Vermeulen, B., Huisman, Y., & Kästner, K. (2017). Tidal controls on river delta morphology. *Nature Geoscience*, 10(9), 637–645. <https://doi.org/10.1038/ngeo3000>
- Houwing, E. J. 1963-. (2000). *Sediment dynamics in the pioneer zone in the land reclamation area of the Wadden Sea, Groningen, The Netherlands* [s.n.]. WorldCat.org.
- Houwing, E.-J. (1999). Determination of the Critical Erosion Threshold of Cohesive Sediments on Intertidal Mudflats Along the Dutch Wadden Sea Coast. *Estuarine, Coastal and Shelf Science*, 49(4), 545–555. <https://doi.org/10.1006/ecss.1999.0518>
- Hoyal, D. C. J. D., & Sheets, B. A. (2009). Morphodynamic evolution of experimental cohesive deltas. *Journal of Geophysical Research: Earth Surface*, 114(F2). <https://doi.org/10.1029/2007JF000882>
- Jacobs, W. (2011). *Sand-mud erosion from a soil mechanical perspective* [Doctoral Thesis, Delft University of Technology]. <http://resolver.tudelft.nl/uuid:6d908f04-14fd-47f3-b292-af4b99a8fb11>
- Jerolmack, D. J. (2009). Conceptual framework for assessing the response of delta channel networks to Holocene sea level rise. *Quaternary Ice Sheet-Ocean Interactions and Landscape Responses*, 28(17), 1786–1800. <https://doi.org/10.1016/j.quascirev.2009.02.015>
- Jerolmack, D. J., & Paola, C. (2007). Complexity in a cellular model of river avulsion. *38th Binghamton Geomorphology Symposium: Complexity in Geomorphology*, 91(3), 259–270. <https://doi.org/10.1016/j.geomorph.2007.04.022>
- Jerolmack, D. J., & Swenson, J. B. (2007). Scaling relationships and evolution of distributary networks on wave-influenced deltas. *Geophysical Research Letters*, 34(23). <https://doi.org/10.1029/2007GL031823>
- Jervey, M. T. (1988). Quantitative Geological Modeling of Siliciclastic Rock Sequences and Their Seismic Expression. In C. K. Wilgus, B. S. Hastings, H. Posamentier, J. V. Wagoner, C. A. Ross, & C. G. St. C. Kendall (Eds.), *Sea-Level Changes: An Integrated Approach* (Vol. 42, p. 0). Society of Economic Paleontologists and Mineralogists. <https://doi.org/10.2110/pec.88.01.0047>
- Jones, L. S., & Schumm, S. A. (1999). Causes of Avulsion: An Overview. In *Fluvial Sedimentology VI* (pp. 169–178). <https://doi.org/10.1002/9781444304213.ch13>
- Kaliakin, V. N. (2017). *Soil Mechanics: Calculations, principles, and methods*. Butterworth-Heinemann. <https://www.sciencedirect.com/book/9780128044919/soil-mechanics>

- Kamphuis, J. W., & Hall, K. R. (1983). Cohesive Material Erosion by Unidirectional Current. *Journal of Hydraulic Engineering*, 109(1), 49–61. [https://doi.org/10.1061/\(ASCE\)0733-9429\(1983\)109:1\(49\)](https://doi.org/10.1061/(ASCE)0733-9429(1983)109:1(49))
- Kolker, A. S., Weathers, H. D., Swann, C., & Renfro, A. A. (2025). Distributary development in a 21st century river: The evolution of Neptune Pass and its delta, the largest new offshoot of the Mississippi River. *PLOS ONE*, 20(4), e0320502. <https://doi.org/10.1371/journal.pone.0320502>
- Koss, J. E., Ethridge, F. G., & Schumm, S. A. (1994). An experimental study of the effects of base-level change on fluvial, coastal plain and shelf systems. *Journal of Sedimentary Research*, 64(2b), 90–98. <https://doi.org/10.1306/D4267F64-2B26-11D7-8648000102C1865D>
- Kozlowski, T. T. (1999). Soil Compaction and Growth of Woody Plants. *Scandinavian Journal of Forest Research*, 14(6), 596–619. <https://doi.org/10.1080/02827589908540825>
- Lafren, J. M., & Beasley, R. P. (1960). *Effect of compaction on critical tractive forces in cohesive soils*. University of Missouri, College of Agriculture, Agricultural Experiment Station. <https://core.ac.uk/download/pdf/75907508.pdf>
- Lauzon, R., & Murray, A. B. (2018). Comparing the Cohesive Effects of Mud and Vegetation on Delta Evolution. *Geophysical Research Letters*, 45(19), 10,437-10,445. <https://doi.org/10.1029/2018GL079405>
- Lauzon, R., & Murray, A. B. (2022). Discharge Determines Avulsion Regime in Model Experiments With Vegetated and Unvegetated Deltas. *Journal of Geophysical Research: Earth Surface*, 127(2), e2021JF006225. <https://doi.org/10.1029/2021JF006225>
- Leonardi, N., Canestrelli, A., Sun, T., & Fagherazzi, S. (2013). Effect of tides on mouth bar morphology and hydrodynamics. *Journal of Geophysical Research: Oceans*, 118(9), 4169–4183. <https://doi.org/10.1002/jgrc.20302>
- Lesser, G. R., Roelvink, J. A., Kester, J. A. T. M. van, & Stelling, G. S. (2004). Development and validation of a three-dimensional morphological model. *Coastal Engineering*, 51(8), 883–915. <https://doi.org/10.1016/j.coastaleng.2004.07.014>
- Li, L., Storms, J. E. A., & Walstra, D. J. R. (2018). On the upscaling of process-based models in deltaic applications. *Geomorphology*, 304, 201–213. <https://doi.org/10.1016/j.geomorph.2017.10.015>
- Liang, M., Kim, W., & Passalacqua, P. (2016). How much subsidence is enough to change the morphology of river deltas? *Geophysical Research Letters*, 43(19), 10,266-10,276. <https://doi.org/10.1002/2016GL070519>
- Liang, M., Van Dyk, C., & Passalacqua, P. (2016). Quantifying the patterns and dynamics of river deltas under conditions of steady forcing and relative sea level rise. *Journal of Geophysical Research: Earth Surface*, 121(2), 465–496. <https://doi.org/10.1002/2015JF003653>
- Lianqiang, S., Jiufa ,Li, Ping ,Dong, Ming ,Ying, Weihua ,Li, & and Shenliang, C. (2007). An Experiment Study of Erosion Characteristics of Sediment Bed at the Yellow River Delta. *Coastal Engineering Journal*, 49(1), 25–43. <https://doi.org/10.1142/S0578563407001526>
- Lim, S. S. (2006). *Experimental Investigation of Erosion in Variably Saturated Clay Soils* [School of Civil and Environment Engineering, The University of New South Wales]. <https://doi.org/10.26190/unsworks/15980>
- Liu, Y., Huang, H., Liu, Y., & Bi, H. (2016). Linking land subsidence over the Yellow River delta, China, to hydrocarbon exploitation using multi-temporal InSAR. *Natural Hazards*, 84(1), 271–291. <https://doi.org/10.1007/s11069-016-2427-5>
- Malarkey, J., Baas, J. H., Hope, J. A., Aspden, R. J., Parsons, D. R., Peakall, J., Paterson, D. M., Schindler, R. J., Ye, L., Lichtman, I. D., Bass, S. J., Davies, A. G., Manning, A. J., & Thorne, P. D. (2015). The pervasive role of biological cohesion in bedform development. *Nature Communications*, 6(1), 6257. <https://doi.org/10.1038/ncomms7257>
- Martin, J., Sheets, B., Paola, C., & Hoyal, D. (2009). Influence of steady base-level rise on channel mobility, shoreline migration, and scaling properties of a cohesive experimental delta. *Journal of Geophysical Research: Earth Surface*, 114(F3). <https://doi.org/10.1029/2008JF001142>

- Meckel, T. A., ten Brink, U. S., & Williams, S. J. (2006). Current subsidence rates due to compaction of Holocene sediments in southern Louisiana. *Geophysical Research Letters*, 33(11). <https://doi.org/10.1029/2006GL026300>
- Meckel, T. A., Ten Brink, U. S., & Williams, S. J. (2007). Sediment compaction rates and subsidence in deltaic plains: Numerical constraints and stratigraphic influences. *Basin Research*, 19(1), 19–31. <https://doi.org/10.1111/j.1365-2117.2006.00310.x>
- Merckelbach, L. M., & Kranenburg, C. (2004). Determining effective stress and permeability equations for soft mud from simple laboratory experiments. *Géotechnique*, 54(9), 581–591. <https://doi.org/10.1680/geot.2004.54.9.581>
- Mesri, G. (2003). Primary Compression and Secondary Compression. In *Soil Behavior and Soft Ground Construction* (pp. 122–166). [https://doi.org/10.1061/40659\(2003\)5](https://doi.org/10.1061/40659(2003)5)
- Mesri, G., & Ajlouni, M. (2007). Engineering Properties of Fibrous Peats. *Journal of Geotechnical and Geoenvironmental Engineering*, 133(7), 850–866. [https://doi.org/10.1061/\(ASCE\)1090-0241\(2007\)133:7\(850\)](https://doi.org/10.1061/(ASCE)1090-0241(2007)133:7(850))
- Mesri, G., & Castro, A. (1987). Ca/Cc Concept and K0 During Secondary Compression. *Journal of Geotechnical Engineering*, 113(3), 230–247. [https://doi.org/10.1061/\(ASCE\)0733-9410\(1987\)113:3\(230\)](https://doi.org/10.1061/(ASCE)0733-9410(1987)113:3(230))
- Mesri, G., Stark, T. D., Ajlouni, M. A., & Chen, C. S. (1997). Secondary Compression of Peat with or without Surcharging. *Journal of Geotechnical and Geoenvironmental Engineering*, 123(5), 411–421. [https://doi.org/10.1061/\(ASCE\)1090-0241\(1997\)123:5\(411\)](https://doi.org/10.1061/(ASCE)1090-0241(1997)123:5(411))
- Meysman, F. J. R., Middelburg, J. J., & Heip, C. H. R. (2006). Bioturbation: A fresh look at Darwin's last idea. *Trends in Ecology & Evolution*, 21(12), 688–695. <https://doi.org/10.1016/j.tree.2006.08.002>
- Milliman, J. D., & Farnsworth, K. L. (2011). *River Discharge to the Coastal Ocean: A Global Synthesis*. Cambridge University Press; Cambridge Core. <https://doi.org/10.1017/CBO9780511781247>
- Minderhoud, P. S. J., Coumou, L., Erban, L. E., Middelkoop, H., Stouthamer, E., & Addink, E. A. (2018). The relation between land use and subsidence in the Vietnamese Mekong delta. *Science of The Total Environment*, 634, 715–726. <https://doi.org/10.1016/j.scitotenv.2018.03.372>
- Minderhoud, P. S. J., Erkens, G., Pham, V. H., Bui, V. T., Erban, L., Kooi, H., & Stouthamer, E. (2017). Impacts of 25 years of groundwater extraction on subsidence in the Mekong delta, Vietnam. *Environmental Research Letters*, 12(6), 064006. <https://doi.org/10.1088/1748-9326/aa7146>
- Minderhoud, P. S. J., Middelkoop, H., Erkens, G., & Stouthamer, E. (2020). Groundwater extraction may drown mega-delta: Projections of extraction-induced subsidence and elevation of the Mekong delta for the 21st century. *Environmental Research Communications*, 2(1), 011005. <https://doi.org/10.1088/2515-7620/ab5e21>
- Moqsud, M. A., & Gochi, T. (2024). Evaluation of biocementation of slope soil for erosion control with low-cost materials. *Scientific Reports*, 14(1), 16065. <https://doi.org/10.1038/s41598-024-67185-5>
- Morton, R. A., & Bernier, J. C. (2010). Recent Subsidence-Rate Reductions in the Mississippi Delta and Their Geological Implications. *Journal of Coastal Research*, 26(3 (263)), 555–561. <https://doi.org/10.2112/JCOASTRES-D-09-00014R1.1>
- Mostafa, T. S., Imran, J., Chaudhry, M. M. H., & Kahn, M. I. B. (2008). Erosion resistance of cohesive soils. *Journal of Hydraulic Research*, 46(6), 777–787. <https://doi.org/10.1080/00221686.2008.9521922>
- Muto, T., & Steel, R. J. (1997). Principles of regression and transgression; the nature of the interplay between accommodation and sediment supply. *Journal of Sedimentary Research*, 67(6), 994–1000. <https://doi.org/10.1306/D42686A8-2B26-11D7-8648000102C1865D>
- Muto, T., & Steel, R. J. (2000). The accommodation concept in sequence stratigraphy: Some dimensional problems and possible redefinition. *Sedimentary Geology*, 130(1), 1–10. [https://doi.org/10.1016/S0037-0738\(99\)00107-4](https://doi.org/10.1016/S0037-0738(99)00107-4)

- Muto, T., & Steel, R. J. (2001). Autostepping during the transgressive growth of deltas: Results from flume experiments. *Geology*, 29(9), 771–774. [https://doi.org/10.1130/0091-7613\(2001\)029%253C0771:ADTTGO%253E2.0.CO;2](https://doi.org/10.1130/0091-7613(2001)029%253C0771:ADTTGO%253E2.0.CO;2)
- Nardin, W., & Edmonds, D. A. (2014). Optimum vegetation height and density for inorganic sedimentation in deltaic marshes. *Nature Geoscience*, 7(10), 722–726. <https://doi.org/10.1038/ngeo2233>
- Nardin, W., & Fagherazzi, S. (2012). The effect of wind waves on the development of river mouth bars. *Geophysical Research Letters*, 39(12). <https://doi.org/10.1029/2012GL051788>
- Nardin, W., Mariotti, G., Edmonds, D. A., Guercio, R., & Fagherazzi, S. (2013). Growth of river mouth bars in sheltered bays in the presence of frontal waves. *Journal of Geophysical Research: Earth Surface*, 118(2), 872–886. <https://doi.org/10.1002/jgrf.20057>
- Nicholls, R. J., & Cazenave, A. (2010). Sea-Level Rise and Its Impact on Coastal Zones. *Science*, 328(5985), 1517–1520. <https://doi.org/10.1126/science.1185782>
- Nienhuis, J. H., Ashton, A. D., Edmonds, D. A., Hoitink, A. J. F., Kettner, A. J., Rowland, J. C., & Törnqvist, T. E. (2020). Global-scale human impact on delta morphology has led to net land area gain. *Nature*, 577(7791), 514–518. <https://doi.org/10.1038/s41586-019-1905-9>
- Nienhuis, J. H., Kim, W., Milne, G. A., Quock, M., Slangen, A. B. A., & Törnqvist, T. E. (2023). River Deltas and Sea-Level Rise. In *Annual Review of Earth and Planetary Sciences* (Vol. 51, Issue Volume 51, 2023, pp. 79–104). Annual Reviews. <https://doi.org/10.1146/annurev-earth-031621-093732>
- Nienhuis, J. H., Törnqvist, T. E., & Esposito, C. R. (2018). Crevasse Splays Versus Avulsions: A Recipe for Land Building With Levee Breaches. *Geophysical Research Letters*, 45(9), 4058–4067. <https://doi.org/10.1029/2018GL077933>
- Okon, L.-U. E., Seelam, J. K., Hemanath, L., Thomas, J., & Narine, R. (2025). Hypothesis-driven sensitivity analysis of Delft3D flexible mesh hydrodynamic model: Insights into coastal processes in the monsoonal tropical Goa Coast, India. *Ocean Dynamics*, 75(9), 79. <https://doi.org/10.1007/s10236-025-01724-0>
- Olariu, C., Zhou, C., Steel, R., Zhang, Z., Yuan, X., Zhang, J., Chen, S., Cheng, D., & Kim, W. (2021). Controls on the stratal architecture of lacustrine delta successions in low-accommodation conditions. *Sedimentology*, 68(5), 1941–1963. <https://doi.org/10.1111/sed.12838>
- Orton, G. J., & Reading, H. G. (1993). Variability of deltaic processes in terms of sediment supply, with particular emphasis on grain size. *Sedimentology*, 40(3), 475–512. <https://doi.org/10.1111/j.1365-3091.1993.tb01347.x>
- Osman, N., & Barakbah, S. S. (2006). Parameters to predict slope stability—Soil water and root profiles. *Ecological Engineering*, 28(1), 90–95. <https://doi.org/10.1016/j.ecoleng.2006.04.004>
- Overeem, I., Hudson, B. D., Syvitski, J. P. M., Mikkelsen, A. B., Hasholt, B., van den Broeke, M. R., Noël, B. P. Y., & Morlighem, M. (2017). Substantial export of suspended sediment to the global oceans from glacial erosion in Greenland. *Nature Geoscience*, 10(11), 859–863. <https://doi.org/10.1038/ngeo3046>
- Overeem, I., Nienhuis, J. H., & Piliouras, A. (2022). Ice-dominated Arctic deltas. *Nature Reviews Earth & Environment*, 3(4), 225–240. <https://doi.org/10.1038/s43017-022-00268-x>
- Panagiotopoulos, I., Voulgaris, G., & Collins, M. B. (1997). The influence of clay on the threshold of movement of fine sandy beds. *Coastal Engineering*, 32(1), 19–43. [https://doi.org/10.1016/S0378-3839\(97\)00013-6](https://doi.org/10.1016/S0378-3839(97)00013-6)
- Partheniades, E. (1965). Erosion and Deposition of Cohesive Soils. *Journal of the Hydraulics Division*, 91(1), 105–139. <https://doi.org/10.1061/JYCEAJ.0001165>
- Paumard, V., Bourget, J., Payenberg, T., George, A. D., Ainsworth, R. B., Lang, S., & Posamentier, H. W. (2020). Controls On Deep-Water Sand Delivery Beyond the Shelf Edge: Accommodation, Sediment Supply, and Deltaic Process Regime. *Journal of Sedimentary Research*, 90(1), 104–130. <https://doi.org/10.2110/jsr.2020.2>
- Perez-Arlucea, M., & Smith, N. D. (1999). Depositional patterns following the 1870s avulsion of the Saskatchewan River (Cumberland Marshes, Saskatchewan, Canada). *Journal of Sedimentary Research*, 69(1), 62–73. <https://doi.org/10.2110/jsr.69.62>

- Pierik, H. J., Stouthamer, E., & Cohen, K. M. (2017). Natural levee evolution in the Rhine-Meuse delta, the Netherlands, during the first millennium CE. *Geomorphology*, 295, 215–234. <https://doi.org/10.1016/j.geomorph.2017.07.003>
- Pizzuto, J. E., & Schwendt, A. E. (1997). Mathematical modeling of autocompaction of a Holocene transgressive valley-fill deposit, Wolfe Glade, Delaware. *Geology*, 25(1), 57–60. [https://doi.org/10.1130/0091-7613\(1997\)025%253C0057:MMOAOA%253E2.3.CO;2](https://doi.org/10.1130/0091-7613(1997)025%253C0057:MMOAOA%253E2.3.CO;2)
- Porcile, G., Bolla Pittaluga, M., Frascati, A., & Sequeiros, O. E. (2023). Modelling the air-sea-land interactions responsible for the direct trigger of turbidity currents by tropical cyclones. *Applied Ocean Research*, 137, 103602. <https://doi.org/10.1016/j.apor.2023.103602>
- Posamentier, H. W., Jervey, M. T., & Vail, P. R. (1988). Eustatic Controls on Clastic Deposition I—Conceptual Framework. In C. K. Wilgus, B. S. Hastings, H. Posamentier, J. V. Wagoner, C. A. Ross, & C. G. St. C. Kendall (Eds.), *Sea-Level Changes: An Integrated Approach* (Vol. 42, p. 0). SEPM Society for Sedimentary Geology. <https://doi.org/10.2110/pec.88.01.0109>
- Prasojo, O. A., Hoey, T. B., Owen, A., & Williams, R. D. (2025). Influence of alluvial slope on avulsion in river deltas. *Earth Surface Dynamics*, 13(3), 349–363. <https://doi.org/10.5194/esurf-13-349-2025>
- Revil, A., Grauls, D., & Brévert, O. (2002). Mechanical compaction of sand/clay mixtures. *Journal of Geophysical Research: Solid Earth*, 107(B11), ECV 11-1-ECV 11-15. <https://doi.org/10.1029/2001JB000318>
- Ribberink, J. S. (1987). *Mathematical modelling of one-dimensional morphological changes in rivers with nonuniform sediment* [PhD Thesis, Delft University of Technology]. <http://resolver.tudelft.nl/uuid:bdfc1519-a71d-4752-83f7-3ebf1bb890e9>
- Rice, J. A., Simms, A. R., Buzas-Stephens, P., Steel, E., Livsey, D., Reynolds, L. C., Yokoyama, Y., & Halihan, T. (2020). Deltaic response to climate change: The Holocene history of the Nueces Delta. *Global and Planetary Change*, 191, 103213. <https://doi.org/10.1016/j.gloplacha.2020.103213>
- Roberts, J., Jepsen, R., Gotthard, D., & Wilbert, L. (1998). Effects of Particle Size and Bulk Density on Erosion of Quartz Particles. *Journal of Hydraulic Engineering*, 124(12), 1261–1267. [https://doi.org/10.1061/\(ASCE\)0733-9429\(1998\)124:12\(1261\)](https://doi.org/10.1061/(ASCE)0733-9429(1998)124:12(1261))
- Rutter, E. H., & Elliott, D. (1997). A Discussion on natural strain and geological structure—The kinetics of rock deformation by pressure solution. *Philosophical Transactions of the Royal Society of London. Series A, Mathematical and Physical Sciences*, 283(1312), 203–219. <https://doi.org/10.1098/rsta.1976.0079>
- Saleh, M., & Becker, M. (2018). New estimation of Nile Delta subsidence rates from InSAR and GPS analysis. *Environmental Earth Sciences*, 78(1), 6. <https://doi.org/10.1007/s12665-018-8001-6>
- Satriyo, N. A., & Soebowo, E. (2018a). Cone penetration test for facies study: A review. *IOP Conference Series: Earth and Environmental Science*, 118(1), 012007. <https://doi.org/10.1088/1755-1315/118/1/012007>
- Slingerland, R., & Smith, N. D. (1998). Necessary conditions for a meandering-river avulsion. *Geology*, 26(5), 435–438. [https://doi.org/10.1130/0091-7613\(1998\)026%253C0435:NCFAMR%253E2.3.CO;2](https://doi.org/10.1130/0091-7613(1998)026%253C0435:NCFAMR%253E2.3.CO;2)
- Slingerland, R., & Smith, N. D. (2004). River Avulsions and Their Deposits. In *Annual Review of Earth and Planetary Sciences* (Vol. 32, Issue Volume 32, 2004, pp. 257–285). Annual Reviews. <https://doi.org/10.1146/annurev.earth.32.101802.120201>
- Smerdon, E. T., & Beasley, R. P. (1959). *The tractive theory applied to stability of open channels in cohesive soils*. University of Missouri. Agricultural Experiment Station. <https://hdl.handle.net/10355/58141>
- Stanley, D. J. (1990). Recent subsidence and northeast tilting of the Nile delta, Egypt. *Marine Geology*, 94(1), 147–154. [https://doi.org/10.1016/0025-3227\(90\)90108-V](https://doi.org/10.1016/0025-3227(90)90108-V)
- Steckler, M. S., Oryan, B., Wilson, C. A., Grall, C., Noonan, S. L., Mondal, D. R., Akhter, S. H., DeWolf, S., & Goodbred, S. L. (2022). Synthesis of the distribution of subsidence of the lower Ganges-Brahmaputra Delta, Bangladesh. *Earth-Science Reviews*, 224, 103887. <https://doi.org/10.1016/j.earscirev.2021.103887>
- Storms, J. E. A., Beylich, A. A., Hansen, L., & Waldmann, N. (2020). Source to sink reconstruction of a Holocene Fjord-infill: Depositional patterns, suspended sediment yields, wind-induced circulation patterns and

- trapping efficiency for Lake Strynevatnet, inner Nordfjord, Norway. *The Depositional Record*, 6(2), 471–485. <https://doi.org/10.1002/dep2.101>
- Storms, J. E. A., Hoogendoorn, R. M., Dam, R. A. C., Hoitink, A. J. F., & Kroonenberg, S. B. (2005). Late-Holocene evolution of the Mahakam delta, East Kalimantan, Indonesia. *Sedimentary Geology*, 180(3), 149–166. <https://doi.org/10.1016/j.sedgeo.2005.08.003>
- Storms, J. E. A., Stive, M. J. F., Roelvink, D. (J.) A., & Walstra, D. J. (2007). Initial Morphologic and Stratigraphic Delta Evolution Related to Buoyant River Plumes. In *Coastal Sediments '07* (pp. 736–748). [https://doi.org/10.1061/40926\(239\)56](https://doi.org/10.1061/40926(239)56)
- Storms, J. E. A., Stive, M. J. F., Roelvink, D. (J.) A., & Walstra, D. J. (2012). Initial Morphologic and Stratigraphic Delta Evolution Related to Buoyant River Plumes. In *Coastal Sediments '07* (pp. 736–748). [https://doi.org/10.1061/40926\(239\)56](https://doi.org/10.1061/40926(239)56)
- Styllas, M. (2014). A simple approach to define Holocene sequence stratigraphy using borehole and cone penetration test data. *Sedimentology*, 61(2), 444–460. <https://doi.org/10.1111/sed.12061>
- Symonds, A. M., Vijverberg, T., Post, S., van der Spek, B., Henrotte, J., & Sokolewicz, M. (2017). Comparison Between MIKE 21 FM, Delft3D, and Delft3D FM Flow Models of Western Port Bay, Australia. *Coastal Engineering Proceedings*, 1(35), currents.11. <https://doi.org/10.9753/icce.v35.currents.11>
- Syvitski, J., Anthony, E., Saito, Y., Zăinescu, F., Day, J., Bhattacharya, J. P., & Giosan, L. (2022). Large deltas, small deltas: Toward a more rigorous understanding of coastal marine deltas. *Global and Planetary Change*, 218, 103958. <https://doi.org/10.1016/j.gloplacha.2022.103958>
- Syvitski, J. P. M., & Brakenridge, G. R. (2012). *Causation and avoidance of catastrophic flooding along the Indus River, Pakistan*. <https://doi.org/DOI:%252010.1130/GSATG165A.1>
- Syvitski, J. P. M., Kettner, A. J., Overeem, I., Hutton, E. W. H., Hannon, M. T., Brakenridge, G. R., Day, J., Vörösmarty, C., Saito, Y., Giosan, L., & Nicholls, R. J. (2009). Sinking deltas due to human activities. *Nature Geoscience*, 2(10), 681–686. <https://doi.org/10.1038/ngeo629>
- Syvitski, J. P. M., Overeem, I., Brakenridge, G. R., & Hannon, M. (2012). Floods, floodplains, delta plains—A satellite imaging approach. *Sedimentary Geology*, 267–268, 1–14. <https://doi.org/10.1016/j.sedgeo.2012.05.014>
- Syvitski, J. P. M., & Saito, Y. (2007). Morphodynamics of deltas under the influence of humans. *Global and Planetary Change*, 57(3), 261–282. <https://doi.org/10.1016/j.gloplacha.2006.12.001>
- Taheri, Z., Esmaili, K., Samadi Borujeni, H., & Khodashenas, S. R. (2020). Experimental Investigation of the Effect of Consolidation Time on Erosion Rate of cohesive sediment. *Irrigation Sciences and Engineering*, 43(2), 171–186. <https://doi.org/10.22055/jise.2018.25421.1753>
- Tan, G., Wang, J., Shu, C., & Lai, Y. (2007). Effects of Consolidation Time and Particle Size on Scour Rates of Cohesive Sediment. *Journal of Hydrodynamics*, 19(2), 160–164. [https://doi.org/10.1016/S1001-6058\(07\)60043-2](https://doi.org/10.1016/S1001-6058(07)60043-2)
- Taylor, D. W., & Merchant, W. (1940). A Theory of Clay Consolidation Accounting for Secondary Compression. *Journal of Mathematics and Physics*, 19(1–4), 167–185. <https://doi.org/10.1002/sapm1940191167>
- Teatini, P., Tosi, L., & Strozzi, T. (2011). Quantitative evidence that compaction of Holocene sediments drives the present land subsidence of the Po Delta, Italy. *Journal of Geophysical Research: Solid Earth*, 116(B8). <https://doi.org/10.1029/2010JB008122>
- Tengbeh, G. T. (1993). The effect of grass roots on shear strength variations with moisture content. *Soil Technology*, 6(3), 287–295. [https://doi.org/10.1016/0933-3630\(93\)90017-9](https://doi.org/10.1016/0933-3630(93)90017-9)
- Terzaghi, K. von. (1923). *Die Berechnung der Durlässigkeitsziffer des tones aus dem Verlauf der hydronamischen Spannungserscheinungen* (Mathematischnaturwissenschaftliche Klasse. Part IIa 132 (3–4)). Akademie der Wissenschaften.
- Thomsen, L., & Gust, G. (2000). Sediment erosion thresholds and characteristics of resuspended aggregates on the western European continental margin. *Deep Sea Research Part I: Oceanographic Research Papers*, 47(10), 1881–1897. [https://doi.org/10.1016/S0967-0637\(00\)00003-0](https://doi.org/10.1016/S0967-0637(00)00003-0)

- Toorman, E. A. (1996). Sedimentation and self-weight consolidation: General unifying theory. *Géotechnique*, 46(1), 103–113. <https://doi.org/10.1680/geot.1996.46.1.103>
- Toorman, E. A. (1999). Sedimentation and self-weight consolidation: Constitutive equations and numerical modelling. *Géotechnique*, 49(6), 709–726. <https://doi.org/10.1680/geot.1999.49.6.709>
- Torfs, H. (1995). *Erosion of Mud/Sand Mixtures* [Doctoral Thesis, Katholieke Universiteit Leuven]. <https://core.ac.uk/download/pdf/35111687.pdf>
- Torfs, H., Mitchener, H., Huysentruyt, H., & Toorman, E. (1996). Settling and consolidation of mud/sand mixtures. *Coastal Engineering*, 29(1), 27–45. [https://doi.org/10.1016/S0378-3839\(96\)00013-0](https://doi.org/10.1016/S0378-3839(96)00013-0)
- Törnqvist, T. E., & Bridge, J. S. (2002). Spatial variation of overbank aggradation rate and its influence on avulsion frequency. *Sedimentology*, 49(5), 891–905. <https://doi.org/10.1046/j.1365-3091.2002.00478.x>
- Townsend, F. C., & McVay, M. C. (1990). SOA: Large Strain Consolidation Predictions. *Journal of Geotechnical Engineering*, 116(2), 222–243. [https://doi.org/10.1061/\(ASCE\)0733-9410\(1990\)116:2\(222\)](https://doi.org/10.1061/(ASCE)0733-9410(1990)116:2(222))
- Tracy, S. R., Black, C. R., Roberts, J. A., & Mooney, S. J. (2011). Soil compaction: A review of past and present techniques for investigating effects on root growth. *Journal of the Science of Food and Agriculture*, 91(9), 1528–1537. <https://doi.org/10.1002/jsfa.4424>
- USACE. (1990). *Settlement Analysis*. Department of the Army. https://www.publications.usace.army.mil/Portals/76/Publications/EngineerManuals/EM_1110-1-1904.pdf
- van Asselen, S., Karssenbergh, D., & Stouthamer, E. (2011). Contribution of peat compaction to relative sea-level rise within Holocene deltas. *Geophysical Research Letters*, 38(24). <https://doi.org/10.1029/2011GL049835>
- van Asselen, S., Stouthamer, E., & Asch, T. W. J. van. (2009). Effects of peat compaction on delta evolution: A review on processes, responses, measuring and modeling. *Earth-Science Reviews*, 92(1), 35–51. <https://doi.org/10.1016/j.earscirev.2008.11.001>
- van der Vegt, H., Storms, J. E. A., Walstra, D. J. R., & Howes, N. C. (2016). Can bed load transport drive varying depositional behaviour in river delta environments? *Sedimentary Geology*, 345, 19–32. <https://doi.org/10.1016/j.sedgeo.2016.08.009>
- van der Vegt, H., Storms, J. E. A., Walstra, D.-J. R., Nordahl, K., Howes, N. C., & Martinius, A. W. (2020). Grain size fractionation by process-driven sorting in sandy to muddy deltas. *The Depositional Record*, 6(1), 217–235. <https://doi.org/10.1002/dep2.85>
- van Ledden, M., van Kesteren, W. G. M., & Winterwerp, J. C. (2004). A conceptual framework for the erosion behaviour of sand–mud mixtures. *Continental Shelf Research*, 24(1), 1–11. <https://doi.org/10.1016/j.csr.2003.09.002>
- van Rijn, L., Bisschop, R., & Rhee, C. van. (2019). Modified Sediment Pick-Up Function. *Journal of Hydraulic Engineering*, 145(1), 06018017. [https://doi.org/10.1061/\(ASCE\)HY.1943-7900.0001549](https://doi.org/10.1061/(ASCE)HY.1943-7900.0001549)
- van Rijn L. C., Albernaz M. Boechat, Perk L., Alonso A. Colina, van Weerdenburg R. J. A., & van Maren D. S. (2025). Critical Bed-Shear Stress of Mud–Sand Mixtures. *Journal of Hydraulic Engineering*, 151(1), 04024050. <https://doi.org/10.1061/JHEND8.HYENG-14092>
- van Rijn, L., Calina Alonso, A., & van Maren, D. (2020). *Literature Review MUSA: on the interaction between mud and sand*. Musa Project.
- Verruijt, A. (2010). *Soil Mechanics*. TU Delft, Department Hydraulic Engineering. <http://resolver.tudelft.nl/uuid:8f397159-1cd5-4171-a9d4-e1b8d650074b>
- von Terzaghi, K. (1923). *Die Berechnung der Durlässigkeitsziffer des tones aus dem Verlauf der hydronamischen Spannungserscheinungen*. (Vol. 132). Mathematischnaturwissenschaftliche Klasse, Part IIa.
- Wake, L. M., Lecavalier, B. S., & Bevis, M. (2016). Glacial Isostatic Adjustment (GIA) in Greenland: A Review. *Current Climate Change Reports*, 2(3), 101–111. <https://doi.org/10.1007/s40641-016-0040-z>

- Wangen, M. (2001). A quantitative comparison of some mechanisms generating overpressure in sedimentary basins. *Tectonophysics*, 334(3), 211–234. [https://doi.org/10.1016/S0040-1951\(01\)00064-6](https://doi.org/10.1016/S0040-1951(01)00064-6)
- Waples, D. W., & Couples, G. D. (1998). Some thoughts on porosity reduction—Rock mechanics, overpressure and fluid flow. *Geological Society, London, Special Publications*, 141(1), 73–81. <https://doi.org/10.1144/GSL.SP.1998.141.01.04>
- Winterwerp, J. C., & van Kesteren, W. G. M. (2004). *Introduction to the Physics of Cohesive Sediment in the Marine Environment* (Vol. 56). Elsevier.
- Winterwerp, J. C., van Kesteren, W. G. M., van Prooijen, B., & Jacobs, W. (2012). A conceptual framework for shear flow-induced erosion of soft cohesive sediment beds. *Journal of Geophysical Research: Oceans*, 117(C10). <https://doi.org/10.1029/2012JC008072>
- Winterwerp, J. C., Zhou, Z., Battista, G., Kessel, T. V., Jagers, H. R. A., Maren, D. S. V., & Wegen, M. V. D. (2018). Efficient Consolidation Model for Morphodynamic Simulations in Low-SPM Environments. *Journal of Hydraulic Engineering*, 144(8), 04018055. [https://doi.org/10.1061/\(ASCE\)HY.1943-7900.0001477](https://doi.org/10.1061/(ASCE)HY.1943-7900.0001477)
- Wolinsky, M. A., Edmonds, D. A., Martin, J., & Paola, C. (2010). Delta allometry: Growth laws for river deltas. *Geophysical Research Letters*, 37(21). <https://doi.org/10.1029/2010GL044592>
- Wu, W., Perera, C., Smith, J., & Sanchez, A. (2018). Critical shear stress for erosion of sand and mud mixtures. *Journal of Hydraulic Research*, 56(1), 96–110. <https://doi.org/10.1080/00221686.2017.1300195>
- Xotta, R., Zoccarato, C., Minderhoud, P. S. J., & Teatini, P. (2022). Modeling the Role of Compaction in the Three-Dimensional Evolution of Depositional Environments. *Journal of Geophysical Research: Earth Surface*, 127(9), e2022JF006590. <https://doi.org/10.1029/2022JF006590>
- Xu, C., Wei, D., Chen, Y., Yang, Y., Zhang, F., Wang, Y. P., & Jia, J. (2022). Sediment erodibility in the Changjiang (Yangtze) subaqueous delta: Spatial-temporal distribution and sedimentary significance. *Anthropocene Coasts*, 5(1), 10. <https://doi.org/10.1007/s44218-022-00011-5>
- Yang, Y., Gao, S., Wang, Y. P., Jia, J., Xiong, J., & Zhou, L. (2019). Revisiting the problem of sediment motion threshold. *Continental Shelf Research*, 187, 103960. <https://doi.org/10.1016/j.csr.2019.103960>
- Yao, P., Su, M., Wang, Z., van Rijn, L. C., Stive, M. J. F., Xu, C., & Chen, Y. (2022). Erosion Behavior of Sand-Silt Mixtures: Revisiting the Erosion Threshold. *Water Resources Research*, 58(9), e2021WR031788. <https://doi.org/10.1029/2021WR031788>
- You, L., Qu, X., Zhong, J., Li, C., Wu, S., Gao, Y., & Cui, J. (2020). Physical simulation experiments on pore evolution in high-temperature and overpressure reservoirs. *Natural Gas Industry B*, 7(1), 30–39. <https://doi.org/10.1016/j.ngib.2019.07.001>
- Zain, B. H. B. (2019). *Effect of Oxidation on the Compression Behaviour of Organic Soils* [Doctoral Thesis, Delft University of Technology]. <https://doi.org/10.4233/uuid:aa7fe90a-7bf5-4c91-aa3e-c6a594a7d59d>
- Zăinescu, F., Storms, J. E. A., Vespremeanu-Stroe, A., Van Der Vegt, H., Schuster, M., & Anthony, E. (2024). Wave-Influenced Delta Morphodynamics, Long-Term Sediment Bypass and Trapping Controlled by Relative Magnitudes of Riverine and Wave-Driven Sediment Transport. *Geophysical Research Letters*, 51(19), e2024GL111069. <https://doi.org/10.1029/2024GL111069>
- Zhang, J., Kim, W., Olariu, C., & Steel, R. (2019). Accommodation- versus supply-dominated systems for sediment partitioning to deep water. *Geology*, 47(5), 419–422. <https://doi.org/10.1130/G45730.1>
- Zhao, J., Li, J., & Xu, Z. (2018). Advances in the origin of overpressures in sedimentary basins. *Petroleum Research*, 3(1), 1–24. <https://doi.org/10.1016/j.ptlrs.2018.03.007>
- Zheng, S., Edmonds, D. A., Wu, B., & Han, S. (2019). Backwater controls on the evolution and avulsion of the Qingshuigou channel on the Yellow River Delta. *Geomorphology*, 333, 137–151. <https://doi.org/10.1016/j.geomorph.2019.02.032>
- Zhou, Z., van der Wegen, M., Jagers, B., & Coco, G. (2016). Modelling the role of self-weight consolidation on the morphodynamics of accretional mudflats. *Environmental Modelling & Software*, 76, 167–181. <https://doi.org/10.1016/j.envsoft.2015.11.002>

- Zoccarato, C., Minderhoud, P. S. J., & Teatini, P. (2018). The role of sedimentation and natural compaction in a prograding delta: Insights from the mega Mekong delta, Vietnam. *Scientific Reports*, *8*(1), 11437. <https://doi.org/10.1038/s41598-018-29734-7>
- Zoccarato, C., Törnqvist, T. E., Teatini, P., & Bridgeman, J. G. (2020). A shallow compaction model for Holocene Mississippi Delta sediments. *Proceedings of the International Association of Hydrological Sciences*, *382*, 565–570. <https://doi.org/10.5194/piahs-382-565-2020>

ACKNOWLEDGEMENT

Pursuing a PhD is an extraordinary journey, marked by challenges, learning, and growth. It is not only demanding because the research tackles uncharted territory, but also because it requires learning and building many things from scratch. My journey was made even more eventful by personal milestones and adversities: the passing of my beloved father, navigating the COVID-19 pandemic, becoming a parent while pursuing a full-time PhD, working part-time, and working full-time to support my family. It was a lonely road, but I have been fortunate to encounter many supportive individuals along the way.

First and foremost, I express my deepest gratitude to my supervisor, promotor, and friend Joep. Despite my limited background in geology, having been trained as a geophysicist, you believed in my ability to complete this project. Your trust inspired me to persevere through countless obstacles. I recall being an awkward new student struggling with Delft3D modeling, trying to keep up with a steep learning curve. Looking back now, I am proud of how far I have come, and this progress would not have been possible without your patience, guidance, and unwavering support. I am also grateful to my second promotor, Allard for your thoughtful insights and encouragement throughout this PhD journey. Your constructive feedback on the manuscripts and reassuring words motivated me to push forward toward completing my PhD.

To Bert, thank you for your invaluable guidance and patience in answering my many questions about Delft3D. Implementing compaction into the model was one of the most challenging aspects of my PhD, requiring the integration of new formulations within thousands of lines of code. Your support made the seemingly impossible feasible. To Dirk-Jan, thank you for ideas to improve my dissertation, linking me with people from Deltares to support my PhD. Your calm and coolness always inspire me that every problem eventually will have an answer. To Helena, thank you for helping me settle in Delft during the early stages of my PhD. Your assistance with both Delft3D and general geology questions was invaluable. I have drawn much inspiration from your exemplary dissertation, and I am grateful for our continued collaboration in writing papers together.

The PhD common room became a less lonely place because of amazing colleagues like Youwei, Andrea, Emilio, Tim, Akeel, and many others. I will always treasure our conversations, drinks, and dinners. Although COVID-19 and parenthood took me away from many student activities, the memories I gathered with you all remain dear to me and have been a source of strength. I am also grateful for the kind and supportive lecturers and staff in our department, especially Hemmo, Marlijn, Lydia, Margot, Ralf, and Giovanni

Losing my father to cancer during the first year of my PhD was an incredibly difficult time. Being far from home made it even harder. To support my family financially during this time, I took on a part-time job at Sumatra House restaurant in Leiden. Tante Nelly welcomed me warmly and taught me invaluable lessons about running a restaurant. I am grateful to her and her staffs (Mba Christine and Tante Eva) for their kindness, patience, and support during those tough times. My time at Sumatra House not only helped me adapt to a new environment and reality but also gave me the confidence to dream of one day running my own restaurant.

Adjusting to life in the Netherlands was not without its challenges. The climate affected my health, leading to an autoimmune condition that impacted my vision. Managing this while juggling a PhD, parenting, and part-time work was grueling. I am deeply thankful to my GP and doctors in Leiden, whose care and support helped me endure this period.

I also extend my heartfelt thanks to Lin and her husband, our kind neighbor in Leiden who shared meals and taught me about Chinese culture, and to my in-laws, Mas Nabriz and Mbak Ganung, for their unwavering support and love for Aisha, my beloved daughter. The Indonesian community in Leiden, Delft, and across the Netherlands provided a sense of home away from home, with their social events and comforting Indonesian cuisine.

I would also like to thank my colleagues at Universitas Indonesia, Pak Supri, Pak Reza, Bu Ika, Bu Anne, Bu Fatimah, Pak Agus, Pak Bisri, Pak Iskandar, Pak Twin, Bu Asri, Pak Aldo, Pak Urwa, Pak Rezky, Pak Felix, and Pak Octria for their support and encouragement to complete my PhD, especially during moments when balancing my PhD with academic responsibilities felt overwhelming.

To my family—Ayah, Mamak, and Nabil—thank you for supporting my dreams, even when it meant being apart. This journey has been a profound learning experience, introducing me to incredible individuals who have become like family. I look forward to spending more family time together in the future. To my wife, the love of my life, thank you for standing by my side and navigating the unpredictable ups and downs of this journey. Your support has been the foundation of my strength. To Aisha and Raffaza, my dear children, thank you for being understanding and loving. Thank you, Mama, Aisha, and Raffaza. I love you all immensely. Lastly, how could someone become this strong? It is all thanks to the source of all strengths, Rabbul ‘Alamin.

CURRICULUM VITAE

PERSONAL DATA

Full Name : Ayunda Aulia Valencia

E-mail : ayunda.aulia@ui.ac.id

Mobile : +6281359950622



EDUCATION BACKGROUND

PhD Candidate in Applied Geology | TU Delft (2018 - Present)

MSc Petroleum Geoscience | Imperial College London (2015 - 2016) GPA: 3.53

MSc Geophysics | Institut Teknologi Bandung (2011 - 2012) | GPA: 3.76 (Cum Laude)

BSc Geophysics | Institut Teknologi Bandung (2007 - 2011) | GPA: 3.55 (Cum Laude)

WORK EXPERIENCES

Lecturer | Universitas Indonesia (2020 – Present)

- Teach earth science courses, supervise undergraduate student theses, and engage in research collaborations with industry and academic partners.
- Advocate for sustainable geoscience principles in curriculum development and student projects.

Research Associate | Academia Sinica Taiwan (2017)

- Analyse subsurface thermal anomalies for submarine landslide detection.
- Improved past landslide detection to predict future landslides and to contribute to sustainable land planning in areas susceptible to landslide-induced tsunami.

Seismologist | IRD French (2014 – 2015)

- Part of Domerapi Project funded by French government to study the internal structure of Merapi Volcano.
- Conducted acquisition and analysis of earthquake data for mitigating environmental risk and contributing to sustainable hazard mitigation planning.

Geophysicist | PT. Pertamina (2011 – 2015)

- Performed seismic processing and interpretation across various Pertamina fields, utilizing advanced geophysical techniques.
- Optimized resource estimation and minimized environmental risks during drilling operations.

PUBLICATIONS

- Valencia, A.A., Storms, J.E.A., Jagers, H.R.A., van der Vegt, H. (2025). *The influence of syn-depositional compaction on clastic sediment distribution in river-dominated deltas: a modelling study. The Depositional Record. (Q1 Scopus - Indexed)*
- Azizah, M. N., Valencia, A. A., and Kuswanto, A. "Application of Electrical Resistivity Method With Peak and Flat Base Electrodes to Detect A Potential Water Leakage Underneath A Water Pool in Kiara Payung, Sumedang, West Java". *Jurnal Geosains Terapan*, vol. 6, no. 2, October 2024, <https://geosainsterapan.id/index.php/id/article/view/111>.
- Herlambang, K.A., Iskandarsyah, Valencia, A.A. (2024). Utilizing the Gravity Method for Initial Estimation of CO2 Storage Capacity in Supat Field, South Sumatera. *IOP Conference Series: Earth and Environmental Science. (Scopus-Indexed)*
- Rustriandayani, Y., Valencia, A. A., and Fadia, T. R. "Identification of Shallow Aquifer Zone Using Vertical Electrical Sounding (VES) Method With Schlumberger Array. Case Study: Universitas Indonesia". *Jurnal Geosains Terapan*, vol. 6, no. 1, April 2024, <https://geosainsterapan.id/index.php/id/article/view/105>
- Valencia, A.A., Storms, J.E.A., Walstra, D.J.R., van der Vegt, H., Jagers, H.R.A. (2023). *The*

impact of clastic syn-sedimentary compaction on fluvial-dominated delta morphodynamics. The Depositional Record, 9(2), 233-252. (Q1 Scopus - Indexed)

- Phillip, T.B., Jackson, C.A.L., Bell, R.E., Valencia, A.A. (2020). *Rivers, reefs and deltas: geomorphological evolution of the Jurassic of the Farsund Basin, offshore southern Norway. Petroleum Geoscience, 26 (1), 81-100. (Q1 Scopus - Indexed)*
- Ramdhan, M., Nugraha, A.D., Widiyantoro, S., Métaixian, J.P., Valencia, A.A. (2015). *Earthquake location determination using data from DOMERAPI and BMKG seismic networks: a preliminary result of Domerapi Project. AIP Conference Proceedings, 1658 (1), 020007. (Scopus - Indexed)*
- Valencia, A.A., Winardhy, I.S. (2013). *Anisotropy and Maturity Study in Shale Gas Reservoir. SEGJ – Japan. (Scopus - Indexed)*



